DISSERTATION

USING CHEMICAL IONIZATION MASS SPECTROMETRY TO PROBE INDOOR AND OUTDOOR ATMOSPHERIC CHEMISTRY

Submitted by

James M. Mattila

Department of Chemistry

In partial fulfillment of the requirements

For the Degree of Doctor of Philosophy

Colorado State University

Fort Collins, Colorado

Spring 2021

Doctoral Committee:

Advisor: Delphine K. Farmer

Melissa M. Reynolds
Megan D. Willis
Ellison M. Carter

ABSTRACT

USING CHEMICAL IONIZATION MASS SPECTROMETRY TO PROBE INDOOR AND OUTDOOR ATMOSPHERIC CHEMISTRY

People spend the majority of their time in indoor environments. Knowledge of the sources, sinks, and chemistry of indoor pollutants is therefore imperative to indoor air quality and human health. We studied the indoor chemistry of cooking and cleaning at the House Observations of Microbial and Environmental Chemistry (HOMEChem) field campaign during summer 2018 at the University of Texas test house (UTest house) in Austin, TX. We performed measurements of several gas-phase cooking- and cleaning-related analytes using a fast (1 Hz), online chemical ionization mass spectrometry (CIMS) measurement technique utilizing iodide reagent ions. Combining these and other measurements of gas-phase analytes and particulate matter present in indoor air during HOMEChem enables us to piece together a holistic story of the indoor chemistry of cooking and cleaning.

We observed enhanced levels of several chlorinated and nitrogenated compounds when cleaning indoors with a commercial bleach solution during HOMEChem. We observed production of several inorganic chlorinated and nitrogenated pollutants from bleaching, including hypochlorous acid, chlorine gas, and chloramines. Levels of hypochlorous acid and nitrogen trichloride observed during cleaning are likely detrimental to human health. Bleach cleaning indoors also lead to the production of secondary organic aerosol—a common outdoor atmospheric pollutant associated with respiratory and cardiovascular issues—as well as potentially harmful organic isocyanates, cyanogen chloride, and chlorocarbons. These results

collectively demonstrate bleach cleaning as a source of indoor pollution which impacts indoor air quality and occupant health.

We characterized indoor reactive organic carbon (ROC) emissions from cooking and cleaning during HOMEChem, and directly compared resultant chemical complexity of indoor air to outdoors. Cooking indoors greatly impacts ROC concentrations and physiochemical properties, and thus carbon reactivities and lifetimes. Cleaning indoors yielded relatively insubstantial changes. Consistently higher indoor ROC concentrations compared to outdoors demonstrated that indoor emissions were a net source of reactive carbon to the outdoor atmosphere, following their removal by ventilation. ROC dominated indoor and outdoor oxidant reactivity compared to other atmospheric carbon species, thereby greatly influencing secondary pollutant formation, including carbon dioxide, ozone, and secondary particulate matter. Most oxidation chemistry to produce these secondary pollutants likely took place outdoors following the ventilation of ROC species, given the low oxidant levels typical of indoor environments.

Moving outdoors, we demonstrated the efficacy of a CIMS instrument utilizing acetate ionization toward quantifying various gas-phase acids in the troposphere. Here, we performed measurements during the Front Range Air Pollution and Photochemistry Experiment (FRAPPE) field campaign in summer 2014. Diurnal increases in mixing ratios were consistent with photochemical sources of nitric, isocyanic, formic, propionic, butyric, valeric, and pyruvic acid. Vertical profiles taken on the 300 m Boulder Atmospheric Observatory tower demonstrated net surface-level emissions of alkanoic acids, but net surface deposition of nitric and pyruvic acid. Nearby traffic emissions and agricultural activity were a primary source of propionic, butyric, and valeric acids, and likely contributed photochemical precursors to nitric and isocyanic acids. The combined diel and vertical profiles of the alkanoic acids and isocyanic acid were

inconsistent with dry deposition and photochemical losses being the only sinks, suggesting additional loss mechanisms.

ACKNOWLEDGEMENTS

Thanks to Dr. Delphine Farmer and the Farmer Group. You are some of the most intelligent and down to earth people I've ever had the pleasure working with. My time spent in this group has solidified my passion for atmospheric and analytical chemistry, and provided such incredible opportunities for multidisciplinary science. It has truly been a privilege. Many thanks to the HOMEChem science team, Paula Olsiewski and the Alfred P. Sloan Foundation, and all others who made possible a field campaign experience that was simultaneously the most stressful and most fun point in my academic career. I also owe my gratitude to past advisors and professors, namely Dr. Christine Hughey, Dr. Isaiah Sumner, Dr. Barbara Reisner, and Dr. Paul Warne, whose passion for education has greatly influenced my approach to science and learning. Finally, I would like to thank Peggy, Jim, Alexis, Helena, and all my other family and friends—I would not be where I am today without your love and support.

DEDICATION

For Daniel Havey

TABLE OF CONTENTS

CHAPTER 1 – ADVANCING KNOWLEDGE OF OUTDOOR AND INDOOR ATMOSPHERIC CHEMISTRY WITH CHEMICAL IONIZATION MASS SPECTROMETRY: A BRIEF OVERVIEW

The Earth's atmosphere is a highly complex and dynamic mixture, containing a plethora of chemically diverse gas-phase and condensed-phase species. Although the atmosphere is predominantly composed of nitrogen (78%), oxygen (21%), and argon (0.9%), trace gases with mixing ratios at part-per-million levels and below can dramatically influence the Earth's climate and near-surface air quality. A variety of biogenic and anthropogenic emission sources introduce organic and inorganic trace gases to the atmosphere, where they may undergo further reactive processes to form secondary and higher-order chemical products. For example, ozone (O_3) is produced in the troposphere via the photochemical oxidation of volatile organic compounds (VOCs) in the presence of nitrogen oxides (NO_x) (Atkinson, 2000), and is a respiratory irritant and principal component of photochemical smog. Anthropogenic sources of VOCs (traffic emissions, oil and natural gas activity, other industrial activities) and NO_x (traffic, other combustion sources) modulate O_3 production rates, thereby affecting air quality and human health (Atkinson, 2000; Abeleira et al., 2017; Abeleira and Farmer, 2017). The ability to characterize sources, sinks, and lifetimes of atmospheric trace gases requires analytical measurement techniques that are sensitive and selective toward analytes of interest, and have adequate time resolution to capture the temporal variability of said analytes at atmospherically-relevant timescales.

In the past couple decades, chemical ionization mass spectrometry (CIMS) has emerged as a fast, field-deployable analytical technique for measuring a variety of atmospheric trace gases

of interest. CIMS is a soft-ionization technique which preserves the chemical structure of parent analytes, thereby facilitating mass spectral interpretation and analysis. The sensitivity and selectivity of CIMS toward individual or entire classes of compounds is dictated by the reagent ion chemistry employed by the instrument's chemical ionization source. Proton-transfer reaction mass spectrometry (PTR-MS) is a chemical ionization method using protonated water clusters ($[H_2O]_nH^+$) as a reagent ion, and is routinely used in atmospheric chemistry measurements to detect a variety of volatile non-methane hydrocarbons and lightly-oxidized VOCs (Hewitt et al., 2003) Here, a charge is imparted to analytes via proton-transfer reactions in the instrument's ionization source. The sensitivity of analytes detected by PTR-MS is thus dictated by their proton affinity relative to that of water (~697 kJ mol^{-1}) (Hewitt et al., 2003). Iodide (I^-) and iodide-water adducts ($I[H_2O]^-$) are commonly used as CIMS reagent ions for the detection of oxygenated and nitrogenated organics, and inorganic halogen species in the atmosphere (Aljawhary et al., 2013; Lee et al., 2014; Brophy and Farmer, 2015; Lee et al., 2018). Ionization with this method occurs via the formation of an iodide-analyte adduct ($[I+M]^-$). CIMS sensitivity to iodide-analyte adducts is controlled by the ion-molecule reaction rate between I^- and M, and the binding enthalpy of the resultant adduct (Lopez-Hilfiker et al., 2016; Iyer et al., 2016). Acetate ($C_2H_3O_2^-$) reagent ions are commonly used to detect organic and inorganic gas-phase acids in the atmosphere, and accomplish ionization via proton abstraction from moieties with higher gas-phase acidities (Aljawhary et al., 2013; Bertram et al., 2011; Brophy and Farmer, 2016). Numerous other reagent ions are routinely employed with CIMS in the positive and negative mode, and continuous developments of novel ionization schemes enable the detection of an ever-increasing suite of atmospheric trace gases.

Modern field-deployable CIMS instruments used for atmospheric measurements are typically equipped with a time-of-flight (TOF) mass analyzer, allowing for mass resolutions orders of magnitude higher than their quadrupole-based predecessors. The ability to effectively resolve mass spectral peaks separated by tenths or hundredths of a mass-to-charge unit is crucial for fully characterizing complex atmospheric samples. For instance, reactive organic trace gases alone may consist of tens or hundreds of thousands of individual molecules in the atmosphere (Goldstein and Galbally, 2007). Incorporating a TOF into the CIMS instrument has also enabled the collection of entire mass spectra at high time resolutions. Atmospheric sampling with TOF-CIMS typically takes place on the order of 1 Hz or lower, which is sufficient for most routine field studies exploring temporal trends of trace gases on the order of minutes to hours (i.e. diel cycles and regional-scale emissions). TOF-CIMS sampling frequencies of 10 Hz have been utilized for more temporally-rigorous applications, such as eddy covariance measurements (Schobesberger et al., 2016; Fulgham et al., 2019).

The broad suite of detectable compounds by CIMS, particularly when utilizing multiple ionization schemes, allows for simultaneous targeted analysis of atmospheric analytes of interest, and untargeted bulk analysis of the chemically complex atmospheric matrix. Targeted analyses of (in)organic halides (Kercher et al., 2009; Lee et al., 2018; Priestley et al., 2018), organic acids (Lee et al., 2014; Brophy and Farmer, 2015; Fulgham et al., 2019), and various other VOCs and atmospherically-relevant trace gases (Lee et al., 2014; Brophy and Farmer, 2015; Massoli et al., 2018; Li et al., 2020) with CIMS techniques have led to greater knowledge of their individual sources, sinks, and lifetimes in the atmosphere. Recent developments in CIMS instrumentation (and other fast online measurements) have markedly advanced our understanding of atmospheric reactive organic carbon (ROC), or all atmospheric carbon excluding methane (CH_4), carbon

monoxide (CO), and carbon dioxide (CO_2). ROC comprises a major source of reactivity toward strong atmospheric oxidants including the hydroxyl radical (OH) and O_3 (Heald and Kroll, 2020). Photochemical oxidation of ROC via these oxidants contributes to the production of secondary pollutants, including CO_2 (a greenhouse gas), particulate matter (deleterious to air quality and human health), and O_3 (Heald and Kroll, 2020). Despite the atmospheric relevance of ROC, our knowledge of the bulk composition and complex reaction pathways of ROC has been stymied by the instrumental challenges of measuring ROC, which is chemically innumerous. Only recently have detailed characterizations of ROC budgets been made possible by vigorous field and laboratory measurements employing various CIMS techniques for the bulk (i.e. untargeted) analysis of a broad suite of compound classes, including low-volatility oxygenates and short-lived intermediates (Hunter et al., 2017; Isaacman-VanWertz et al., 2018; Heald and Kroll, 2020). Targeted and untargeted CIMS methods have also shown recent promise in characterizing the emerging and chemically numerous class of per- and polyfluoroalkyl substances (PFAS) in the atmosphere (Riedel et al., 2019). PFAS tend to persist in the environment due to their chemical inertness, and exposure to and bioaccumulation of PFAS can lead to adverse health outcomes in humans (USEPA).

Chemical ionization mass spectrometry measurements have also been recently applied to the atmosphere of indoor environments. Despite the fact that people in the United States (and likely other areas in the developed world) spend the majority of their time indoors (Klepeis et al., 2001), our understanding of the indoor atmosphere pales in comparison to that of outdoors. Notably, CIMS instruments have been deployed indoors to study VOC emissions and chemistry from building materials and cooking activities (Liu et al., 2019; Duncan et al., 2019), and the chemistry of indoor pollutants produced from cleaning products (Wong et al., 2017; Wang et al.,

2019; Zhou et al., 2020; Finewax et al., 2020). Price et al. (2019) recently used various CIMS techniques to characterize the ROC budgets of various indoor environments. Here, they gained valuable insight toward typical carbon mass concentrations, bulk physiochemical properties (i.e. volatilities and carbon oxidation states), and oxidant reactivities of indoor ROC (Price et al., 2019).

The majority of this dissertation (Chapters 2 – 4) focuses on indoor atmospheric measurements performed with a TOF-CIMS instrument utilizing iodide ionization during the House Observations of Microbial and Environmental Chemistry (HOMEChem) field campaign at the University of Texas in summer 2018 (described by Farmer et al. (2019)). We pair these measurements with other online measurements of gas-phase and particulate species performed during HOMEChem to develop a more complete story of the indoor chemistry taking place during indoor experiments. Chapter 2 reports measurements of inorganic chlorinated and nitrogenated compounds produced indoors during bleach cleaning experiments at HOMEChem, which are paired with sophisticated kinetic chemical modeling to elucidate production mechanisms responsible for these analytes. Chapter 3 focuses on the production of various organic pollutants produced during bleach cleaning experiments, including organic isocyanates, cyanogen chloride, chlorocarbons, and secondary organic aerosol. Chapter 4 explores the carbon mass concentrations, bulk physiochemical properties, and atmospheric oxidant reactivities of indoor ROC emissions during a variety of cooking and cleaning experiments during HOMEChem, and directly contrasts this indoor air complexity to that of the outdoor atmosphere. In Chapter 5, the focus of this dissertation shifts toward the outdoor atmosphere, to demonstrate the efficacy of a TOF-CIMS instrument utilizing acetate ionization toward studying the tropospheric sources and sinks of various gas-phase acids in the Colorado Front Range.

REFERENCES

Abeleira, A., Pollack, I., Sive, B., Zhou, Y., Fischer, E., and Farmer, D.: Source characterization of volatile organic compounds in the Colorado Northern Front Range Metropolitan Area during spring and summer 2015, J. Geophys. Res. Atmos., 122, 3595-3613, 2017.

Abeleira, A. J., and Farmer, D. K.: Summer ozone in the northern Front Range metropolitan area: weekend–weekday effects, temperature dependences, and the impact of drought, Atmos. Chem. Phys., 17, 6517-6529, 2017.

Aljawhary, D., Lee, A. K. Y., and Abbatt, J. P. D.: High-resolution chemical ionization mass spectrometry (ToF-CIMS): application to study SOA composition and processing, Atmos. Meas. Tech., 6, 3211-3224, 2013.

Atkinson, R.: Atmospheric chemistry of VOCs and NOx, Atmos. Environ., 34, 2063-2101, 2000.

Bertram, T. H., Kimmel, J. R., Crisp, T. A., Ryder, O. S., Yatavelli, R. L. N., Thornton, J. A., Cubison, M. J., Gonin, M., and Worsnop, D. R.: A field-deployable, chemical ionization time-of-flight mass spectrometer, Atmos. Meas. Tech., 4, 1471-1479, doi:10.5194/amt-4-1471-2011, 2011.

Brophy, P., and Farmer, D. K.: A switchable reagent ion high resolution time-of-flight chemical ionization mass spectrometer for real-time measurement of gas phase oxidized species: characterization from the 2013 southern oxidant and aerosol study, Atmos. Meas. Tech., 8, 2945-2959, doi:10.5194/amt-8-2945-2015, 2015.

Brophy, P., and Farmer, D. K.: Clustering, methodology, and mechanistic insights into acetate chemical ionization using high-resolution time-of-flight mass spectrometry, Atmos. Meas. Tech., 9, 3969-3986, doi:10.5194/amt-9-3969-2016, 2016.

Duncan, S. M., Tomaz, S., Morrison, G., Webb, M., Atkin, J., Surratt, J. D., and Turpin, B. J.: Dynamics of residential water-soluble organic gases: Insights into sources and sinks, Environ. Sci. Technol., 53, 1812-1821, 2019.

Farmer, D. K., Vance, M. E., Abbatt, J. P. D., Abeleira, A., Alves, M. R., Arata, C., Boedicker, E., Bourne, S., Cardoso-Saldaña, F., Corsi, R., DeCarlo, P. F., Goldstein, A. H., Grassian, V. H., Hildebrandt Ruiz, L., Jimenez, J. L., Kahan, T. F., Katz, E. F., Mattila, J. M., Nazaroff, W. W., Novoselac, A., O'Brien, R. E., Or, V. W., Patel, S., Sankhyan, S., Stevens, P. S., Tian, Y., Wade, M., Wang, C., Zhou, S., and Zhou, Y.: Overview of HOMEChem: House Observations of Microbial and Environmental Chemistry, Environ. Sci. Process. Impacts, 21, 1280-1300, 10.1039/C9EM00228F, 2019.

Finewax, Z., Pagonis, D., Claflin, M. S., Handschy, A. V., Brown, W. L., Jenks, O., Nault, B. A., Day, D. A., Lerner, B. M., and Jimenez, J. L.: Quantification and source characterization of

volatile organic compounds from exercising and application of chlorine-based cleaning products in a university athletic center, Indoor Air, 10.1111/ina.12781, 2020.

Fulgham, S. R., Brophy, P., Link, M., Ortega, J., Pollack, I., and Farmer, D. K.: Seasonal flux measurements over a Colorado pine forest demonstrate a persistent source of organic acids, ACS Earth Space Chem., 3, 2017-2032, 2019.

Goldstein, A. H., and Galbally, I. E.: Known and unexplored organic constituents in the earth's atmosphere, Environ. Sci. Technol., 41, 1514-1521, 2007.

Heald, C. L., and Kroll, J.: The fuel of atmospheric chemistry: Toward a complete description of reactive organic carbon, Sci Adv, 6, eaay8967, 2020.

Hewitt, C. N., Hayward, S., and Tani, A.: The application of proton transfer reaction-mass spectrometry (PTR-MS) to the monitoring and analysis of volatile organic compounds in the atmosphere, J. Environ. Monit., 5, 1-7, 2003.

Hunter, J. F., Day, D. A., Palm, B. B., Yatavelli, R. L., Chan, A. W., Kaser, L., Cappellin, L., Hayes, P. L., Cross, E. S., and Carrasquillo, A. J.: Comprehensive characterization of atmospheric organic carbon at a forested site, Nat. Geosci., 10, 748-753, 2017.

Isaacman-VanWertz, G., Massoli, P., O'Brien, R., Lim, C., Franklin, J. P., Moss, J. A., Hunter, J. F., Nowak, J. B., Canagaratna, M. R., and Misztal, P. K.: Chemical evolution of atmospheric organic carbon over multiple generations of oxidation, Nat. Chem., 10, 462-468, 2018.

Iyer, S., Lopez-Hilfiker, F., Lee, B. H., Thornton, J. A., and Kurtén, T.: Modeling the detection of organic and inorganic compounds using iodide-based chemical ionization, J. Phys. Chem. A, 120, 576-587, 2016.

Kercher, J., Riedel, T., and Thornton, J.: Chlorine activation by N_2O_5: simultaneous, in situ detection of $ClNO_2$ and N_2O_5 by chemical ionization mass spectrometry, Atmos. Meas. Tech., 2, 193-204, 2009.

Klepeis, N. E., Nelson, W. C., Ott, W. R., Robinson, J. P., Tsang, A. M., Switzer, P., Behar, J. V., Hern, S. C., and Engelmann, W. H.: The National Human Activity Pattern Survey (NHAPS): a resource for assessing exposure to environmental pollutants, J. Expo. Anal. Environ. Epidemiol., 11, 231, 2001.

Lee, B. H., Lopez-Hilfiker, F. D., Mohr, C., Kurten, T., Worsnop, D. R., and Thornton, J. A.: An iodide-adduct high-resolution time-of-flight chemical-ionization mass spectrometer: application to atmospheric inorganic and organic compounds, Environ. Sci. Technol., 48, 6309-6317, doi:10.1021/es500362a, 2014.

Lee, B. H., Lopez-Hilfiker, F. D., Veres, P. R., McDuffie, E. E., Fibiger, D. L., Sparks, T. L., Ebben, C. J., Green, J. R., Schroder, J. C., and Campuzano-Jost, P.: Flight deployment of a high-

resolution time-of-flight chemical ionization mass spectrometer: observations of reactive halogen and nitrogen oxide species, J. Geophys. Res. Atmos., 123, 7670–7686, 2018.

Li, H., Riva, M., Rantala, P., Heikkinen, L., Daellenbach, K., Krechmer, J. E., Flaud, P.-M., Worsnop, D., Kulmala, M., and Villenave, E.: Terpenes and their oxidation products in the French Landes forest: insights from Vocus PTR-TOF measurements, Atmos. Chem. Phys., 20, 1941–1959, 2020.

Liu, Y., Misztal, P. K., Xiong, J., Tian, Y., Arata, C., Weber, R. J., Nazaroff, W. W., and Goldstein, A. H.: Characterizing sources and emissions of volatile organic compounds in a northern California residence using space-and time-resolved measurements, Indoor Air, 29, 630-644, 2019.

Lopez-Hilfiker, F. D., Iyer, S., Mohr, C., Lee, B. H., D'Ambro, E. L., Kurten, T., and Thornton, J. A.: Constraining the sensitivity of iodide adduct chemical ionization mass spectrometry to multifunctional organic molecules using the collision limit and thermodynamic stability of iodide ion adducts, Atmos. Meas. Tech., 9, 1505-1512, doi:10.5194/amt-9-1505-2016, 2016.

Massoli, P., Stark, H., Canagaratna, M. R., Krechmer, J. E., Xu, L., Ng, N. L., Mauldin III, R. L., Yan, C., Kimmel, J., and Misztal, P. K.: Ambient measurements of highly oxidized gas-phase molecules during the southern oxidant and aerosol study (SOAS) 2013, ACS Earth Space Chem., 2, 653-672, 2018.

Price, D. J., Day, D. A., Pagonis, D., Stark, H., Algrim, L. B., Handschy, A. V., Liu, S., Krechmer, J. E., Miller, S. L., and Hunter, J. F.: Budgets of Organic Carbon Composition and Oxidation in Indoor Air, Environ. Sci. Technol., 53, 13053-13063, 2019.

Priestley, M., Breton, M. L., Bannan, T. J., Worrall, S. D., Bacak, A., Smedley, A. R., Reyes-Villegas, E., Mehra, A., Allan, J., and Webb, A. R.: Observations of organic and inorganic chlorinated compounds and their contribution to chlorine radical concentrations in an urban environment in northern Europe during the wintertime, Atmos. Chem. Phys., 18, 13481-13493, 2018.

Riedel, T. P., Lang, J. R., Strynar, M. J., Lindstrom, A. B., and Offenberg, J. H.: Gas-Phase Detection of Fluorotelomer Alcohols and Other Oxygenated Per-and Polyfluoroalkyl Substances by Chemical Ionization Mass Spectrometry, Environ. Sci. Technol. Lett., 6, 289-293, 2019.

Schobesberger, S., Lopez-Hilfiker, F. D., Taipale, D., Millet, D. B., D'Ambro, E. L., Rantala, P., Mammarella, I., Zhou, P. T., Wolfe, G. M., Lee, B. H., Boy, M., and Thornton, J. A.: High upward fluxes of formic acid from a boreal forest canopy, Geophys. Res. Lett., 43, 9342-9351, doi:10.1002/2016gl069599, 2016.

USEPA: Per- and Polyfluoroalkyl Substances (PFAS): https://www.epa.gov/pfas, access: January 29, 2021.

Wang, C., Collins, D. B., and Abbatt, J. P. D.: Indoor illumination of terpenes and bleach emissions leads to particle formation and growth, Environ. Sci. Technol., 53, 11615-12150, 2019.

Wong, J. P. S., Carslaw, N., Zhao, R., Zhou, S., and Abbatt, J. P. D.: Observations and impacts of bleach washing on indoor chlorine chemistry, Indoor Air, 27, 1082-1090, 2017.

Zhou, S., Liu, Z., Wang, Z., Young, C. J., VandenBoer, T. C., Guo, B. B., Zhang, J., Carslaw, N., and Kahan, T. F.: Hydrogen peroxide emission and fate indoors during non-bleach cleaning: a chamber and modeling study, Environ. Sci. Technol., 54, 15643-15651, 2020.

CHAPTER 2 – MULTIPHASE CHEMISTRY CONTROLS INORGANIC CHLORINATED AND NITROGENATED COMPOUNDS IN INDOOR AIR DURING BLEACH CLEANING[1]

2.1 Introduction

Hypochlorite (OCl^-) bleach solutions (hereafter "bleach") are widely used indoors as a disinfectant in both workplace and household environments (Coons, 1978; Rutala and Weber, 1997; Zock et al., 2009), due to their potent oxidizing and antimicrobial properties. Cleaning with bleach produces reactive chlorinated and nitrogenated compounds in the indoor environment, which can detrimentally impact indoor air quality and human health. Several chlorinated volatile organic compounds (Cl-VOCs), including chloroform ($CHCl_3$) and carbon tetrachloride (CCl_4), have been measured in indoor air following bleach use (Odabasi, 2008; Odabasi et al., 2014). $CHCl_3$ and CCl_4 are toxic and likely carcinogenic to humans (Fouw, 1999; USEPA, 2010); exposure to these compounds in indoor environments is therefore of concern. Reactions of hypochlorous acid (HOCl) and ammonia (NH_3) in bleach produce chloramines (NH_2Cl, $NHCl_2$, NCl_3) (Drago, 1957; Jafvert and Valentine, 1992), which can then volatilize to indoor air. Nitrogen trichloride (NCl_3) is a known respiratory irritant. Workers exposed to elevated levels of NCl_3 in indoor swimming pools have reported increased asthma symptoms and other respiratory issues (Massin et al., 1998; Thickett et al., 2002; Dang et al., 2010; Jacobs et al., 2007). Mixing bleach with acidified solutions such as vinegar or hydrochloric acid can liberate dangerous levels of chlorine gas (Cl_2) to indoor air (Nazaroff and Weschler, 2004). Not

[1]Mattila, J. M., Lakey, P. S. J., Shiraiwa, M., Wang, C., Abbatt, J. P. D., Arata, C., Goldstein, A. H., Ampollini, L., Katz, E. F., DeCarlo, P. F., Zhou, S., Kahan, T. F., Cardoso-Saldaña, F. J., Hildebrandt Ruiz, L., Abeleira, A., Boedicker, E., Vance, M. E., and Farmer, D. K.: Multiphase chemistry controls inorganic chlorinated and nitrogenated compounds in indoor air during bleach cleaning, Environ. Sci. Technol., 54, 1730-1739, 10.1021/acs.est.9b05767, 2020.

surprisingly, increased asthma symptoms and other respiratory issues are common among cleaning workers frequently exposed to bleach emissions indoors (Rosenman et al., 2003; Medina-Ramon et al., 2005; Médina-Ramón et al., 2006; Sastre et al., 2011).

Studies of the indoor emissions and chemistry resulting from bleach use are limited. Until recently, existing studies relied on passive sampling techniques or modeled predictions of bleach emissions to indoor air (Odabasi, 2008; Odabasi et al., 2014; Shepherd et al., 1996), hindering investigation of the rapid chemistry and indoor lifetimes of bleach-related compounds. By sampling indoor air with a fast (>1 Hz), online measurement technique during bleach use, Wong et al. (2017) provided insight on the production pathways and indoor lifetimes for several reactive compounds including HOCl, Cl_2, dichloramine ($NHCl_2$), NCl_3, nitryl chloride ($ClNO_2$), and dichlorine monoxide (Cl_2O). While HOCl removal was mostly attributable (~90%) to very high ventilation rates (~13 air exchanges hr^{-1}), they noted that uptake to and reactions on indoor surfaces may be more significant in typical indoor environments with much lower ventilation rates (Wong et al., 2017). Photochemical modeling revealed that indoor levels of OH and Cl radicals could increase to $>10^6$ and 10^5 molecules cm^{-3}, respectively after mopping via HOCl and Cl_2 photolysis depending on prevalent light levels, thereby increasing the oxidative capacity of the indoor atmosphere toward volatile organic compounds (VOCs) (Wong et al., 2017). $ClNO_2$ also photolyzes in the presence of ultraviolet light to produce Cl and nitrogen dioxide radicals (NO_2; a key atmospheric oxidant and air pollutant) (Ganske et al., 1992); it is therefore an important reservoir species for NO_2 and Cl radicals in the outdoor atmosphere (Jeong et al., 2019; Priestley et al., 2018; Von Glasow, 2008). Though Wong et al. (2017) identified $ClNO_2$ in indoor air during bleach cleaning, no measurements of indoor $ClNO_2$ mixing ratios during these periods exist to date. The potential of bleach-related $ClNO_2$ as a source of Cl and NO_2 radicals to

indoors therefore remains unknown (Gligorovski and Weschler, 2013). Dawe et al. (2019) measured time-resolved hydrogen chloride (HCl) mixing ratios after bleach applications in a house, and reported enhancements of ~0.1 part-per-billion by volume (ppbv) due to cleaning events. This HCl may be emitted directly from the bleach, or could be formed through reactions (dark or photochemical) of HOCl, Cl_2, or $ClNO_2$ with VOCs (or some combination of these processes) (Dawe et al., 2019).

The mechanisms controlling indoor lifetimes of compounds produced from bleach use are largely uncharacterized, and thus it remains difficult to assess their significance toward human exposure to toxic compounds. To address this need, we present an array of analytical measurements performed while cleaning with a commercial bleach solution indoors during the House Observations of Microbial and Environmental Chemistry (HOMEChem) campaign in summer 2018 (Farmer et al., 2019). We combine measurement data with multiphase kinetic modeling (detailed in Methods and Appendix 1; section A1.1.1) to gain insight on specific production and removal pathways of several inorganic chlorinated and nitrogenated compounds during bleach use. We focus on aqueous reactions within the bleach, heterogeneous chemistry occurring on indoor surfaces, and photochemistry initiated by transmission of outdoor sunlight to indoors. Additionally, we assess how observations herein pertain to indoor air quality and human health.

2.2 Methods

2.2.1 Bleach cleaning experiments

We performed measurements at The University of Texas at Austin's test house (UTest House) during the HOMEChem campaign from 1 to 28 June 2018. HOMEChem was designed to investigate emissions and chemistry from typical indoor activities such as cooking, cleaning and

human occupancy through a series of highly controlled, reproducible experiments. The UTest House has an internal area of 110 m^2, and an internal volume of 250 m^3. Air exchange rates (AER) in the house were controlled using an HVAC system (0.6 ± 0.1 hr^{-1} during bleach cleaning experiments). A floorplan and other details of the UTest house during HOMEChem are presented in Farmer et al. (2019).

One volunteer performed bleach cleaning events in the UTest house. The volunteer prepared bleach solutions according to manufacturer instructions in a plastic bucket by mixing 120 mL commercial sodium hypochlorite-based bleach solution (6% sodium hypochlorite (NaOCl) by mass) into 3.8 L tap water. During each cleaning event, the volunteer applied bleach solution to the kitchen and living room area floors of the test house (40 m^2) with a sponge mop for 10 minutes. The volunteer left the house immediately after mopping. We determined the mass of solution applied to the floor (0.7 ± 0.4 kg) by weighing the solution bucket before and after each cleaning event. Cleaning events took place under sequential and layered experimental regimes. During sequential experiments, four cleaning events took place throughout the day, in the absence of other indoor activities such as cooking or extensive human occupancy. Doors and windows of the test house were opened for 30 minutes following the first two mopping events to reestablish background-level indoor pollutant concentrations. During layered experiments, a single cleaning event occurred at 17:30 local time following several cooking and occupancy-related activities performed throughout the day. More details on these sequential and layered experiments are found in Farmer et al. (2019). We present data from two sequential experiments (07 and 10 June 2018) and four layered experiments (08, 19, 21, and 25 June 2018). All measurements presented herein are reported in local time (Central Daylight Time; CDT; UTC – 05:00).

2.2.2 HOMEChem measurements

We performed measurements at HOMEChem with a time-of-flight chemical ionization mass spectrometer (TOF-CIMS; Tofwerk AG and Aerodyne Research Inc.) (Lee et al., 2014; Brophy and Farmer, 2016, 2015; Lopez-Hilfiker et al., 2016), paired with iodide (I^-) chemical ionization (hereafter "I^- CIMS"). I^- CIMS detects a variety of gaseous oxygenated, nitrogenated, and halogenated VOCs, as well as inorganic halogenated compounds (Priestley et al., 2018; Lee et al., 2014; Lopez-Hilfiker et al., 2016; Kercher et al., 2009; Aljawhary et al., 2013; Lee et al., 2018). I^- CIMS operation, data processing, and field setup are detailed in the SI (section A1.1.3 and A1.1.4). We performed offline calibrations for HOCl, Cl_2, $ClNO_2$, and N_2O_5, enabling direct mixing ratio calculations of these compounds. Details of these calibrations are provided in the SI (section A1.1.5). We calculate mixing ratios for Cl_2O, $NHCl_2$, and NCl_3 using a voltage scanning approach first proposed by Lopez-Hilfiker et al. (2016). Details and potential sources of bias of this approach are outlined in the SI (section A1.1.6).

We measured gaseous nitrous acid (HONO) with a TOF-CIMS instrument (Tofwerk AG and Aerodyne Research Inc.) paired with acetate chemical ionization. This instrument shared a sampling inlet with our I^- CIMS (SI section A1.1.4). Details of this ionization chemistry are found in Bertram et al. (2011) and Brophy and Farmer (2016). HONO calibration details are described by Wang et al. (2020). We measured gaseous monochloramine (NH_2Cl) and $NHCl_2$ with a proton-transfer-reaction time-of-flight mass spectrometer (PTR-TOF-MS; Ionicon Analytik GmbH, PTR-TOF 8000) (hereafter "PTR"). Instrument details (Cappellin et al., 2010) and field setup during HOMEChem (Farmer et al., 2019) are found elsewhere. We describe PTR mixing ratio calculations in the SI (section A1.1.2). We measured NH_3 with a cavity ring-down spectrometer (Picarro G2103) (Ampollini et al., 2019); nitric oxide (NO) with a Model 42i-TL

TRACE Level NO_x Analyzer (Thermo Fisher Scientific); and NO_2 with a cavity attenuated phase shift spectroscopy method (Environnement AS32M) (Kebabian et al., 2008). We detected sub-micron non-refractory particulate chloride (Cl^-), ammonium (NH_4^+) and organic mass concentrations with a high-resolution aerosol mass spectrometer (HR-AMS; Aerodyne Research, Inc.) (DeCarlo et al., 2006). We performed near-window photon flux measurements in the test house (from sunlight filtered through windows) with a USB4000 Ocean Optics Spectrometer. Farmer et al. (2019) provides additional details of NH_3, NO, NO_2, AMS, and photon flux measurements during HOMEChem; additional measurement details are in SI section A1.1.2.

2.2.3 Multiphase kinetic modeling

The kinetic multilayer model of surface and bulk chemistry with a boundary layer (KM-SUB-BL) includes chemical reactions in both the aqueous bleach and indoor air, as well as reactive uptake to indoor particulate matter (PM) and surfaces (Morrison et al., 2019; Shiraiwa et al., 2010). This model also considers photochemistry, AER, and indoor production rates of relevant compounds. We propose these processes are important to multiphase indoor chemistry during bleach cleaning, and use them within the model to help explain experimental observations herein.

The indoor gas-phase was separated into two components: a 'well-mixed main room' and a 'near-bleach boundary layer' using a multiple-layer approach based on our previous KM-BL model (Morrison et al., 2019). Table A1.1 lists chemical reactions in the aqueous bleach. Table A1.2 lists gas-phase reactions and reactive uptake onto PM and room surfaces. We used literature rate coefficients for these mechanisms whenever possible; otherwise, justifications are provided in the Tables or text. Losses to PM considered an effective uptake coefficient and the PM surface area concentration, which was constrained to measurement data in the model (Figure

A1.1). We treated losses of gas-phase compounds to room surfaces as first-order processes; we varied these loss rates in the model to reproduce measurement data. Table A1.3 lists the Henry's Law coefficients and gas-phase diffusion coefficients for all semi-volatile and volatile compounds included in the model. Table A1.4 summarizes parameters that varied across bleach cleaning experiments including AER, pH of the bleach, and reaction rate coefficients that varied between different days and times. We adjusted parameters in Table A1.4 (except for AER) in the model to reproduce experimental observations. We used observational constraints to adjust upper-bound photolysis rates (calculated from near-window photon flux measurements) by a factor of 50 to estimate average indoor photolysis rates; further details/justifications regarding these adjustments are in SI section A1.1.1. Figure A1.15 demonstrates the sensitivity of model predictions on variable parameters adjusted in the model. Additional model details are in SI section A1.1.1.

2.3 Results and discussion

Bleach contains an equilibrium mixture of HOCl and OCl^- (pH ~9.5 when diluted for cleaning; SI section A1.1.1). The interaction of bleach solution with indoor air and surfaces leads to several chemical transformations in the indoor environment. Figure 2.1 provides a detailed schematic of relevant multiphase chemical mechanisms indoors during bleach cleaning. We assess specific production and removal processes in the following sections.

2.3.1 Indoor and outdoor measurements of bleach-related compounds

Bleach cleaning events during the HOMEChem campaign coincided with a spike and subsequent decay in indoor mixing ratios of several gaseous chlorinated and nitrogenated compounds (Figure 2.2 and A1.2). Peak indoor HOCl and Cl_2 mixing ratios ranged from 15-370 and 60-130 ppbv, respectively, during bleach cleaning events performed throughout

HOMEChem. These levels are consistent with previous work (Wong et al., 2017). We observe peak indoor mixing ratios of 8-34 ppbv for $ClNO_2$. We measure NH_2Cl, and NCl_3 at the ppbv level, and typically measure Cl_2O at the part-per-trillion by volume (pptv) level. We measure $NHCl_2$ at the pptv level with I^- CIMS, and at the ppbv level with PTR. We discuss these measurement discrepancies further in the "Chloramines" section.

Outdoor mixing ratios of these gaseous bleach-related compounds were typically several orders of magnitude lower than peak levels measured indoors during bleach cleaning events (Table A1.5). For example, indoor-to-outdoor concentration ratios for HOCl, Cl_2, and $ClNO_2$ reached orders of 10^4 during bleach cleaning. Infiltration of outdoor air was therefore not a source of these compounds to indoors, and generation of these compounds occurred on rapid timescales and entirely within the house. Additionally, we report indoor mixing ratios of these compounds below the instrumental detection limit of our I^- CIMS (detection limits reported in Table A1.5; see Methods and SI section A1.1.3 for details on I^- CIMS) during unoccupied background conditions with no indoor activities performed (described in Farmer et al. (2019)), affirming that generation occurred exclusively from bleach use. We did not observe any significant enhancements in bleach-related compounds while mopping the floor with a tap water control, indicating that impurities in the water used to prepare bleach solutions were not an important source of these compounds to indoor air.

To quantify timescales of removal pathways, we determine first-order decay constants for HOCl, Cl_2, $ClNO_2$, Cl_2O, NH_2Cl, $NHCl_2$, and NCl_3 from indoor air during bleach cleaning events. By fitting an exponential function to the decay portions of indoor mixing ratio time series data, we extract total first-order loss rate constants for each compound (Figure 2.3). All

compounds were ventilated from indoor air at the AER, though this typically accounted for <50% total observed loss rates, suggesting other important removal pathways.

2.3.2 Inorganic chlorine compounds

HOCl present in the aqueous bleach volatilized to the gas-phase following its application. Ventilation accounted for <10% HOCl removal from indoor air (Figure 2.3), necessitating other loss mechanisms. Heterogeneous reactions of HOCl on acidic aerosol surfaces to generate Cl_2 is a known process in the troposphere (Riedel et al., 2012; Xue et al., 2015):

$$HOCl + H^+ + Cl^- \rightarrow Cl_2 + H_2O \quad \textbf{[1]}$$

This mechanism requires a high uptake coefficient of HOCl to particle surfaces in our kinetic model ($\gamma_{HOCl} = 0.4$; describes probability of uptake) compared to previously reported values (10^{-3}-10^{-4}) (Lawler et al., 2011; Pratte and Rossi, 2006) to reproduce the decay of HOCl and the formation of Cl_2 observed during HOMEChem. The high uptake coefficient required by the model likely indicates that another variable (e.g. reactive surface area) used to calculate this heterogeneous reaction rate (reaction 26 in Table A1.2) is underestimated. Further, we estimate that interior surfaces of the test house comprise ~10^5 more surface area than indoor PM (discussed further in section 2.3.5). Though we do not explicitly account for this chemistry in our model, it is likely that this mechanism occurred predominantly on acidified, chloride-containing interior surfaces (i.e. where aerosols or gas-phase acids have deposited) rather than particle surfaces.

Cl_2 production occurred primarily via reactions of HOCl on indoor surfaces (Eq. 1) (Riedel et al., 2012). By systematically varying bleach solution pH in the model we determined aqueous production of Cl_2 in the bleach was negligible at solution pH >2, and therefore

unimportant under these experimental conditions. Production of Cl_2O, the anhydride of HOCl, occurred in the aqueous bleach via:

$$2HOCl \rightleftharpoons Cl_2O + H_2O \quad \textbf{[2]}$$

Removal of Cl_2 and Cl_2O occurred faster than the AER (Figure 2.3); we attribute this to additional losses onto indoor surfaces. We treat these as reactive losses in the model, and therefore do not consider desorption from surfaces. The actual mechanisms behind these losses remain uncertain and warrant further investigation. We note that relative trends in magnitudes of HOCl, Cl_2, and Cl_2O loss rates across different bleach cleaning experiments are fairly consistent (i.e. 10 June > 08 June >> 25 June), suggesting similar loss pathways among these compounds.

We observed lower HOCl-to-Cl_2 concentration ratios (≤3) compared to those previously reported by Wong et al. (2017) (≥10). AER (and therefore loss via ventilation) herein are between one and two orders of magnitude lower than that reported in Wong et al. (2017). The lower HOCl mixing ratios relative to Cl_2 observed here imply that uptake to acidified, chloride-containing surfaces was a more important HOCl sink (and Cl_2 source) during HOMEChem. Additionally, Wong et al. (2017) note the presence of Cl_2 and other inorganic chlorine species in bleach headspace measurements as solution 'impurities'. We cannot rule out the possibility of such impurities as possible sources of chlorinated compounds to indoor air, but do not account for this in our model due to lack of experimental constraints.

Large depositions of organic and inorganic compounds from substantial cooking events likely interfere with this chemistry, either by altering surface pH or providing an additional chemical sink for HOCl and Cl_2O. Specifically, we are unable to model HOCl (and subsequently Cl_2O) on 19 June 2018 (Figure A1.2), the day after a Thanksgiving experiment with extensive cooking, baking, and human occupancy activities (detailed further in Farmer et al. (2019)).

HOCl and Cl_2 photolyzed during bleach cleaning experiments via transmission of outdoor light through test house windows (see SI; section A1.1.1 and A1.1.2). Photolysis was not a significant removal pathway of these compounds from indoor air, accounting for about 0.03% and 0.1% total loss of HOCl and Cl_2, respectively. Photolysis did, however, act as a source of OH and Cl radicals to the indoor environment:

$$HOCl + hv \rightarrow OH + Cl \ (\lambda < 420\ nm) \quad \textbf{[3]}$$

$$Cl_2 + hv \rightarrow 2Cl \ (\lambda < 493\ nm) \quad \textbf{[4]}$$

Kinetic modeling predicts OH and Cl production rates up to 4×10^6 and 4×10^7 molecules cm^{-3} s^{-1} during bleach cleaning, respectively (Figure 2.4). HOCl and Cl_2 photolysis typically accounted for the majority of OH and Cl produced, respectively (Figure 2.4, Table A1.6 and A1.7). For comparison, OH and Cl production rates on the order of 10^6 molecules cm^{-3} s^{-1} were previously predicted indoors via the photolysis of 20 and 200 ppbv Cl_2 and HOCl, respectively, by a halogen lamp (Dawe et al., 2019). We do not report predicted steady-state OH or Cl concentrations indoors due to a lack of constrained sinks (i.e. indoor VOCs) in our model. These production rates could serve as constraints in future models to assess steady-state indoor OH and Cl radical concentrations during bleach use. Wong et al. (2017) demonstrated that OH and Cl radical concentrations may reach levels up to or higher than typical outdoor levels during bleach cleaning (>10^6 and 10^5 molecules cm^{-3}, respectively), depending on lighting conditions.

Oxidation via OH and Cl radicals may shorten the lifetimes of several VOCs in indoor and outdoor atmospheres (Wong et al., 2017; Gligorovski and Weschler, 2013). This oxidation subsequently contributes to the production of secondary organic aerosol (SOA), an air pollutant associated with a number of detrimental health effects (Gligorovski and Weschler, 2013; Nel, 2005; Jimenez et al., 2009). We hypothesize that observed OH and Cl production during bleach

cleaning herein increased the oxidative capacity of the indoor atmosphere toward VOCs substantially, and possibly enhanced indoor SOA production during HOMEChem. Wang et al. (2019) observed rapid SOA formation in a chamber study when exposing >100 ppbv Cl_2 and HOCl to limonene—an indoor VOC arising from cleaning products and air fresheners—in dark conditions, and subsequently illuminating the chamber with nearby fluorescent lights or diffuse sunlight from outdoors. The authors speculate volatile dark reaction products react with Cl and OH (from Cl_2 and HOCl photolysis) to generate lower volatility products, which subsequently condense to form SOA. We will discuss observations of VOC oxidation and SOA production during bleach cleaning at HOMEChem in a separate publication. OH- and/or Cl-induced oxidation of VOCs also plays a key role in O_3 production in the outdoor atmosphere (Priestley et al., 2018; Gligorovski and Weschler, 2013). While this process may similarly impact the indoor atmosphere during bleach use, further assessment is beyond the scope of this work given the present lack of indoor VOC constraints and the spatial heterogeneity of spectral irradiance.

2.3.3 $ClNO_2$

Production of gaseous $ClNO_2$ in the outdoor atmosphere is attributable to reactions of dinitrogen pentoxide (N_2O_5) on aerosol surfaces containing Cl^- (Behnke et al., 1997). However, indoor N_2O_5 was below the instrumental detection limit of our I^- CIMS (1 pptv; Table A1.5) during bleach cleaning and unoccupied daytime periods. We therefore expect this was not a major production pathway of ppbv-level $ClNO_2$. We do not completely rule out the possibility of this mechanism acting as a minor $ClNO_2$ source indoors, and note Wong et al. (2017) considered this mechanism as a possible $ClNO_2$ source during bleach cleaning. $ClNO_2$ is also produced via aqueous reactions of HOCl and nitrite (NO_2^-) (Cachaza et al., 1976; Frenzel et al., 1998):

$$HOCl + NO_2^- \rightarrow ClNO_2 + OH^- \quad \textbf{[5]}$$

We propose this mechanism as a major $ClNO_2$ production pathway during bleach cleaning. We assume these reactions are pseudo first-order in our model (i.e. NO_2^- remains in excess).

A possible source of NO_2^- to the bleach is via dissolution of gaseous HONO from indoor air, though this is difficult to confirm given the lack of available HONO measurements during most bleach cleaning experiments (Figure A1.3). Even on days with reliable HONO measurements (Figure A1.3; 19 and 25 June 2018), decreases in gas-phase HONO mixing ratios alone cannot account for the observed $ClNO_2$ production. Recent studies demonstrate an equilibrium between gas-phase HONO and NO_2^- present on indoor surfaces (Collins et al., 2018; Wang et al., 2020), i.e. surface-bound NO_2^- acts as a large, labile source of HONO to indoors. Wang et al. (2020) demonstrated the persistence of this HONO reservoir (likely attributable to surface-bound NO_2^-) inside the test house during HOMEChem. We therefore speculate that NO_2^- initially present on floor surfaces where bleach was applied, combined with uptake of gaseous HONO to the applied bleach, drove aqueous $ClNO_2$ production. Wang et al. (2020) performed offline surface measurements of NO_2^- during HOMEChem, wherein they reported a lower-bound surface concentration of 10^{12} molecules cm^{-2}. Combining this NO_2^- source with HONO dissolution yields $\leq$17% NO_2^- required for observed $ClNO_2$ production. This result could suggest the presence of another unknown NO_2^- source, or confirm these surface NO_2^- concentration measurements are indeed underestimated. Wong et al. (2017) measured $ClNO_2$ as an impurity in bleach solution. We note the possibility of primary emissions from the applied bleach as a source of $ClNO_2$ to indoor air, though we are unable to quantitatively assess this source in our model.

We observe considerably higher (by 5-15 ppbv) peak $ClNO_2$ mixing ratios on days where cooking activities took place prior to cleaning with bleach (Figure A1.2; 08, 19, 25 June 2018) (detailed in Methods and Farmer et al. (2019)). Cooking acts as a source of HONO to the indoor

environment (Liu et al., 2019; Zhou et al., 2018). Elevated indoor HONO from cooking likely increased NO_2^- levels in the applied bleach, thereby enhancing $ClNO_2$ production. Additionally, the pseudo first-order rate coefficients for aqueous $ClNO_2$ production from HOCl + NO_2^- in our model are higher on days where cooking occurred before bleach cleaning (Table A1.1 and A1.4), possibly due to higher NO_2^- concentrations in solution.

The decay rate of $ClNO_2$ from indoor air relative to AER suggests additional removal processes beyond ventilation alone (Figure 2.3). In agreement with previous predictions (Dawe et al., 2019), photolysis was not a significant loss pathway for $ClNO_2$ (~0.03% total loss), nor a major source of Cl radical, accounting for ≤2% total Cl production during all bleach cleaning experiments (Table A1.7). Uptake by indoor surfaces, or the aqueous and organic films present on those surfaces, is likely. Haskins et al. (2019) reported heterogeneous reactions of $ClNO_2$ on acidified, chloride-containing particle surfaces as an important pathway for both $ClNO_2$ loss and Cl_2 production in the outdoor atmosphere:

$$ClNO_2 + H^+ + Cl^- \rightarrow Cl_2 + HONO \qquad \textbf{[6]}$$

Roberts et al. (2008) derived an uptake coefficient of $\gamma_{ClNO2} \approx 10^{-3}$ for this reaction on an acidified NaCl slurry. The addition of this mechanism with $\gamma_{ClNO2} = 10^{-3}$ into our model yielded insignificant changes to predicted $ClNO_2$ and Cl_2 mixing ratios (Figure A1.4), suggesting that this mechanism (using $\gamma_{ClNO2} \leq 10^{-3}$) is an insignificant indoor $ClNO_2$ sink, and Cl_2 source during bleach cleaning. Using this mechanism to fully explain observed $ClNO_2$ loss requires that $\gamma_{ClNO2} \approx 10^{-1}$; though this would result in a net production of indoor HONO, which is not observed in our measurements (Figure A1.4). Magnitude of Cl_2 mixing ratios increase <5% using $\gamma_{ClNO2} = 10^{-1}$ (Figure A1.4), further suggesting that Cl_2 production occurred primarily via Eq. 1. We therefore do not expect Eq. 6 to be significant in controlling $ClNO_2$ (or Cl_2) lifetimes during bleach

cleaning, and note that the fate of deposited $ClNO_2$ on indoor surfaces remains uncertain. Heal et al. (2007) demonstrated that $ClNO_2$ dissociates in aqueous media to form Cl^- and nitronium ion (NO_2^+); NO_2^+ may then undergo nitration reactions with dissolved organics. We speculate that this chemistry occurs in aqueous indoor films to provide an additional $ClNO_2$ sink, though we do not assess this process further given a lack of relevant experimental constraints.

2.3.4 Chloramines

Gaseous NH_3 partitioned into the aqueous bleach, producing NH_2Cl, $NHCl_2$, and NCl_3 via (Jafvert and Valentine, 1992):

$$NH_3 + HOCl \rightarrow NH_2Cl + H_2O \quad \textbf{[7]}$$

$$NH_2Cl + HOCl \rightarrow NHCl_2 + H_2O \quad \textbf{[8]}$$

$$NHCl_2 + HOCl \rightarrow NCl_3 + H_2O \quad \textbf{[9]}$$

This chemistry resulted in a loss of gaseous NH_3 from indoor air (Figure 2.5). After bleach cleaning, indoor NH_3 mixing ratios re-equilibrated to pre-cleaning levels via indoor sources including human occupancy, off-gassing of building materials, and temperature-dependent reservoirs present on indoor surfaces (Ampollini et al., 2019). Kinetic modeling suggests that reactive uptake of NH_3 was favorable due to reactions with HOCl (e.g. Eq. 7), and was limited by gas-phase diffusion of NH_3 through a boundary layer above the floor surface (see SI section A1.1.1).

We successfully reproduce $NHCl_2$ and NCl_3 levels measured by I^- CIMS in our model using Eq. 7-9, but cannot reproduce NH_2Cl and $NHCl_2$ levels measured by PTR using these mechanisms (Figure 2.5). $NHCl_2$ measured by PTR is several orders of magnitude higher than that measured by I^- CIMS. These discrepancies in $NHCl_2$ measurements are possibly driven by uncertainties associated with PTR and I^- CIMS mixing ratio calculations (see SI sections A1.1.2

and A1.1.6, respectively). The aforementioned model-measurement discrepancy may also be driven by chloramine production mechanisms not accounted for in the model. We hypothesize surface-bound NH_3 (Ampollini et al., 2019; Wang et al., 2020) and other amines (Weaver et al., 2009; Li and Blatchley, 2007) initially present on the test house floor entered the bleach solution upon application, leading to additional chloramine production. However, we do not assess this hypothesis further given the lack of relevant experimental constraints to include in our model.

Relative trends in NH_2Cl, $NHCl_2$, and NCl_3 loss rates across different bleach cleaning experiments are fairly consistent, suggesting similar loss pathways for these compounds (Figure 2.3). These loss rates are consistently faster than the AER. Given the lack of literature regarding the destruction of these compounds in the gas-phase, we attribute this to additional losses to indoor surfaces.

2.3.5 Nitrogen oxides

Indoor NO mixing ratios decreased during bleach cleaning (Figure A1.3). The gas-phase reaction of NO radicals with chlorine monoxide (ClO) radicals is a well-known process (Xue et al., 2015; Zahniser and Kaufman, 1977):

$$NO + ClO \rightarrow NO_2 + Cl \qquad \textbf{[10]}$$

However predicted ClO production (reactions 5, 8, 10, 12, and 16 in Table A1.2) was insufficient to constitute a significant loss pathway of NO. HOCl reacts with NO in the gas-phase (Cook et al., 1981), but the kinetics are too slow to explain the decay rate of indoor NO observed here—the rate coefficient associated with this reaction would have to be 10^2-10^3 times higher to reproduce measurement data. The mechanisms by which this removal takes place therefore remain uncertain. We propose reactions of HOCl and NO on indoor surfaces could explain the observed loss of NO during bleach cleaning:

$$HOCl + NO \rightarrow HCl + NO_2 \quad \textbf{[11]}$$

The importance of surface-mediated reactions of nitrogen oxides has been demonstrated previously (Raff et al., 2009), and the high abundance of gas-phase HOCl during bleach cleaning supports this mechanism as a viable loss pathway for indoor NO. By assuming a total indoor surface area of 430 m^2 (estimated via a detailed interior floorplan of the test house) we calculate uptake coefficients on the order of 10^{-6} for interior surface uptake of NO (reaction 50 in Table A1.2) and 10^{-7}-10^{-6} for HOCl (reactions 50 and 51 in Table A1.2). No studies of this heterogeneous chemistry exist to our knowledge. We therefore note the proposed reaction warrants further experimental assessment. This reaction serves as a potentially important source of indoor HCl. We predict HCl enhancements (Figure A1.3) of 15-20 ppbv when bleach cleaning occurred during periods of elevated NO, i.e. after cooking activities on 08, 19, and 25 June 2018 (Figure A1.3) (Zhou et al., 2019; Zhou et al., 2018); and 1-2 ppbv when NO is near background levels (~5 ppbv) (Figure A1.3; 10 June 2018). We note these 'background NO' HCl enhancements are an order of magnitude larger than those observed by Dawe et al. (2019) during a sequential bleach cleaning under similar experimental conditions; possibly driven by underestimated HCl sinks in our model.

NO_2 mixing ratios increased by up to 25 ppbv during bleach cleaning (Figure A1.3). We consider Eq. 11 to be an important NO_2 production pathway during these periods, though this mechanism does not fully account for the observed NO_2 enhancements. Kinetic modeling suggests reactions of $ClNO_2$ and NO_2^- in the aqueous bleach accounted for additional NO_2 production (Frenzel et al., 1998):

$$ClNO_2 + NO_2^- \rightarrow 2NO_2 + Cl^- \quad \textbf{[12]}$$

$ClNO_2$ photolysis was not a significant source of indoor NO_2, accounting for <0.1% total measured NO_2 during bleach cleaning.

2.3.6 Further assessing uptake of chlorinated compounds to indoor particles and surfaces

Bleach cleaning events coincided with increases in indoor particulate Cl^- mass concentrations, likely from reactive uptake (e.g. reactions 44-47 and 49-51 in Table A1.2) or non-reactive partitioning of gaseous chlorinated compounds onto indoor PM (Figure A1.5) (Wong et al., 2017). This is in accord with Wong et al. (2017), who also saw particulate Cl^- levels rise in concert with gas-phase chlorine species during bleach use. Enhancements in particulate Cl^- were more pronounced on days with higher PM surface area and mass concentrations (Figure A1.1 and A1.5; 08, 19, 21, 25 June 2018), arising from cooking activities performed prior to bleach cleaning. Additionally, reactions of chlorinated compounds from bleach on particle surfaces were more prominent during periods of elevated indoor PM mass concentrations (e.g. reactions 22-26, 36, and 37 in Table A1.2), though other indoor surfaces such as walls and floors were likely much more important for heterogeneous chemistry/reactive uptake. We do not observe a correlation between particulate Cl^- and NH_4^+ during these periods, suggesting that uptake of Cl to indoor PM during bleach cleaning likely does not enhance particulate ammonium chloride (NH_4Cl).

We further assess uptake of bleach-related compounds to indoor surfaces during a sequential bleach cleaning experiment performed on 07 June 2018 (Figure A1.6). In contrast to the sequential experiment on 10 June 2018, we opened doors and windows 30 minutes earlier during the first two cleaning events. This coincided with a rapid decay of HOCl, Cl_2, Cl_2O, $ClNO_2$, $NHCl_2$, and NCl_3 from indoor air, as indoor mixing ratios of these compounds were still elevated prior to this perturbation. After closing doors and windows, we observe a subsequent

rise in indoor mixing ratios of these compounds. Given the absence of other emission sources (as we assume the applied bleach has fully evaporated at this point), we attribute this to the desorption of these compounds from indoor surfaces, following their initial uptake from indoor air. These observations are consistent with Wang et al. (2020), who demonstrated the gas-surface partitioning equilibria for a diversity of compounds present in indoor air. This allows indoor surfaces to act as large, labile reservoirs of compounds to indoor air following the perturbation of steady-state conditions (i.e. opening doors and windows for extensive time periods).

2.3.7 Health and environmental implications

The highly oxidative properties of HOCl introduce potential health concerns to indoor environments upon its liberation to the gas-phase. Schwartz-Narbonne et al. (2018) found that at hundreds of ppbv, gaseous HOCl undergoes chlorohydrin formation reactions with squalene, a major component of human skin oil, on the order of minutes. The authors also speculate this chemistry occurs on phospholipids lining the lungs upon inhalation of HOCl fumes, and potentially leads to skin and respiratory tract irritation associated with bleach use (Schwartz-Narbonne et al., 2018). Because indoor gas-phase HOCl reached hundreds of ppbv for several minutes herein (Figure 2.2 and A1.2), this chemistry on human dermal surfaces likely occurs during typical bleach cleaning. Exposure to hundreds of pptv gaseous NCl_3 in indoor settings is associated with increased asthma symptoms and other respiratory issues (Massin et al., 1998; Thickett et al., 2002). Gaseous NCl_3 reached several ppbv indoors for periods of an hour or more during bleach cleaning at HOMEChem (Figure 2.5 and A1.2), which is potentially of harm to individuals with asthma or sensitive breathing passages. Inhalation of Cl_2 leads to acute respiratory harm at the part-per-million level (White and Martin, 2010). The World Health Organization (WHO) recommends ambient Cl_2 levels below 34 ppbv to mitigate symptoms of

chronic Cl_2 exposure, including sensory irritation and decreased respiratory capacity (White and Martin, 2010). Acute injury resulting from Cl_2 levels observed during experimental conditions herein (Figure 2.2 and A1.2) is therefore unlikely, but prolonged exposures may be of health concern.

The detrimental effects to human health of bleach-related compounds may be enhanced under different indoor conditions. For instance, considerably higher HOCl, Cl_2, or NCl_3 mixing ratios than those observed herein are likely achievable when using a higher concentration of applied bleach solution, or cleaning in an indoor environment with lower ventilation rates. While $ClNO_2$ photolysis was not a significant source of indoor NO_2 herein, it may be more important in homes with more prominent windows allowing for larger volumes of the indoors to be sunlit.

This work emphasizes that indoor chemical reactions occur through extensive multiphase processes including interactions between chlorinated and nitrogenated compounds, with clear signatures of high concentrations for gas-phase species in indoor air. The chemical fates of several bleach-related gas-phase compounds lost to indoor surfaces remain unclear, and warrant further investigation. We propose a novel mechanism for the heterogeneous, halogen-mediated production of NO_2 on indoor surfaces, though further mechanistic studies are required to confirm its importance to the indoor environment. This study also serves as a unique opportunity to probe atmospherically-relevant multiphase chemistry, in that the mechanisms identified herein likely occur in not only indoor environments, but also in condensed phases present in the outdoor atmosphere.

2.4 Author contributions

J. M. M. contributed iodide CIMS data collection, and analyses performed herein.

2.5 Data availability

Data used herein are available at https://osf.io/aqc57/.

2.6 Chapter 2 figures

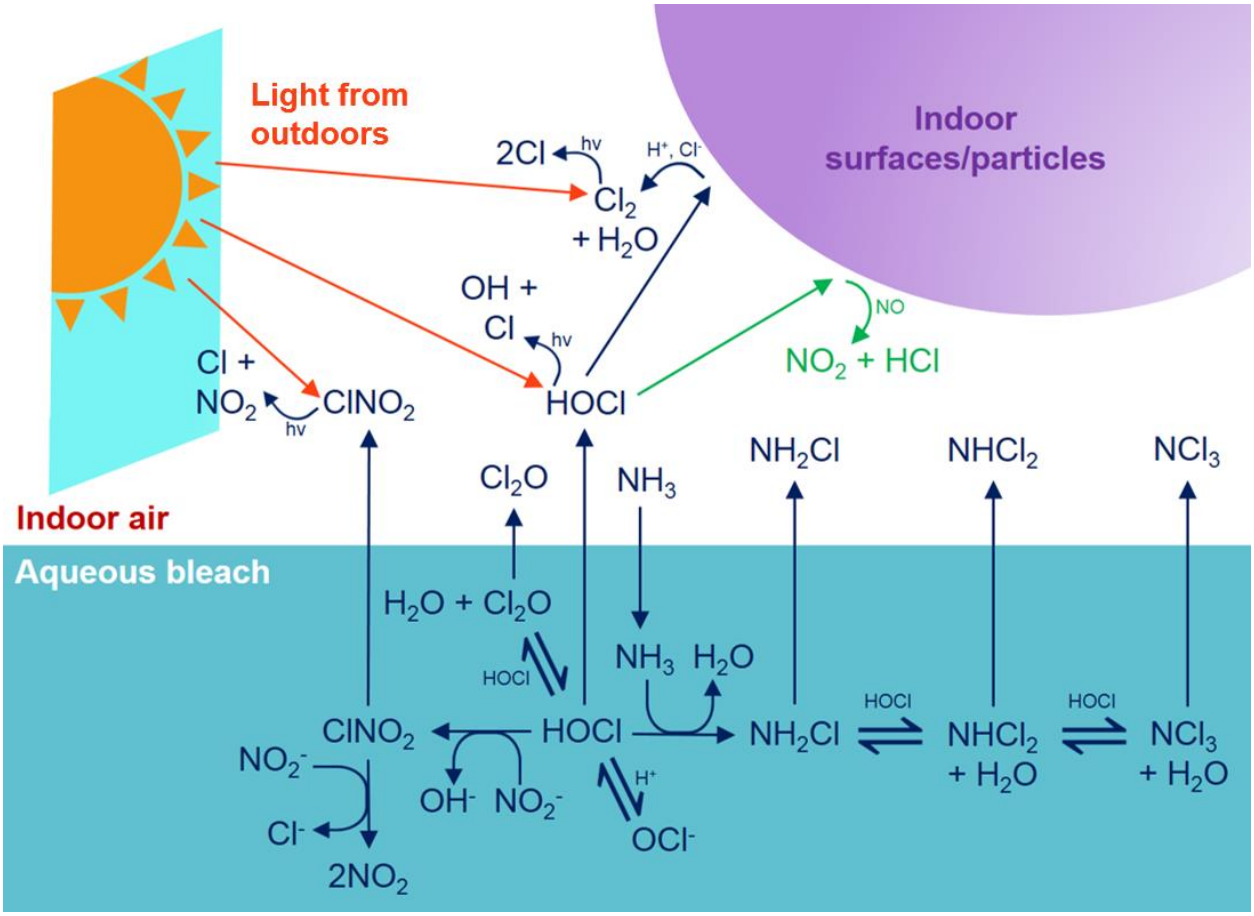

Figure 2.1. Depiction of indoor transformative chemical processes relevant to this work. A mechanism proposed in this work is denoted by green text/arrows (see "Nitrogen oxides" section of Results and Discussion). We do not depict loss via ventilation or uncharacterized losses to surfaces here.

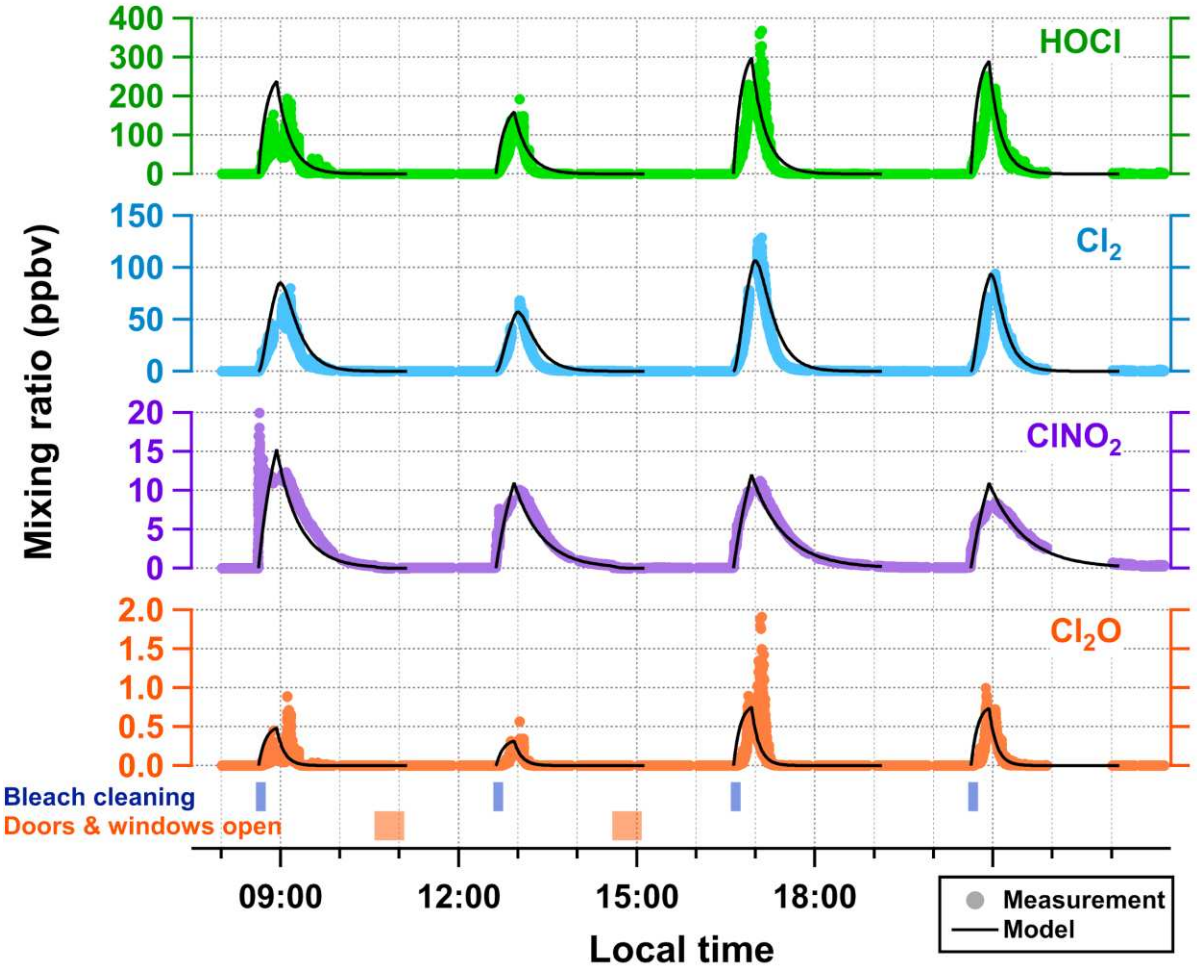

Figure 2.2. Indoor mixing ratio time series data (colored markers) for HOCl, Cl_2, $ClNO_2$, and Cl_2O during a bleach cleaning experiment on 10 June 2018. Solid black traces represent predicted mixing ratios from kinetic modeling. Blue and orange shaded areas above horizontal axis correspond to local times during which bleach cleaning and door/window opening took place, respectively.

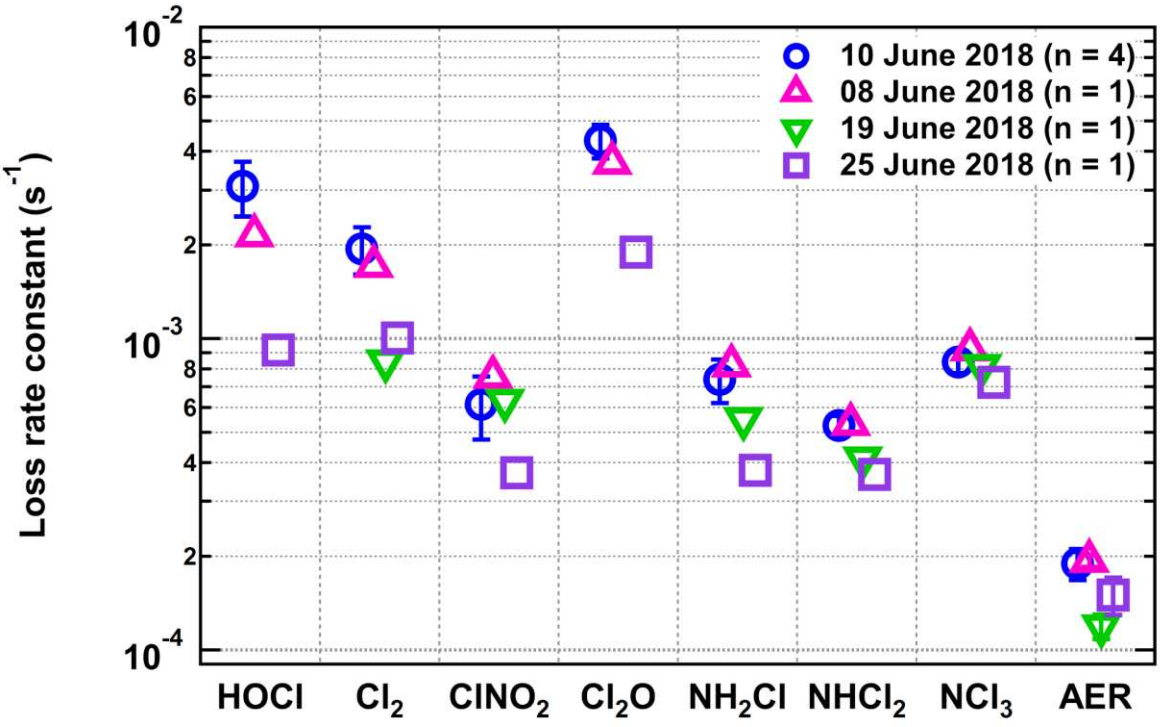

Figure 2.3. First-order loss rate constants (vertical axis) corresponding to air exchange rates (AER), and total loss of several bleach-related compounds (horizontal axis) from indoor air during various bleach cleaning experiments during HOMEChem. Variable "n" in the figure legend corresponds to number of bleach cleaning events performed on each day represented by the colored markers. Markers corresponding to 10 June 2018 (blue circles) represent average rate constants across four mopping events performed that day. Error bars represent uncertainties propagated from first-order rate constants determined by an exponential function fit to measurement data.

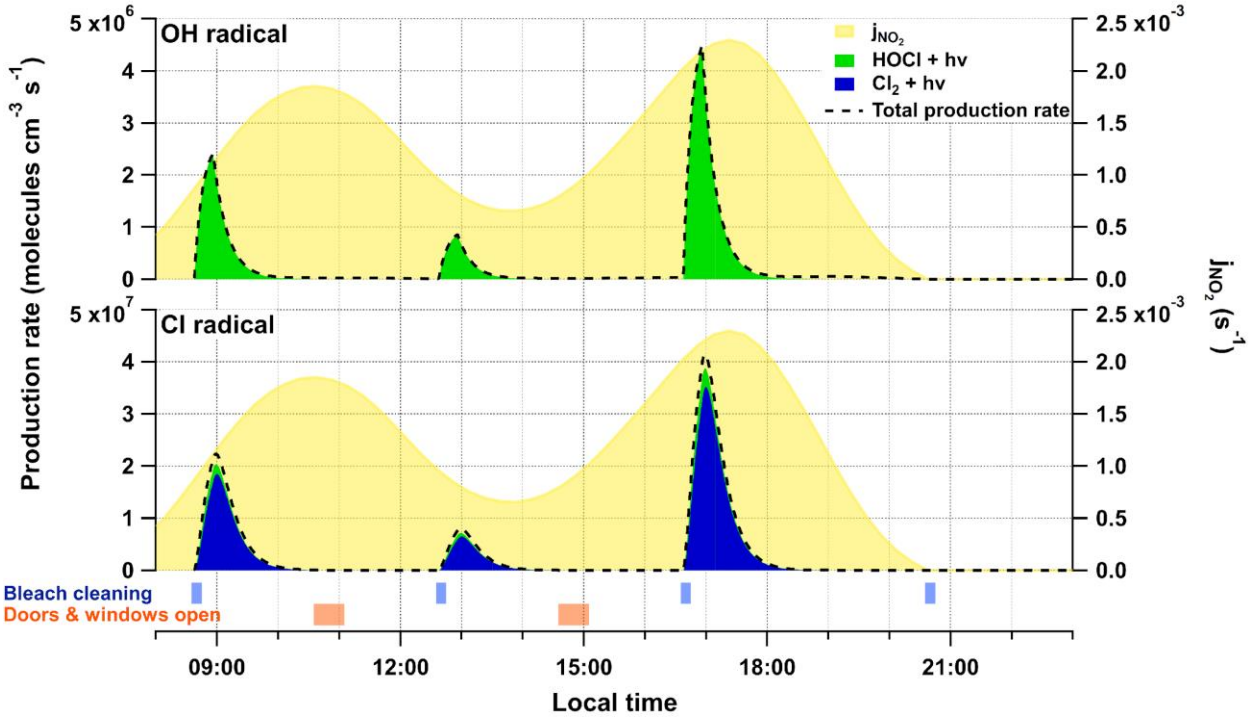

Figure 2.4. Time series of total predicted OH (top panel) and Cl (bottom panel) radical production rates from kinetic modeling (dashed black lines) during a bleach cleaning experiment on 10 June 2018. Colored areas under the dashed black line are proportional to contributions from individual mechanisms (see figure legend) to respective radical production rates. Shaded yellow area behind production rate data correspond to campaign-averaged diel profiles of NO_2 photolysis rate constants (j_{NO2}) in the test house calculated from spectral irradiance measured near west- and east-facing windows (see SI section A1.1.2), and are used here as a proxy for transmission of outdoor light. Blue and orange shaded areas above horizontal axis correspond to local times during which bleach cleaning and door/window opening took place, respectively.

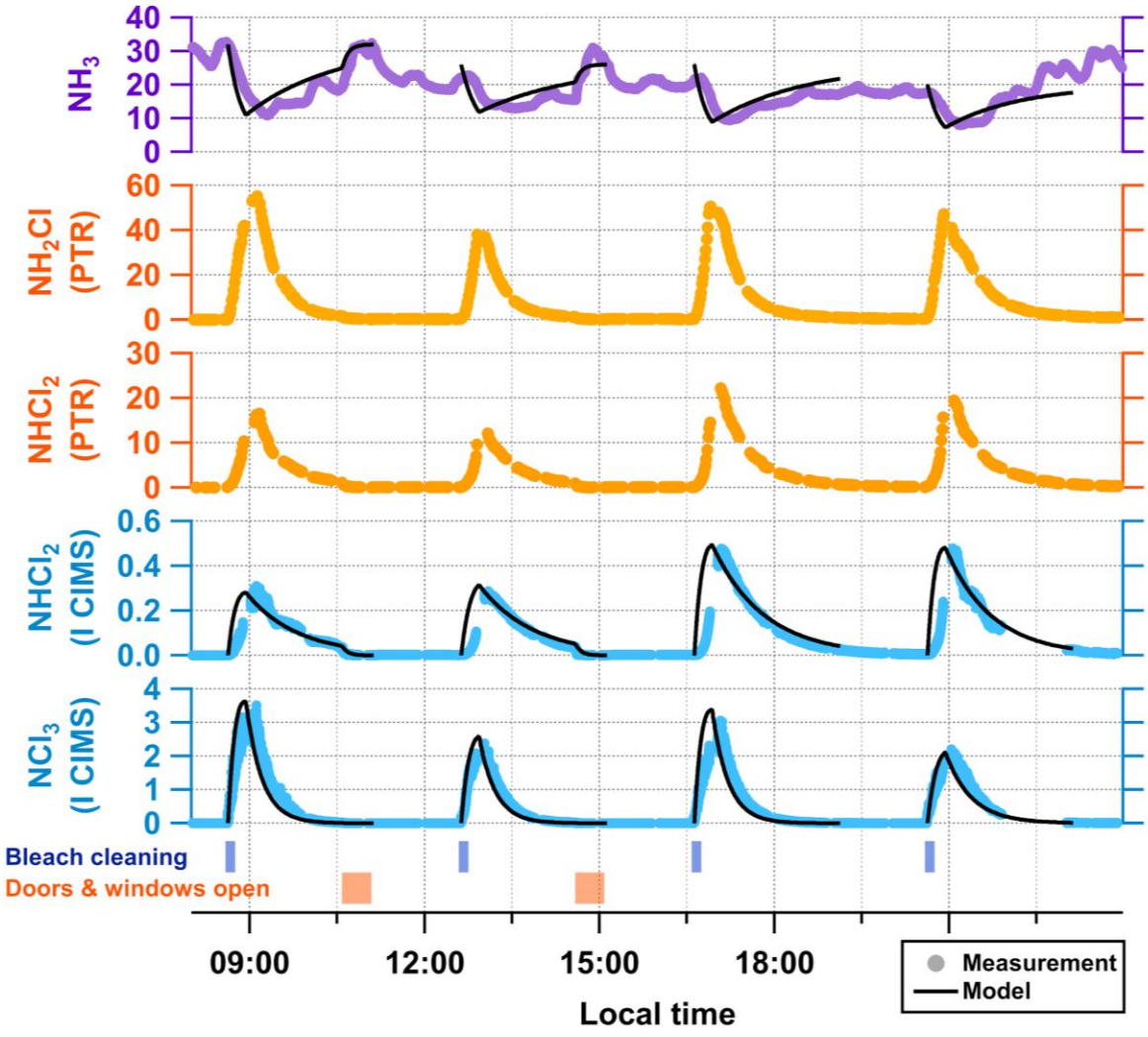

Figure 2.5. Time series of measured indoor NH_3, NH_2Cl, $NHCl_2$, and NCl_3 mixing ratios (colored markers; units of ppbv) during a bleach cleaning experiment on 10 June 2018, with corresponding kinetic modeling results for aqueous production in the applied bleach (solid black traces). Orange and blue colored markers correspond to PTR and I^- CIMS measurements, respectively. Blue and orange shaded areas above horizontal axis correspond to local times during which bleach cleaning and door/window opening took place, respectively.

REFERENCES

Aljawhary, D., Lee, A. K. Y., and Abbatt, J. P. D.: High-resolution chemical ionization mass spectrometry (ToF-CIMS): application to study SOA composition and processing, Atmos. Meas. Tech., 6, 3211-3224, 2013.

Ampollini, L., Katz, E. F., Bourne, S., Tian, Y., Novoselac, A., Goldstein, A. H., Lucic, G., Waring, M. S., and DeCarlo, P.: Observations and contributions of real-time indoor ammonia concentrations during HOMEChem, Environ. Sci. Technol., 10.1021/acs.est.9b02157, 2019.

Behnke, W., George, C., Scheer, V., and Zetzsch, C.: Production and decay of $ClNO_2$ from the reaction of gaseous N_2O_5 with NaCl solution: bulk and aerosol experiments, J. Geophys. Res. Atmos., 102, 3795-3804, 1997.

Bertram, T. H., Kimmel, J. R., Crisp, T. A., Ryder, O. S., Yatavelli, R. L. N., Thornton, J. A., Cubison, M. J., Gonin, M., and Worsnop, D. R.: A field-deployable, chemical ionization time-of-flight mass spectrometer, Atmos. Meas. Tech., 4, 1471-1479, doi:10.5194/amt-4-1471-2011, 2011.

Brophy, P., and Farmer, D. K.: A switchable reagent ion high resolution time-of-flight chemical ionization mass spectrometer for real-time measurement of gas phase oxidized species: characterization from the 2013 southern oxidant and aerosol study, Atmos. Meas. Tech., 8, 2945-2959, doi:10.5194/amt-8-2945-2015, 2015.

Brophy, P., and Farmer, D. K.: Clustering, methodology, and mechanistic insights into acetate chemical ionization using high-resolution time-of-flight mass spectrometry, Atmos. Meas. Tech., 9, 3969-3986, doi:10.5194/amt-9-3969-2016, 2016.

Cachaza, J., Casado, J., Castro, A., and Quintela, M. L.: Kinetics of oxidation of nitrite by hypochlorite ions in aqueous basic solution, Can. J. Chem., 54, 3401-3406, 1976.

Cappellin, L., Biasioli, F., Fabris, A., Schuhfried, E., Soukoulis, C., Märk, T. D., and Gasperi, F.: Improved mass accuracy in PTR-TOF-MS: Another step towards better compound identification in PTR-MS, Int. J. Mass Spectrom., 290, 60-63, 2010.

Collins, D. B., Hems, R. F., Zhou, S., Wang, C., Grignon, E., Alavy, M., Siegel, J. A., and Abbatt, J. P.: Evidence for gas–surface equilibrium control of indoor nitrous acid, Environ. Sci. Technol., 52, 12419-12427, 2018.

Cook, J. E. L., Ennis, C. A., Leck, T. J., and Birks, J. W.: Studies of reactions of importance in the stratosphere. IV. Rate constant for the reaction Cl+HOCl→HCl+ClO over the temperature range 243–365 K, J. Chem. Phys., 74, 545-549, 1981.

Coons, D.: Bleach: facts, fantasy, and fundamentals, J. Am. Oil Chem Soc., 55, 104-108, 1978.

Dang, B., Chen, L., Mueller, C., Dunn, K. H., Almaguer, D., Roberts, J. L., and Otto, C. S.: Ocular and respiratory symptoms among lifeguards at a hotel indoor waterpark resort, J. Occup. Environ. Med., 52, 207-213, 2010.

Dawe, K. E. R., Furlani, T. C., Kowal, S. F., Kahan, T. F., VandenBoer, T. C., and Young, C. J.: Formation and emission of hydrogen chloride in indoor air, Indoor Air, 29, 70-78, 2019.

DeCarlo, P. F., Kimmel, J. R., Trimborn, A., Northway, M. J., Jayne, J. T., Aiken, A. C., Gonin, M., Fuhrer, K., Horvath, T., Docherty, K. S., Worsnop, D. R., and Jimenez, J. L.: Field-deployable, high-resolution, time-of-flight aerosol mass spectrometer, Anal. Chem., 78, 8281-8289, doi:10.1021/ac061249n, 2006.

Drago, R. S.: Chloramine, J. Chem. Educ., 34, 523-576, 1957.

Farmer, D. K., Vance, M. E., Abbatt, J. P. D., Abeleira, A., Alves, M. R., Arata, C., Boedicker, E., Bourne, S., Cardoso-Saldaña, F., Corsi, R., DeCarlo, P. F., Goldstein, A. H., Grassian, V. H., Hildebrandt Ruiz, L., Jimenez, J. L., Kahan, T. F., Katz, E. F., Mattila, J. M., Nazaroff, W. W., Novoselac, A., O'Brien, R. E., Or, V. W., Patel, S., Sankhyan, S., Stevens, P. S., Tian, Y., Wade, M., Wang, C., Zhou, S., and Zhou, Y.: Overview of HOMEChem: House Observations of Microbial and Environmental Chemistry, Environ. Sci. Process. Impacts, 21, 1280-1300, 10.1039/C9EM00228F, 2019.

Fouw, J.: Environmental Health Criteria 208, Carbon Tetrachloride, 1999.

Frenzel, A., Scheer, V., Sikorski, R., George, C., Behnke, W., and Zetzsch, C.: Heterogeneous interconversion reactions of $BrNO_2$, $ClNO_2$, Br_2, and Cl_2, J. Phys. Chem. A, 102, 1329-1337, 1998.

Ganske, J., Berko, H., and Finlayson-Pitts, B.: Absorption cross sections for gaseous $ClNO_2$ and Cl_2 at 298 K: Potential organic oxidant source in the marine troposphere, J. Geophys. Res. Atmos., 97, 7651-7656, 1992.

Gligorovski, S., and Weschler, C. J.: The oxidative capacity of indoor atmospheres, in, ACS Publications, 2013.

Haskins, J. D., Lee, B. H., Lopez-Hilifiker, F. D., Peng, Q., Jaegle, L., Reeves, J. M., Schroder, J. C., Campuzano-Jost, P., Fibiger, D., and McDuffie, E. E.: Observational constraints on the formation of Cl_2 from the reactive uptake of $ClNO_2$ on aerosols in the polluted marine boundary layer, J. Geophys. Res. Atmos., 124, 8851-8869, 10.1029/2019JD030627, 2019.

Heal, M. R., Harrison, M. A., and Cape, J. N.: Aqueous-phase nitration of phenol by N_2O_5 and $ClNO_2$, Atmos. Environ., 41, 3515-3520, 2007.

Jacobs, J., Spaan, S., Van Rooy, G., Meliefste, C., Zaat, V., Rooyackers, J., and Heederik, D.: Exposure to trichloramine and respiratory symptoms in indoor swimming pool workers, Eur. Respir. J., 29, 690-698, 2007.

Jafvert, C. T., and Valentine, R. L.: Reaction scheme for the chlorination of ammoniacal water, Environ. Sci. Technol., 26, 577-586, 1992.

Jeong, D., Seco, R., Gu, D., Lee, Y., Nault, B. A., Knote, C. J., Mcgee, T., Sullivan, J. T., Jimenez, J. L., Campuzano-Jost, P., Blake, D. R., Sanchez, D., Guenther, A. B., Tanner, D., Huey, L. G., Long, R., Anderson, B. E., Hall, S. R., Ullmann, K., Shin, H., Henderson, S. C., Lee, Y., Kim, D., Ahn, J., and Kim, S.: Integration of airborne and ground observations of nitryl chloride in the Seoul metropolitan area and the implications on regional oxidation capacity during KORUS-AQ 2016, Atmos. Chem. Phys., 19, 12779–12795, 10.5194/acp-2018-1216, 2019.

Jimenez, J. L., Canagaratna, M. R., Donahue, N. M., Prevot, A. S. H., Zhang, Q., Kroll, J. H., DeCarlo, P. F., Allan, J. D., Coe, H., and Ng, N. L.: Evolution of organic aerosols in the atmosphere, Science, 326, 1525-1529, 2009.

Kebabian, P. L., Wood, E. C., Herndon, S. C., and Freedman, A.: A practical alternative to chemiluminescence-based detection of nitrogen dioxide: Cavity attenuated phase shift spectroscopy, Environ. Sci. Technol., 42, 6040-6045, 2008.

Kercher, J., Riedel, T., and Thornton, J.: Chlorine activation by N_2O_5: simultaneous, in situ detection of $ClNO_2$ and N_2O_5 by chemical ionization mass spectrometry, Atmos. Meas. Tech., 2, 193-204, 2009.

Lawler, M., Sander, R., Carpenter, L., Lee, J., Glasow, R. v., Sommariva, R., and Saltzman, E.: HOCl and Cl_2 observations in marine air, Atmos. Chem. Phys., 11, 7617-7628, 2011.

Lee, B. H., Lopez-Hilfiker, F. D., Mohr, C., Kurten, T., Worsnop, D. R., and Thornton, J. A.: An iodide-adduct high-resolution time-of-flight chemical-ionization mass spectrometer: application to atmospheric inorganic and organic compounds, Environ. Sci. Technol., 48, 6309-6317, doi:10.1021/es500362a, 2014.

Lee, B. H., Lopez-Hilfiker, F. D., Veres, P. R., McDuffie, E. E., Fibiger, D. L., Sparks, T. L., Ebben, C. J., Green, J. R., Schroder, J. C., and Campuzano-Jost, P.: Flight deployment of a high-resolution time-of-flight chemical ionization mass spectrometer: observations of reactive halogen and nitrogen oxide species, J. Geophys. Res. Atmos., 123, 7670–7686, 2018.

Li, J., and Blatchley, E. R.: Volatile disinfection byproduct formation resulting from chlorination of organic−nitrogen precursors in swimming pools, Environ. Sci. Technol., 41, 6732-6739, 2007.

Liu, J., Li, S., Zeng, J., Mekic, M., Yu, Z., Zhou, W., Loisel, G., Gandolfo, A., Song, W., and Wang, X.: Assessing indoor gas phase oxidation capacity through real-time measurements of HONO and NO_x in Guangzhou, China, Environ. Sci. Process. Impacts, 21, 1393-1402, 2019.

Lopez-Hilfiker, F. D., Iyer, S., Mohr, C., Lee, B. H., D'Ambro, E. L., Kurten, T., and Thornton, J. A.: Constraining the sensitivity of iodide adduct chemical ionization mass spectrometry to multifunctional organic molecules using the collision limit and thermodynamic stability of iodide ion adducts, Atmos. Meas. Tech., 9, 1505-1512, doi:10.5194/amt-9-1505-2016, 2016.

Massin, N., Bohadana, A. B., Wild, P., Héry, M., Toamain, J. P., and Hubert, G.: Respiratory symptoms and bronchial responsiveness in lifeguards exposed to nitrogen trichloride in indoor swimming pools, Occup. Environ. Med., 55, 258-263, 10.1136/oem.55.4.258, 1998.

Medina-Ramon, M., Zock, J., Kogevinas, M., Sunyer, J., Torralba, Y., Borrell, A., Burgos, F., and Anto, J.: Asthma, chronic bronchitis, and exposure to irritant agents in occupational domestic cleaning: a nested case-control study, Occup. Environ. Med., 62, 598-606, 2005.

Médina-Ramón, M., Zock, J.-P., Kogevinas, M., Sunyer, J., Basagaña, X., Schwartz, J., Burge, P., Moore, V., and Antó, J. M.: Short-term respiratory effects of cleaning exposures in female domestic cleaners, Eur. Respir. J., 27, 1196-1203, 2006.

Morrison, G., Lakey, P. S., Abbatt, J., and Shiraiwa, M.: Indoor boundary layer chemistry modeling, Indoor Air, 29, 956-967, 10.1111/ina.12601, 2019.

Nazaroff, W. W., and Weschler, C. J.: Cleaning products and air fresheners: exposure to primary and secondary air pollutants, Atmos. Environ., 38, 2841-2865, 2004.

Nel, A.: Air pollution-related illness: effects of particles, Science, 308, 804-806, 2005.

Odabasi, M.: Halogenated volatile organic compounds from the use of chlorine-bleach-containing household products, Environ. Sci. Technol., 42, 1445-1451, 2008.

Odabasi, M., Elbir, T., Dumanoglu, Y., and Sofuoglu, S. C.: Halogenated volatile organic compounds in chlorine-bleach-containing household products and implications for their use, Atmos. Environ., 92, 376-383, 2014.

Pratte, P., and Rossi, M. J.: The heterogeneous kinetics of HOBr and HOCl on acidified sea salt and model aerosol at 40–90% relative humidity and ambient temperature, Phys. Chem. Chem. Phys., 8, 3988-4001, 2006.

Priestley, M., Breton, M. L., Bannan, T. J., Worrall, S. D., Bacak, A., Smedley, A. R., Reyes-Villegas, E., Mehra, A., Allan, J., and Webb, A. R.: Observations of organic and inorganic chlorinated compounds and their contribution to chlorine radical concentrations in an urban environment in northern Europe during the wintertime, Atmos. Chem. Phys., 18, 13481-13493, 2018.

Raff, J. D., Njegic, B., Chang, W. L., Gordon, M. S., Dabdub, D., Gerber, R. B., and Finlayson-Pitts, B. J.: Chlorine activation indoors and outdoors via surface-mediated reactions of nitrogen oxides with hydrogen chloride, Proc. Natl. Acad. Sci. U.S.A., 106, 13647-13654, 2009.

Riedel, T. P., Bertram, T. H., Crisp, T. A., Williams, E. J., Lerner, B. M., Vlasenko, A., Li, S.-M., Gilman, J., De Gouw, J., and Bon, D. M.: Nitryl chloride and molecular chlorine in the coastal marine boundary layer, Environ. Sci. Technol., 46, 10463-10470, 2012.

Roberts, J. M., Osthoff, H. D., Brown, S. S., and Ravishankara, A.: N_2O_5 oxidizes chloride to Cl_2 in acidic atmospheric aerosol, Science, 321, 1059-1059, 2008.

Rosenman, K. D., Reilly, M. J., Schill, D. P., Valiante, D., Flattery, J., Harrison, R., Reinisch, F., Pechter, E., Davis, L., and Tumpowsky, C. M.: Cleaning products and work-related asthma, J. Occup. Environ. Med., 45, 556-563, 2003.

Rutala, W. A., and Weber, D. J.: Uses of inorganic hypochlorite (bleach) in health-care facilities, Clin. Microbiol. Rev., 10, 597-610, 1997.

Sastre, J., Madero, M. F., Fernández-Nieto, M., Sastre, B., del Pozo, V., Potro, M. G. d., and Quirce, S.: Airway response to chlorine inhalation (bleach) among cleaning workers with and without bronchial hyperresponsiveness, Am. J. Ind. Med., 54, 293-299, 2011.

Schwartz-Narbonne, H., Wang, C., Zhou, S., Abbatt, J. P. D., and Faust, J.: Heterogeneous chlorination of squalene and oleic acid, Environ. Sci. Technol., 53, 1217, 10.1021/acs.est.8b04248, 2018.

Shepherd, J. L., Corsi, R. L., and Kemp, J.: Chloroform in indoor air and wastewater: the role of residential washing machines, J. Air Waste Manage., 46, 631-642, 1996.

Shiraiwa, M., Pfrang, C., and Pöschl, U.: Kinetic multi-layer model of aerosol surface and bulk chemistry (KM-SUB): the influence of interfacial transport and bulk diffusion on the oxidation of oleic acid by ozone, Atmos. Chem. Phys., 10, 3673-3691, 2010.

Thickett, K., McCoach, J., Gerber, J., Sadhra, S., and Burge, P.: Occupational asthma caused by chloramines in indoor swimming-pool air, Eur. Respir. J., 19, 827-832, 2002.

USEPA: Integrated Risk Information System (IRIS), in, U.S. Environmental Protection Agency (USEPA), 2010.

Von Glasow, R.: Atmospheric chemistry: Pollution meets sea salt, Nat. Geosci., 1, 292, 2008.

Wang, C., Collins, D. B., and Abbatt, J. P. D.: Indoor illumination of terpenes and bleach emissions leads to particle formation and growth, Environ. Sci. Technol., 53, 11615-12150, 2019.

Wang, C., Collins, D. B., Arata, C., Goldstein, A. H., Mattila, J. M., Farmer, D. K., Ampollini, L., DeCarlo, P. F., Novoselac, A., Vance, M. E., Nazaroff, W. W., and Abbatt, J. P. D.: Surface reservoirs dominate dynamic gas-surface partitioning of many indoor air constituents, Sci Adv, 6, aay8973, 10.1126/sciadv.aay8973 2020.

Weaver, W. A., Li, J., Wen, Y., Johnston, J., Blatchley, M. R., and Blatchley III, E. R.: Volatile disinfection by-product analysis from chlorinated indoor swimming pools, Water Res., 43, 3308-3318, 2009.

White, C. W., and Martin, J. G.: Chlorine gas inhalation: human clinical evidence of toxicity and experience in animal models, Proc. Am. Thorac. Soc., 7, 257-263, 10.1513/pats.201001-008SM, 2010.

Wong, J. P. S., Carslaw, N., Zhao, R., Zhou, S., and Abbatt, J. P. D.: Observations and impacts of bleach washing on indoor chlorine chemistry, Indoor Air, 27, 1082-1090, 2017.

Xue, L., Saunders, S., Wang, T., Gao, R., Wang, X., Zhang, Q., and Wang, W.: Development of a chlorine chemistry module for the Master Chemical Mechanism, Geosci. Model Dev., 8, 3151-3162, 2015.

Zahniser, M., and Kaufman, F.: Kinetics of the reactions of ClO with O and with NO, J. Chem. Phys., 66, 3673-3681, 1977.

Zhou, S., Young, C. J., VandenBoer, T. C., Kowal, S. F., and Kahan, T. F.: Time-resolved measurements of nitric oxide, nitrogen dioxide, and nitrous acid in an occupied New York home, Environ. Sci. Technol., 52, 8355-8364, 2018.

Zhou, S., Young, C. J., VandenBoer, T. C., and Kahan, T. F.: Role of location, season, occupant activity, and chemistry in indoor ozone and nitrogen oxide mixing ratios, Environ. Sci. Process. Impacts, 21, 1374-1383, 10.1039/C9EM00129H, 2019.

Zock, J.-P., Plana, E., Antó, J. M., Benke, G., Blanc, P. D., Carosso, A., Dahlman-Höglund, A., Heinrich, J., Jarvis, D., and Kromhout, H.: Domestic use of hypochlorite bleach, atopic sensitization, and respiratory symptoms in adults, J. Allergy Clin. Immun., 124, 731-738, 2009.

CHAPTER 3 – DARK CHEMISTRY DURING BLEACH CLEANING ENHANCES OXIDATION OF ORGANICS AND SECONDARY ORGANIC AEROSOL PRODUCTION INDOORS[1]

3.1 Introduction

Cleaning with sodium hypochlorite (NaOCl) bleach solutions introduces various primary and secondary volatile pollutants to the indoor environment. Chlorocarbons such as chloroform ($CHCl_3$) and carbon tetrachloride (CCl_4) are toxic and likely carcinogens, and are emitted to indoor air during bleach cleaning (Odabasi, 2008; Farmer et al., 2019). Chloramines (NH_2Cl, $NHCl_2$, NCl_3) are respiratory irritants emitted from bleach as solution impurities, and are produced from bleach reacting with indoor amines present in air and on surfaces (Massin et al., 1998; Thickett et al., 2002; Dang et al., 2010; Jacobs et al., 2007; Wong et al., 2017; Mattila et al., 2020). Hypochlorous acid (HOCl) is emitted from bleach (Mattila et al., 2020; Wong et al., 2017), and indoor HOCl levels during typical bleach cleaning chlorinates squalene (a major component of skin oil), possibly leading to skin and respiratory irritation (Schwartz-Narbonne et al., 2018). With the recent rise in disinfectant and bleach use (Chang et al., 2020), understanding the chemical processes controlling indoor lifetimes of, and thus exposure to, bleach-related pollutants is imperative for indoor air quality and human health.

Many bleach-related emissions, including HOCl, chlorine (Cl_2), nitryl chloride ($ClNO_2$), and chloramines are driven by multiphase chemistry occurring in the aqueous bleach and on

[1]Mattila, J. M., Arata, C., Wang, C., Katz, E. F., Abeleira, A., Zhou, Y., Zhou, S., Goldstein, A. H., Abbatt, J. P., and DeCarlo, P. F.: Dark chemistry during bleach cleaning enhances oxidation of organics and secondary organic aerosol production indoors, Environ. Sci. Technol. Lett., 7, 795-801, 2020.

interior surfaces (Wong et al., 2017; Mattila et al., 2020). This same chemistry also elevates indoor nitrogen dioxide (NO_2) and ozone (O_3) (Mattila et al., 2020), which are respiratory irritants and key components of photochemical smog in the outdoor atmosphere. Bleach cleaning can induce gas-phase radical chemistry, producing hydroxyl (OH) and chlorine (Cl) radicals indoors via photolysis of HOCl and Cl_2 (Wong et al., 2017; Mattila et al., 2020; Dawe et al., 2019). Dawe et al. (2019) demonstrated that bleach-related Cl radicals may react with indoor volatile organic compounds (VOCs) to yield corrosive hydrogen chloride (HCl). OH and Cl radicals can oxidize VOCs to produce lower-volatility oxygenated VOCs (OVOCs). OVOCs can then condense on pre-existing indoor particulate matter (PM) to form secondary organic aerosol (SOA), an air pollutant associated with numerous respiratory and cardiovascular diseases (Nel, 2005; Jimenez et al., 2009). In a recent smog chamber study, Wang et al. (2019) exposed monoterpenes (limonene and α-pinene; $C_{10}H_{16}$) to gaseous HOCl/Cl_2 in dark conditions to produce OVOC products, and subsequently observed SOA production when illuminating the chamber with fluorescent light or sunlight from nearby windows. Limonene and α-pinene are common indoor VOCs that are released from cooking, cleaning, and personal care products (Wang et al., 2019), suggesting that this bleach-induced SOA production may occur indoors.

However, the extent to which bleach cleaning can induce VOC oxidation chemistry and SOA formation in actual homes remains largely uncharacterized. Here, we use measurements from the House Observations of Microbial and Environmental Chemistry (HOMEChem) campaign to demonstrate that bleach-related oxidation chemistry occurs in a realistic indoor residential environment, and that indoor air can thus include an array of highly oxidized, potentially toxic molecules from this secondary chemistry and not just from direct emissions (Farmer et al., 2019).

3.2 Materials and methods

The HOMEChem campaign took place at the University of Texas at Austin's UTest House in summer 2018, and included bleach cleaning experiments (Farmer et al., 2019; Mattila et al., 2020). During each cleaning event, a single volunteer prepared a bleach solution according to manufacturer instructions and mopped the floors for ten minutes. On 10 June 2018, we sequentially bleach mopped four times throughout the day. Enhanced ventilation (opening doors and windows) followed the first two bleach mops. On 19 and 25 June 2018, we performed a single bleach mop following prior cooking and terpene cleaning activities.

We measured gas-phase C_2H_3NO, C_3H_5NO, CHO_2Cl, $C_2H_3O_2Cl$, $C_3H_5O_3Cl$, and other oxygenated/nitrogenated VOCs indoors with a time-of-flight chemical ionization mass spectrometer (TOF-CIMS; Tofwerk AG and Aerodyne Research Inc.) utilizing iodide (I^-) reagent ions (I^- CIMS) (Mattila et al., 2020; Farmer et al., 2019). We calculate mixing ratios for these compounds following Mattila et al. (2020). A multi-channel online gas chromatography system measured limonene, α-pinene, isoprene (C_5H_8), $CHCl_3$, and tetrachloroethene (C_2Cl_4) (Swarthout et al., 2013; Farmer et al., 2019; Abeleira et al., 2017). C_2Cl_4 mixing ratios may be overcalculated due to an interference. A high-resolution time-of-flight aerosol mass spectrometer (HR-AMS; Aerodyne Research, Inc.) measured submicron non-refractory particulate organic mass concentrations and ion fragments (Farmer et al., 2019; DeCarlo et al., 2006). A proton transfer reaction time-of-flight mass spectrometer detected cyanogen chloride (ClCN) (Cappellin et al., 2010; Farmer et al., 2019); mixing ratios calculated following Zhao and Zhang (2004). We measured isocyanic acid (HNCO) with a TOF-CIMS (Tofwerk AG and Aerodyne Research Inc.) utilizing acetate reagent ions (Farmer et al., 2019; Wang et al., 2020); Wang et al. (2020) discuss HNCO calibration methods, with additional details to be described in an upcoming paper.

Farmer et al. (2019) and Mattila et al. (2020) describe photon flux measurements (USB4000 Ocean Optics spectrometer) and subsequent derivation of indoor photolysis rates. All chemical measurements switched between indoor and outdoor inlets, except for the chromatography system, which only sampled indoors (Farmer et al., 2019). Measurement time resolution and other instrument details are provided elsewhere (Farmer et al., 2019).

3.3 Results and discussion

3.3.1 Dark terpene oxidation and SOA production

Indoor limonene, α-pinene, and isoprene decreased substantially during all bleach cleaning experiments. Bleach cleaning on 19 June 2018 provides a particularly useful case study (Figure 3.1). Indoor limonene and α-pinene mixing ratios were elevated due to prior cleaning with a terpene-based solution, while isoprene was elevated due to human occupancy (Figure 3.1a) (Farmer et al., 2019). Persistent cloud coverage suppressed outdoor sunlight intensity, and therefore photochemistry on this day (Figure A2.1). This is exemplified by the lack of outdoor isoprene hydroperoxyperoxides or isoprene epoxydiols (Figure A2.1)—both OH-oxidation products of isoprene (Paulot et al., 2009), and markers for outdoor photochemistry. Minimal outdoor sunlight was transmitted through the house windows, and indoor photochemistry was thus negligible during this experiment.

While indoor monoterpene and isoprene levels decreased following bleach mopping, several OVOCs increased, including oxidation products of isoprene ($C_5H_{10}O_5$) and monoterpenes ($C_{10}H_{16}O_4$ and $C_{10}H_{16}O_5$) (Figure 3.1b) (Brophy and Farmer, 2015; Massoli et al., 2018; Li et al., 2020). OVOC production and VOC depletion was comparable during a replicate experiment (25 June 2018; Figure A2.2) in which outdoor sunlight transmission to indoors was much higher (Figure A2.1), consistent with non-photochemical reaction mechanisms. Aqueous and

heterogeneous oxidation chemistry (i.e. HOCl-induced peroxidation of unsaturated moieties (Panasenko et al., 2013)) was likely responsible for these and other oxidized products (Wang et al., 2019). OVOC production occurred prior to observed decreases in indoor isoprene/monoterpene mixing ratios (Figure A2.3), indicating that gas-phase oxidation did not control their respective oxidation products. Wang et al. (2020) demonstrated gas-surface partitioning behavior of indoor isoprene and monoterpenes at HOMEChem. We suspect that surface-bound terpenes on interior floors underwent aqueous and/or heterogeneous oxidation following bleach application, thus depleting these surface reservoirs. Reestablishing gas-surface equilibrium following this perturbation could explain the delayed decrease in terpene mixing ratios. We note that gas-phase oxidation may be important in producing other bleach-related OVOCs (i.e. $C_2H_4O_5$ and $C_4H_6O_6$).

Outdoors, OVOCs often form SOA as these oxygenated compounds can have lower vapor pressures than their volatile precursors. Consistent with this idea, we observed enhanced signals in oxygenated organic aerosol fragments ($C_3H_5O^+$, $C_3H_6O^+$, $C_3H_7O^+$, $C_3H_7O_2^+$, $C_4H_7O^+$, $C_5H_5O^+$, $C_5H_7O^+$, $C_6H_7O^+$) measured by HR-AMS, likely arising from the uptake of OVOCs produced during bleach cleaning to pre-existing indoor PM from cooking events earlier that day (Figure 3.1c and S2c) (Farmer et al., 2019). However, although the summed signal of these fragments ($\Sigma C_xH_yO^+$) increased significantly during bleach cleaning above pre-cleaning indoor levels (by ~25%), total submicron organic aerosol mass did not elevate substantially during or after bleach cleaning (Figure 3.1c and S2c). That is, these $C_xH_yO^+$ fragments constituted a minor fraction (<3%) of total organic PM_1 mass during these periods. This lack of substantial SOA production after bleach cleaning despite elevated precursor levels must be due to the relatively short timescales for SOA formation (air exchange rate (AER) = 0.5 ± 0.1 h^{-1}; calculation

described in Chapter 2 section SI2.1.2.1) combined with the extensive interior surfaces, which act as a large, competitive sink for condensable OVOCs (Weschler and Nazaroff, 2008, 2017). We previously demonstrated the importance of interior surfaces for surface-related processes during bleach cleaning at HOMEChem, given that they comprised ~10^5 more surface area over PM (Mattila et al., 2020). These observations collectively suggest that bleach cleaning will enhance deposition of OVOCs to interior surfaces, contributing more to secondary organic grime accumulation than SOA (Weschler and Nazaroff, 2017), although the chemical composition of the bleach cleaning-related surface grime will likely be similar to the enhanced organic aerosol observed by the HR-AMS. Factor analysis of HR-AMS data also revealed enhanced signals attributable to cooking organic aerosol (detailed in Appendix 2 section A2.1.1). We hypothesize that mopping liberated semivolatile, surface-bound organics from prior cooking activities into indoor air (Lunderberg et al., 2020; Or et al., 2020). The re-condensation of these cooking-related organics onto indoor PM thus enhanced observed SOA.

3.3.2 Dark production of chlorinated and nitrogenated VOCs

Indoor mixing ratios of several chlorinated and nitrogenated VOCs increased during bleach cleaning at HOMEChem (Figure 3.2a-d). These compounds remained elevated up to several hours after cleaning. We observed substantial production of these compounds across each cleaning event, even during the final cleaning replicate performed at 20:35 local time on 10 June 2018—after sunset when no indoor photochemistry is expected to occur (Figure 3.2e; indoor lights were turned off when the volunteers exited the house immediately after mopping) (Mattila et al., 2020). Even during the daytime cleaning events, indoor lighting fixtures played a negligible role in initiating photochemistry (Mattila et al., 2020); either dark secondary chemistry, or primary emission from solution (as impurities) must have controlled these

compounds indoors. We use inlet sniff tests performed during the campaign, and rates/time scales of production to further assess the role of primary emission and secondary production of these indoor pollutants (SI section A2.1.2). We additionally provide a detailed scheme of dark chemical mechanisms relevant to the production of these secondary VOCs (Figure A2.4).

In the absence of industrial accidents or combustion-related activities (Priestley et al., 2018; Blomqvist et al., 2003), organic isocyanates are not typically observed in the atmosphere, let alone the indoor environment. Thus surprisingly, we observed 1 – 2 ppbv of C_2H_3NO and 0.1 – 0.2 ppbv of C_3H_5NO indoors during bleach cleaning (Figure 3.2a). These formulae are consistent with methyl and ethyl isocyanate, respectively. While gas-phase oxidation of amides by OH radicals could produce these compounds (Borduas et al., 2015; Borduas et al., 2016), the fact that these isocyanates were observed under dark indoor conditions means that OH levels were unlikely sufficient to initiate this chemistry. Instead, we speculate that these organic isocyanates are produced following the uptake of surface-bound and/or gas-phase amides to the applied bleach, where aqueous HOCl reacts with amide moieties to produce isocyanates (Figure A2.4a) (Hawkins et al., 2003).

Isocyanates pose known health risks. The Occupational Safety and Health Administration (OSHA) permissible exposure limit (PEL) for methyl isocyanate is 20 ppbv, though we acknowledge these limits pertain to workplace, rather than household exposure. The highest indoor levels of methyl isocyanate while bleaching at HOMEChem were an order of magnitude lower (2 ppbv), but we emphasize that reduced ventilation (i.e. lower AER) would increase concentrations of any air toxic produced indoors. Chronic exposure to methyl isocyanate levels observed herein are likely of concern. For comparison, the California Office of Environmental

Health Hazard Assessment (OEHHA) Chronic Reference Exposure Level (REL) for methyl isocyanate is 0.4 ppbv.

We observed 1 – 2 ppbv increases in cyanogen chloride (ClCN) during bleach cleaning (Figure 3.2b). ClCN is a commonly observed disinfection byproduct of water chlorination. During HOMEChem, it possibly arose from aqueous reactions between HOCl and glycine or other amino acids present in surface organic grime/films (Figure A2.4b) (Na and Olson, 2006; Yang and Shang, 2004; Shang et al., 2000; Li and Blatchley, 2007); and/or formaldehyde with monochloramine (NH_2Cl) (Figure A2.4b) (Pedersen et al., 1999). Formaldehyde is a common indoor VOC arising from off-gassing of building materials and combustion sources (Gupta et al., 1982). Multiphase kinetic modeling revealed that aqueous reactions between ammonia and HOCl in the applied bleach solution yielded NH_2Cl during bleach cleaning at HOMEChem, though other surface-bound amines likely also contributed to observed enhancements of indoor NH_2Cl mixing ratios (Mattila et al., 2020). ClCN is highly toxic and an asphyxiant, though levels observed during bleach cleaning (≤2 ppbv) are far below the OSHA PEL of 300 ppbv.

Isocyanic acid (HNCO) mixing ratios increased by 0.1 – 0.3 ppbv (Figure 3.2b). HNCO may arise via aqueous reactions of formamide (CH_3NO) and HOCl—analogous to the production of aforementioned organic isocyanates, or via hydrolysis of ClCN under basic conditions (i.e. bleach solution) (Hawkins et al., 2003; Bailey and Bishop, 1973; Roberts and Liu, 2019). HNCO is potentially toxic at exposures > 1 ppbv (Roberts et al., 2011). Observations of HNCO while cleaning and cooking at HOMEChem will be detailed in a separate publication.

Indoor production rates of C_2H_3NO, C_3H_5NO, ClCN, and HNCO progressively decreased with each sequential bleach application (section A2.1.2). This is consistent with the progressive reduction of aforementioned surface-bound precursors, where subsequent mopping events would

presumably involve a cleaner floor with less organic/nitrogenated matter. Additionally, indoor levels of these compounds increased several minutes after HOCl, a tracer for primary emission from bleach during HOMEChem (Mattila et al., 2020), indicating that secondary chemical production occurred following bleach application (section A2.1.2). While inlet sniff tests suggest these compounds were impurities in the original bleach concentrate (excluding ClCN; section A2.1.2), secondary chemistry is required to explain observed production during cleaning.

Indoor CHO_2Cl and $C_2H_3O_2Cl$ increased by 0.3 – 0.5 ppbv, and $C_3H_5O_3Cl$ by 30 – 70 pptv (parts-per-trillion by volume) during bleach cleaning (Figure 3.2c). These chemical formulae are consistent with chloroformic, chloroacetic, and chlorolactic acid, respectively. We detected these chlorinated organic acids (or Cl-acids) during inlet sniff tests, and their production occurred at time scales comparable to HOCl, indicating that primary emission of these impurities explains observed mixing ratios during cleaning (section A2.1.2).

Aqueous Cl-acid production is not unprecedented, though it is typically only considered relevant in water disinfection chemistry. For example, chloroacetic acid is produced via aqueous reactions of free chlorine and dissolved organic matter (i.e. humic acid) and is a commonly observed byproduct of drinking water chlorination (Yang and Shang, 2004). These organic precursors were likely present on the floors of the test house (in organic grime layers/films). It is possible this chemistry constituted a minor secondary production source of chloroacetic acid (and possibly other Cl-acids); further assessment is therefore warranted. Chloroacetic acid is a hazardous alkylating agent, and interferes with enzymatic processes involved in the Krebs cycle (Shimizu et al., 2002; Sakai et al., 2005). Studies on health effects of airborne exposure to these Cl-acids are lacking.

Bleach cleaning was a source of $CHCl_3$ and C_2Cl_4 to indoor air (Figure 3.2d), similar to previous studies (Odabasi et al., 2014; Odabasi, 2008). Indoor $CHCl_3$ and C_2Cl_4 increased above pre-cleaning levels by hundreds of pptv. These chlorocarbons likely arose via reactions of free chlorine with organic compounds initially present on the test house floors, producing volatile chlorocarbon products. For example, $CHCl_3$ is produced from HOCl reactions with acetone or other methyl ketones (Figure A2.4c) (Deborde and Von Gunten, 2008). Previous studies have also identified these chlorocarbons in bleach as impurities (Odabasi et al., 2014; Odabasi, 2008). We did not perform inlet sniff tests for these chlorocarbons, nor are we able to reliably assess temporal trends in production given the low time-resolution of these measurements. We speculate both primary emission and secondary chemistry contributed to observed chlorocarbon mixing ratios. Indoor mixing ratios of $CHCl_3$ and C_2Cl_4 ($\leq$ 0.7 and 0.2 ppbv, respectively) were below the OSHA PEL (50 ppm for $CHCl_3$; 100 ppm for C_2Cl_4). However, long-term exposure may increase their associated carcinogenic risks (Odabasi et al., 2014). The OEHHA Chronic REL for $CHCl_3$ is 60 ppbv.

3.3.3 Implications for indoor chemistry and air quality

While Wang et al. (2019) demonstrated the importance of dark $HOCl/Cl_2$ chemistry on gas-phase composition via monoterpene oxidation, they only observed SOA formation under irradiated conditions. Injecting gas-phase $HOCl/Cl_2$ into a dry chamber simulated bleach fumes that reacted with monoterpenes via dark gas-phase and/or heterogeneous oxidation chemistry (Wang et al., 2019). Realistic cleaning conditions involve application of bleach solution to indoor surfaces, and thus the potential for additional aqueous oxidation chemistry. In contrast to Wang et al. (2019), our observations suggest that these dark multiphase reactions between bleach-related oxidants and terpenes (or other organics) can drive non-photochemical VOC

oxidation and SOA formation indoors. Photochemically-driven VOC oxidation and SOA formation during bleach use may be more important under different indoor conditions. For example, more windows could increase transmission of photochemistry-inducing light to indoors.

To our knowledge, this work represents the first direct observations of SOA formation in a realistic residential environment, despite the short timescales available for oxidative chemistry and gas-particle partitioning. Further, our observations corroborate previous work demonstrating how bleach produces potentially harmful indoor pollutants (Odabasi et al., 2014; Odabasi, 2008; Wong et al., 2017; Mattila et al., 2020). This 'indoor smog' demonstrates the importance of chemical transformations in the indoor environments for influencing air quality, and suggests a chemically distinct mechanism for producing outdoor pollutants such as OVOCs and isocyanates. This chemistry contributes to indoor SOA formation, though most of the lower volatility organic oxidation products likely partition to indoor surfaces and contribute to secondary organic grime and organic films.

3.4 Author contributions

J. M. M. contributed iodide CIMS data collection, and analyses performed herein.

3.5 Data availability

Data used herein are available at https://osf.io/aqc57/.

3.6 Chapter 3 figures

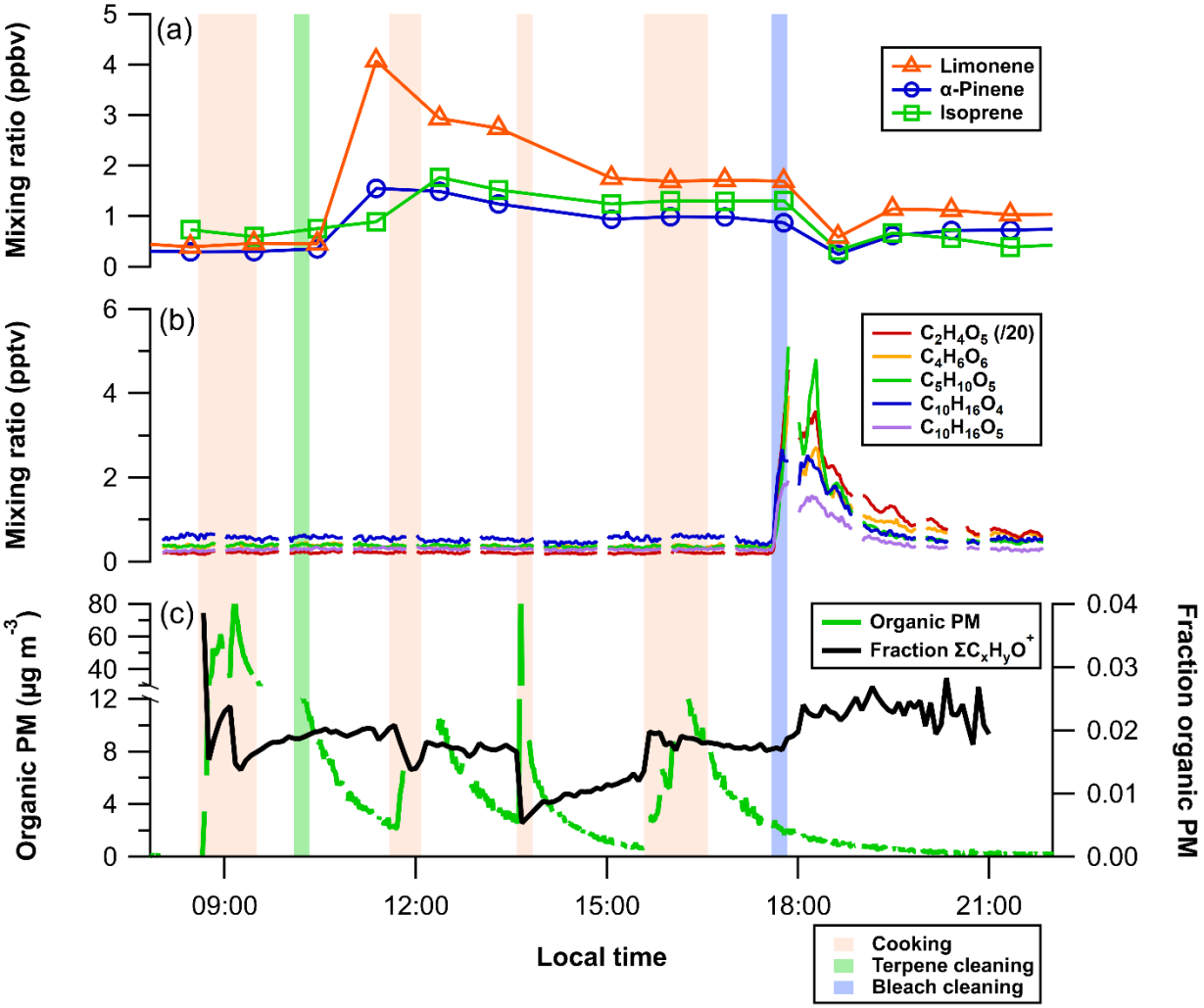

Figure 3.1. Indoor time series of (a) limonene (orange triangles), α-pinene (blue circles), and isoprene (green squares); (b) OVOCs detected by I^- CIMS (colored traces); and (c) organic PM mass concentrations (green), and fractional contribution of $\Sigma C_xH_yO^+$ HR-AMS fragments ($C_3H_5O^+$, $C_3H_6O^+$, $C_3H_7O^+$, $C_3H_7O_2^+$, $C_4H_7O^+$, $C_5H_5O^+$, $C_5H_7O^+$, $C_6H_7O^+$) to total organic PM (black) on 19 June 2018. Shaded areas correspond to local times during which cooking (orange), terpene cleaning (green), and bleach cleaning (blue) took place.

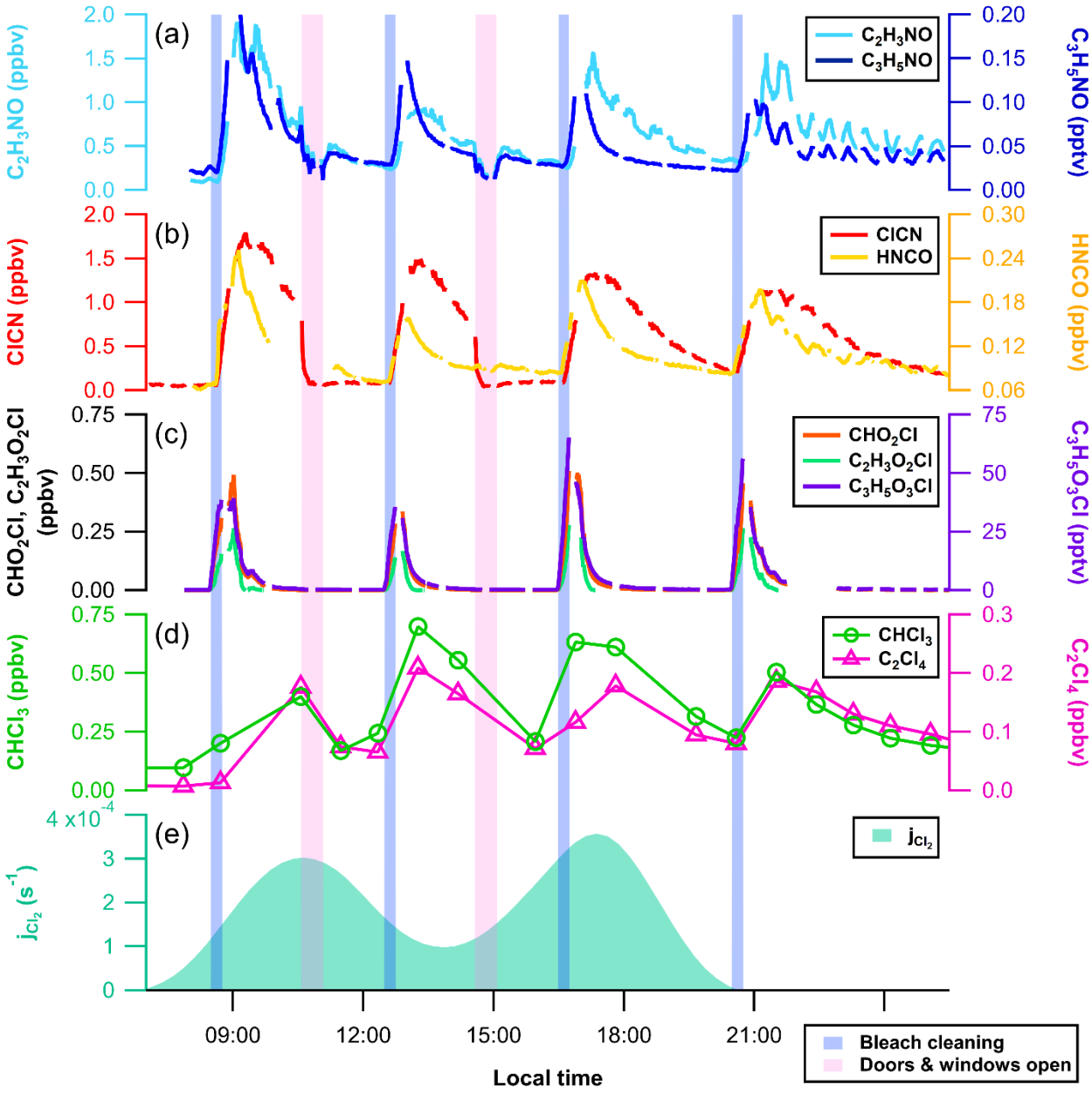

Figure 3.2. (a-d) Indoor mixing ratio time series of chlorinated and nitrogenated VOCs (various colored markers and traces) produced during a bleach cleaning experiment on 10 June 2018; (e) campaign-average upper-bound diel profiles of indoor Cl_2 photolysis rates (j_{Cl2}; shaded green area; see Mattila et al. (2020)), used here as a proxy for sunlight transmitted to indoors. Blue and pink shaded areas correspond to local times during which bleach cleaning, and opening of test house doors and windows took place, respectively.

REFERENCES

Abeleira, A., Pollack, I., Sive, B., Zhou, Y., Fischer, E., and Farmer, D.: Source characterization of volatile organic compounds in the Colorado Northern Front Range Metropolitan Area during spring and summer 2015, J. Geophys. Res. Atmos., 122, 3595-3613, 2017.

Bailey, P. L., and Bishop, E.: Hydrolysis of cyanogen chloride, J. Chem. Soc., 912-916, 1973.

Blomqvist, P., Hertzberg, T., Dalene, M., and Skarping, G.: Isocyanates, aminoisocyanates and amines from fires—a screening of common materials found in buildings, Fire Mater., 27, 275-294, 2003.

Borduas, N., da Silva, G., Murphy, J. G., and Abbatt, J. P.: Experimental and theoretical understanding of the gas phase oxidation of atmospheric amides with OH radicals: kinetics, products, and mechanisms, J. Phys. Chem. A, 119, 4298-4308, 2015.

Borduas, N., Abbatt, J. P., Murphy, J. G., So, S., and da Silva, G.: Gas-Phase Mechanisms of the Reactions of Reduced Organic Nitrogen Compounds with OH Radicals, Environ. Sci. Technol., 50, 11723-11734, doi:10.1021/acs.est.6b03797, 2016.

Brophy, P., and Farmer, D. K.: A switchable reagent ion high resolution time-of-flight chemical ionization mass spectrometer for real-time measurement of gas phase oxidized species: characterization from the 2013 southern oxidant and aerosol study, Atmos. Meas. Tech., 8, 2945-2959, doi:10.5194/amt-8-2945-2015, 2015.

Cappellin, L., Biasioli, F., Fabris, A., Schuhfried, E., Soukoulis, C., Märk, T. D., and Gasperi, F.: Improved mass accuracy in PTR-TOF-MS: Another step towards better compound identification in PTR-MS, Int. J. Mass Spectrom., 290, 60-63, 2010.

Chang, A., Schnall, A. H., Law, R., Bronstein, A. C., Marraffa, J. M., Spiller, H. A., Hays, H. L., Funk, A. R., Mercurio-Zappala, M., and Calello, D. P.: Cleaning and Disinfectant Chemical Exposures and Temporal Associations with COVID-19—National Poison Data System, United States, January 1, 2020–March 31, 2020, 496, 2020.

Dang, B., Chen, L., Mueller, C., Dunn, K. H., Almaguer, D., Roberts, J. L., and Otto, C. S.: Ocular and respiratory symptoms among lifeguards at a hotel indoor waterpark resort, J. Occup. Environ. Med., 52, 207-213, 2010.

Dawe, K. E. R., Furlani, T. C., Kowal, S. F., Kahan, T. F., VandenBoer, T. C., and Young, C. J.: Formation and emission of hydrogen chloride in indoor air, Indoor Air, 29, 70-78, 2019.

Deborde, M., and Von Gunten, U.: Reactions of chlorine with inorganic and organic compounds during water treatment—kinetics and mechanisms: a critical review, Water Res., 42, 13-51, 2008.

DeCarlo, P. F., Kimmel, J. R., Trimborn, A., Northway, M. J., Jayne, J. T., Aiken, A. C., Gonin, M., Fuhrer, K., Horvath, T., Docherty, K. S., Worsnop, D. R., and Jimenez, J. L.: Field-deployable, high-resolution, time-of-flight aerosol mass spectrometer, Anal. Chem., 78, 8281-8289, doi:10.1021/ac061249n, 2006.

Farmer, D. K., Vance, M. E., Abbatt, J. P. D., Abeleira, A., Alves, M. R., Arata, C., Boedicker, E., Bourne, S., Cardoso-Saldaña, F., Corsi, R., DeCarlo, P. F., Goldstein, A. H., Grassian, V. H., Hildebrandt Ruiz, L., Jimenez, J. L., Kahan, T. F., Katz, E. F., Mattila, J. M., Nazaroff, W. W., Novoselac, A., O'Brien, R. E., Or, V. W., Patel, S., Sankhyan, S., Stevens, P. S., Tian, Y., Wade, M., Wang, C., Zhou, S., and Zhou, Y.: Overview of HOMEChem: House Observations of Microbial and Environmental Chemistry, Environ. Sci. Process. Impacts, 21, 1280-1300, 10.1039/C9EM00228F, 2019.

Gupta, K., Ulsamer, A., and Preuss, P.: Formaldehyde in indoor air: sources and toxicity, Environ. Int., 8, 349-358, 1982.

Hawkins, C., Pattison, D., and Davies, M. J.: Hypochlorite-induced oxidation of amino acids, peptides and proteins, Amino acids, 25, 259-274, 2003.

Jacobs, J., Spaan, S., Van Rooy, G., Meliefste, C., Zaat, V., Rooyackers, J., and Heederik, D.: Exposure to trichloramine and respiratory symptoms in indoor swimming pool workers, Eur. Respir. J., 29, 690-698, 2007.

Jimenez, J. L., Canagaratna, M. R., Donahue, N. M., Prevot, A. S. H., Zhang, Q., Kroll, J. H., DeCarlo, P. F., Allan, J. D., Coe, H., and Ng, N. L.: Evolution of organic aerosols in the atmosphere, Science, 326, 1525-1529, 2009.

Li, H., Riva, M., Rantala, P., Heikkinen, L., Daellenbach, K., Krechmer, J. E., Flaud, P.-M., Worsnop, D., Kulmala, M., and Villenave, E.: Terpenes and their oxidation products in the French Landes forest: insights from Vocus PTR-TOF measurements, Atmos. Chem. Phys., 20, 1941–1959, 2020.

Li, J., and Blatchley, E. R.: Volatile disinfection byproduct formation resulting from chlorination of organic−nitrogen precursors in swimming pools, Environ. Sci. Technol., 41, 6732-6739, 2007.

Lunderberg, D., Kristensen, K., Tian, Y., Arata, C., Misztal, P. K., Liu, Y., Kreisberg, N. M., Katz, E. F., DeCarlo, P., and Patel, S.: Surface emissions modulate indoor SVOC concentrations through volatility-dependent partitioning, Environ. Sci. Technol., 54, 6751-6760, 2020.

Massin, N., Bohadana, A. B., Wild, P., Héry, M., Toamain, J. P., and Hubert, G.: Respiratory symptoms and bronchial responsiveness in lifeguards exposed to nitrogen trichloride in indoor swimming pools, Occup. Environ. Med., 55, 258-263, 10.1136/oem.55.4.258, 1998.

Massoli, P., Stark, H., Canagaratna, M. R., Krechmer, J. E., Xu, L., Ng, N. L., Mauldin III, R. L., Yan, C., Kimmel, J., and Misztal, P. K.: Ambient measurements of highly oxidized gas-phase

molecules during the southern oxidant and aerosol study (SOAS) 2013, ACS Earth Space Chem., 2, 653-672, 2018.

Mattila, J. M., Lakey, P. S. J., Shiraiwa, M., Wang, C., Abbatt, J. P. D., Arata, C., Goldstein, A. H., Ampollini, L., Katz, E. F., DeCarlo, P. F., Zhou, S., Kahan, T. F., Cardoso-Saldaña, F. J., Hildebrandt Ruiz, L., Abeleira, A., Boedicker, E., Vance, M. E., and Farmer, D. K.: Multiphase chemistry controls inorganic chlorinated and nitrogenated compounds in indoor air during bleach cleaning, Environ. Sci. Technol., 54, 1730-1739, 10.1021/acs.est.9b05767, 2020.

Na, C., and Olson, T. M.: Mechanism and kinetics of cyanogen chloride formation from the chlorination of glycine, Environ. Sci. Technol., 40, 1469-1477, 2006.

Nel, A.: Air pollution-related illness: effects of particles, Science, 308, 804-806, 2005.

Odabasi, M.: Halogenated volatile organic compounds from the use of chlorine-bleach-containing household products, Environ. Sci. Technol., 42, 1445-1451, 2008.

Odabasi, M., Elbir, T., Dumanoglu, Y., and Sofuoglu, S. C.: Halogenated volatile organic compounds in chlorine-bleach-containing household products and implications for their use, Atmos. Environ., 92, 376-383, 2014.

Or, V. W., Wade, M., Patel, S., Alves, M. R., Kim, D., Schwab, S., Przelomski, H., O'Brien, R., Rim, D., and Corsi, R.: Glass Surface Evolution Following Gas Adsorption and Particle Deposition from Indoor Cooking Events as Probed by Microspectroscopic Imaging and Characterization, Environ. Sci. Process. Impacts, 22, 1698-1709, 10.1039/D0EM00156B, 2020.

Panasenko, O., Gorudko, I., and Sokolov, A.: Hypochlorous acid as a precursor of free radicals in living systems, Biochemistry (Moscow), 78, 1466-1489, 2013.

Paulot, F., Crounse, J. D., Kjaergaard, H. G., Kürten, A., Clair, J. M. S., Seinfeld, J. H., and Wennberg, P. O.: Unexpected epoxide formation in the gas-phase photooxidation of isoprene, Science, 325, 730-733, 2009.

Pedersen, E. J., Urbansky, E. T., Mariñas, B. J., and Margerum, D. W.: Formation of cyanogen chloride from the reaction of monochloramine with formaldehyde, Environ. Sci. Technol., 33, 4239-4249, 1999.

Priestley, M., Le Breton, M., Bannan, T. J., Leather, K. E., Bacak, A., Reyes-Villegas, E., De Vocht, F., Shallcross, B. M., Brazier, T., and Anwar Khan, M.: Observations of Isocyanate, Amide, Nitrate, and Nitro Compounds From an Anthropogenic Biomass Burning Event Using a ToF-CIMS, J. Geophys. Res. Atmos., 123, 7687-7704, 2018.

Roberts, J. M., Veres, P. R., Cochran, A. K., Warneke, C., Burling, I. R., Yokelson, R. J., Lerner, B., Gilman, J. B., Kuster, W. C., Fall, R., and de Gouw, J.: Isocyanic acid in the atmosphere and its possible link to smoke-related health effects, Proc. Natl. Acad. Sci. U.S.A., 108, 8966-8971, doi:10.1073/pnas.1103352108, 2011.

Roberts, J. M., and Liu, Y.: Solubility and solution-phase chemistry of isocyanic acid, methyl isocyanate, and cyanogen halides, Atmos. Chem. Phys., 19, 4419-4437, 2019.

Sakai, A., Shimizu, H., Kono, K., and Furuya, E.: Monochloroacetic acid inhibits liver gluconeogenesis by inactivating glyceraldehyde-3-phosphate dehydrogenase, Chem. Res. Toxicol., 18, 277-282, 2005.

Schwartz-Narbonne, H., Wang, C., Zhou, S., Abbatt, J. P. D., and Faust, J.: Heterogeneous chlorination of squalene and oleic acid, Environ. Sci. Technol., 53, 1217, 10.1021/acs.est.8b04248, 2018.

Shang, C., Gong, W.-L., and Blatchley, E. R.: Breakpoint chemistry and volatile byproduct formation resulting from chlorination of model organic-N compounds, Environ. Sci. Technol., 34, 1721-1728, 2000.

Shimizu, H., Dote, T., Usuda, K., Toshina, Y., Kato, J., Sakai, A., Furuya, E., and Kono, K.: Therapeutic effects of glucose infusion on monochloroacetic acid exposure in rats, Toxicol. Ind. Health, 18, 389-395, 2002.

Swarthout, R. F., Russo, R. S., Zhou, Y., Hart, A. H., and Sive, B. C.: Volatile organic compound distributions during the NACHTT campaign at the Boulder Atmospheric Observatory: Influence of urban and natural gas sources, J. Geophys. Res. Atmos., 118, 2013.

Thickett, K., McCoach, J., Gerber, J., Sadhra, S., and Burge, P.: Occupational asthma caused by chloramines in indoor swimming-pool air, Eur. Respir. J., 19, 827-832, 2002.

Wang, C., Collins, D. B., and Abbatt, J. P. D.: Indoor illumination of terpenes and bleach emissions leads to particle formation and growth, Environ. Sci. Technol., 53, 11615-12150, 2019.

Wang, C., Collins, D. B., Arata, C., Goldstein, A. H., Mattila, J. M., Farmer, D. K., Ampollini, L., DeCarlo, P. F., Novoselac, A., Vance, M. E., Nazaroff, W. W., and Abbatt, J. P. D.: Surface reservoirs dominate dynamic gas-surface partitioning of many indoor air constituents, Sci Adv, 6, aay8973, 10.1126/sciadv.aay8973 2020.

Weschler, C. J., and Nazaroff, W. W.: Semivolatile organic compounds in indoor environments, Atmos. Environ., 42, 9018-9040, 2008.

Weschler, C. J., and Nazaroff, W. W.: Growth of organic films on indoor surfaces, Indoor Air, 27, 1101-1112, 2017.

Wong, J. P. S., Carslaw, N., Zhao, R., Zhou, S., and Abbatt, J. P. D.: Observations and impacts of bleach washing on indoor chlorine chemistry, Indoor Air, 27, 1082-1090, 2017.

Yang, X., and Shang, C.: Chlorination byproduct formation in the presence of humic acid, model nitrogenous organic compounds, ammonia, and bromide, Environ. Sci. Technol., 38, 4995-5001, 2004.

Zhao, J., and Zhang, R.: Proton transfer reaction rate constants between hydronium ion (H_3O^+) and volatile organic compounds, Atmos. Environ., 38, 2177-2185, 2004.

CHAPTER 4 – CONTRASTING CHEMICAL COMPLEXITY OF INDOOR AND OUTDOOR REACTIVE ORGANIC CARBON

4.1 Introduction

Organic species in the atmosphere influence biogeochemical cycles, global climate, and human health (Heald and Kroll, 2020). Reactive organic carbon (ROC), or all atmospheric organic carbon excluding methane (CH_4), comprises a substantial portion of carbon emissions to the outdoor atmosphere (Heald and Kroll, 2020). ROC is chemically diverse, including all non-methane volatile organic compounds (VOCs) and lower-volatility organics including particulate organic carbon. ROC dominates hydroxyl radical (OH) reactivity outdoors, and therefore plays a key role in the formation of secondary atmospheric pollutants including carbon dioxide (CO_2), ozone (O_3), and particulate matter (PM) (Heald and Kroll, 2020; Atkinson, 2000; Jimenez et al., 2009). CO_2 and O_3 are greenhouse gases that lead to global warming through radiative forcing (Masson-Delmotte et al., 2018). O_3 and PM are key components of photochemical smog, which strongly affects visibility and air quality (Geddes and Murphy, 2012). Recent innovations in fast, online measurements of volatile and particulate organics have allowed for more comprehensive accounting of the total atmospheric carbon budget. Prior to this, our understanding was hindered by the inability to routinely measure low-volatility oxidized species and short-lived intermediates (Heald and Kroll, 2020). Several recent field studies with broad instrumental coverage of ROC have greatly advanced our knowledge of outdoor sources, transformation processes, and secondary pollutant formation (Heald and Kroll, 2020; Hunter et al., 2017; Isaacman-VanWertz et al., 2018).

Despite the fact that people in the United States typically spend a majority of their time indoors (Klepeis et al., 2001), the organic carbon budgets of built indoor environments are understudied compared to the outdoor atmosphere. The sources, properties, and fates of indoor ROC impact indoor air quality through both direct exposure and indirect exposure to secondary pollutants formed through indoor chemistry and oxidation. Further, volatile organic emissions from consumer products including paints, cleaning agents, and personal care products can contribute to outdoor pollution following their removal from indoors via ventilation (McDonald et al., 2018; Gkatzelis et al., 2020). Price et al. (2019) recently performed a comprehensive characterization of indoor ROC budgets in a museum, a classroom, and various residential environments. Here, they generally found higher carbon mass concentrations indoors compared to those previously observed outdoors (Price et al., 2019). They additionally found indoor ROC was high enough to yield substantial reactive fluxes toward various atmospheric oxidants (e.g. OH, O_3, nitrate and chlorine radicals), despite low oxidant levels compared to outdoors (Price et al., 2019). However, ROC was dominantly removed from indoors by ventilation, and most secondary oxidation chemistry actually took place outdoors following this removal (Price et al., 2019). While this study focused on emissions and chemistry in several types of built indoor environments, we lack knowledge on how a variety of common indoor activities (e.g. cooking, cleaning) affect ROC budgets specific to a single controlled indoor environment. Further, no direct comparisons of indoor and outdoor ROC using measurements from an identical suite of analytical measurement techniques exist to date. Directly comparing indoor and outdoor ROC is necessary for reliably assessing the importance of indoor emissions as a net source of ROC to outdoors, or vice versa.

Here, we describe online measurements of gaseous and particulate organics performed indoors at the University of Texas at Austin test house (UTest house) during the House Observations of Microbial and Environmental Chemistry (HOMEChem) field campaign in summer 2018 (described further in Methods and Farmer et al. (2019)). These measurements involved multiple instruments to cover the range of gases and particles present in the indoor environment, and were thus collated to ensure comparability and to avoid measurement overlap (see Methods). We used these measurements to probe the magnitudes and bulk properties of indoor ROC emissions from various cooking and cleaning activities. We also performed simultaneous measurements of outdoor air during indoor HOMEChem experiments, allowing us to directly compare the chemical complexity of indoor and outdoor air. From this, we determine how cooking and cleaning impact the bulk physiochemical properties of indoor ROC, and assess the importance of indoor air as a source of ROC (and thus secondary oxidation products) to the outdoor atmosphere.

4.2 Results

4.2.1 Indoor and outdoor reactive organic carbon (ROC) concentrations

We show indoor and outdoor ROC mass concentrations during HOMEChem in Figure 4.1. Indoor ROC when the house was unoccupied with no indoor activities taking place (223 μg C m^{-3} median) was considerably higher than outdoor ROC measured throughout the campaign (54 μg C m^{-3} median). Cleaning indoors with chlorine bleach and an "all-natural" cleaning product did not substantially elevate ROC from background levels (medians of 232 and 251 μg C m^{-3}, respectively). Cooking-based experiments greatly enhanced indoor ROC levels. A stir-frying experiment resulted in median indoor ROC of 568 μg C m^{-3}. Experiments performed on 8 June and 25 June 2018 in which various cooking and cleaning activities throughout the entire

day without enhanced ventilation (hereafter "layered" experiments) yielded median indoor ROC of 485 and 590 μg C m^{-3}, respectively. Indoor ROC was the highest during a simulated Thanksgiving Day experiment, with a median of 1740 μg C m^{-3}, and a maximum value of 4030 μg C m^{-3}.

Particulate organic carbon was a minor fraction of ROC during HOMEChem, comprising 0 – 2% of indoor ROC, and ~3% of outdoor ROC. As PM is linked to negative health effects (Shiraiwa et al., 2017), the small role for particulate organic carbon clearly demonstrates how minor components of indoor air by mass can have an outsized impact on health effects. Even during Thanksgiving, when particulate organic carbon reached >100 μg C m^{-3}, it still only accounted for ~2% of the total ROC.

Indoor ROC during unoccupied periods at HOMEChem was of similar magnitude to the median of 77 occupied residences located across the United States and other industrialized nations (306 μg C m^{-3}) (Logue et al., 2011; Price et al., 2019), and over twice the reported mean indoor ROC for a museum (100 μg C m^{-3}) and classroom (89 μg C m^{-3}) (Figure 4.1) (Price et al., 2019). A likely driving factor in the latter set of observations was higher air exchange rates (AER) in the museum (0.8 h^{-1}) and classroom (2 – 11 h^{-1}) compared to the UTest house (0.5 ± 0.1 h^{-1}) (Farmer et al., 2019), leading to faster removal of indoor VOCs via ventilation. Outdoor ROC during HOMEChem was comparable to summertime urban air in Pittsburgh, Pennsylvania (47 μg C m^{-3} mean) (Heald et al., 2008); higher than summertime in an alpine forest in the Rocky Mountains (30 μg C m^{-3} mean) (Hunter et al., 2017), a forest in the Appalachian Mountains (37 μg C m^{-3} mean) (Heald et al., 2020), and rural northeastern US (18 μg C m^{-3} mean) (Heald et al., 2008); and lower than springtime urban air in Pasadena, California (74 μg C m^{-3} mean) (Heald et al., 2020). Indoor ROC levels observed during stir-frying and layered experiments are of similar

magnitude to reported outdoor ROC values in Mexico City (455 μg C m^{-3} mean) (Heald et al., 2008), and ROC during Thanksgiving at HOMEChem was several times higher than these levels. We used a different suite of measurement techniques to derive ROC compared to previous studies, and note resulting comparisons of ROC concentrations are likely not one-to-one. However, our measurements covered a broad range of physiochemical properties (discussed later), and likely captured a majority of total ROC (Isaacman-VanWertz et al., 2017).

4.2.2 Prominent chemical constituents of ROC

The largest contributors to indoor ROC during unoccupied periods were acetic acid (11.7% of ROC), methanol (8.7%), formic acid (8.7%), propane (6.2%), ethanol (5.7%), and acetone (2.3%) (Figure 4.2a). These compounds had strong background sources, and consequently were also highly prominent constituents of ROC during other HOMEChem activities. Off-gassing of various building materials (wood, adhesives, solvents, etc.) likely contributed to background formic and acetic acid, methanol, and acetone (Liu et al., 2019; Bari et al., 2015). We attribute the elevated background propane with gas pilot light usage (Farmer et al., 2019). VOCs emitted from cooking and other activities (e.g. ethanol; discussed later this section) sorb into surface reservoirs, which subsequently influenced background VOC concentrations via air-surface partitioning (Wang et al., 2020).

Indoor ROC during Thanksgiving was dominated by ethanol (47%), produced from various cooking activities (and background emissions) (Figure 4.2b) (Liu et al., 2019). Other prominent cooking-related emissions during Thanksgiving included limonene (8.8% of ROC), acetic acid (4.0%), citral (+ other isomers; 3.8%), methanol (2.5%), acetaldehyde (2.0%), and propionic acid (1.9%). Peeling and adding an orange to a cranberry sauce elevated limonene and citral. Adding balsamic vinegar to roasted brussels sprouts elevated acetic acid. Propionic acid

(and propionate salts) are commonly used as preservatives in bakery products (Rahim and Talib, 2010). We observe substantial propionic acid emissions while roasting bread for turkey stuffing. Elevated methanol and acetaldehyde emissions during various types of cooking activities have been previously reported (Klein et al., 2016; Kabir and Kim, 2011). Acetone (2.0% of ROC) is a human metabolic emission, and was likely elevated due to extensive occupancy during these periods (Farmer et al., 2019).

Like Thanksgiving, ROC during stir-frying and layered experiments was dominated by ethanol (43 – 59%), with smaller contributions from other cooking and/or background-related emissions (Figure A3.1b-d). Prominent chemical constituents of ROC during bleach cleaning resembled unoccupied periods (Figure A3.1a,e). While several chlorinated and nitrogenated VOCs increased substantially during bleach cleaning, they contributed insubstantially to ROC. For instance, Mattila et al. (2020a) observed significant enhancements in methyl isocyanate and cyanogen chloride mixing ratios during bleach cleaning at HOMEChem, but these compounds only contributed to 0.4% and 0.2% of bleach cleaning ROC, respectively. When cleaning with the all-natural product, indoor air was strongly influenced by citurs-scent compounds present in the applied solution, including limonene (10.7% of ROC), citral (+ other isomers; 2.7%), and α-pinene (1.7%).

Outdoors, ROC was mainly comprised of acetone (13.7% of ROC), acetic acid (8.2%), acetaldehyde (4.7%), propane (4.6%), and methanol (4.5%) (Figure 4.2c). In contrast to background indoor air, outdoor ROC features higher contributions from several non-methane hydrocarbons (NMHCs), including ethane (4.2% of ROC), isobutane (3.7%), isoprene (3.5%), n-butane (2.6%), and isopentane (1.7%). Outdoor air composition near the UTest house was likely influenced by nearby highway traffic emissions (< 1 km from MoPac Expressway and U.S.

Route 183) (Patel et al., 2020), and regional-scale oil and natural gas (ONG) activity. Traffic and ONG activity are major anthropogenic sources of NMHCs to the atmosphere (Kourtidis et al., 1999; Borbon et al., 2001; Abeleira et al., 2017). Acetone, acetaldehyde, and other carbonyls are produced from traffic exhaust (Grosjean et al., 2001), and photochemical oxidation of hydrocarbons (Calvert and Madronich, 1987). The outdoor air in Austin, TX also contains biogenic emissions from prominent broadleaf deciduous trees and grasslands native to this area. These vegetative emissions likely influenced observed outdoor isoprene and acetic acid mixing ratios (Khare et al., 1999; Fuentes et al., 2000).

4.2.3 Bulk physiochemical properties of ROC

We investigate various physiochemical properties of indoor and outdoor ROC, including carbon number (nC), carbon oxidation state (OS_C), and volatility. Carbon number and oxidation state relate to trends in molecular structure, and can provide clues toward the degree of atmospheric oxidation (or atmospheric age) of organic species. Increasing atmospheric age generally corresponds to an increased OS_C and decreased nC (via fragmentation reactions) (Kroll et al., 2011; Isaacman-VanWertz et al., 2018), with generally lower reactivities toward oxidants (Isaacman-VanWertz et al., 2018). Volatility, discussed hereafter in terms of saturation vapor concentration (C*; μg m^{-3}), influences the likelihood of a compound existing in the gas phase or a condensed phase (PM, surface films, etc.). Indoors, VOCs with $\log_{10}C^* > 7$ are deemed highly-volatile, while those ≤7 are considered to be semi/intermediate volatility (Price et al., 2019). Less volatile compounds are more likely to partition to wall surfaces (Wang et al., 2020), and participate in subsequent multiphase chemistry (Mattila et al., 2020b).

The majority (>60%) of indoor and outdoor ROC consisted of reduced compounds ($OS_C \leq 0$) with high volatilities ($\log_{10}C^* > 7$) and $nC \leq 6$. We provide histograms of ROC mass

concentrations binned by nC, OS_C, and $\log_{10}C^*$ during unoccupied indoor, Thanksgiving, and outdoor sampling (Figure 4.3 and A3.2). The prominence of ethanol ($\log_{10}C^* = 8.2$, nC = 2, $OS_C = -2$) during Thanksgiving considerably altered bulk property distributions relative to unoccupied periods, with an additionally large spike in the nC = 10 bin from limonene and citral emissions (Figure 4.3a-c). We report qualitatively similar relative trends in unoccupied indoor property distributions compared to outdoors, but with higher mass concentration magnitudes observed indoors (Figure 4.3d-f).

During unoccupied periods, median ROC physiochemical properties represented small (nC = 3), reduced ($OS_C = -1.5$), and highly-volatile ($\log_{10}C^* = 7.9$) organic compounds. Bleach cleaning did not substantially change these bulk properties compared to unoccupied background levels (Table A3.1). Cleaning with the all-natural cleaner resulted in lower median $\log_{10}C^*$ (7.7) and OS_C (-1.6), and higher median nC (4) compared to background conditions—attributable to emissions of larger, reduced VOCs (i.e. monoterpenes, citral) from the cleaning solution (Figure A3.1f). During cooking-related experiments, ethanol emissions drove changes to bulk indoor ROC properties (Figure 4.2 and A3.1d). However, when excluding ethanol from the analysis, median $\log_{10}C^*$ during stir-frying (8.0) was higher than that of background conditions (7.7). This observation was mainly driven the abundance of high-volatility NMHC emissions related to gas stove use, e.g. ethyne and ethene (6.3% and 1.2% of non-ethanol stir-frying ROC, respectively). Conversely, median bulk properties during Thanksgiving shift toward lower volatilities ($\log_{10}C^* = 7.1$) and higher nC (6) when excluding ethanol, demonstrating the importance of larger, lower-volatility VOC emissions toward indoor air composition during this period. A decreased median C* by nearly an order of magnitude during Thanksgiving compared to background levels has strong implications toward the propensity of indoor VOCs to partition to

condensed phases, and thus their eventual fates and lifetimes indoors. We speculate lower-volatility Thanksgiving emissions enhanced organic grime layers/films on indoor surfaces relative to other experimental periods.

Figure 4.4a,b shows the chemical complexity of Thanksgiving VOC emissions compared to stir-frying. Indoor air composition during Thanksgiving was drastically altered by a multitude of VOCs spanning a wide range of volatilities ($\log_{10}C^* = 2 - 11+$) and carbon numbers ($nC = 1 - 10$). During stir-frying, only a few prominent emissions strongly influenced ROC (ethanol, ethene, ethyne). We cooked a much greater diversity of foods using various different cooking methods (stovetop, oven roasting, etc.) throughout the course of the Thanksgiving experiment compared to stir-frying experiments, which contributed to the greater complexity of VOC emissions. Although bulk ROC properties did not change substantially from background levels during either layered experiment (Table A3.1), VOC emissions during these experiments exhibited a similar chemical complexity to that of Thanksgiving (Figure 4.4c,d).

Outdoors, median bulk ROC properties were fairly similar to indoors, albeit with higher carbon oxidation states ($nC = 3$, $OS_C = -1.3$). Oxidant (O_3, OH, Cl, etc.) levels are greater outdoors compared to indoors resulting in more VOC oxidation (Price et al., 2019). Interestingly (and counterintuitively), the median $\log_{10}C^*$ outdoors (8.3) was higher than unoccupied indoors. We suspect this combination of observations was driven by the prevalence of both oxidized VOCs (from outdoor photochemical processes) and high volatility NMHCs (from traffic and industrial emissions) in outdoor ROC (Figure 4.2). Figure A3.3 compares the chemical complexity of outdoor and unoccupied indoor ROC.

4.2.4 Indoor and outdoor oxidant reactivities toward ROC

Figure 4.5 shows indoor and outdoor OH and O_3 reactivities during HOMEChem. We calculated indoor OH and O_3 reactivities during unoccupied periods (14.3 s^{-1} and $3.1 \cdot 10^{-6}$ s^{-1}, respectively), similar to those observed previously in an unoccupied museum (19 s^{-1} and $3.9 \cdot 10^{-6}$ s^{-1}, respectively) (Price et al., 2019). Like the museum study (Price et al., 2019), a combination of highly-abundant oxidized VOCs (including acetaldehyde, methanol, ethanol) and unsaturated NMHCs (isoprene, limonene, α-pinene) influenced indoor OH reactivity during unoccupied backgrounds herein (Table A3.2). During bleach cleaning, OH reactivity did not change from unoccupied background levels, though O_3 reactivity decreased due to bleach-related oxidation of terpenes and other unsaturated VOCs with high reactivities toward O_3 (Mattila et al., 2020a). OH and O_3 reactivities increased by several times above background levels when cleaning with the all-natural product, attributable to limonene emissions from solution (Table A3.2 and A3.3). Stir-frying and layered experiments substantially increased OH reactivity (mainly from ethanol; Table A3.2), with modest increases in O_3 reactivity. During Thanksgiving, OH reactivity increased by over an order of magnitude above background levels (200 s^{-1}), and O_3 reactivity by nearly two orders of magnitude ($2 \cdot 10^{-4}$ s^{-1}). Limonene dominated indoor oxidant reactivity during Thanksgiving, contributing to 49% OH reactivity and 93% O_3 reactivity (Table A3.2 and A3.3).

Outdoor OH and O_3 reactivities (5.7 and $1.3 \cdot 10^{-6}$ s^{-1}, respectively) were considerably lower than indoors (Figure 4.5). For reference, published summertime outdoor OH and O_3 reactivities in urban areas typically range from 10 – 50 s^{-1} and $(5 – 10) \cdot 10^{-6}$ s^{-1}—considerably higher than outdoor values reported herein (Price et al., 2019; Heald et al., 2020). Our conservative approach to estimating k_{OH} and k_{O3} for unspeciated chemical formulas may have caused undercalculated OH and O_3 reactivities (see Appendix 3; section A3.1.1). Like indoors,

outdoor OH reactivity was controlled by oxidized VOCs and unsaturated terpenes (Table A3.2). Heald et al. (2020) reported similar diversity in organic compound classes influencing OH reactivity in outdoor urban air, albeit with relatively higher contributions from non-terpene NMHCs. Limonene, α-pinene, and isoprene controlled outdoor O_3 reactivity, contributing to 45%, 25%, and 19% of this reactivity, respectively (Table A3.3).

4.3 Discussion

ROC constituted a sizeable fraction (18%) of the total reactive carbon mass concentrations (calculated as ROC + CH_4 + CO) of unoccupied indoor air (1.2 mg C m^{-3}), and a smaller portion (5.4%) of reactive carbon outdoors (1.0 mg C m^{-3}) (Figure 4.6a-c). CH_4 was the dominant reactive carbon species in outdoor and unoccupied indoor air, contributing to 90% and 73% of reactive carbon mass, respectively. During Thanksgiving, cooking-related ROC, along with increased CO emissions from gas range usage elevated total reactive carbon levels to 4.9 mg C m^{-3}. Here, CO and ROC contributed to 49% and 32% of reactive carbon mass, respectively. While a minor component of the reactive carbon mass, ROC dominated (≥86%) the total indoor and outdoor OH reactivity toward atmospheric carbon (Figure 4.6d-f). These observations further demonstrate the importance of atmospheric ROC as a fuel toward environmentally-detrimental secondary oxidation products. While oxidant levels are typically low indoors, our results highlight how the introduction of indoor oxidants through, for example, ozone generators or other air cleaning devices, would have substantial ROC fuel with which to react and form secondary products in the indoor environment.

Because indoor ROC was consistently higher than outdoors during HOMEChem, the removal of indoor air via ventilation/exfiltration was a net source of ROC to outdoors. The unoccupied UTest house emitted approximately 0.7 g C day^{-1} from ROC during HOMEChem.

Given that there are about 140 million residences in the United States (USCB, 2019), and assuming the UTest house is representative of a U.S. residential home, this corresponds to $3 \cdot 10^{10}$ g C yr^{-1} from ROC emitted from residences nationwide (compared to estimated global emissions of $1 \cdot 10^{15}$ g C yr^{-1}) (Safieddine et al., 2017; Heald and Kroll, 2020). Our work further suggests that nationwide residential ROC and VOC reactivity emissions to outdoors, and resultant secondary pollutant formation, could increase by several factors on Thanksgiving Day or other events where substantial indoor cooking activities take place across the country. While recent work has shown the importance of volatile chemical products in contributing to urban smog and secondary organic aerosol (McDonald et al., 2018), this study suggests that both building materials and cooking on residential and commercial scales may be important and emerging sources of secondary pollution precursors to the outdoor atmosphere.

4.4 Methods

4.4.1 Indoor experiments during HOMEChem

We performed measurements of gas-phase and particulate organics indoors during the House Observations of Microbial and Environmental Chemistry (HOMEChem) campaign in summer 2018 at the University of Austin, TX test house (UTest House) (Farmer et al., 2019). These measurements took place during various experiments which simulate various indoor activities, including cooking, cleaning, and human occupancy (Farmer et al., 2019).

Farmer et al. (2019) described the HOMEChem experiment. Briefly, these experiments at HOMEChem generally followed "sequential" and "layered" regimes. During sequential experiments, we performed multiple replicates of an indoor activity (i.e. cooking, cleaning, etc.) to isolate and characterize emissions and chemistry specific to a particular activity (~1.5 h per replicate, with enhanced ventilation with outdoor air in between first two replicates). Sequential

stir-frying took place on 12 June 2018 (n = 3); bleach cleaning on 10 June 2018 (n = 4); and cleaning with an "all-natural" cleaner on 13 June 2018 (n = 3). During layered experiments (08 and 25 June 2018), we performed prolonged indoor experiments (~12 h) which combined various cooking and cleaning activities. Additionally, we performed a "Thanksgiving" experiment on 27 June 2018 (over ~12 h period) to simulate the indoor environment during a typical American Thanksgiving Day holiday. Measurements during an extensive unoccupied period took place on 15 June 2018 for ~15 h, allowing us to characterize house background emissions in the absence of cooking, cleaning, and human occupancy. We assess how background ROC varies throughout the campaign in SI section A3.1.2. We also performed frequent measurements of outdoor air throughout the campaign (Farmer et al., 2019), enabling us to directly compare indoor air composition to outdoors. We describe methods for calculating AER during HOMEChem in Chapter 2 section SI2.1.2.1.

4.4.2 HOMEChem measurements

We measured various gas-phase organics using a proton transfer reaction time-of-flight mass spectrometer (PTR-TOF-MS; IONICON Analytik GmbH PTR-TOF 8000; hereafter "PTR") (Cappellin et al., 2010), an online multichannel gas chromatography system (hereafter "GC") (Swarthout et al., 2013; Abeleira et al., 2017), and time-of-flight chemical ionization mass spectrometers (TOF-CIMS; Tofwerk AG and Aerodyne Research Inc.) utilizing iodide (I^-) and acetate ($C_2H_3O_2^-$) reagent ions (hereafter "ICIMS" and "ACIMS," respectively) (Bertram et al., 2011; Lee et al., 2014). PTR sensitivities were estimated following methodologies of Zhao and Zhang (2004). Mattila et al. (2020b) provide details on ICIMS calibrations and sensitivity estimations. Wang et al. (2020) provide ACIMS calibration details. We measured submicron non-refectory organic particulate matter mass concentrations with a high-resolution aerosol mass

spectrometer (HR-AMS, hereafter "AMS"; Aerodyne Research, Inc.). We additionally measured indoor and outdoor CH_4 and CO mixing ratios using a Picarro G2401 (Farmer et al., 2019). Indoor ethane, propane, and isobutane mixing ratios measured by GC are likely undercalculated (detailed in SI section A3.1.3). We only measured indoor air with the GC during HOMEChem; we detail methods for estimating outdoor GC mixing ratios in SI section A3.1.4. Farmer et al. (2019) provide further detail on HOMEChem measurements.

We combined PTR, GC, ICIMS, ACIMS, and AMS measurements to derive total indoor and outdoor ROC mass concentrations. GC measurements contributed 46 isomerically-resolved compounds to ROC. PTR, ICIMS, and ACIMS contributed 211, 76, and five chemical formulas to ROC, respectively. We ensured formulas from PTR, ICIMS and ACIMS did not overlap with each other (nor with formulas from GC), given these methods do not provide isomeric resolution. AMS contributed particulate organic carbon mass concentrations to ROC calculations. We provide time series of indoor and outdoor ROC mass concentrations, and relative instrumental contributions in Figures A3.4 – A3.6. We list all chemically-speciated compounds used to calculate ROC and respective instrumental methods used in Table A3.4.

We further analyzed gas-phase ROC components by C*, nC, and OS_C. We calculated OS_C as 2O/C - H/C, where O/C and H/C are the oxygen-to-carbon and hydrogen-to-carbon ratios of a given compound, respectively. We used the Estimation Programs Interface (EPI; USEPA) suite to determine vapor pressures (and therefore C*) of speciated compounds (when available) (USEPA, 2020). For all other compounds/formulas, we calculated C* using SIMPOL.1 (Pankow and Asher, 2008). Formulas identified as fragments in the PTR dataset were excluded from the C* analysis, as estimated C* values for these fragments likely are not representative of parent compounds.

4.4.3 Oxidant reactivity calculations

We calculated OH and O_3 reactivities (s^{-1}) toward VOCs as the product of VOC number densities (molecules cm^{-3}) and the corresponding second-order rate coefficients (cm^{-3} $molecule^{-1}$ s^{-1}) for OH-VOC reactions (k_{OH+VOC}) or O_3-VOC reactions (k_{O3+VOC}). Summing OH and O_3 reactivities for all VOCs comprising ROC allowed us to determine total indoor and outdoor OH and O_3 reactivities. We provide k_{OH+VOC} and k_{O3+VOC} values used for these calculations in Table A3.4. We provide additional reactivity calculation details in SI section A3.1.1.

4.5 Author contributions

J. M. M. contributed iodide CIMS data collection, and analyses performed herein.

4.6 Data availability

Data used herein are available at https://osf.io/aqc57/.

4.7 Chapter 4 figures

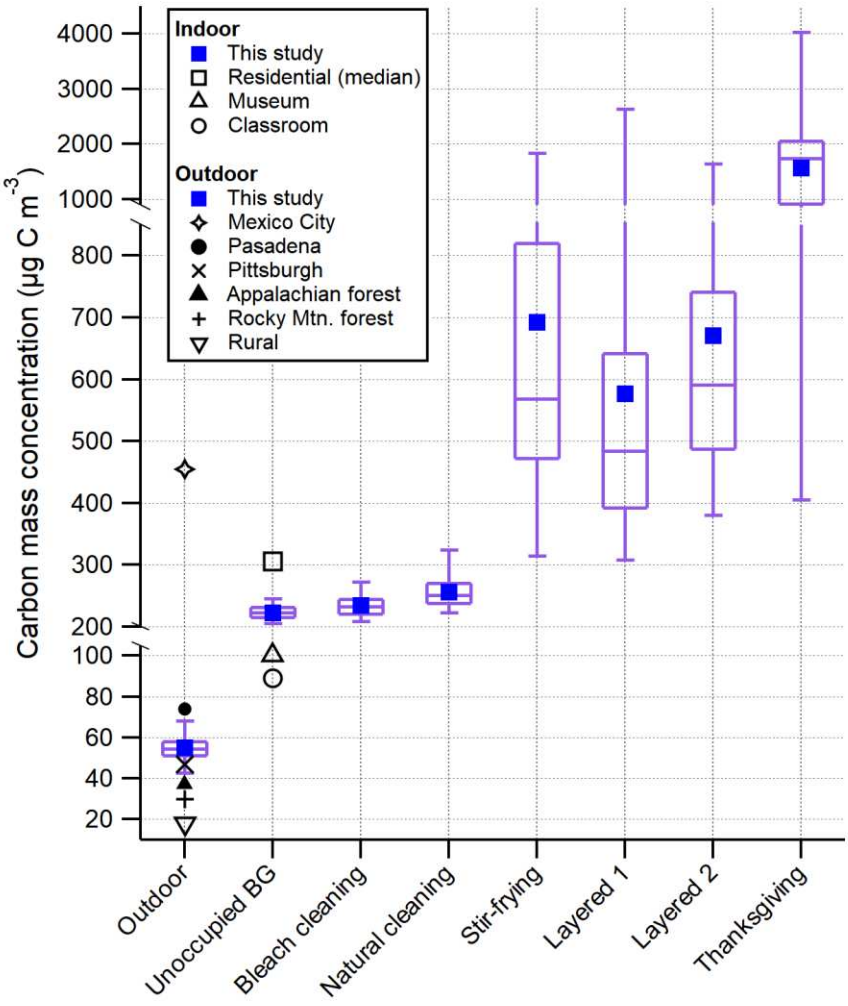

Figure 4.1. Indoor and outdoor reactive organic carbon (ROC) mass concentrations during HOMEChem, and comparisons to literature. Horizontal lines inside of box plots represent median ROC of each sampling period at HOMEChem; upper- and lower- bounds of boxes represent 75th and 25th percentiles of ROC during these periods, respectively; top and bottom whiskers of these box plots represent maximum and minimum ROC values during these periods, respectively. Solid blue square markers represent mean ROC concentrations during each HOMEChem sampling period. Black markers (various shapes) represent mean (unless noted otherwise) indoor and outdoor ROC values from the literature—"Residential," "Museum," and "Classroom" from Price et al. (2019); "Mexico City," "Pittsburgh," and "Rural" from Heald et al. (2008); "Pasadena" and "Appalachian forest" from Heald et al. (2020); and "Rocky Mtn. forest" from Hunter et al. (2017). "Unoccupied BG" corresponds to periods of indoor sampling during unoccupied background periods during HOMEChem. "Layered 1 and 2" correspond to layered experiments during HOMEChem performed on 08 and 25 June 2018, respectively. Details of HOMEChem experiments are provided in the main text and Farmer et al. (2019).

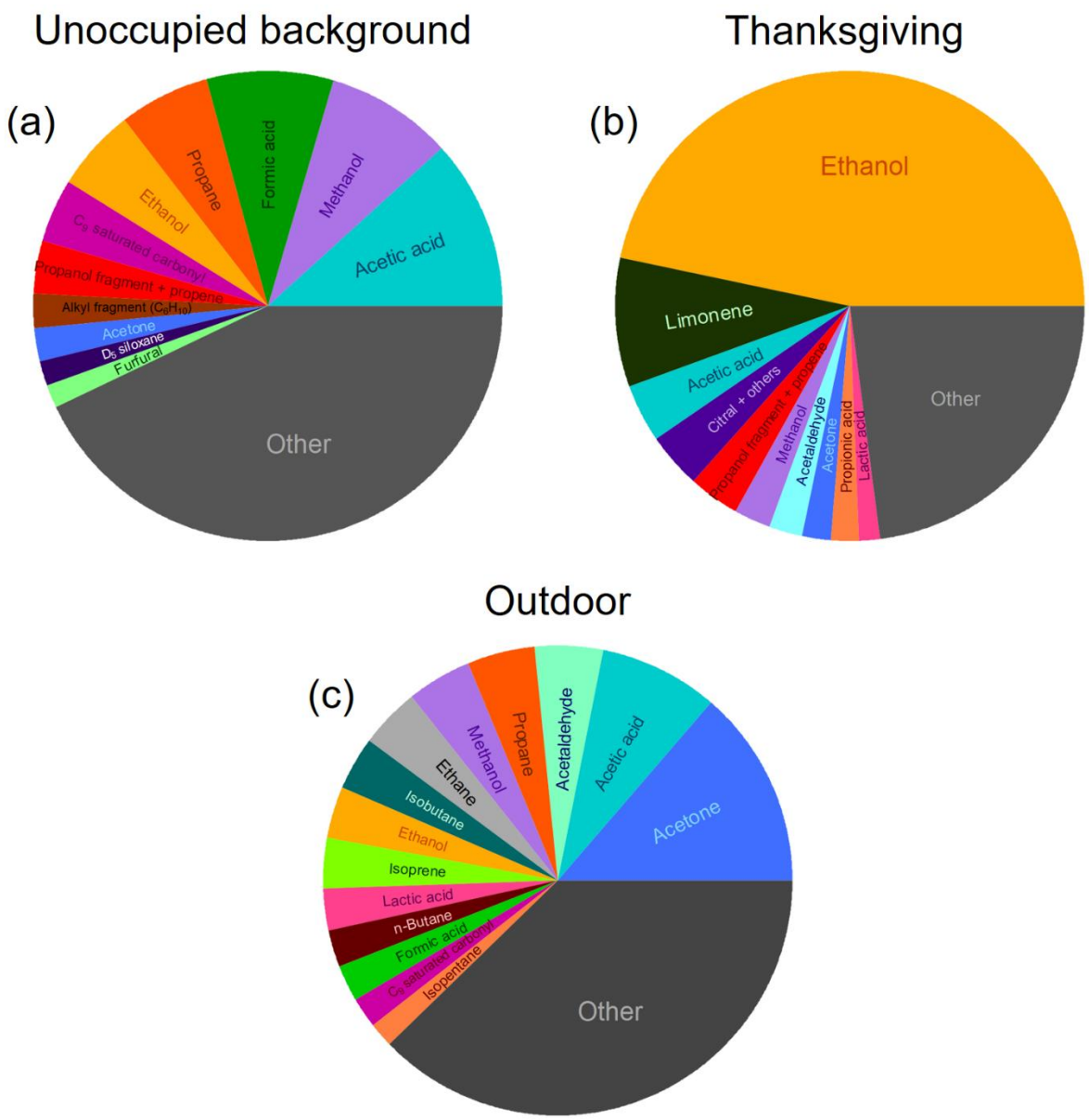

Figure 4.2. Contributions of individual compounds to reactive organic carbon mass concentrations during (a) unoccupied backgrounds indoors, (b) a Thanksgiving experiment indoors, and (c) outdoor sampling.

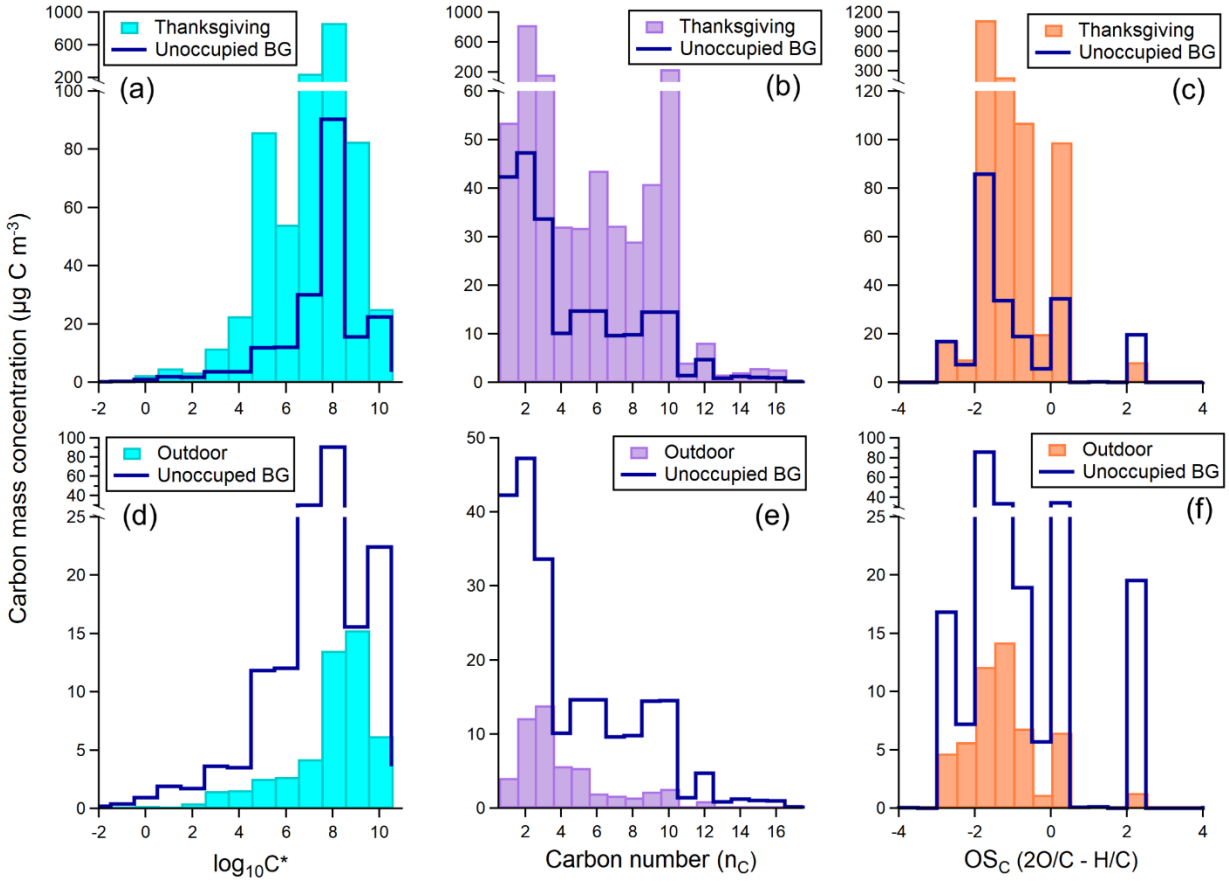

Figure 4.3. Reactive organic carbon (ROC) mass concentration distributions during (a-c) Thanksgiving indoors, and (d-f) outdoor sampling. We bin ROC by (a,d) $\log_{10}C^*$, (b,e) carbon number (nC), and (c,f) carbon oxidation state (OS_C). We include distributions during unoccupied background periods indoors for comparison (solid blue trace). Figure A3.2 shows replicates the distributions as fractions of total ROC.

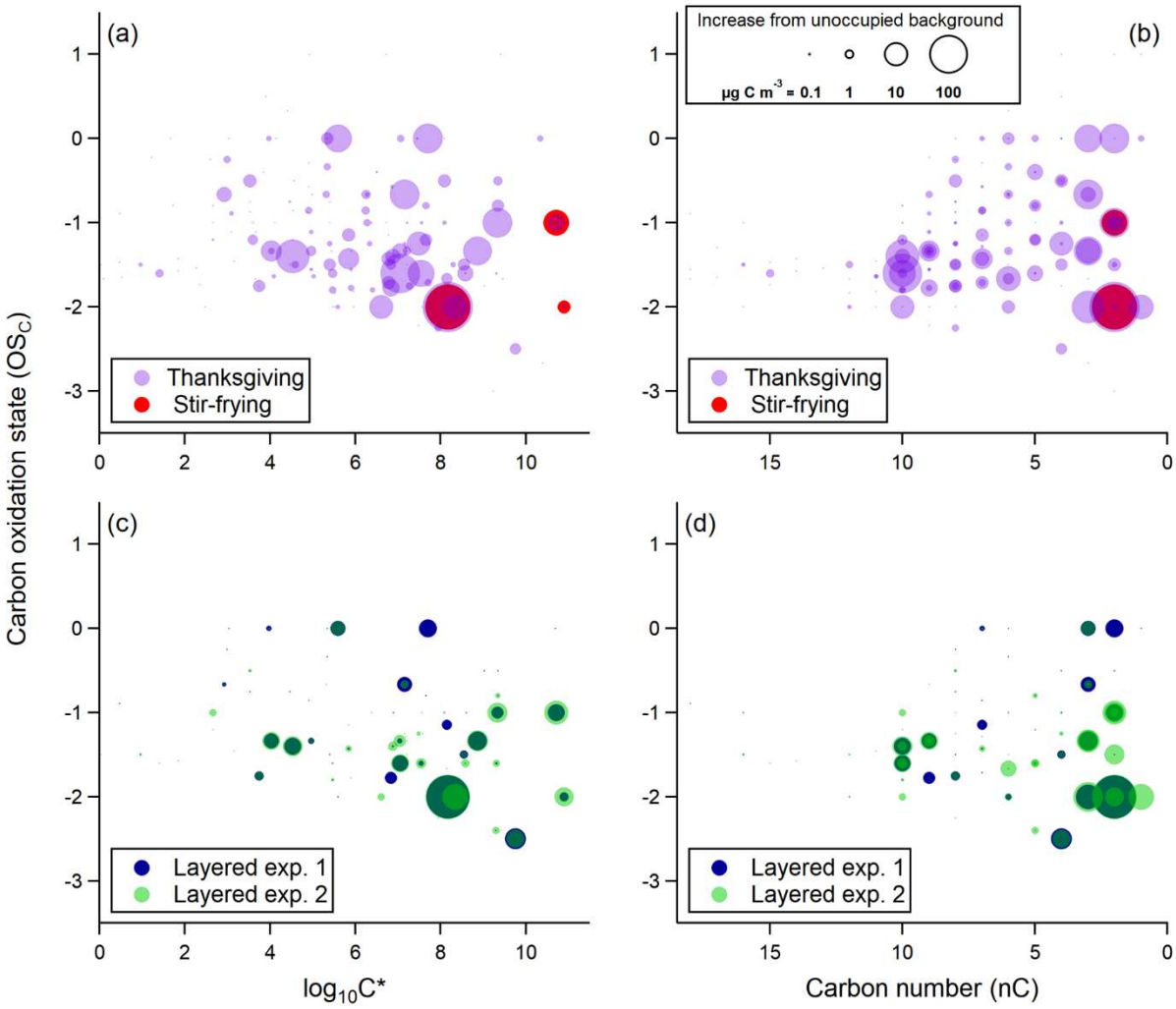

Figure 4.4. Two-dimensional visualizations of indoor reactive organic carbon oxidation states (OS_C) as a function of (a,c) $\log_{10}C^*$ and (b,d) carbon number (nC). We compare these bulk properties during Thanksgiving and stir-frying experiments in panels (a) and (b), and on layered experiments performed on 08 and 25 June 2018 (or "Layered exp. 1" and Layered exp. 2," respectively). Markers are sized by increase in average carbon mass concentration relative to unoccupied background periods, as shown by the legend in panel (b).

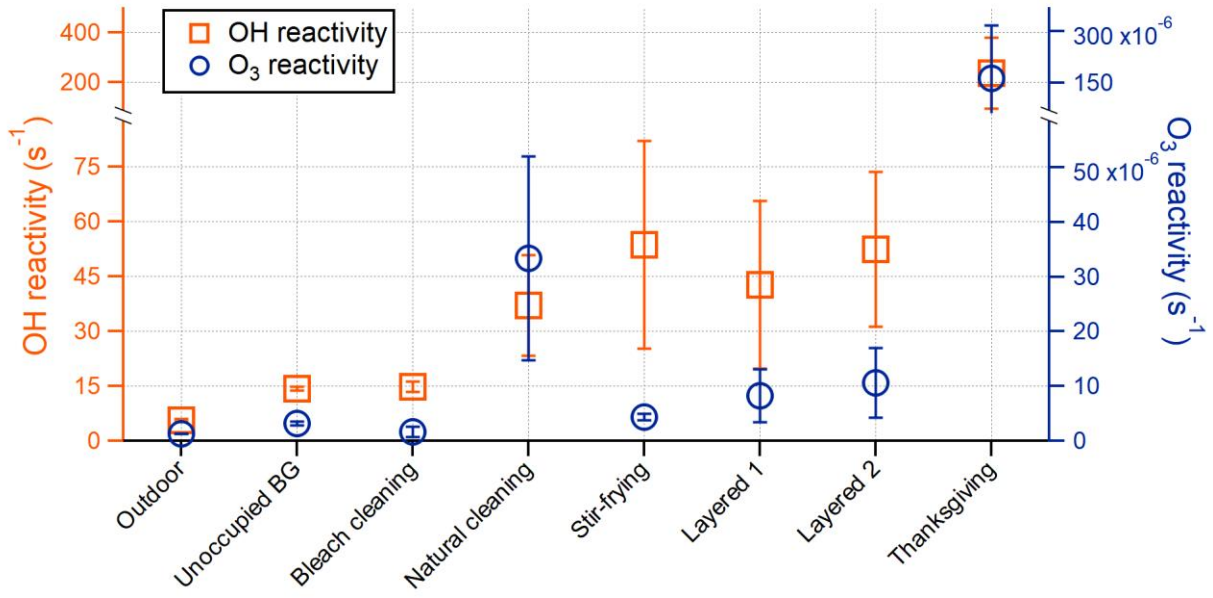

Figure 4.5. Average indoor and outdoor hydroxyl radical (OH; orange square markers) and ozone (O_3; blue circle markers) reactivities toward reactive organic carbon. Error bars represent ± one standard deviation of average reactivities. "Unoccupied BG" corresponds to periods of indoor sampling during unoccupied background periods. "Layered 1 and 2" correspond to layered experiments performed on 08 and 25 June 2018, respectively.

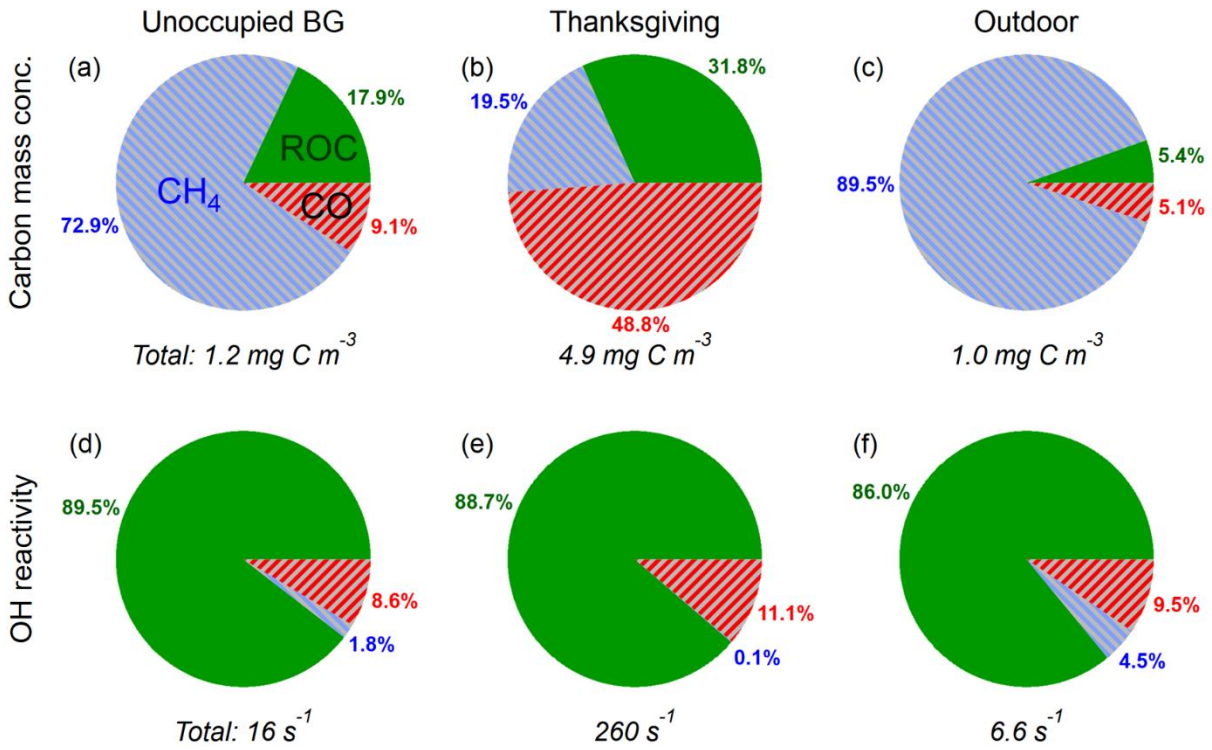

Figure 4.6. (a-c) Carbon mass concentrations, and (d-f) OH reactivities toward reactive organic carbon (ROC), methane (CH_4), and carbon monoxide (CO) during (a,d) indoor unoccupied background periods, (b,e) an indoor Thanksgiving experiment, and (c,f) outdoor sampling during HOMEChem. "Total" mass concentration and OH reactivity values below each pie chart represent summed contributions from ROC, CH_4, and CO (i.e. total reactive carbon).

REFERENCES

Abeleira, A., Pollack, I., Sive, B., Zhou, Y., Fischer, E., and Farmer, D.: Source characterization of volatile organic compounds in the Colorado Northern Front Range Metropolitan Area during spring and summer 2015, J. Geophys. Res. Atmos., 122, 3595-3613, 2017.

Atkinson, R.: Atmospheric chemistry of VOCs and NOx, Atmos. Environ., 34, 2063-2101, 2000.

Bari, M. A., Kindzierski, W. B., Wheeler, A. J., Héroux, M.-È., and Wallace, L. A.: Source apportionment of indoor and outdoor volatile organic compounds at homes in Edmonton, Canada, Build. Environ. , 90, 114-124, 2015.

Bertram, T. H., Kimmel, J. R., Crisp, T. A., Ryder, O. S., Yatavelli, R. L. N., Thornton, J. A., Cubison, M. J., Gonin, M., and Worsnop, D. R.: A field-deployable, chemical ionization time-of-flight mass spectrometer, Atmos. Meas. Tech., 4, 1471-1479, doi:10.5194/amt-4-1471-2011, 2011.

Borbon, A., Fontaine, H., Veillerot, M., Locoge, N., Galloo, J., and Guillermo, R.: An investigation into the traffic-related fraction of isoprene at an urban location, Atmos. Environ., 35, 3749-3760, 2001.

Calvert, J. G., and Madronich, S.: Theoretical study of the initial products of the atmospheric oxidation of hydrocarbons, J. Geophys. Res. Atmos., 92, 2211-2220, 1987.

Cappellin, L., Biasioli, F., Fabris, A., Schuhfried, E., Soukoulis, C., Märk, T. D., and Gasperi, F.: Improved mass accuracy in PTR-TOF-MS: Another step towards better compound identification in PTR-MS, Int. J. Mass Spectrom., 290, 60-63, 2010.

Farmer, D. K., Vance, M. E., Abbatt, J. P. D., Abeleira, A., Alves, M. R., Arata, C., Boedicker, E., Bourne, S., Cardoso-Saldaña, F., Corsi, R., DeCarlo, P. F., Goldstein, A. H., Grassian, V. H., Hildebrandt Ruiz, L., Jimenez, J. L., Kahan, T. F., Katz, E. F., Mattila, J. M., Nazaroff, W. W., Novoselac, A., O'Brien, R. E., Or, V. W., Patel, S., Sankhyan, S., Stevens, P. S., Tian, Y., Wade, M., Wang, C., Zhou, S., and Zhou, Y.: Overview of HOMEChem: House Observations of Microbial and Environmental Chemistry, Environ. Sci. Process. Impacts, 21, 1280-1300, 10.1039/C9EM00228F, 2019.

Fuentes, J. D., Lerdau, M., Atkinson, R., Baldocchi, D., Bottenheim, J., Ciccioli, P., Lamb, B., Geron, C., Gu, L., and Guenther, A.: Biogenic hydrocarbons in the atmospheric boundary layer: a review, Bull. Amer. Meteor. Soc., 81, 1537-1576, 2000.

Geddes, J. A., and Murphy, J. G.: The science of smog: a chemical understanding of ground level ozone and fine particulate matter, Metropolitan sustainability, Woodhead Publishing, 2012.

Gkatzelis, G. I., Coggon, M. M., McDonald, B. C., Peischl, J., Aikin, K. C., Gilman, J. B., Trainer, M., and Warneke, C.: Identifying Volatile Chemical Product Tracer Compounds in US Cities, Environ. Sci. Technol., 55, 188-199, 10.1021/acs.est.0c05467, 2020.

Grosjean, D., Grosjean, E., and Gertler, A. W.: On-road emissions of carbonyls from light-duty and heavy-duty vehicles, Environ. Sci. Technol., 35, 45-53, 2001.

Heald, C., Goldstein, A., Allan, J., Aiken, A., Apel, E., Atlas, E. L., Baker, A., Bates, T., Beyersdorf, A., and Blake, D.: Total observed organic carbon (TOOC) in the atmosphere: a synthesis of North American observations, Atmos. Chem. Phys., 8, 2007-2025, 2008.

Heald, C. L., Gouw, J. d., Goldstein, A. H., Guenther, A. B., Hayes, P. L., Hu, W., Isaacman-VanWertz, G., Jimenez, J. L., Keutsch, F. N., and Koss, A. R.: Contrasting Reactive Organic Carbon Observations in the Southeast United States (SOAS) and Southern California (CalNex), Environ. Sci. Technol., 54, 14923-14935, 2020.

Heald, C. L., and Kroll, J.: The fuel of atmospheric chemistry: Toward a complete description of reactive organic carbon, Sci Adv, 6, eaay8967, 2020.

Hunter, J. F., Day, D. A., Palm, B. B., Yatavelli, R. L., Chan, A. W., Kaser, L., Cappellin, L., Hayes, P. L., Cross, E. S., and Carrasquillo, A. J.: Comprehensive characterization of atmospheric organic carbon at a forested site, Nat. Geosci., 10, 748-753, 2017.

Isaacman-VanWertz, G., Massoli, P., O'Brien, R., Nowak, J., Canagaratna, M., Jayne, J., Worsnop, D., Su, L., Knopf, D., and Misztal, P.: Using advanced mass spectrometry techniques to fully characterize atmospheric organic carbon: current capabilities and remaining gaps, Faraday Discuss., 200, 579-598, 2017.

Isaacman-VanWertz, G., Massoli, P., O'Brien, R., Lim, C., Franklin, J. P., Moss, J. A., Hunter, J. F., Nowak, J. B., Canagaratna, M. R., and Misztal, P. K.: Chemical evolution of atmospheric organic carbon over multiple generations of oxidation, Nat. Chem., 10, 462-468, 2018.

Jimenez, J. L., Canagaratna, M. R., Donahue, N. M., Prevot, A. S. H., Zhang, Q., Kroll, J. H., DeCarlo, P. F., Allan, J. D., Coe, H., and Ng, N. L.: Evolution of organic aerosols in the atmosphere, Science, 326, 1525-1529, 2009.

Kabir, E., and Kim, K.-H.: An investigation on hazardous and odorous pollutant emission during cooking activities, J. Haz. Mat., 188, 443-454, 2011.

Khare, P., Kumar, N., Kumari, K. M., and Srivastava, S. S.: Atmospheric formic and acetic acids: An overview, Reviews of Geophysics, 37, 227-248, doi:10.1029/1998rg900005, 1999.

Klein, F., Platt, S. M., Farren, N. J., Detournay, A., Bruns, E. A., Bozzetti, C., Daellenbach, K. R., Kilic, D., Kumar, N. K., and Pieber, S. M.: Characterization of gas-phase organics using proton transfer reaction time-of-flight mass spectrometry: cooking emissions, Environ. Sci. Technol., 50, 1243-1250, 2016.

Klepeis, N. E., Nelson, W. C., Ott, W. R., Robinson, J. P., Tsang, A. M., Switzer, P., Behar, J. V., Hern, S. C., and Engelmann, W. H.: The National Human Activity Pattern Survey (NHAPS): a resource for assessing exposure to environmental pollutants, J. Expo. Anal. Environ. Epidemiol., 11, 231, 2001.

Kourtidis, K., Ziomas, I., Rappenglueck, B., Proyou, A., and Balis, D.: Evaporative traffic hydrocarbon emissions, traffic CO and speciated HC traffic emissions from the city of Athens, Atmos. Environ., 33, 3831-3842, 1999.

Kroll, J. H., Donahue, N. M., Jimenez, J. L., Kessler, S. H., Canagaratna, M. R., Wilson, K. R., Altieri, K. E., Mazzoleni, L. R., Wozniak, A. S., and Bluhm, H.: Carbon oxidation state as a metric for describing the chemistry of atmospheric organic aerosol, Nat. Chem., 3, 133-139, 2011.

Lee, B. H., Lopez-Hilfiker, F. D., Mohr, C., Kurten, T., Worsnop, D. R., and Thornton, J. A.: An iodide-adduct high-resolution time-of-flight chemical-ionization mass spectrometer: application to atmospheric inorganic and organic compounds, Environ. Sci. Technol., 48, 6309-6317, doi:10.1021/es500362a, 2014.

Liu, Y., Misztal, P. K., Xiong, J., Tian, Y., Arata, C., Weber, R. J., Nazaroff, W. W., and Goldstein, A. H.: Characterizing sources and emissions of volatile organic compounds in a northern California residence using space-and time-resolved measurements, Indoor Air, 29, 630-644, 2019.

Logue, J., McKone, T., Sherman, M., and Singer, B.: Hazard assessment of chemical air contaminants measured in residences, Indoor air, 21, 92-109, 2011.

Masson-Delmotte, V., Zhai, P., Portner, H., Roberts, D., Skea, J., Shukla, P. R., Pirani, A., Moufouma-Okia, W., Pean, C., Pidcock, R., Connors, S., Matthews, J. B. R., Chen, Y., Shou, X., Gomis, M. I., Lonnoy, E., Maycock, T., Tignor, M., and Waterfield, T.: Global Warming of 15 °C. An IPCC Special Report on the impacts of global warming of 1.5 °C above pre-industrial levels and related global greenhouse gas emission pathways, in the context of strengthining the global response to the threat of climate change, sustainable developement, and efforts to eradicate poverty, Intergovernmental Panel on Climate Change, 2018.

Mattila, J. M., Arata, C., Wang, C., Katz, E. F., Abeleira, A., Zhou, Y., Zhou, S., Goldstein, A. H., Abbatt, J. P., and DeCarlo, P. F.: Dark chemistry during bleach cleaning enhances oxidation of organics and secondary organic aerosol production indoors, Environ. Sci. Technol. Lett., 7, 795-801, 2020a.

Mattila, J. M., Lakey, P. S. J., Shiraiwa, M., Wang, C., Abbatt, J. P. D., Arata, C., Goldstein, A. H., Ampollini, L., Katz, E. F., DeCarlo, P. F., Zhou, S., Kahan, T. F., Cardoso-Saldaña, F. J., Hildebrandt Ruiz, L., Abeleira, A., Boedicker, E., Vance, M. E., and Farmer, D. K.: Multiphase chemistry controls inorganic chlorinated and nitrogenated compounds in indoor air during bleach cleaning, Environ. Sci. Technol., 54, 1730-1739, 10.1021/acs.est.9b05767, 2020b.

McDonald, B. C., De Gouw, J. A., Gilman, J. B., Jathar, S. H., Akherati, A., Cappa, C. D., Jimenez, J. L., Lee-Taylor, J., Hayes, P. L., and McKeen, S. A.: Volatile chemical products emerging as largest petrochemical source of urban organic emissions, Science, 359, 760-764, 2018.

Pankow, J. F., and Asher, W. E.: SIMPOL. 1: a simple group contribution method for predicting vapor pressures and enthalpies of vaporization of multifunctional organic compounds, Atmos. Chem. Phys., 8, 2773-2796, 2008.

Patel, K., Wang, D., Chhabra, P., Bean, J., Dhulipala, S. V., and Hildebrandt Ruiz, L.: Effects of Sources and Meteorology on Ambient Particulate Matter in Austin, Texas, ACS Earth Space Chem., 4, 602-613, 2020.

Price, D. J., Day, D. A., Pagonis, D., Stark, H., Algrim, L. B., Handschy, A. V., Liu, S., Krechmer, J. E., Miller, S. L., and Hunter, J. F.: Budgets of Organic Carbon Composition and Oxidation in Indoor Air, Environ. Sci. Technol., 53, 13053-13063, 2019.

Rahim, A., and Talib, M.: Determination of propionates and propionic acid in bakery products using gas chromatography, International Food Research Journal, 17, 1107-1112, 2010.

Safieddine, S. A., Heald, C. L., and Henderson, B. H.: The global nonmethane reactive organic carbon budget: A modeling perspective, Geophys. Res. Lett., 44, 3897-3906, 2017.

Shiraiwa, M., Ueda, K., Pozzer, A., Lammel, G., Kampf, C. J., Fushimi, A., Enami, S., Arangio, A. M., Fröhlich-Nowoisky, J., and Fujitani, Y.: Aerosol health effects from molecular to global scales, Environ. Sci. Technol., 51, 13545-13567, 2017.

Swarthout, R. F., Russo, R. S., Zhou, Y., Hart, A. H., and Sive, B. C.: Volatile organic compound distributions during the NACHTT campaign at the Boulder Atmospheric Observatory: Influence of urban and natural gas sources, J. Geophys. Res. Atmos., 118, 2013.

USCB: U.S. Census Bureau QuickFacts: United States, https://www.census.gov/quickfacts/fact/table/US/VET605219, United States Census Bureau, 2019.

USEPA: Estimation Programs Interface Suite for Microsoft Windows, in, v 4.1, Washington, DC, 2020.

Wang, C., Collins, D. B., Arata, C., Goldstein, A. H., Mattila, J. M., Farmer, D. K., Ampollini, L., DeCarlo, P. F., Novoselac, A., Vance, M. E., Nazaroff, W. W., and Abbatt, J. P. D.: Surface reservoirs dominate dynamic gas-surface partitioning of many indoor air constituents, Sci Adv, 6, aay8973, 10.1126/sciadv.aay8973 2020.

Zhao, J., and Zhang, R.: Proton transfer reaction rate constants between hydronium ion (H_3O^+) and volatile organic compounds, Atmos. Environ., 38, 2177-2185, 2004.

CHAPTER 5 – TROPOSPHERIC SOURCES AND SINKS OF GAS-PHASE ACIDS IN THE COLORADO FRONT RANGE[1]

5.1 Introduction

Organic acids comprise a major fraction of gas-phase acids in the troposphere. They influence the acidity of precipitation, fog, and cloud droplets, particularly in rural areas (Keene and Galloway, 1984; Andreae et al., 1988), and can thus impact ecosystem health (Sverdrup et al., 2001; Himanen et al., 2012). Organic acids are also involved in the formation of secondary organic aerosol (SOA) (Vogel et al., 2013; Yatavelli et al., 2014; Yatavelli et al., 2015), which affects human health, visibility, and climate. Yatavelli et al. (2015) estimated that molecules containing carboxylic acid moieties account for 10 – 50% of continental Northern Hemispheric organic aerosol mass. Sources and sinks determine tropospheric concentrations of gas-phase organic acids, and thus their impacts on biological health and air quality. However, several model-measurement comparisons for tropospheric formic and acetic acid indicate missing sources, potentially coupled to missing sinks (Paulot et al., 2011; Yuan et al., 2015; Millet et al., 2015; Schobesberger et al., 2016). Model-measurement comparisons for other tropospheric organic acids are lacking. Field and laboratory measurements investigating the sources and sinks of these compounds are therefore necessary to reduce model uncertainties and improve our understanding of organic acids in the troposphere.

[1]Mattila, J. M., Brophy, P., Kirkland, J., Hall, S., Ullmann, K., Fischer, E. V., Brown, S., McDuffie, E., Tevlin, A., and Farmer, D. K.: Tropospheric sources and sinks of gas-phase acids in the Colorado Front Range, Atmospheric Chemistry and Physics, 18, 12315-12327, 10.5194/acp-18-12315-2018, 2018.

A variety of primary biogenic and anthropogenic sources can introduce organic acids into the troposphere. Several organic acids have been identified in vegetative emissions (Kesselmeier et al., 1998; Kesselmeier, 2001), soil emissions (Sanhueza and Andreae, 1991; Enders et al., 1992), and biomass burning (Goode et al., 2000). Automobile exhaust is also a primary source of alkanoic acids, with formic (CH_2O_2) and acetic ($C_2H_4O_2$) acid typically being the most abundant in these emissions (Kawamura et al., 1985; Kawamura et al., 2000; Friedman et al., 2017). Secondary production from the photochemical oxidation of volatile organic compounds (VOCs) serves as another major source. Photochemical oxidation of isoprene (C_5H_8) produces several organic acids, including formic and pyruvic acid ($C_3H_4O_3$) (Orzechowska and Paulson, 2005; Jacob and Wofsy, 1988; Paulot et al., 2009; Paulot et al., 2011). Friedman et al. (2017) measured formic, propionic ($C_3H_6O_2$), and butyric acid ($C_4H_8O_2$) in photochemically-aged diesel exhaust. Wet and dry deposition, and photochemical loss processes are the major known tropospheric sinks of organic acids (Grosjean, 1989; Talbot et al., 1995; Atkinson et al., 2006; Grosjean, 1983). Despite their ubiquity, our understanding of tropospheric organic acid sources and sinks is incomplete. This is especially apparent for formic acid—measured tropospheric concentrations are often several times higher than modeled values (Paulot et al., 2011; Yuan et al., 2015; Millet et al., 2015; Schobesberger et al., 2016). Model simulations have also failed to capture the temporal variation and vertical gradients of formic acid (Millet et al., 2015). These model-measurement discrepancies are likely due to underestimated sources and/or overestimated sinks, as well as missing sources and sinks that are not considered altogether.

Gas-phase inorganic acids, including nitric (HNO_3) and isocyanic acid (HNCO), also impact air quality. HNO_3 is produced in the troposphere from nitrogen dioxide (NO_2) reactions with hydroxyl radical (OH), and through the reaction of NO_2 with ozone (O_3). Anthropogenic

emissions of nitrogen oxides (NO_x = NO + NO_2) from fossil fuel combustion and agricultural activity constitute a major secondary source of HNO_3 (Shepherd et al., 1991; Dignon, 1992; Kurvits and Marta, 1998; Almaraz et al., 2018). HNO_3 readily partitions into the aqueous-phase, contributes to acid deposition, and reduces the vapor pressure of water during cloud droplet growth—affecting the growth rate and resulting size of these droplets (Kulmala et al., 1993). HNO_3 also reacts with ammonia (NH_3) in the gas- or aqueous-phase to form ammonium nitrate (NH_4NO_3) aerosols (Adams et al., 1999). HNCO is of growing interest because exposure levels > 1 ppb_v are linked to various human health issues, including atherosclerosis, cataracts, and rheumatoid arthritis (Jaisson et al., 2011; Roberts et al., 2011). Primary emission and secondary photochemical production sources of gas-phase HNCO have been identified and reported (Borduas et al., 2013; Roberts et al., 2014), but the magnitudes of these sources remain highly uncertain (Young et al., 2012). Combustion processes, including biomass burning, gasoline/diesel fuel combustion, and tobacco smoke are a primary source of HNCO (Roberts et al., 2011; Roberts et al., 2014; Link et al., 2016). Secondary sources of HNCO include OH oxidation of amine and amide precursors, which are particularly important in urban environments (Link et al., 2016; Roberts et al., 2014; Borduas et al., 2013). HNCO readily partitions into the aqueous-phase given its high solubility at atmospherically relevant pH values, and can hydrolyze to NH_3 (Roberts et al., 2011). Wet and dry deposition are other known HNCO sinks (Young et al., 2012; Roberts et al., 2014).

Here, we present ambient measurements of various gas-phase organic and inorganic acids taken during the Front Range Air Pollution and Photochemistry Éxperiment (FRAPPÉ) in Weld County, CO (McDuffie et al., 2016; Tevlin et al., 2017; Pfister et al., 2017b; Wild et al., 2017). We use diel trends and vertical profiles of these compounds, as well as correlations in timeseries

data to investigate their tropospheric sources and sinks. The peri-urban Boulder Atmospheric Observatory (BAO) site lies at the intersection of agricultural sources, traffic, oil and gas development, and other industrial processes, providing a contrast to the strictly urban or forest sites that are often the focus of atmospheric chemistry measurements.

5.2 Methods

5.2.1 Site description

Measurements took place at the BAO tower in Weld County, CO during the FRAPPÉ field campaign in summer 2014. This work focuses on measurements taken between 4 and 13 August 2014. The land surrounding the tower is a sparsely vegetated region of the Colorado Front Range located on the outskirts of several urbanized Colorado municipalities (Boulder, Denver, Fort Collins, and Greeley). The site lies about 2 km west of highway traffic from Interstate 25, is surrounded by oil and natural gas (ONG) wells, and is near (> 7 km) concentrated animal feeding operations (CAFOs) (Figure 5.1) (Kaimal and Gaynor, 1983; Brown et al., 2013; Swarthout et al., 2013; Abeleira et al., 2017; Tevlin et al., 2017).

The 300 m BAO tower was equipped with an elevator carriage capable of continuous vertical movement between altitudes of 0 – 285 m, allowing for the generation of vertical profiles of measured compounds. A timeseries of carriage altitude throughout the reported measurement period is provided in Figure A4.1. The carriage height was typically parked at 100 m (accounting for 62% of data described herein). This carriage housed a high-resolution time-of-flight chemical ionization mass spectrometer (TOF-CIMS) allowing for fast (1 Hz) detection of gas-phase compounds (discussed further in section 5.2.2), as well as an IRGASON Integrated CO_2 and H_2O Open-Path Gas Analyzer, and 3-D Sonic Anemometer (Campbell Scientific) for air temperature, water vapor, and wind speed/direction measurements. Additional meteorological

measurements at 10, 100, and 300 m were provided by the BAO Tower Meteorological Station. A filter radiometer (Metcon, GmbH, Shetter et al. (2003)) measured downwelling NO_2 photolysis rates (j_{NO2}) near the base of the tower, from which total photolysis rates were calculated. Instruments to measure various trace gases of interest, including NO_x/O_3 (custom built Cavity Ring-Down Spectroscopy), $CO/CO_2/CH_4/H_2O$ (Picarro 6401 Cavity Ring-Down Spectrometer), and NH_3 (QC-TILDAS; Aerodyne Research, Inc.) were also housed on the carriage during the campaign. The $CO/CO_2/CH_4/H_2O$ measurement details can be found in McDuffie et al. (2016) and Zaragoza et al. (2017). Instrument details on the NH_3 measurements are provided by Tevlin et al. (2017). All measurements presented here are reported in local time (Mountain Daylight Time; MDT; UTC – 6). Rainfall did not exceed 0.3 cm day^{-1} near the site throughout the reported measurement period. We plot j_{NO2} by hour of day as a proxy for solar exposure (Figure 5.2). Solar exposure at the site peaks around 12:00.

5.2.2 TOF-CIMS measurements

The TOF-CIMS (Tofwerk AG and Aerodyne Research, Inc.) has been described extensively elsewhere (DeCarlo et al., 2006; Veres et al., 2008; Bertram et al., 2011; Lee et al., 2014; Brophy and Farmer, 2015, 2016; Lopez-Hilfiker et al., 2016). When coupled to acetate (CH_3COO^-) reagent ions, this instrument detects an array of molecules including HNO_3, HNCO, formic, propionic, butyric, valeric ($C_5H_{10}O_2$), and pyruvic acid in the atmosphere at high acquisition rates (i.e. < 1 s time resolution). Acetate reagent ions provide high sensitivity and selectivity for gas-phase acids (Veres et al., 2008; Bertram et al., 2011; Brophy and Farmer, 2015, 2016). Acetate reagent ions are generated by passing N_2 saturated with acetic anhydride through a ^{210}Po ionizer (NRD). These reagent ions enter the ion-molecule reactor along with sampled ambient air and selectively ionize gas-phase acids (HA) via either a proton-exchange

reaction (Veres et al., 2008) or a clustering reaction with HA followed by declustering prior to detection (Brophy and Farmer, 2016). Under both mechanisms, the analyte of interest is detected by the mass spectrometer as a deprotonated, gas-phase anion (A^-). Detection of acetic acid is not possible using this ion chemistry.

Ambient air was sampled through a 1 m inlet of 0.635 cm OD PEEK tubing at a sampling rate of approximately 2000 sccm. Instrument background is monitored hourly at the beginning of each data acquisition period using an overflow of ultra zero grade air (UZA, Airgas). Hourly online two-point external standard calibrations of formic acid are also taken in UZA prior to each ambient air measurement period, enabling direct calculation of instrument sensitivity to formic acid, and thus formic acid mixing ratios. Formic acid standard is generated from a permeation tube (Dynacal, VICI) in a heated oven held at 40 °C. Ultra-high purity (UHP) nitrogen (Airgas) flows through this permeation system, introducing the standard into the TOF-CIMS. Mass spectral data acquisition is controlled with TofDaq Recorder (Tofwerk AG), and automated using home-built programs (LabVIEW, National Instruments). Instrument sensitivity to formic acid during the campaign was 2.35×10^4 ncps ppb_v^{-1} (defined in section 5.2.3), determined from a Gaussian fit to the histogram of sensitivity values. The low dispersion in these sensitivity values (% RSD = 1.4) indicates high instrument stability throughout the campaign. We used offline external calibrations of other detected compounds to estimate mixing ratios for other gas-phase acids detected during the campaign (see Appendix 4).

5.2.3 Mass spectral data processing and analysis

We process mass spectral data in Igor Pro (WaveMetrics Inc., Version 6) with Tofware (Tofwerk AG, Aerodyne Research Inc, Version 2.5.10), which determines mass spectral baseline, fitted peak shape, and peak resolution, and applies a TOF duty cycle correction (m/z =

59). We mass calibrate post-acquisition using a three-parameter fit and the O_2^-, Cl^-, CHO_2^-, NO_2^-, $C_2H_3O_2^-$, NO_3^- and I^- peaks; these peaks were fully resolved during the measurements with consistently high signal throughout the measurement and calibration periods. Additional conjugate bases of various other organic acids (such as $C_3H_3O_2^-$ and $C_3H_5O_3^-$), as well as the [acetic acid + acetate] cluster ($C_4H_7O_4^-$) are included in the mass calibration when signal is sufficiently high and the peaks do not contain interferences. During FRAPPÉ, the mass accuracy of the TOF-CIMS was 2 ppm (campaign average of mass calibrant ions), and the resolution ($m/\Delta m$) was > 3000. Tofware's high-resolution peak fitting procedures extract timeseries of detected compounds. Further data analysis, including background subtraction, normalization, mixing ratio calculation, and the generation of diel and vertical profiles are performed in Igor Pro. Mass spectral data are normalized to convert raw instrumental ion counts per second (cps) to normalized cps (ncps) by multiplying the measured analyte signal by the ratio of acetate reagent ion signal taken during an instrumental background to reagent ion signal taken during periods of analyte measurements (Bertram et al., 2011).

5.3 Results

Campaign statistics for each measured acid are reported in Table 5.1. Formic acid was the most abundant compound quantified by TOF-CIMS, with an average mixing ratio of 1.9 ppb_v. Compounds with negative minimum mixing ratio values are reported as below the instrumental limit of detection (LOD). We determined correlation coefficients between each measured gas-phase acid, and for each gas-phase acid compared to CO (subsampled from 8:30 to 10:30), NH_3, air temperature, and j_{NO2} (Table 5.2). Timeseries for measured acid mixing ratios are provided in Figure A4.2.

We bin mixing ratio data from periods of constant carriage height (100 m) by hour of the day to generate diel profiles for all gas-phase acids (Figure 5.2). A diel maximum occurs between 09:00 – 10:00 for HNO_3, and 12:00 – 15:00 for all other acids. Secondary maxima occur around 09:00 – 10:00 for propionic, butyric, and valeric acid.

We select three typical vertical profiles to investigate noon, night, and morning trends (Figure 5.3); these profiles started at 12:00 on 12 August 2014, 03:30 on 13 August 2014, and 10:00 on 13 August 2014. We observe hysteresis in analyte measurements during periods of downward carriage movement, potentially due to shaking of the elevator carriage affecting acetate ion generation, so focus our analysis solely on profiles collected during upward carriage movement. Unfortunately, these three profiles are the sole profiles in which upward carriage movement occurred simultaneously with ambient air sampling during morning or noon periods, preventing us from replicating those time periods. Vertical profiles for nearly all gas-phase acids show a strong, near-surface gradient below 75 m. Negative gradients (i.e. mixing ratio decreases with height above ground) imply upward fluxes and net surface-level emission, while positive gradients imply downward fluxes, or net deposition. HNO_3 and pyruvic acid exhibit surface-level deposition in their noon, night, and morning vertical profiles. HNCO had a strong negative near-surface gradient during noon, and a weaker negative gradient during morning. All alkanoic acids exhibit surface-level emission in their noon, night, and morning vertical profiles (except for butyric acid during nighttime). Noon, night, and morning vertical profiles of O_3, NO_x, CO, air temperature, and relative humidity are reported in Figure A4.3.

5.4 Discussion

5.4.1 Alkanoic acids

Formic acid at BAO (1.9 ppb_v average) is comparable to previous measurements in urban and rural areas (Glasius et al., 2000; Kawamura et al., 1985; Veres et al., 2011). All alkanoic acid mixing ratios increase throughout the day (Figure 5.2), consistent with previously reported diurnal trends (Veres et al., 2011; Brophy and Farmer, 2015). Additionally, formic acid mixing ratios correlate strongly with j_{NO2} ($r^2 = 0.738$). These data point to a photochemical source of alkanoic acids, consistent with known reaction mechanisms. For example, ozonolysis of alkenes and photooxidation of isoprene are photochemical sources of formic acid in the troposphere (Orzechowska and Paulson, 2005; Jacob and Wofsy, 1988; Paulot et al., 2009; Paulot et al., 2011; Millet et al., 2015). Alkanoic acids are also produced during photooxidation of diesel exhaust (Friedman et al., 2017).

Vertical profiles indicate an additional, non-photochemical surface source of alkanoic acids. Alkanoic acid vertical profiles exhibit negative gradients, demonstrating upward fluxes from near the surface (< 75 m) to the atmosphere throughout the day and night (with the exception of butyric acid at night) (Figure 5.3). Possible drivers of this near-surface source are explored below. While photochemistry is an important atmospheric source of all observed alkanoic acids, the persistent near-surface gradient through both night and day requires an additional non-photochemical source at or near the surface.

Light- and temperature-dependent primary emissions of alkanoic acids from the stomata of plants have been reported previously (Kesselmeier et al., 1998), and could contribute to their observed diurnal increases (Figure 5.2). However, vegetation in the region is sparse, particularly during the hot, dry Front Range summer. Further, the near-surface source persists through both day and night, while biogenic light-dependent emissions typically cease during the night when stomata are closed and photosynthesis has stopped. Soil emissions are another plausible source

of alkanoic acids, but typically thought to be minor (Sanhueza and Andreae, 1991; Enders et al., 1992). We thus expect that biogenic sources of the alkanoic acids were minor during the campaign.

Traffic emissions are a primary, and potentially secondary, source of propionic, butyric, and valeric acid. These compounds have been observed as primary and secondary emissions from automobile exhaust (Kawamura et al., 1985; Kawamura et al., 2000; Friedman et al., 2017). Peaks in the diel profiles of these compounds between 09:00 – 10:00 are consistent with morning rush-hour traffic and NO_x (Figure A4.5). NO_x is commonly used as a tracer for near-field automobile emissions (Abeleira et al., 2017). CO is also an effective tracer for primary automobile emissions in the Front Range (Abeleira et al., 2017). Propionic, butyric, and valeric acid correlate particularly well with CO during morning rush-hour periods ($r^2 = 0.635$ for propionic, $r^2 = 0.615$ for butyric, and $r^2 = 0.721$ for valeric), suggesting that traffic dominated the source of these acids during that time. Correlations between the three acids and CO throughout the entire timeseries were lower ($r^2 = 0.237$ for propionic, $r^2 = 0.062$ for butyric, and $r^2 = 0.128$ for valeric), indicating that other sources influenced their gas-phase mixing ratios throughout the rest of the day. Much like CO, propionic, butyric, and valeric acid showed noticeable increases in measured mixing ratios from winds between 90° – 180° during morning rush-hour periods, consistent with the hypothesis that nearby traffic dominated the propionic, butyric, and valeric acid sources during morning rush hour (Figure 5.4). McDuffie et al. (2016) and Zaragoza et al. (2017) have shown that wind direction analysis alone is not effective for determining the direction/magnitude of upwind sources near BAO, due to significant mixing and recirculation of air near the site. However, we use these profiles merely to show that these acids share the same incoming air parcels measured at the site as CO—i.e. these compounds are transported to the site

from the same traffic source, irrespective of the exact direction of this source relative to the site. Formic acid behaves quite differently from the other alkanoic acids with respect to a potential traffic source. While automobile emissions are a known production source of formic acid (Kawamura et al., 1985; Kawamura et al., 2000; Friedman et al., 2017), formic acid did not exhibit a morning rush hour maximum, was only weakly correlated to CO during rush hour (r^2 = 0.026), and did not share the rush hour directionality with the other acids (Figure 5.4). Despite the demonstrable importance of traffic emissions as a source of alkanoic acids in the troposphere during morning rush-hour periods, the reduction of these emissions during other times of day make it unlikely that traffic was the dominant surface-level alkanoic acid source persisting throughout the noon, night, and morning vertical profiles (Figure 5.3).

Agricultural activity is another primary emission source of alkanoic acids (McGinn et al., 2003; Paulot et al., 2011), and may have contributed to the observed alkanoic acid mixing ratios. NH_3 in the Colorado Front Range comes primarily from agricultural sources (Tevlin et al., 2017). NH_3 correlates more strongly with butyric (r^2 = 0.453) and valeric (r^2 = 0.355) acids than propionic acid (r^2 = 0.221) throughout the entire day. Like NH_3 (Figure A4.6), all three acids increase with winds from 0° – 90°, which is likely attributable to transport from nearby CAFOs (Figure A4.7). Correlations between these acids and NH_3 were stronger during daytime (12:00 – 5:00) periods (r^2 = 0.517 for propionic, r^2 = 0.649 for butyric, and r^2 = 0.426 for valeric), suggesting that agricultural activity was predominantly a daytime source. Agricultural sources of formic acid have been suggested previously (Paulot et al., 2011). The weak correlation with NH_3 (r^2 = 0.044 for entire day, r^2 = 0.228 during daytime) suggests that agricultural activity was likely a minor daytime source of formic acid.

Photochemical oxidation of VOCs is an established atmospheric source of formic acid, and is consistent with the observed formic acid diel cycle and correlation with j_{NO2} ($r^2 = 0.738$). Formic acid is produced during ozonolysis of ethene and propene (Atkinson et al., 2006; Millet et al., 2015), both of which have known combustion sources (Gilman et al., 2013), and during OH oxidation of diesel emissions (Friedman et al., 2017). ONG wells were dominantly to the east of the site (Figure 5.1). These wells were a potential source of formic acid precursors due to the combustion processes associated with their operation (such as gas flaring). Isoprene is a known photochemical precursor of formic acid (Jacob and Wofsy, 1988; Orzechowska and Paulson, 2005; Paulot et al., 2009), though it has been observed in relatively low mixing ratios at BAO during the summer (0.2 ± 0.3 ppb_v average) (Abeleira et al., 2017). Further, anthropogenic sources dominate summertime OH reactivity at the site (Abeleira et al., 2017), and reports of isoprene oxidation as a major source of formic acid typically occur in heavily vegetated areas (Jacob and Wofsy, 1988; Stavrakou et al., 2012; Millet et al., 2015). The diurnal increases in propionic, butyric, and valeric acid reported here are consistent with previous field observations (Satsumabayashi et al., 1995; Veres et al., 2011) and reported photochemical production mechanisms of these compounds (Satsumabayashi et al., 1995; Orzechowska et al., 2005).

Photochemical sources are unlikely responsible for the near-surface source that persists thought the day. We note that while photochemical processing of anthropogenic precursors is a known source of HNO_3 and pyruvic acid (see section 5.4.2), the vertical profiles of these two acids are dominated by dry deposition and not surface sources. However, HNCO also has known photochemical and traffic sources, and displays a negative (upward flux) daytime, but not nighttime, near-surface vertical gradient (see section 5.4.3). While it is possible that

photochemical or traffic sources could cause the surface source implied by the alkanoic acid vertical profiles, it is less likely that they are responsible for the nighttime source.

The identity of the surface-level non-photochemical source thus remains unclear. Several other recent studies invoke missing alkanoic acid sources—i.e. sources not typically considered when modeling tropospheric VOC budgets. Paulot et al. (2011) suggested that photochemical aging of aerosols could serve as a major missing source of formic and acetic acid. Model-measurement discrepancies led Schobesberger et al. (2016) to suggest significant, unresolved surface-level sources of formic acid, although that study noted temperature and light dependences similar to emission parameterizations of other well-characterized biogenic VOCs. Millet et al. (2015) and Nguyen et al. (2015) also observed similar model-measurement discrepancies of formic acid, which were attributed to missing/underestimated chemical production and/or biogenic emissions sources.

Multiple processes could be responsible for the observed surface-level source of alkanoic acids. We hypothesize that reactions between O_3 and organic surfaces (i.e. soil, organic films) could be one non-photochemical surface-level source of alkanoic acids near the site, though unlikely to account for the entire source. Reactions of O_3 on organic surfaces such as organic films (Donaldson et al., 2005), plant surfaces (Cape et al., 2009; Jud et al., 2016), and human skin (Liu et al., 2016; Liu et al., 2017) have been reported previously. Soil organic matter and organic films are often rich in alkenes (Vancampenhout et al., 2009; Donaldson et al., 2005; Simpson et al., 2006), which undergo ozonolysis reactions in the presence of O_3 (Criegee, 1975; Wolff et al., 1997). Hydroxyalkyl hydroperoxides formed via the ozonolysis of alkenes can further decompose to alkanoic acids (Moortgat et al., 1997; Anglada et al., 2002; Hasson et al., 2003; Millet et al., 2015). O_3 mixing ratios measured at the site were relatively high at nighttime

(~ 40 ppb_v) (Figure A4.8), further suggesting that this process may contribute to the persistent upward flux of alkanoic acids through both day and night. We report noon, night, and morning vertical profile measurements of O_3 in Figure A4.3. The positive concentration gradient of O_3 with respect to height during nighttime is consistent with a nocturnal surface-level sink of O_3, and the hypothesis that O_3 reacts with organic surfaces to produce alkanoic acids. Known photochemical production mechanisms are the dominant O_3 source throughout the daytime, and no net surface-level exchanges are observed in the morning or noon vertical profiles. However, we emphasize that while O_3 reactions with surfaces could act as one source of organic acids, there is no evidence that they account for the entire surface-level organic acid source.

Wet and dry deposition are major sinks of alkanoic acids (Grosjean, 1989; Talbot et al., 1995). Removal via reactions with OH are slow, corresponding to atmospheric lifetimes of several days (Dagaut et al., 1988). $C_1 – C_5$ alkanoic acids have negligible absorption cross sections at wavelengths greater than ~250 nm (Singleton et al., 1987; Vicente et al., 2009); photolysis is thus not considered to be a major tropospheric alkanoic acid sink. Wet deposition was minimal in the Front Range during the study period due to the lack of rainfall events during the reported measurement period. Dry deposition should thus have been the only major alkanoic acid sink during the night. However, the vertical profiles showed upward fluxes of these compounds at night (Figure 5.3). The nocturnal decrease in mixing ratio necessitates an additional non-photochemical sink for these compounds, consistent with previous suggestions by Brophy and Farmer (2015). Cloud processing, gas-particle phase partitioning, and aqueous-phase reactions are possible alkanoic acid sinks. The high Henry's Law constants (H) of these acids suggest that aqueous-phase partitioning (aqueous aerosols, fog and cloud droplets, etc.) would be favorable ($H = 5.5 \times 10^3$, 5.7×10^3, 4.7×10^3, and 2.2×10^3 mol L^{-1} atm^{-1} for formic, propionic,

butyric, and valeric acid, respectively at T = 298 K) (Khan et al., 1995). However, this was likely not a significant sink given the arid climate of the Front Range. Carlton and Turpin (2013) suggest that liquid water concentration in the Front Range during summer is ~1 μg m^{-3}. Combining this with known constants, campaign mean mixing ratios, and meteorological conditions, aqueous-phase partitioning accounts for an estimated loss of $< 2 \times 10^{-10}$ ppb_v of each alkanoic acid (see SI). While this ignores effects of pH and other dissolved ions on solubility, aqueous partitioning is unlikely a substantial loss process for the alkanoic acids during the measurement campaign. Gas-phase reactions between the alkanoic acids and atmospheric bases, such as NH_3, amines, or amides have not been reported extensively. Grosjean (1989) suggested that carboxylic acids can react with NH_3 in the atmosphere to produce carboxylate ammonium salts, though the importance of this process as a tropospheric sink of alkanoic acids remains uncertain.

5.4.2 Nitric and pyruvic acid

HNO_3 and pyruvic acid follow similar diel and vertical trends ($r^2 = 0.603$), and their diel profiles are consistent with photochemical sources (Figure 5.2). Additionally, pyruvic acid correlates particularly well with j_{NO2} ($r^2 = 0.783$). Unlike the alkanoic acids, HNO_3 and pyruvic acid exhibit persistent net deposition to the surface near the site during the noon, night, and morning periods (Figure 5.3).

Traffic was likely an important secondary source of HNO_3 and pyruvic acid. HNO_3 is produced from NO_2 + OH, and pyruvic acid is produced from photooxidation of diesel exhaust (Friedman et al., 2017), including from 1,3,5-trimethylbenzene in the presence of NO_x (Praplan et al., 2014). Both NO_x and 1,3,5-trimethylbenzene are abundant components of automobile exhaust (Nelson and Quigley, 1984; Khoder, 2007). However, correlations between these acids

and CO during morning rush-hour traffic were weak ($r^2 = 0.274$ for HNO_3, and $r^2 = 0.264$ for pyruvic acid), perhaps unsurprising as CO is directly emitted from traffic exhaust, whereas HNO_3 and pyruvic acid require photochemistry. This observation suggests that regional, rather than nearby traffic is the source of these two acids. Neither HNO_3 nor pyruvic acid correlate with NH_3. However, agricultural activity is a known source of NO_x, which is primarily emitted from fertilizer and heavy-duty diesel farm vehicles (Shepherd et al., 1991; Kurvits and Marta, 1998). We therefore speculate that agricultural sources also served as a secondary source of HNO_3 near the site. Reports of pyruvic acid from agricultural sources are sparse, and we cannot evaluate the potential of this source with the data presented here. ONG and industrial activities are also sources of NO_x in the Front Range (Pfister et al., 2017a), and thus likely secondary sources of HNO_3. There is no evidence for strong surface-level emission sources of HNO_3 or pyruvic acid in the vertical profile data.

Vertical profiles of both HNO_3 and pyruvic acid are consistent with dry deposition (Figure 5.3). While both HNO_3 and pyruvic acid readily partition into the aqueous-phase ($H = 2.1 \times 10^5$ mol L^{-1} atm^{-1} and 3.1×10^5 mol L^{-1} atm^{-1} for HNO_3 and pyruvic acid, respectively) (Khan et al., 1995; Schwartz and White, 1981), we estimate that aqueous-phase partitioning is a negligible sink for both compounds. Photochemistry is not a major sink of HNO_3, but pyruvic acid readily undergoes photolysis—corresponding to a typical atmospheric lifetime of a few hours (Grosjean, 1983). However, the reaction of pyruvic acid with OH is negligible, corresponding to a lifetime on the order of months (Grosjean, 1983). Reactions between ambient NH_3 and HNO_3 produce NH_4NO_3 aerosol (Li et al., 2014), though we estimate that this process would not be a significant sink of gas-phase HNO_3 (see SI).

5.4.3 Isocyanic acid

The afternoon diurnal peak of HNCO is consistent with photochemical production sources (Figure 5.2). The diel profile of HNCO at BAO is similar to that observed previously in rural NE Colorado during BioCORN 2011, which was attributed to secondary photochemical production from amine and formamide (Roberts et al., 2014). The daytime vertical profiles show clear, upward fluxes of HNCO from the surface (Figure 5.3). This vertical gradient is strongest at noon, smaller in the morning and unclear at night, implying a surface source that is driven by photochemistry.

Roberts et al. (2014) suggested that farmland and cattle feedlots located along Interstate 25 serve as a source of photochemical precursors (various amine and amide compounds) of HNCO in the Colorado Front Range. This is supported by the correlation between HNCO and temperature ($r^2 = 0.773$) as these agricultural precursors are likely temperature-dependent. Sintermann et al. (2014) reported that alkaline compounds such as amines undergo enhanced volatilization from agricultural sites when air temperatures are higher due to a decrease in temperature-dependent solubility and an increase in soil/waste pH due to accelerated hydrolysis of urea. HNCO mixing ratios were possibly influenced by additional sources, including traffic, ONG wells, and industrial activity. Traffic exhaust is a primary emission source of HNCO (Brady et al., 2014; Link et al., 2016), but the lack of a morning rush-hour peak or correlation with CO suggests that it was not a strong primary source of HNCO at the site (Figure 5.2). Link et al. (2016) found that diesel exhaust was a precursor for photochemical HNCO production, but Jathar et al. (2017) suggested that the kinetics do not substantially outcompete dilution, and that urban HNCO is not strongly enhanced by diesel exhaust photochemistry.

Dry deposition is a major sink of HNCO (Roberts et al., 2014; Young et al., 2012), although HNCO readily partitions into the aqueous-phase ($H = 10^5$ mol L^{-1} atm^{-1}), where it can

hydrolyze to NH_3 (Roberts et al., 2011). We estimate that aqueous partitioning of HNCO was negligible. No major sinks of HNCO aside from wet deposition, dry deposition, and aqueous-phase chemistry have been reported, and photochemical loss reactions are negligible, with a photolysis lifetime of several months (Roberts et al., 2011), and an OH oxidation lifetime of several years (Tsang, 1992; Roberts et al., 2011; Borduas et al., 2016). HNCO has a relatively high gas-phase acidity (Wight and Beauchamp, 1980; Veres et al., 2010), and we hypothesize that non-photochemical gas-phase acid-base reactions could be a nighttime sink for HNCO.

5.5 Conclusions

Diurnal increases in all gas-phase acids are consistent with photochemical sources. We observe net surface-level emissions of alkanoic acids through both day and night, suggesting additional non-photochemical surface sources. We speculate that reactions between O_3 and organic surfaces (i.e. soil, organic films) near the site could be driving this persistent upward alkanoic acid flux. Correlations with chemical tracers suggest that traffic emissions and agricultural activity near the site are a primary source of propionic, butyric, and valeric acid, and potentially a secondary source of HNO_3, and HNCO.

Dry deposition is the dominant sink of HNO_3 and pyruvic acid, but was not large enough to out-compete the surface source of the alkanoic acids. Which sinks control the lifetime of the alkanoic acids remain unclear. A non-photochemical sink of HNCO on top of dry deposition is also suggested by the vertical profile data and warrants further investigation.

5.6 Author contributions

J. M. M. contributed analysis of all data herein.

5.7 Data availability

Data used herein are available at https://osf.io/aqc57/.

5.8 Chapter 5 figures

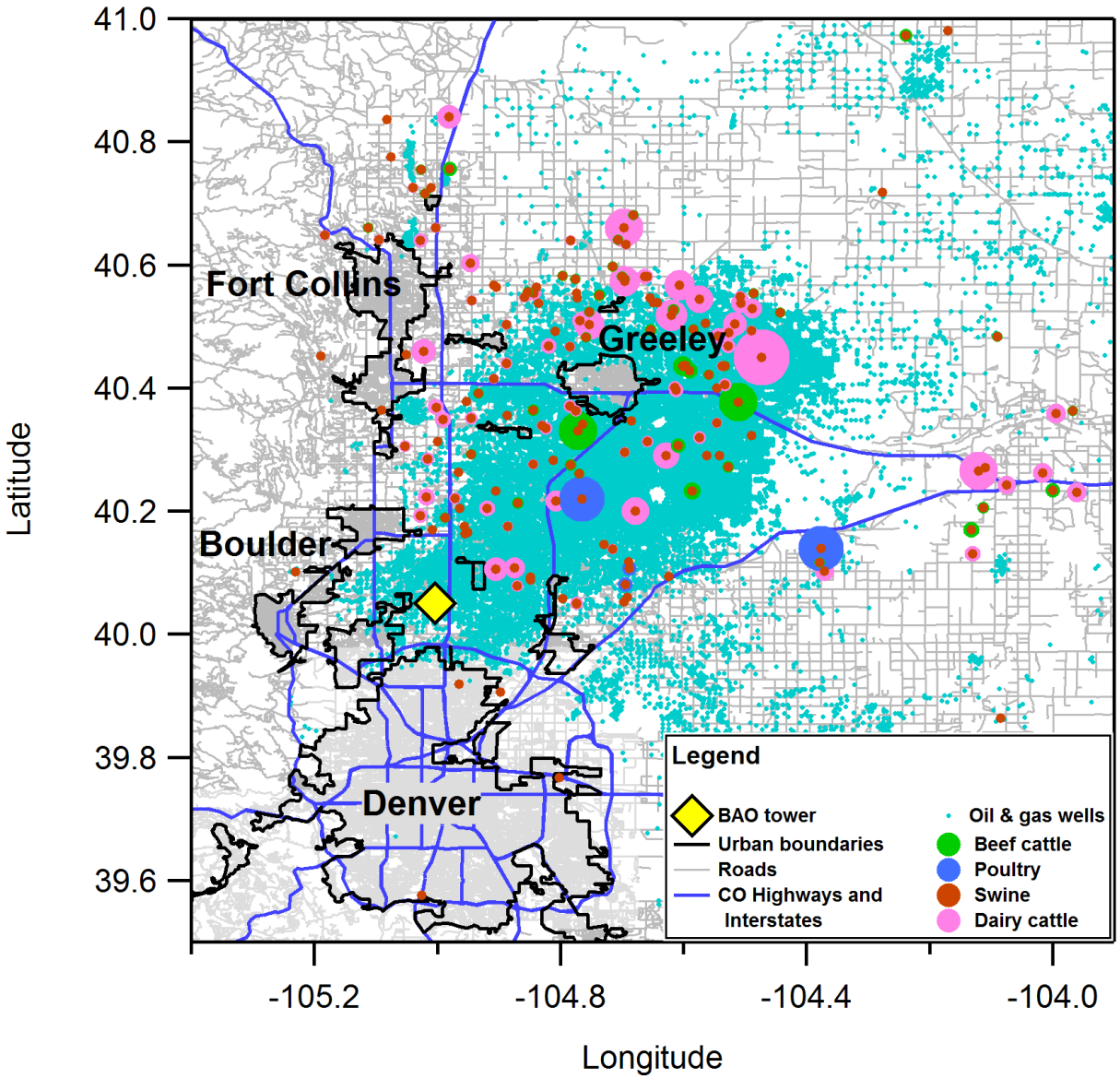

Figure 5.1. Area surrounding BAO site, including major nearby urban municipalities, roads and highways, ONG wells, and CAFOs. CAFOs are colored by operation type and sized by number of animal units per operation.

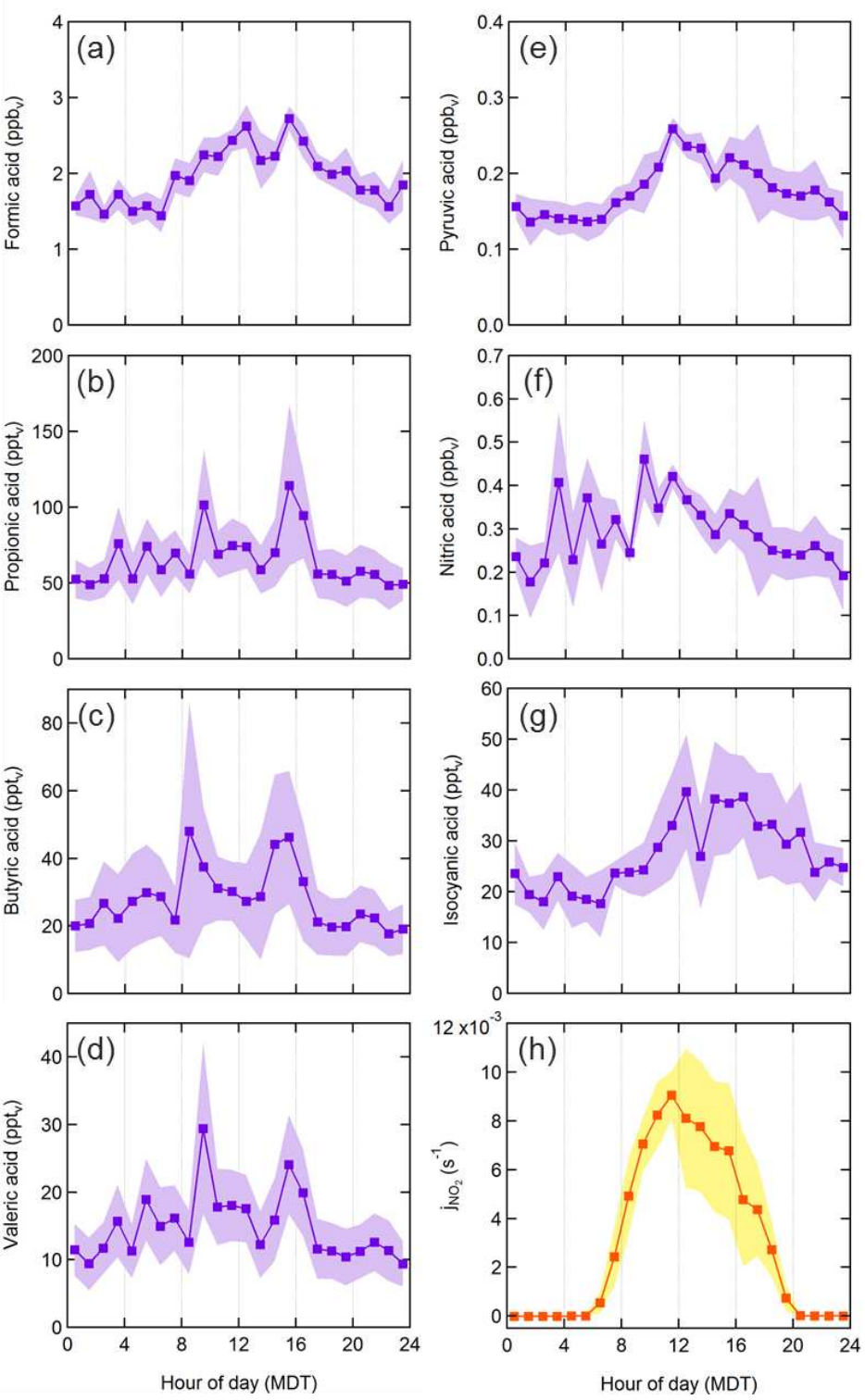

Figure 5.2. (a–g) Diel profiles for all detected gas-phase acids at 100 m. (h) Diel profile for j_{NO2} measured at the site. Data are binned by hour. Data points are means of hourly bins. Shaded area represents ± one standard deviation of binned data.

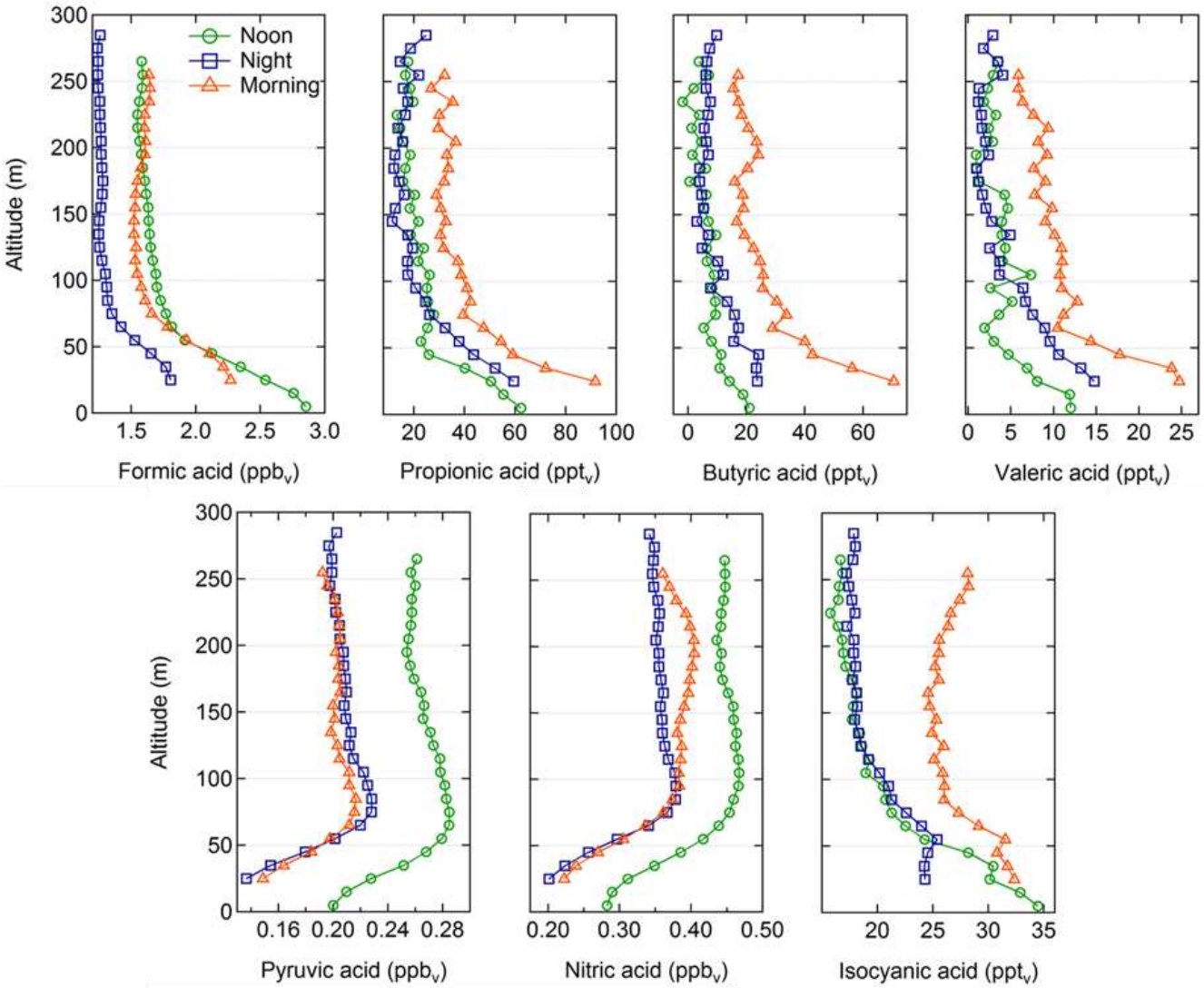

Figure 5.3. Vertical profiles for all detected gas-phase acids at representative noon, night, and morning periods, showing mixing ratio as a function of altitude. Data are binned by altitude (10 m per bin). Data points are means of each bin. Error bars have been removed for clarity, and are included in Figure A4.4.

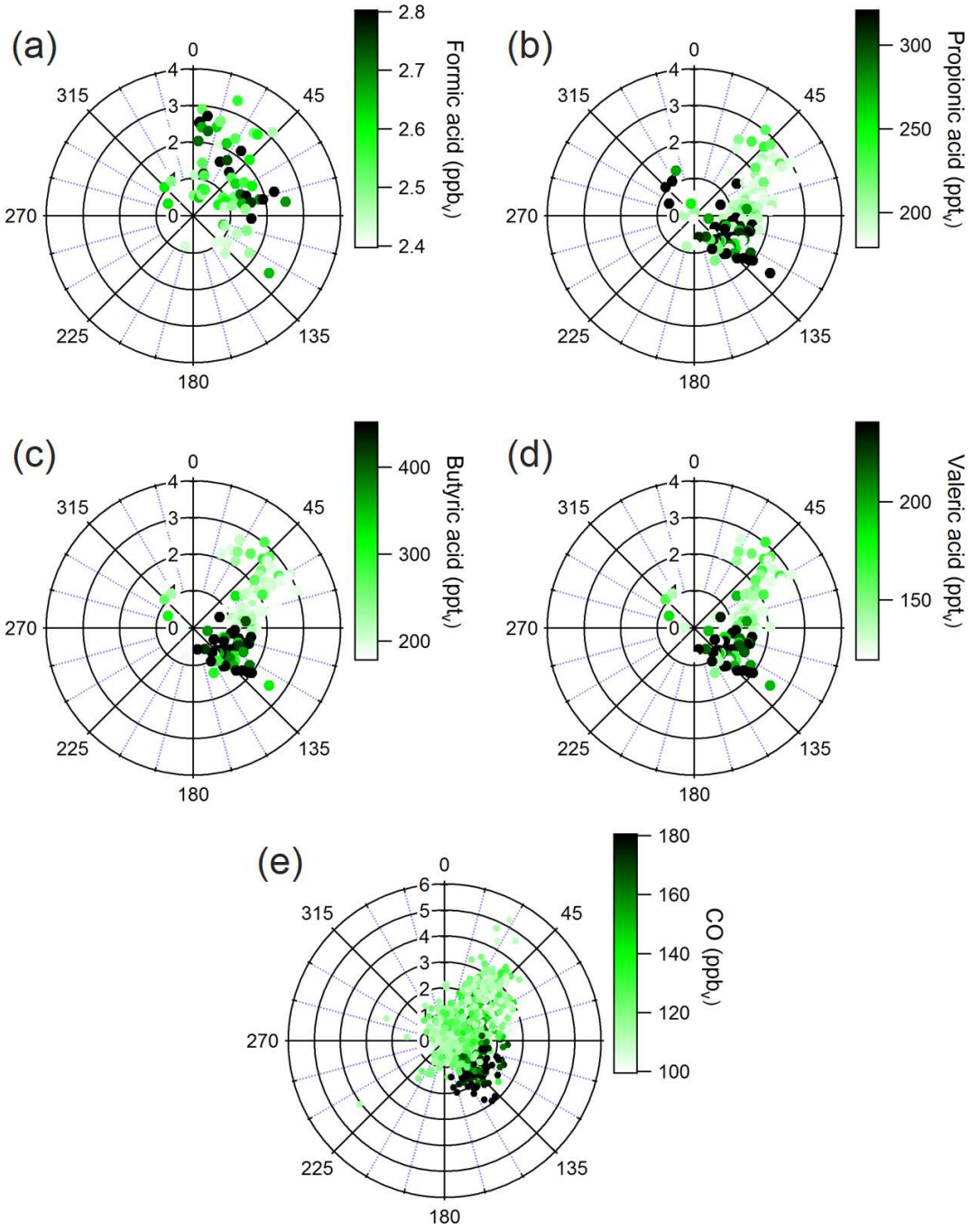

Figure 5.4. Wind plots of (a) formic acid, (b) propionic acid, (c) butyric acid, (d) valeric acid, and (e) CO measured at the site. Data are selected during periods of morning rush-hour traffic (08:30–10:30). Data points are colored by mixing ratio. Radial and angular axes represent wind speed (m s^{-1}) and direction (degrees), respectively. Degrees correspond to cardinal directions (i.e. 0° is N, 90° is E, etc.).

5.9 Chapter 5 tables

Table 5.1 – Campaign statistics for measured gas-phase acids.

Gas-phase acid	Mean (ppb_v)	Max (ppb_v)	Min. (ppb_v)	Standard deviation (ppb_v)
Formic	1.9	3.6	1.0	0.4
Propionic	0.06	0.70	Below LOD	0.03
Butyric	0.03	0.16	Below LOD	0.02
Valeric	0.01	0.06	Below LOD	0.01
Pyruvic	0.18	0.51	Below LOD	0.06
Nitric	0.30	1.11	0.00	0.07
Isocyanic	0.03	0.07	0.00	0.01

Table 5.2 – Correlation coefficients (r^2) for each gas-phase acid in the leftmost column compared to other gas-phase acids, chemical tracers, and other meteorological parameters in the table header (Propion. = propionic acid, Isocyan. = isocyanic acid, Temp. = air temperature).

	Formic	Isocyan.	Pyruvic	Propion.	Valeric	Nitric	Butyric	CO	NH_3	Temp.	j_{NO2}
Formic	—	0.375	0.194	0.257	0.120	0.091	0.089	0.026	0.044	0.504	0.738
Isocyan.	0.375	—	0.030	0.102	0.007	0.005	0.001	0.093	0.002	0.773	0.411
Pyruvic	0.194	0.030	—	0.077	0.074	0.603	0.068	0.264	0.002	0.560	0.783
Propion.	0.257	0.102	0.077	—	0.776	0.231	0.714	0.635	0.221	0.058	0.310
Valeric	0.120	0.007	0.074	0.776	—	0.312	0.856	0.721	0.355	0.005	0.331
Nitric	0.091	0.005	0.603	0.231	0.312	—	0.332	0.274	0.113	0.005	0.382
Butyric	0.089	0.001	0.068	0.714	0.856	0.332	—	0.615	0.453	0.017	0.365

REFERENCES

Abeleira, A., Pollack, I. B., Sive, B., Zhou, Y., Fischer, E. V., and Farmer, D. K.: Source characterization of volatile organic compounds in the Colorado Northern Front Range Metropolitan Area during spring and summer 2015, J. Geophys. Res.-Atmos., 122, 3595-3613, doi:10.1002/2016jd026227, 2017.

Adams, P. J., Seinfeld, J. H., and Koch, D. M.: Global concentrations of tropospheric sulfate, nitrate, and ammonium aerosol simulated in a general circulation model, J. Geophys. Res.-Atmos., 104, 13791-13823, doi:10.1029/1999jd900083, 1999.

Almaraz, M., Bai, E., Wang, C., Trousdell, J., Conley, S., Faloona, I., and Houlton, B. Z.: Agriculture is a major source of NOx pollution in California, Sci. Adv., 4, eaao3477, doi:10.1126/sciadv.aao3477, 2018.

Andreae, M. O., Talbot, R. W., Andreae, T. W., Harriss, R. C.: Formic and Acetic Acid Over the Central Amazon Region, Brazil 1. Dry Season, J. Geophys. Res., 93, 1616-1624, doi:10.1029/JD093iD02p01616, 1988.

Anglada, J. M., Aplincourt, P., Bofill, J. M., and Cremer, D.: Atmospheric formation of OH radicals and H2O2 from alkene ozonolysis under humid conditions, Chem. Phys. Chem., 3, 215-221, doi:10.1002/1439-7641(20020215)3:2<215::AID-CPHC215>3.0.CO;2-3, 2002.

Atkinson, R., Baulch, D. L., Cox, R. A., Crowley, J. N., Hampson, R. F., Hynes, R. G., Jenkin, M. E., Rossi, M. J., and Troe, J.: Evaluated kinetic and photochemical data for atmospheric chemistry: Volume II–gas phase reactions of organic species, Atmos. Chem. Phys., 6, 3625-4055, doi:10.5194/acp-6-3625-2006, 2006.

Bertram, T. H., Kimmel, J. R., Crisp, T. A., Ryder, O. S., Yatavelli, R. L. N., Thornton, J. A., Cubison, M. J., Gonin, M., and Worsnop, D. R.: A field-deployable, chemical ionization time-of-flight mass spectrometer, Atmos. Meas. Tech., 4, 1471-1479, doi:10.5194/amt-4-1471-2011, 2011.

Borduas, N., Abbatt, J. P., and Murphy, J. G.: Gas phase oxidation of monoethanolamine (MEA) with OH radical and ozone: kinetics, products, and particles, Environ. Sci. Technol., 47, 6377-6383, doi:10.1021/es401282j, 2013.

Borduas, N., Abbatt, J. P., Murphy, J. G., So, S., and da Silva, G.: Gas-Phase Mechanisms of the Reactions of Reduced Organic Nitrogen Compounds with OH Radicals, Environ. Sci. Technol., 50, 11723-11734, doi:10.1021/acs.est.6b03797, 2016.

Borduas, N., Place, B., Wentworth, G., Abbatt, J., and Murphy, J.: Solubility and reactivity of HNCO in water: insights into HNCO's fate in the atmosphere, 16, 703-714, 2016.

Brady, J. M., Crisp, T. A., Collier, S., Kuwayama, T., Forestieri, S. D., Perraud, V., Zhang, Q., Kleeman, M. J., Cappa, C. D., and Bertram, T. H.: Real-time emission factor measurements of isocyanic acid from light duty gasoline vehicles, Environ. Sci. Technol., 48, 11405-11412, doi:10.1021/es504354p, 2014.

Brophy, P., and Farmer, D. K.: A switchable reagent ion high resolution time-of-flight chemical ionization mass spectrometer for real-time measurement of gas phase oxidized species: characterization from the 2013 southern oxidant and aerosol study, Atmos. Meas. Tech., 8, 2945-2959, doi:10.5194/amt-8-2945-2015, 2015.

Brophy, P., and Farmer, D. K.: Clustering, methodology, and mechanistic insights into acetate chemical ionization using high-resolution time-of-flight mass spectrometry, Atmos. Meas. Tech., 9, 3969-3986, doi:10.5194/amt-9-3969-2016, 2016.

Brown, S. S., Thornton, J. A., Keene, W. C., Pszenny, A. A. P., Sive, B. C., Dube, W. P., Wagner, N. L., Young, C. J., Riedel, T. P., Roberts, J. M., VandenBoer, T. C., Bahreini, R., Ozturk, F., Middlebrook, A. M., Kim, S., Hubler, G., and Wolfe, D. E.: Nitrogen, Aerosol Composition, and Halogens on a Tall Tower (NACHTT): Overview of a wintertime air chemistry field study in the front range urban corridor of Colorado, J. Geophys. Res.-Atmos., 118, 8067-8085, doi:10.1002/jgrd.50537, 2013.

Cape, J. N., Hamilton, R., and Heal, M. R.: Reactive uptake of ozone at simulated leaf surfaces: implications for ‘non-stomatal’ozone flux, Atmos. Environ., 43, 1116-1123, doi:10.1016/j.atmosenv.2008.11.007, 2009.

Carlton, A. G., and Turpin, B. J.: Particle partitioning potential of organic compounds is highest in the Eastern US and driven by anthropogenic water, Atmos. Chem. Phys., 13, 10203-10214, doi:10.5194/acp-13-10203-2013, 2013.

Criegee, R.: Mechanism of Ozonolysis, Angew. Chem. Int. Edit., 14, 745-752, doi:10.1002/anie.197507451, 1975.

Dagaut, P., Wallington, T. J., Liu, R., and Kurylo, M. J.: The gas phase reactions of hydroxyl radicals with a series of carboxylic acids over the temperature range 240–440 K, Int. J. Chem. Kinet., 20, 331-338, 1988.

DeCarlo, P. F., Kimmel, J. R., Trimborn, A., Northway, M. J., Jayne, J. T., Aiken, A. C., Gonin, M., Fuhrer, K., Horvath, T., Docherty, K. S., Worsnop, D. R., and Jimenez, J. L.: Field-deployable, high-resolution, time-of-flight aerosol mass spectrometer, Anal. Chem., 78, 8281-8289, doi:10.1021/ac061249n, 2006.

Dignon, J.: Nox and Sox Emissions from Fossil-Fuels - a Global Distribution, Atmos. Environ. A-Gen., 26, 1157-1163, doi:10.1016/0960-1686(92)90047-O, 1992.

Donaldson, D. J., Mmereki, B. T., Chaudhuri, S. R., Handley, S., and Oh, M.: Uptake and reaction of atmospheric organic vapours on organic films, Faraday Discuss., 130, 227-239, 2005.

Enders, G., Dlugi, R., Steinbrecher, R., Clement, B., Daiber, R., Voneijk, J., Gab, S., Haziza, M., Helas, G., Herrmann, U., Kessel, M., Kesselmeier, J., Kotzias, D., Kourtidis, K., Kurth, H. H., Mcmillen, R. T., Roider, G., Schurmann, W., Teichmann, U., and Torres, L.: Biosphere Atmosphere Interactions - Integrated Research in a European Coniferous Forest Ecosystem, Atmos. Environ. A-Gen., 26, 171-189, doi:10.1016/0960-1686(92)90269-Q, 1992.

Fischer, M., and Warneck, P.: The dissociation constant of pyruvic acid: determination by spectrophotometric measurements, 95, 523-527, 1991.

Friedman, B., Link, M. F., Fulgham, S. R., Brophy, P., Galang, A., Brune, W. H., Jathar, S. H., and Farmer, D. K.: Primary and Secondary Sources of Gas-Phase Organic Acids from Diesel Exhaust, Environ. Sci. Technol., 51, 10872-10880, doi:10.1021/acs.est.7b01169, 2017.

Gilman, J. B., Lerner, B. M., Kuster, W. C., and de Gouw, J. A.: Source signature of volatile organic compounds from oil and natural gas operations in northeastern Colorado, Environ. Sci. Technol., 47, 1297-1305, doi:10.1021/es304119a, 2013.

Glasius, M., Wessel, S., Christensen, C. S., Jacobsen, J. K., Jorgensen, H. E., Klitgaard, K. C., Petersen, L., Rasmussen, J. K., Hansen, T. S., Lohse, C., Boaretto, E., and Heinemeier, J.: Sources to formic acid studied by carbon isotopic analysis and air mass characterization, Atmos. Environ., 34, 2471-2479, doi:10.1016/S1352-2310(99)00416-1, 2000.

Goode, J. G., Yokelson, R. J., Ward, D. E., Susott, R. A., Babbitt, R. E., Davies, M. A., and Hao, W. M.: Measurements of excess O3, CO2, CO, CH4, C2H4, C2H2, HCN, NO, NH3, HCOOH, CH3COOH, HCHO, and CH3OH in 1997 Alaskan biomass burning plumes by airborne Fourier transform infrared spectroscopy (AFTIR), J. Geophys. Res.-Atmos., 105, 22147-22166, 2000.

Grosjean, D.: Atmospheric Reactions of Pyruvic-Acid, Atmos. Environ., 17, 2379-2382, doi:10.1016/0004-6981(83)90242-1, 1983.

Grosjean, D.: Organic acids in southern California air: Ambient concentrations, mobile source emissions, in situ formation and removal processes, Environ. Sci. Technol., 23, 1506-1514, 1989.

Hasson, A. S., Chung, M. Y., Kuwata, K. T., Converse, A. D., Krohn, D., and Paulson, S. E.: Reaction of Criegee Intermediates with Water Vapor An Additional Source of OH Radicals in Alkene Ozonolysis?, J. Phys. Chem. A, 107, 6176-6182, 2003.

Himanen, M., Prochazka, P., Hanninen, K., and Oikari, A.: Phytotoxicity of low-weight carboxylic acids, Chemosphere, 88, 426-431, doi:10.1016/j.chemosphere.2012.02.058, 2012.

Jacob, D. J., and Wofsy, S. C.: Photochemistry of Biogenic Emissions over the Amazon Forest, J. Geophys. Res.-Atmos., 93, 1477-1486, doi:10.1029/JD093iD02p01477, 1988.

Jaisson, S., Pietrement, C., and Gillery, P.: Carbamylation-derived products: bioactive compounds and potential biomarkers in chronic renal failure and atherosclerosis, Clin. Chem., 57, 1499-1505, doi:10.1373/clinchem.2011.163188, 2011.

Jathar, S. H., Heppding, C., Link, M. F., Farmer, D. K., Akherati, A., Kleeman, M. J., de Gouw, J. A., Veres, P. R., and Roberts, J. M.: Investigating diesel engines as an atmospheric source of isocyanic acid in urban areas, Atmos. Chem. Phys, 17, 8959-8970, doi:10.5194/acp-17-8959-2017, 2017.

Jud, W., Fischer, L., Canaval, E., Wohlfahrt, G., Tissier, A., and Hansel, A.: Plant surface reactions: an opportunistic ozone defence mechanism impacting atmospheric chemistry, Atmos. Chem. Phys., 16, 277-292, doi:10.5194/acp-16-277-2016, 2016.

Kaimal, J. C., and Gaynor, J. E.: The Boulder Atmospheric Observatory, J. Clim. Appl. Meteorol., 22, 863-880, doi:10.1175/1520-0450(1983)022<0863:Tbao>2.0.Co;2, 1983.

Kawamura, K., Ng, L. L., and Kaplan, I. R.: Determination of organic acids (C1-C10) in the atmosphere, motor exhausts, and engine oils, Environ. Sci. Technol., 19, 1082-1086, doi:10.1021/es00141a010, 1985.

Kawamura, K., Steinberg, S., and Kaplan, I. R.: Homologous series of C 1–C 10 monocarboxylic acids and C 1–C 6 carbonyls in Los Angeles air and motor vehicle exhausts, 34, 4175-4191, Atmos. Environ., 2000.

Keene, W. C., and Galloway, J. N.: Organic Acidity in Precipitation of North-America, Atmos. Environ., 18, 2491-2497, doi:10.1016/0004-6981(84)90020-9, 1984.

Kesselmeier, J., Bode, K., Gerlach, C., and Jork, E. M.: Exchange of atmospheric formic and acetic acids with trees and crop plants under controlled chamber and purified air conditions, Atmos. Environ., 32, 1765-1775, doi:10.1016/S1352-2310(97)00465-2, 1998.

Kesselmeier, J.: Exchange of short-chain oxygenated volatile organic compounds (VOCs) between plants and the atmosphere: A compilation of field and laboratory studies, J. Atmos. Chem., 39, 219-233, doi:10.1023/A:1010632302076, 2001.

Khan, I., Brimblecombe, P., and Clegg, S. L.: Solubilities of Pyruvic-Acid and the Lower (C-1-C-6) Carboxylic-Acids - Experimental-Determination of Equilibrium Vapor-Pressures above Pure Aqueous and Salt-Solutions, J. Atmos. Chem., 22, 285-302, doi:10.1007/Bf00696639, 1995.

Khoder, M. I.: Ambient levels of volatile organic compounds in the atmosphere of Greater Cairo, Atmos. Environ., 41, 554-566, doi:10.1016/j.atmosenv.2006.08.051, 2007.

Kulmala, M., Laaksonen, A., Korhonen, P., Vesala, T., Ahonen, T., and Barrett, J. C.: The Effect of Atmospheric Nitric-Acid Vapor on Cloud Condensation Nucleus Activation, J. Geophys. Res.-Atmos., 98, 22949-22958, doi:10.1029/93jd02070, 1993.

Kurvits, T., and Marta, T.: Agricultural NH3 and NOx emissions in Canada, Environ. Pollut., 102, 187-194, 1998.

Lee, B. H., Lopez-Hilfiker, F. D., Mohr, C., Kurten, T., Worsnop, D. R., and Thornton, J. A.: An iodide-adduct high-resolution time-of-flight chemical-ionization mass spectrometer: application to atmospheric inorganic and organic compounds, Environ. Sci. Technol., 48, 6309-6317, doi:10.1021/es500362a, 2014.

Levanov, A., Isaikina, O. Y., and Lunin, V.: Dissociation constant of nitric acid, 91, 1221-1228, 2017.

Li, Y., Schwandner, F. M., Sewell, H. J., Zivkovich, A., Tigges, M., Raja, S., Holcomb, S., Molenar, J. V., Sherman, L., Archuleta, C., Lee, T., and Collett, J. L.: Observations of ammonia, nitric acid, and fine particles in a rural gas production region, Atmos. Environ., 83, 80-89, doi:10.1016/j.atmosenv.2013.10.007, 2014.

Link, M. F., Friedman, B., Fulgham, R., Brophy, P., Galang, A., Jathar, S. H., Veres, P., Roberts, J. M., and Farmer, D. K.: Photochemical processing of diesel fuel emissions as a large secondary source of isocyanic acid (HNCO), Geophys. Res. Lett., 43, 4033-4041, doi:10.1002/2016gl068207, 2016.

Liu, S., Li, R., Wild, R. J., Warneke, C., de Gouw, J. A., Brown, S. S., Miller, S. L., Luongo, J. C., Jimenez, J. L., and Ziemann, P. J.: Contribution of human-related sources to indoor volatile organic compounds in a university classroom, Indoor Air, 26, 925-938, doi:10.1111/ina.12272, 2016.

Liu, S., Thompson, S. L., Stark, H., Ziemann, P. J., and Jimenez, J. L.: Gas-Phase Carboxylic Acids in a University Classroom: Abundance, Variability, and Sources, Environ. Sci. Technol., 51, 5454-5463, doi:10.1021/acs.est.7b01358, 2017.

Lopez-Hilfiker, F. D., Iyer, S., Mohr, C., Lee, B. H., D'Ambro, E. L., Kurten, T., and Thornton, J. A.: Constraining the sensitivity of iodide adduct chemical ionization mass spectrometry to multifunctional organic molecules using the collision limit and thermodynamic stability of iodide ion adducts, Atmos. Meas. Tech., 9, 1505-1512, doi:10.5194/amt-9-1505-2016, 2016.

McDuffie, E. E., Edwards, P. M., Gilman, J. B., Lerner, B. M., Dube, W. P., Trainer, M., Wolfe, D. E., Angevine, W. M., deGouw, J., Williams, E. J., Tevlin, A. G., Murphy, J. G., Fischer, E. V., McKeen, S., Ryerson, T. B., Peischl, J., Holloway, J. S., Aikin, K., Langford, A. O., Senff, C. J., Alvarez, R. J., Hall, S. R., Ullmann, K., Lantz, K. O., and Brown, S. S.: Influence of oil and gas emissions on summertime ozone in the Colorado Northern Front Range, J. Geophys. Res.-Atmos., 121, 8712-8729, doi:10.1002/2016jd025265, 2016.

McGinn, S. M., Janzen, H. H., and Coates, T.: Atmospheric ammonia, volatile fatty acids, and other odorants near beef feedlots, J. Environ. Qual., 32, 1173-1182, doi: 10.2134/jeq2003.1173, 2003.

Millet, D. B., Baasandorj, M., Farmer, D. K., Thornton, J. A., Baumann, K., Brophy, P., Chaliyakunnel, S., de Gouw, J. A., Graus, M., Hu, L., Koss, A., Lee, B. H., Lopez-Hilfiker, F. D., Neuman, J. A., Paulot, F., Peischl, J., Pollack, I. B., Ryerson, T. B., Warneke, C., Williams, B. J., and Xu, J.: A large and ubiquitous source of atmospheric formic acid, Atmos. Chem. Phys., 15, 6283-6304, doi:10.5194/acp-15-6283-2015, 2015.

Moortgat, G. K., Bauer, D., Burrows, J. P., Crowley, J. N., Helleis, F., Horie, O., Koch, S., Limbach, S., Neeb, P., and Raber, W.: Laboratory Studies of Peroxy Radicals, Carbonyl Compounds and Ozonolysis Reactions of Tropospheric Importance, in: Chemical Processes in Atmospheric Oxidation, Springer, 162-169, 1997.

Nelson, P. F., and Quigley, S. M.: The Hydrocarbon Composition of Exhaust Emitted from Gasoline Fueled Vehicles, Atmos. Environ., 18, 79-87, doi:10.1016/0004-6981(84)90230-0, 1984.

Nguyen, T. B., Crounse, J. D., Teng, A. P., St Clair, J. M., Paulot, F., Wolfe, G. M., and Wennberg, P. O.: Rapid deposition of oxidized biogenic compounds to a temperate forest, P. Natl. Acad. Sci. USA, 112, E392-401, doi:10.1073/pnas.1418702112, 2015.

Orzechowska, G. E., Nguyen, H. T., and Paulson, S. E.: Photochemical sources of organic acids. 2. Formation of C5-C9 carboxylic acids from alkene ozonolysis under dry and humid conditions, J. Phys. Chem. A., 109, 5366-5375, doi:10.1021/jp050167k, 2005.

Orzechowska, G. E., and Paulson, S. E.: Photochemical sources of organic acids. 1. Reaction of ozone with isoprene, propene, and 2-butenes under dry and humid conditions using SPME, J. Phys. Chem. A., 109, 5358-5365, doi:10.1021/jp050166s, 2005.

Paulot, F., Crounse, J. D., Kjaergaard, H. G., Kroll, J. H., Seinfeld, J. H., and Wennberg, P. O.: Isoprene photooxidation: new insights into the production of acids and organic nitrates, Atmos. Chem. Phys., 9, 1479-1501, doi:10.5194/acp-9-1479-2009, 2009.

Paulot, F., Wunch, D., Crounse, J. D., Toon, G. C., Millet, D. B., DeCarlo, P. F., Vigouroux, C., Deutscher, N. M., Abad, G. G., Notholt, J., Warneke, T., Hannigan, J. W., Warneke, C., de Gouw, J. A., Dunlea, E. J., De Maziere, M., Griffith, D. W. T., Bernath, P., Jimenez, J. L., and Wennberg, P. O.: Importance of secondary sources in the atmospheric budgets of formic and acetic acids, Atmos. Chem. Phys., 11, 1989-2013, doi:10.5194/acp-11-1989-2011, 2011.

Pfister, G., Flocke, F., Hornbrook, R., and Orlando, J.: Process-Based and Regional Source Impact Analysis for FRAPPÉ and DISCOVER-AQ 2014, National Center for Atmospheric Research, 2017a.

Pfister, G. G., Reddy, P. J., Barth, M. C., Flocke, F. F., Fried, A., Herndon, S. C., Sive, B. C., Sullivan, J. T., Thompson, A. M., and Yacovitch, T. I.: Using Observations and Source-Specific Model Tracers to Characterize Pollutant Transport During FRAPPÉ and DISCOVER-AQ, J. Geophys. Res.-Atmos., 122, doi:10.1002/2017JD027257, 2017b.

Praplan, A. P., Hegyi-Gaeggeler, K., Barmet, P., Pfaffenberger, L., Dommen, J., and Baltensperger, U.: Online measurements of water-soluble organic acids in the gas and aerosol phase from the photooxidation of 1,3,5-trimethylbenzene, Atmos. Chem. Phys., 14, 8665-8677, doi:10.5194/acp-14-8665-2014, 2014.

Roberts, J. M., Veres, P. R., Cochran, A. K., Warneke, C., Burling, I. R., Yokelson, R. J., Lerner, B., Gilman, J. B., Kuster, W. C., Fall, R., and de Gouw, J.: Isocyanic acid in the atmosphere and its possible link to smoke-related health effects, P. Natl. Acad. Sci. USA, 108, 8966-8971, doi:10.1073/pnas.1103352108, 2011.

Roberts, J. M., Veres, P. R., VandenBoer, T. C., Warneke, C., Graus, M., Williams, E. J., Lefer, B., Brock, C. A., Bahreini, R., Ozturk, F., Middlebrook, A. M., Wagner, N. L., Dube, W. P., and de Gouw, J. A.: New insights into atmospheric sources and sinks of isocyanic acid, HNCO, from recent urban and regional observations, J. Geophys. Res.-Atmos., 119, 1060-1072, doi:10.1002/2013jd019931, 2014.

Sanhueza, E., and Andreae, M. O.: Emission of Formic and Acetic-Acids from Tropical Savanna Soils, Geophys. Res. Lett., 18, 1707-1710, doi:10.1029/91gl01565, 1991.

Satsumabayashi, H., Kurita, H., Chang, Y. S., Carmichael, G. R., and Ueda, H.: Photochemical Formations of Lower Aldehydes and Lower Fatty-Acids under Long-Range Transport in Central Japan, Atmos. Environ., 29, 255-266, doi:10.1016/1352-2310(94)00231-9, 1995.

Schobesberger, S., Lopez-Hilfiker, F. D., Taipale, D., Millet, D. B., D'Ambro, E. L., Rantala, P., Mammarella, I., Zhou, P. T., Wolfe, G. M., Lee, B. H., Boy, M., and Thornton, J. A.: High upward fluxes of formic acid from a boreal forest canopy, Geophys. Res. Lett., 43, 9342-9351, doi:10.1002/2016gl069599, 2016.

Schwartz, S. E., and White, W. H.: Solubility equilibria of the nitrogen oxides and oxyacids in dilute aqueous solution, Adv. Environ. Sci. Eng., 4, 1981.

Seinfeld, J. H., and Pandis, S. N.: Atmospheric Chemistry and Physics, 1 ed., Wiley-Interscience, Canada, 1998.

Shepherd, M. F., Barzetti, S., and Hastie, D. R.: The Production of Atmospheric Nox and N2o from a Fertilized Agricultural Soil, Atmos. Environ. A-Gen., 25, 1961-1969, doi:10.1016/0960-1686(91)90277-E, 1991.

Shetter, R. E., Junkermann, W., Swartz, W. H., Frost, G. J., Crawford, J. H., Lefer, B. L., Barrick, J. D., Hall, S. R., Hofzumahaus, A., Bais, A., Calvert, J. G., Cantrell, C. A., Madronich, S., Muller, M., Kraus, A., Monks, P. S., Edwards, G. D., McKenzie, R., Johnston, P., Schmitt, R., Griffioen, E., Krol, M., Kylling, A., Dickerson, R. R., Lloyd, S. A., Martin, T., Gardiner, B., Mayer, B., Pfister, G., Roth, E. P., Koepke, P., Ruggaber, A., Schwander, H., and van Weele, M.: Photolysis frequency of NO2: Measurement and modeling during the International

Photolysis Frequency Measurement and Modeling Intercomparison (IPMMI), J. Geophys. Res.-Atmos., 108, doi:10.1029/2002jd002932, 2003.

Simpson, A. J., Lam, B., Diamond, M. L., Donaldson, D. J., Lefebvre, B. A., Moser, A. Q., Williams, A. J., Larin, N. I., and Kvasha, M. P.: Assessing the organic composition of urban surface films using nuclear magnetic resonance spectroscopy, Chemosphere, 63, 142-152, doi:10.1016/j.chemosphere.2005.07.013, 2006.

Singleton, D. L., Paraskevopoulos, G., and Irwin, R. S.: UV Absorption Cross-Sections of the Monomer and Dimer of Formic-Acid, J. Photochem., 37, 209-216, doi:10.1016/0047-2670(87)85001-3, 1987.

Sintermann, J., Schallhart, S., Kajos, M., Jocher, M., Bracher, A., Munger, A., Johnson, D., Neftel, A., and Ruuskanen, T.: Trimethylamine emissions in animal husbandry, Biogeosciences, 11, 5073-5085, doi:10.5194/bg-11-5073-2014, 2014.

Smith, R. M., and Martell, A. E.: NIST Standard Reference Database 46, in, 2004.

Stavrakou, T., Muller, J. F., Peeters, J., Razavi, A., Clarisse, L., Clerbaux, C., Coheur, P. F., Hurtmans, D., De Maziere, M., Vigouroux, C., Deutscher, N. M., Griffith, D. W. T., Jones, N., and Paton-Walsh, C.: Satellite evidence for a large source of formic acid from boreal and tropical forests, Nat. Geosci., 5, 26-30, doi:10.1038/Ngeo1354, 2012.

Sverdrup, L. E., Kallqvist, T., Kelley, A. E., Furst, C. S., and Hagen, S. B.: Comparative toxicity of acrylic acid to marine and freshwater microalgae and the significance for environmental effects assessments, Chemosphere, 45, 653-658, 2001.

Swarthout, R. F., Russo, R. S., Zhou, Y., Hart, A. H., and Sive, B. C.: Volatile organic compound distributions during the NACHTT campaign at the Boulder Atmospheric Observatory: Influence of urban and natural gas sources, J. Geophys. Res.-Atmos., 118, 10614-10637, doi:10.1002/jgrd.50722, 2013.

Talbot, R. W., Mosher, B. W., Heikes, B. G., Jacob, D. J., Munger, J. W., Daube, B. C., Keene, W. C., Maben, J. R., and Artz, R. S.: Carboxylic-Acids in the Rural Continental Atmosphere over the Eastern United-States during the Shenandoah Cloud and Photochemistry Experiment, J. Geophys. Res.-Atmos., 100, 9335-9343, doi:10.1029/95jd00507, 1995.

Tevlin, A. G., Li, Y., Collett, J. L., McDuffie, E. E., Fischer, E. V., and Murphy, J. G.: Tall Tower Vertical Profiles and Diurnal Trends of Ammonia in the Colorado Front Range, J. Geophys. Res.-Atmos., 122, 12468-12487, doi:10.1002/2017jd026534, 2017.

Tsang, W.: Chemical kinetic data base for propellant combustion. II. Reactions involving CN, NCO, and HNCO, J. Phys. Chem. Ref. Data, 21, 753-791, 1992.

Vancampenhout, K., Wouters, K., De Vos, B., Buurman, P., Swennen, R., and Deckers, J.: Differences in chemical composition of soil organic matter in natural ecosystems from different

climatic regions–A pyrolysis–GC/MS study, Soil Biol. Biochem., 41, 568-579, doi:10.1016/j.soilbio.2008.12.023, 2009.

Veres, P., Roberts, J. M., Warneke, C., Welsh-Bon, D., Zahniser, M., Herndon, S., Fall, R., and de Gouw, J.: Development of negative-ion proton-transfer chemical-ionization mass spectrometry (NI-PT-CIMS) for the measurement of gas-phase organic acids in the atmosphere, Int. J. Mass Spectrom., 274, 48-55, doi:10.1016/j.ijms.2008.04.032, 2008.

Veres, P., Roberts, J. M., Burling, I. R., Warneke, C., de Gouw, J., and Yokelson, R. J.: Measurements of gas-phase inorganic and organic acids from biomass fires by negative-ion proton-transfer chemical-ionization mass spectrometry, J. Geophys. Res.-Atmos., 115, doi:10.1029/2010JD014033, 2010.

Veres, P. R., Roberts, J. M., Cochran, A. K., Gilman, J. B., Kuster, W. C., Holloway, J. S., Graus, M., Flynn, J., Lefer, B., Warneke, C., and de Gouw, J.: Evidence of rapid production of organic acids in an urban air mass, Geophys. Res. Lett., 38, doi:10.1029/2011gl048420, 2011.

Vicente, A., Antunes, R., Almeida, D., Franco, I. J., Hoffmann, S. V., Mason, N. J., Eden, S., Duflot, D., Canneaux, S., Delwiche, J., Hubin-Franskin, M. J., and Limao-Vieira, P.: Photoabsorption measurements and theoretical calculations of the electronic state spectroscopy of propionic, butyric, and valeric acids, Phys. Chem. Chem. Phys., 11, 5729-5741, doi: 10.1039/B823500G, 2009.

Vogel, A., Äijälä, M., Brüggemann, M., Ehn, M., Junninen, H., Petäjä, T., Worsnop, D., Kulmala, M., Williams, J., and Hoffmann, T.: Online atmospheric pressure chemical ionization ion trap mass spectrometry (APCI-IT-MS n) for measuring organic acids in concentrated bulk aerosol–a laboratory and field study, Atmos. Meas. Tech., 6, 431-443, doi:10.5194/amt-6-431-2013, 2013.

Wight, C. A., and Beauchamp, J. L.: Acidity, Basicity, and Ion-Molecule Reactions of Isocyanic Acid in the Gas-Phase by Ion-Cyclotron Resonance Spectroscopy, J. Phys. Chem., 84, 2503-2506, doi:10.1021/j100457a004, 1980.

Wild, R. J., Dube, W. P., Aikin, K. C., Eilerman, S. J., Neuman, J. A., Peischl, J., Ryerson, T. B., and Brown, S. S.: On-road measurements of vehicle NO2/NOx emission ratios in Denver, Colorado, USA, Atmos. Environ., 148, 182-189, doi:10.1016/j.atmosenv.2016.10.039, 2017.

Wolff, S., Turner, W. V., Gäb, S., Mönninghoff, S., Ruppert, L., and Brockmann, K.: Laboratory Studies of the Formation of Hydroperoxides in Ozonolysis of Anthropogenic and Biogenic Alkenes, in: Chemical Processes in Atmospheric Oxidation, Springer, 106-112, 1997.

Yatavelli, R. L. N., Stark, H., Thompson, S. L., Kimmel, J. R., Cubison, M. J., Day, D. A., Campuzano-Jost, P., Palm, B. B., Hodzic, A., and Thornton, J. A.: Semicontinuous measurements of gas–particle partitioning of organic acids in a ponderosa pine forest using a MOVI-HRToF-CIMS, Atmos. Chem. Phys., 14, 1527-1546, doi:10.5194/acp-14-1527-2014, 2014.

Yatavelli, R. L. N., Mohr, C., Stark, H., Day, D. A., Thompson, S. L., Lopez-Hilfiker, F. D., Campuzano-Jost, P., Palm, B. B., Vogel, A. L., Hoffmann, T., Heikkinen, L., Aijala, M., Ng, N. L., Kimmel, J. R., Canagaratna, M. R., Ehn, M., Junninen, H., Cubison, M. J., Petaja, T., Kulmala, M., Jayne, J. T., Worsnop, D. R., and Jimenez, J. L.: Estimating the contribution of organic acids to northern hemispheric continental organic aerosol, Geophys. Res. Lett., 42, 6084-6090, doi:10.1002/2015gl064650, 2015.

Young, P. J., Emmons, L. K., Roberts, J. M., Lamarque, J. F., Wiedinmyer, C., Veres, P., and VandenBoer, T. C.: Isocyanic acid in a global chemistry transport model: Tropospheric distribution, budget, and identification of regions with potential health impacts, J. Geophys. Res.-Atmos., 117, D10308, doi:10.1029/2011jd017393, 2012.

Yuan, B., Veres, P. R., Warneke, C., Roberts, J. M., Gilman, J. B., Koss, A., Edwards, P. M., Graus, M., Kuster, W. C., Li, S. M., Wild, R. J., Brown, S. S., Dube, W. P., Lerner, B. M., Williams, E. J., Johnson, J. E., Quinn, P. K., Bates, T. S., Lefer, B., Hayes, P. L., Jimenez, J. L., Weber, R. J., Zamora, R., Ervens, B., Millet, D. B., Rappengluck, B., and de Gouw, J. A.: Investigation of secondary formation of formic acid: urban environment vs. oil and gas producing region, Atmos. Chem. Phys., 15, 1975-1993, doi:10.5194/acp-15-1975-2015, 2015.

Zaragoza, J., Callahan, S., McDuffie, E. E., Kirkland, J., Brophy, P., Durrett, L., Farmer, D. K., Zhou, Y., Sive, B., and Flocke, F.: Observations of Acyl Peroxy Nitrates During the Front Range Air Pollution and Photochemistry Éxperiment (FRAPPÉ), J. Geophys. Res.-Atmos., 122, doi:10.1002/2017JD027337, 2017.

CHAPTER 6 – CONCLUSIONS

The work comprising the majority of this dissertation (Chapters 2 – 4) demonstrated the efficacy of time-of-flight chemical ionization mass spectrometry (TOF-CIMS) as a fast, online, field-deployable instrumental method for probing the atmospheric chemistry of the indoor atmosphere. Combining iodide TOF-CIMS measurements with a variety of other online atmospheric measurement techniques performed during the House Observations of Microbial and Environmental Chemistry (HOMEChem) field campaign allowed us to develop a more holistic understanding of the indoor atmospheric chemistry taking place during cooking, cleaning, and even during unoccupied house backgrounds.

Pairing these HOMEChem measurements with kinetic multiphase chemical modeling provided valuable insight toward the chemical mechanisms controlling the production of volatile inorganic chlorinated and nitrogenated compounds while cleaning with a commercial bleach solution indoors. We observed substantial multiphase chemical production of hypochlorous acid (HOCl), chlorine (Cl_2), and nitryl chloride ($ClNO_2$) during cleaning, which are typically observed in the outdoor atmosphere of urban and marine areas. Photolysis of indoor HOCl and Cl_2 during bleach cleaning may lead to substantial production of hydroxyl (OH) and chlorine radicals (Cl), thereby substantially increasing the oxidative capacity of the indoor environment toward volatile organic compounds (VOCs). We also observed substantial production of chloramine compounds (NH_2Cl, $NHCl_2$, NCl_3) via multiphase chemistry between HOCl and ammonia (NH_3) or other amines. Exposure to levels of HOCl and nitrogen trichloride (NCl_3) observed herein are likely detrimental to human health. Additionally, we discovered that dark (i.e. non-photochemical) multiphase chemistry during bleach cleaning produced several organic

pollutants indoors, including organic isocyanates (R-NCO), cyanogen chloride (ClCN), chlorocarbons (including chloroform; $CHCl_3$), and secondary organic aerosol (SOA). These observations collectively demonstrated bleach cleaning to be a source of indoor pollution, thereby affecting indoor air quality and occupant health.

Combining our iodide TOF-CIMS measurements with other HOMEChem measurements also enabled us to characterize reactive organic carbon (ROC) emissions indoors during cooking and cleaning, and allowed us to directly compare the resultant chemical complexity of indoor air to outdoors. We discovered that cooking indoors substantially alters indoor ROC concentrations and composition, particularly during a simulated Thanksgiving Day experiment, while cleaning yielded relatively insubstantial changes. Consistently higher indoor ROC concentrations compared to outdoors demonstrated that indoor emissions acted as a net source of ROC to the outdoor atmosphere, following its removal by ventilation. Reactive organic carbon (ROC) comprises a substantial fraction of carbon emitted to the atmosphere, wherein it fuels oxidation chemistry to produce secondary pollutants including ozone (O_3), carbon dioxide (CO_2), and particulate matter (PM). ROC dominated indoor and outdoor oxidant reactivity compared to other atmospheric carbon species, thereby greatly influencing secondary pollutant formation potential.

The penultimate chapter of this dissertation demonstrated the efficacy of acetate measurements in characterizing the tropospheric sources and sinks of various gas-phase acids in the Colorado Front Range. We found that photochemical production sources influenced mixing ratios and diel profiles of nitric (HNO_3), isocyanic (HNCO), formic (CH_2O_2), propionic ($C_3H_6O_2$), butyric ($C_4H_8O_2$), valeric ($C_5H_{10}O_2$), and pyruvic acid ($C_3H_4O_3$). Vertical profile measurements of these acids revealed persistent surface-level emissions of alkanoic acids, and

net surface deposition of nitric and pyruvic acid. Regional traffic and agricultural emissions also influenced tropospheric mixing ratios of these acids. We propose reactions between tropospheric O_3 and unsaturated surface organics as a 'missing' surface-level source of alkanoic acids. Additionally, combined diel and vertical profiles of alkanoic acids and isocyanic acid revealed additional missing loss mechanisms in addition to dry deposition and photochemical loss.

The fast, online measurements of atmospheric trace gases afforded by TOF-CIMS have greatly enriched our understanding of indoor and outdoor atmospheric chemistry. Our ability to detect and quantify a diversity of atmospheric constituents with TOF-CIMS stems from the continuous development and characterization of novel CIMS ionization schemes, calibration methods, and parameterizations of instrumental sensitivity for bulk chemical analysis. TOF-CIMS measurements hold promise for probing the unexplored indoor atmospheric chemistry of various other cooking methods, cleaning product emissions, and personal care product usage. Additionally, with the ever-increasing use of chemistry-based indoor air purification methods (i.e. cold-fogging, ozone generators, air ionization devices) in the era of COVID-19, TOF-CIMS measurements in field (i.e. test house) and laboratory (i.e. smog chamber) settings have potential for comprehensively characterizing the indoor oxidation chemistry, secondary pollutant production, and impacts on indoor air quality resulting from the use of these purification methods. As mentioned in Chapter 1, TOF-CIMS will also continue to be applicable toward untargeted (i.e. bulk) analyses of atmospheric ROC, volatile per- and polyfluoroalkyl substances (PFAS), and other chemically complex trace gases in the atmosphere.

APPENDIX 1 – CHAPTER 2 SUPPLEMENTAL INFORMATION (A1)

A1.1 Chapter 2 supplemental information (SI) text

A1.1.1 Detailed kinetic model description including assumptions and simplifications

The building interior has a volume of 250 m^3 and the bleached surface area was 40 m^2. In the model, we assume that the bleach thickness was 0.01 cm. We did not treat changes in the bleach thickness over time as the thickness was unmeasured and the rate of evaporation was unknown. Bleach contains ~6% NaOCl by mass. The bleach had been diluted by a factor of 32 before being applied to the floor. The model considers an initial concentration of aqueous OCl^- of 1.5×10^{19} molecules cm^{-3}. The pH of the bleach was varied in the model until the gas-phase HOCl and Cl_2O data were well fit. This approach resulted in a pH range of 9.2 – 9.6. These values are reasonable considering the bleach pH of ~12.6 and a dilution factor of 32 with possible further acidification by other molecules present on the floor. The pH was assumed to remain constant over time as changes were unmeasured. During the experiments, the bleach was applied throughout a period of 10 minutes. However, in the model, applying the bleach over this extended time period was challenging, and the best model-measurement agreement was obtained when the reactions were switched on ~2.5 minutes after bleach cleaning had started. After a set time (0.31 – 0.56 hours; determined by observations in measurement data), we assumed that the bleach had fully evaporated away and sorption and desorption from the bleach mixture in the model was switched off. Anything remaining in the bleach was then assumed to act as a residue on the floor.

Mass-transport across the boundary layer provides kinetic limitations for uptake into the bleach and was assumed to be influenced by eddy diffusion such that the gas-phase diffusion coefficient ($D_{h,Z}$) at a height, h, above a surface could be calculated as:

$$D_{h,Z} = D_{g,Z} + K_e \times h^2$$

where $D_{g,Z}$ is the gas-phase diffusion coefficient under non-turbulent conditions and K_e is the turbulence intensity. The values of $D_{g,Z}$ are listed in Table A1.3 while the values of K_e are listed in Table A1.4. Air exchange rates are also listed in Table A1.4 and were constrained by measurements described in Section A1.1.2.

We include photolysis rates (j) derived from solar irradiance measurements performed indoors during HOMEChem (section A1.1.2; Figure A1.7). These solar irradiance measurements were performed directly adjacent to windows in the house; resultant photolysis rates likely do not account for the spatial variability due to the inhomogeneous transmission of outdoor light to indoors. We therefore treat these measured photolysis rates as upper-limits, and accordingly tune these values in our model to match measurement observations. Sensitivity tests revealed that the photolysis rate of $ClNO_2$, NO_3 and HONO were insensitive up to the maximum photolysis rate while the photolysis rate of Cl_2 and HOCl had to be at least a factor of 10 and 5 lower than the maximum value, respectively, in order to reproduce respective measurement data. The model results were still slightly sensitive to the NO_2 photolysis rate when the maximum value was decreased by a factor of 50. Modeled O_3 mixing ratios were very sensitive to indoor photolysis processes (e.g. reactions 8, 33, 35, and 41 in Table A1.2). The slight enhancements in measured indoor O_3 (measurement details in Farmer et al. (2019)) are reproducible across bleach cleaning experiments, even during the evening in the absence of transmission of outdoor sunlight (20:35 on 10 June 2018; Figure A1.8). We therefore suspect these enhancements were not driven by

photochemistry. NO reacts with ClO to produce NO_2 and Cl (Zahniser and Kaufman, 1977; Xue et al., 2015). However, we observe consistent decays in NO mixing ratios across bleach cleaning experiments, even in the absence of transmission of outdoor sunlight (20:35 on 10 June 2018; Figure A1.3 and A1.8). We therefore do not consider NO loss to be driven by photochemistry (i.e. loss via ClO is unlikely). We determined that measurement observations herein are best reproduced by decreasing upper-limit photolysis rates by a factor of 50. Photolysis rates used in the model are reported in Table A1.4.

Other unknown or uncertain parameters including some rate coefficients, losses to surfaces and uptake coefficients (see Table A1.4) were varied systematically and iteratively until the measurements could be reproduced. A surface mass accommodation of 1 and a desorption lifetime of 1 ns was assumed for all (semi)volatile species.

A1.1.2 Additional HOMEChem measurement details

A1.1.2.1 Air exchange rate

We determine the air exchange rate (AER) of the test house via the monitoring of a continuously emitted inert tracer gas (butane-d3, Cambridge Isotope Laboratories) with a PTR-TOF-MS. This method is detailed in Liu et al. (2018). AER values calculated during bleach cleaning experiments are in Table A1.4.

A1.1.2.2 PTR-TOF-MS sensitivity estimation

We estimate PTR-TOF-MS sensitivity toward NH_2Cl and $NHCl_2$ following Zhao and Zhang (2004), and assuming a proton-transfer reaction rate of a typical VOC ($k = 2.5 \times 10^{-9}$ cm^3 s^{-1}). Typically, PTR-TOF-MS sensitivity errors for uncalibrated VOCs are around ± 50%. Given our limited information in constraining PTR-TOF-MS sensitivity toward NH_2Cl and $NHCl_2$, these errors could be larger. PTR-TOF-CIMS sensitivities can depend on humidity, and

calibrations were conducted at 0% RH. Fluctuations in sensitivity due to indoor RH should be negligible during this study given the low variability in the humidity of indoor air during the experiments (typically ± 2% RH).

A1.1.2.3 Particulate matter surface area

We determine particulate matter (PM) surface area with an Ultra High Sensitivity Aerosol Spectrometer (UHSAS; Droplet Measurement Technologies, Inc.) (Figure A1.1). The UHSAS sampled PM between 60 - 1000 nm through a copper sampling line (8 m length; 0.635 cm ID; 0.9525 cm OD), attached to a valve-switching system which included a HEPA bypass and a Nafion dryer. Additional details of these measurements at HOMEChem are found in Farmer et al.[1] We acknowledge that this submicron aerosol surface area is an underestimate of the total PM surface area during cooking events.

A1.1.2.4 Indoor photolysis rates

Wavelength-resolved spectra of sunlight entering the house were measured using an Ocean Optics USB4000 spectrometer attached with a 1 m fiber optic cable (Thorlabs) and a Spectralon cosine receptor. Photon fluxes (F) were estimated as being equal to the measured irradiance. This estimation is likely accurate under sunny conditions at low solar zenith angles (i.e. when sunlight entering the house is largely collimated and unidirectional), as discussed in (Kowal et al., 2017). Irradiance likely underestimates photon flux when sunlight is highly diffuse, such as on cloudy days. The average photon fluxes reported near the windows (shown in Figure 2.4 in the manuscript) are therefore likely underestimated by up to 25%. Photolysis rate constants (J) of HOCl, Cl_2, $ClNO_2$, NO_2, NO_3, and HONO were calculated (Figure A1.7; Table A1.2) as described previously using the measured photon fluxes (F) and reported absorption cross sections (σ) and photolysis quantum yields (ϕ) (Kowal et al., 2017):

$$J = \int_{\lambda_i}^{\lambda_j} \sigma(\lambda)\phi(\lambda)F(\lambda)d\lambda$$

Continuous measurements were made directly adjacent to windows at 1-minute resolution. As a result, these rate constants represent local values. Indoor solar photon flux has been shown to decrease linearly with distance from windows and displayed high spatial heterogeneity (Farmer et al., 2019; Kowal et al., 2017). We therefore treat these local photolysis rates as upper bounds. We note that the main function of these measurements was to characterize the indoor diel profile, rather than the absolute magnitudes, of photolysis rates, in that the magnitudes of these rates were tuned in our kinetic model to match indoor observations (see section A1.1.1). Additional details of these measurements during HOMEChem are found in Farmer et al. (2019). Kowal et al. (2017) demonstrated that UV photon fluxes from indoor lighting fixtures decay very rapidly with distance. We therefore expect negligible photolysis due to indoor lighting during HOMEChem.

A1.1.2.5 Additional AMS measurement details

Cooking organic aerosol is largely comprised of molecules with lower oxidation states (e.g. oleic acid and other unsaturated fatty acids) (Abdullahi et al., 2013). Xu et al. (2018) reported an AMS relative ionization efficiency (RIE) of 2-7 for cooking organic aerosol. Organic PM mass concentration data reported in Figure A1.5 use RIE = 1.4, a value typical for ambient organic aerosols (Xu et al., 2018). As a result, these organic PM mass concentrations during cooking events (e.g. Figure A1.5a-d) are likely overestimated. We use an RIE of 1.3 for AMS measurements of non-refractory particulate Cl^- during all experiments herein.

A1.1.3 I^- TOF-CIMS operation and data processing

Ultra-high purity (UHP) N_2 (Airgas) flowed (~0.7 L min^{-1}) through a heated oven (50 °C) containing methyl iodide (CH_3I) permeation tubes (VICI, Dynacalibrator). The resulting CH_3I-

saturated N_2 stream passed through a ^{210}Po ionizer to generate I^- reagent ions, which then entered the ion-molecule reactor (IMR) region of the instrument. Here, analytes sampled from ambient air (M) form charged iodide-analyte adducts ($[I+M]^-$) via clustering reactions with I^-, or ligand switching reactions with IH_2O^- (Aljawhary et al., 2013; Lopez-Hilfiker et al., 2016); followed by transmission via ion optics to the TOF region of the instrument for detection. We controlled mass spectral data acquisition with TofDaq Recorder (Tofwerk AG; extraction frequency = 26 kHz; m/z range = 1.63 – 456.80).

We processed I^- TOF-CIMS data in Igor Pro (WaveMetrics Inc., version 6) with Tofware (Tofwerk AG, Aerodyne Research Inc., version 2.5.10), which calculated mass spectral baseline, fitted peak shape, and mass resolution. Tofware uses the integrated area of fitted peak functions to mass spectral data to calculate signal time series of mass spectral peaks. The peak fitting algorithm featured in Tofware automatically calculates relative isotopic contributions of fitted peak functions based on the elemental assignment of a mass spectral peak. From this, we are able to confirm the elemental compositions of peaks in our TOF-CIMS spectra, including the chlorinated and nitrogenated compounds discussed herein. Mass calibration took place post-acquisition using a three-parameter fit to the NO_2^-, I^-, IH_2O^-, $ICH_2O_2^-$, $IC_3H_6O_3^-$, and I_3^- peaks. These peaks had consistently high resolution and contained no interferences nor overlapping peaks throughout the campaign. TOF-CIMS mass accuracy was 4 ppm (campaign average of mass calibrant ions), and resolution ($m/\Delta m$) was > 4000. Tofware's high-resolution peak fitting algorithm extracted time series of mass spectral signal (Hz) for detected analytes. We performed additional data analysis, including background subtraction, normalization, and mixing ratio calculation/estimation in Igor Pro. We normalized measured analyte data to the total reagent ion signal following Bertram et al. (2011), by multiplying mass spectral signal by the ratio of the

average total reagent ion signal during an hourly background measurement to the total reagent ion signal during periods of analyte measurement. Here, we calculated total reagent ion signal as the sum of I^- and IH_2O^- signal. This normalization method ensured that any changes in analyte signal were not due to variations in total reagent ion signal. We calculated I^- TOF-CIMS instrumental detection limits for various bleach-related compounds measured at HOMEChem following Bertram et al. (2011), and provide them in Table A1.5.

A1.1.4 Shared TOF-CIMS sampling inlet setup and on-site alkanoic acid calibrations at HOMEChem

Our I^- TOF-CIMS, and an acetate (Ac^-) TOF-CIMS shared a sampling inlet and calibration system, outlined in Figure A1.9. We deployed both TOF-CIMS instruments in a temperature-controlled trailer directly adjacent to the UTest house. We sampled ambient air from inside the house through perfluoroalkoxy alkane (PFA) tubing (0.3175 cm ID) extending from the kitchen area of the UTest house to inside the trailer at ~4 L min^{-1}. We also sampled outdoor air through PFA tubing (0.3175 cm ID), extending from roughly 1 m above the trailer to inside the trailer at ~4 L min^{-1}. These indoor and outdoor sampling lines met at the three-way solenoid isolation valve (NResearch Inc.). Total indoor and outdoor sampling inlet lengths were 7 m and 5 m, respectively, for the I^- TOF-CIMS; and 10 m and 8 m, respectively, for the Ac^- TOF-CIMS.

Ambient sampling typically followed an automated hourly indoor/outdoor switching cycle (Figure A1.10). At the start of each hour, we performed two-minute instrumental background measurements by introducing an overflow of ultra-zero grade air (UZA, Airgas) to both TOF-CIMS using a mass-flow controller (MFC). Indoor/outdoor ambient sampling comprised the remainder of the hourly cycle. We neglect data collected within 60 seconds of a valve-switching event to avoid the influence of potential sampling line effects. Sampled air

entered the IMR of both TOF-CIMS at ~2 L min^{-1}. We performed inline measurements of ambient temperature and relative humidity (RH) using a digital sensor (Sensirion SHT21) controlled by an EyeOn control system (Aerodyne Research Inc.). We automated valves, MFCs, and mass spectral data acquisition using homebuilt programs (LabVIEW, National Instruments).

We generated gas-phase calibration standards of formic (CH_2O_2), acetic ($C_2H_4O_2$), propionic ($C_3H_6O_2$), butyric ($C_4H_8O_2$), and valeric acid ($C_5H_{10}O_2$) by flowing ultra-high purity (UHP) N_2 (Airgas) through a heated oven (40 °C) containing permeation tubes (VICI, Dynacal) of each compound. We determined temperature-dependent mass losses gravimetrically, enabling us to calculate measured mixing ratios of each standard. We performed single-point hourly standard addition calibrations on 12-16, 18, 25, and 27 June 2018 by introducing gas-phase calibrant into the ambient sampling stream and measuring the signal change due to a known stepwise change in mixing ratio (Figure A1.9). Standard additions took place at nights between the hours of 21:00 and 05:00, i.e. in the absence of interferences from indoor experiments. Using a sufficiently small calibrant flow during standard additions (~0.1 L min^{-1}; 2.5% of total sample flow) ensured that any analyte dilution from this flow was negligible. We also performed five-point external standard calibrations of these compounds on 9, 14, 23, and 28 June 2018 by diluting gas-phase calibrant in UZA (Airgas) using an MFC (MKS Instruments) (Figure A1.9). All tubing used downstream of our calibration source was 0.3175 cm ID PFA.

A1.1.5 I^- TOF-CIMS calibrations for Cl_2, HOCl, N_2O_5, and $ClNO_2$

We performed in-laboratory I^- TOF-CIMS calibrations for Cl_2, HOCl, N_2O_5, and $ClNO_2$ shortly after the conclusion of the HOMEChem campaign. We detect all calibrant compounds as iodide-analyte adducts. We minimize lengths of Teflon tubing (PFA; 0.3175 cm ID) used in all calibration setups to mitigate any inlet-effects.

A1.1.5.1 Cl_2 and HOCl calibrations

We conducted five-point external standard calibrations for Cl_2 using a gas-phase standard (Airgas; 2 ppm Cl_2 in UHP N_2; 99.5% purity). We calibrated the instrument for HOCl based on the methodology of Foster et al. (1999) and Lawler et al. (2011). Here, we flowed UHP N_2 (Airgas; ~100 sccm) over the headspace of a ~0.3 M NaOCl solution (RICCA; commercial grade), generating a steady flow of a gaseous mixture containing HOCl and Cl_2. This initial headspace flow entered the instrument inlet to measure HOCl and Cl_2 I^- TOF-CIMS response. We then redirected the headspace flow into a glass tube (2.5 cm OD) containing an aqueous slurry of NaCl (EMD Millipore; GR ACS) and HCl (EMD Millipore; GR ACS), converting HOCl to Cl_2 (Foster et al., 1999). We held the glass tube containing this slurry in an ice bath to inhibit volatilization of HCl. We determined I^- TOF-CIMS sensitivity to HOCl from the measured increase in Cl_2 signal, and associated decrease in HOCl signal following this conversion. We calculated Cl_2 and HOCl I^- TOF-CIMS sensitivities of 4. ± 1. Hz $pptv^{-1}$ and 0.4 ± 0.2 Hz $pptv^{-1}$, respectively.

A1.1.5.2 N_2O_5 calibration

We flowed ~10 sccm UZA (Airgas) through a Hg lamp (UVP) to generate ozone (O_3), which reacted with ~15 sccm nitrogen dioxide (NO_2; Praxair, Inc.) gas to produce NO_3, which further reacted with NO_2 to generate a flow of gaseous N_2O_5. We determined mixing ratios of N_2O_5 produced via this process using a custom-built cavity ring-down spectroscopy (CRDS) instrument (Dubé et al., 2006; Fuchs et al., 2008; Wagner et al., 2011). We directed the N_2O_5 standard to the I^- TOF-CIMS sampling inlet to determine instrumental sensitivity to $IN_2O_5^-$ and 'total N_2O_5' (taken as $IN_2O_5^-$ + NO_3^-; Lopez-Hilfiker et al. (2016)) via five-point external standard calibrations. We calculated a total N_2O_5 I^- TOF-CIMS sensitivity of 50. ± 10. Hz $pptv^{-1}$.

A1.1.5.3 $ClNO_2$ calibration

We determined instrumental response to $ClNO_2$ via five-point external standard calibrations. Here, we flowed ~25 sccm gaseous N_2O_5 into a glass tube (2.5 cm OD) containing an aqueous NaCl (EMD Millipore; GR ACS) slurry, thereby converting N_2O_5 to $ClNO_2$ (Leu et al., 1995; Finlayson-Pitts, 2003). We determined <10% N_2O_5 formed HNO_3 as a side-product, based on our I^- TOF-CIMS sensitivity to HNO_3 determined via external standard calibration utilizing an HNO_3 permeation tube standard (KIN-TEK Analytical, Inc.). We calculated a $ClNO_2$ I^- TOF-CIMS sensitivity of 6. ± 3. Hz $pptv^{-1}$.

A1.1.5.4 Accounting for dependence of I^- TOF-CIMS sensitivities on ambient humidity

Water vapor present in the IMR region of the TOF-CIMS affects I^- TOF-CIMS sensitivities for several compounds. Ambient humidity was therefore as a potential matrix effect during our HOMEChem measurements. We accounted for this by performing our post-campaign calibrations (and associated instrumental background measurements) of Cl_2, HOCl, N_2O_5, and $ClNO_2$ with a dilution flow of humidified ultra zero grade air (UZA; Airgas). We flowed UZA through a glass bubbler containing LC-MS grade H_2O (EMD Millipore), generating a UZA flow saturated with H_2O. We controlled the final relative humidity (RH) of this flow by mixing a second flow of UZA downstream of the bubbler, and measured its final RH using an in-line RH sensor (OMEGA Engineering, Inc; HX71-V1). Mass-flow controllers (MFCs; MKS) modulated UZA flow rates. We maintained a setpoint RH during calibrations with a proportional-integral-derivative (PID) loop using homebuilt software (LabVIEW; National Instruments) interfaced with the MFCs and RH sensor. The UZA dilution flows used for these calibrations/backgrounds were humidified such that the partial pressure of water vapor in the IMR ($P_{H2O,IMR}$) was

comparable to that during ambient sampling at HOMEChem ($P_{H2O,IMR} \approx 1.4$ mbar, corresponding to ~55% RH measured in-line during HOMEChem).

Figure A1.11 shows how in-laboratory external standard calibrations of C_1-C_5 alkanoic acids using a dilution flow of humidified UZA effectively reproduce the RH matrix effects observed during standard addition calibrations performed at HOMEChem (described in section A1.1.4), further displaying the efficacy of this approach. Trends in I^- TOF-CIMS C_1-C_3 alkanoic acid sensitivities as a function of RH are consistent with previous work (Lee et al., 2014).

We assess the RH-dependent sensitivity of N_2O_5 and $ClNO_2$ further by performing external standard calibrations under various humidity conditions. We observe a similar trend in humidity-dependent N_2O_5 I^- TOF-CIMS sensitivity to that observed by Kercher et al. (2009). As humidity in the IMR increases, $IN_2O_5^-$ sensitivity increases and NO_3^- sensitivity decreases, while the total N_2O_5 sensitivity remains fairly constant (albeit decreases slightly with increasing humidity); indicating that the mass-dependent transmission efficiency of these compounds through the instrument is also fairly constant (Figure A1.12). $ClNO_2$ sensitivity does not vary significantly under the HOMEChem conditions as $P_{H2O,IMR} > 0.6$ mbar (~30% RH measured in-line during HOMEChem) (Figure A1.13). This trend in RH-dependent I^- TOF-CIMS $ClNO_2$ sensitivity agrees with that observed by Kercher et al. (2009)

We did not further assess RH-dependent I^- TOF-CIMS sensitivity for Cl_2 because the RH-dependent Cl_2 sensitivities reported by Lee et al. (2014) were relatively invariable as $P_{H2O,IMR} > 0.4$ mbar. We anticipate a similar result as trends in RH-dependent I^- TOF-CIMS sensitivity are fairly consistent across instruments (irrespective of the absolute magnitude of these trends). We do not further characterize the RH-dependent I^- TOF-CIMS sensitivity of HOCl. Some variability in calculated HOCl mixing ratios may thus be caused by variations in

ambient RH during HOMEChem. However, indoor RH typically varied ±2% during the experiments, and we expect a subsequently negligible fluctuation in I^- TOF-CIMS sensitivity to HOCl.

Our instrumental background measurements at HOMEChem were performed with dry (RH = 0%) UZA, and therefore may not be a true representation of analyte background signals measured in sampled indoor air (RH ≈ 55%, corresponding to $P_{H2O,IMR} \approx 1.4$ mbar in Austin, TX). To address this, we performed post-campaign measurements of I^- TOF-CIMS background signals for HOCl, Cl_2, Cl_2O, $ClNO_2$, $NHCl_2$, and NCl_3 (detected as $[I+M]^-$ adducts) while sampling UZA of variable RH. The RH of UZA (RH_{UZA}) during these experiments ranged from 0 – 70% (corresponding to $P_{H2O,IMR} = 0 – 1.4$ mbar in Fort Collins, CO). Instrumental background signals for all compounds tested were higher by a factor of 3 – 8 when $RH_{UZA} = 70\%$ compared to $RH_{UZA} = 0\%$. However, measured background signals for these compounds at HOMEChem were typically on the order of $10^0 – 10^1$ Hz, while respective measured signals reached orders of $10^4 – 10^5$ Hz during bleach cleaning. We therefore conclude that the lack of humidity in the I^- TOF-CIMS background measurements of these compounds performed during HOMEChem does not significantly impact their respective background-subtracted I^- TOF-CIMS signals (and subsequently mixing ratios) measured during bleach cleaning.

A1.1.6 Voltage scanning for I^- TOF-CIMS sensitivity estimation

Transmission of iodide-analyte adducts though the TOF-CIMS is controllable by systematically increasing (or 'scanning') the voltage gradient (dV), and therefore electric field strength, between any adjacent pair of ion optics components in the ion transmission region of the instrument (Lopez-Hilfiker et al., 2016; Brophy and Farmer, 2016). Increasing electric field strength leads to enhanced collisionally-induced dissociation of these adducts, and a decrease in

their overall transmission. Cluster transmission decreases in a sigmoidal fashion with increasing dV (Lopez-Hilfiker et al., 2016; Brophy and Farmer, 2016). An important empirical parameter related to I^- TOF-CIMS sensitivity, dV_{50}, is calculated as the half-maximum of a sigmoidal fit to these data (Lopez-Hilfiker et al., 2016; Brophy and Farmer, 2016). dV_{50} is a proxy for I^- adduct binding enthalpy (Lopez-Hilfiker et al., 2016); the strength of these adducts dictate their transmission through the instrument, thereby directly influencing TOF-CIMS sensitivity to these adducts (Lopez-Hilfiker et al., 2016; Iyer et al., 2016).

In this study, we scanned the 'SSQ back - lens skimmer' component relation. Details of this component relation, and how we perform these voltage scanning experiments are found in Brophy and Farmer (2016). We plot the logarithm of I^- TOF-CIMS sensitivities for a variety of calibrant compounds (C_1-C_5 alkanoic acids, HNO_3, N_2O_5) against their respective dV_{50} values (Figure A1.14). We determined calibrant sensitivities via in-laboratory external standard calibrations performed shortly after HOMEChem (detailed in section A1.1.5). We also performed voltage scanning experiments during these calibration periods to determine calibrant dV_{50} values. We performed these experiments under variable $P_{H2O,IMR}$ settings (see section A1.1.5) to assess how ambient humidity affects the dV_{50}-sensitivity relationship (Figure A1.14). Here, we observe a linear (r^2 = 0.92-0.98) relationship between log(sensitivity) and dV_{50}, with linearity typically increasing as humidity increases. Further, the spread between linear fits in log(sensitivity) space decreases above 0.6 mbar, suggesting that variability in estimated sensitivity attributable to $P_{H2O,IMR}$ decreases with increasing water vapor present. Additionally, we performed voltage scanning during various periods throughout HOMEChem to determine dV_{50} values of gas-phase compounds present in ambient air (i.e during bleach cleaning).

We used this relationship as a model for sensitivity (and therefore mixing ratio) estimation by inputting dV_{50} values of compounds detected in ambient air during HOMEChem into the linear regressions used in Figure A1.14. We choose the dV_{50}-sensitivity relationship at $P_{H2O,IMR}$ = 1.5 mbar to estimate Cl_2O, $NHCl_2$, and NCl_3 sensitivities during HOMEChem, as these humidity settings most closely match those observed during bleach cleaning activities. We considered N_2O_5 a 'maximally' sensitive compound, in that it forms strongly bound adducts with I^- at the collision limit (see section A1.1.5) (Lopez-Hilfiker et al., 2016; Huey et al., 1995). Therefore, any compound with a $dV_{50} \geq$ that of total N_2O_5 ($IN_2O_5^- + NO_3^-$) (dV_{50} = 29.5 ± 0.5 V) was assigned the same sensitivity as total N_2O_5 (i.e. the 'collision-limit' sensitivity). Cl_2O and NCl_3 had higher dV_{50} values than N_2O_5 during HOMEChem (36. ± 2. V and 37.1 ± 0.3 V, respectively), and were therefore assigned the collision-limit sensitivity. $NHCl_2$ had a dV_{50} of 25.9 ± 0.8 V, and was assigned an estimated sensitivity of 10 ± 10 Hz $pptv^{-1}$. The large magnitude of error in estimated $NHCl_2$ sensitivity is associated with uncertainty in the dV_{50}-sensitivity relationship model.

The calibrant compounds used in the generation of this sensitivity estimation model are representative of those whose I^- adducts do not undergo substantial dissociation or fragmentation upon transmission through the TOF-CIMS. We note the abundance of ICl^- in our I^- TOF-CIMS spectra during bleach cleaning events at HOMEChem—likely a fragmentation product of labile chlorine-containing molecules initially bound to I^-. This observation is consistent with Wong et al. (2017), who observed similar fragmentation in their I^- TOF-CIMS spectra during their indoor bleach cleaning measurements. We hypothesize that I^- adducts of many chlorine-containing molecules undergo fragmentation during their transmission through the TOF-CIMS, resulting in overestimated sensitivities (and therefore underestimated mixing ratios) from this model. Our

model overestimates HOCl and $ClNO_2$ sensitivities by 1 and 3 orders of magnitude, respectively, which could be driven by adduct fragmentation. Reported Cl_2O, $NHCl_2$ and NCl_3 mixing ratios could therefore also be further underestimated from this fragmentation.

A1.2 Chapter 2 SI figures

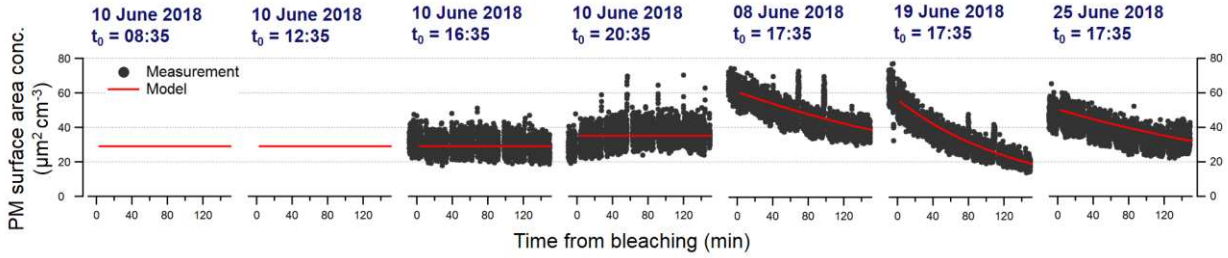

Figure A1.1. Measured indoor particulate matter (PM) surface area concentrations during various bleach cleaning experiments performed at HOMEChem (black markers). Red traces represent corresponding kinetic modeling results. t_0 indicates local times at which bleach mopping experiments began.

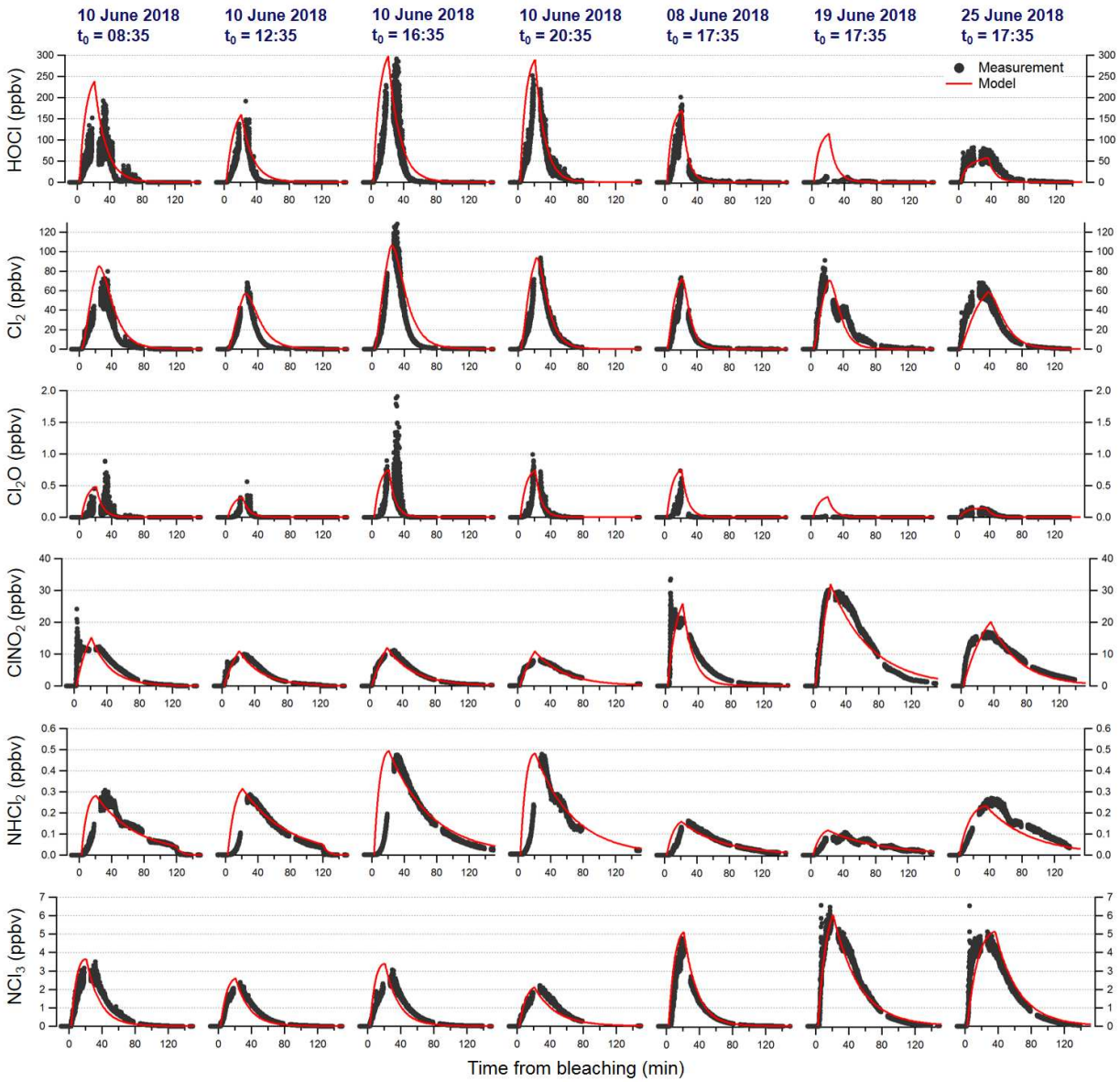

Figure A1.2. Measured indoor mixing ratios for HOCl, Cl_2, Cl_2O, $ClNO_2$, $NHCl_2$, and NCl_3 during various bleach cleaning experiments performed at HOMEChem (black markers). Red traces represent corresponding kinetic modeling results. t_0 indicates local times at which bleach mopping experiments began.

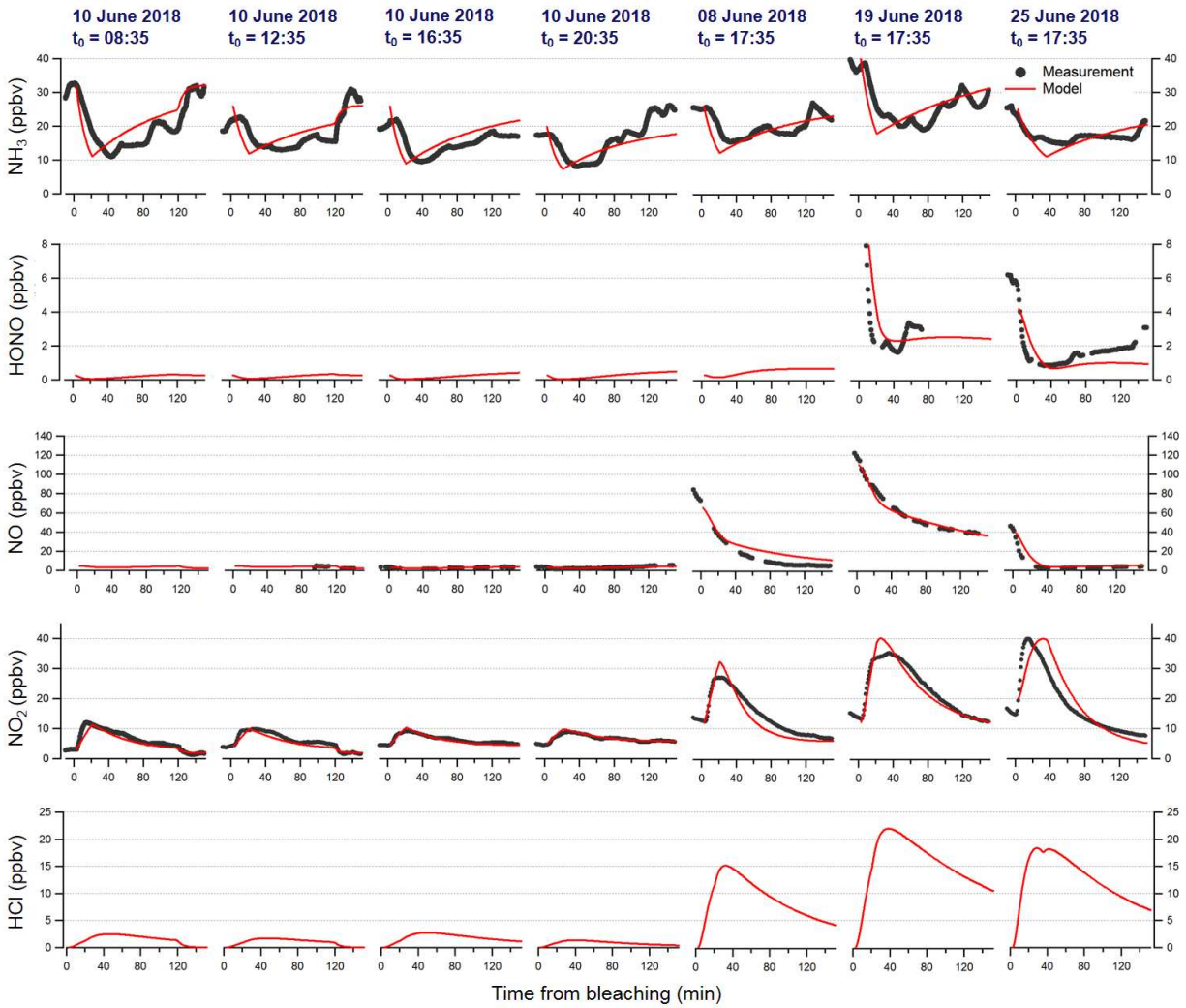

Figure A1.3. Measured indoor mixing ratios for NH_3, HONO, NO, and NO_2 during various bleach cleaning experiments performed at HOMEChem (black markers). Red traces represent kinetic modeling results for measured species, as well as predicted HCl mixing ratios. t_0 indicates local times at which bleach mopping experiments began.

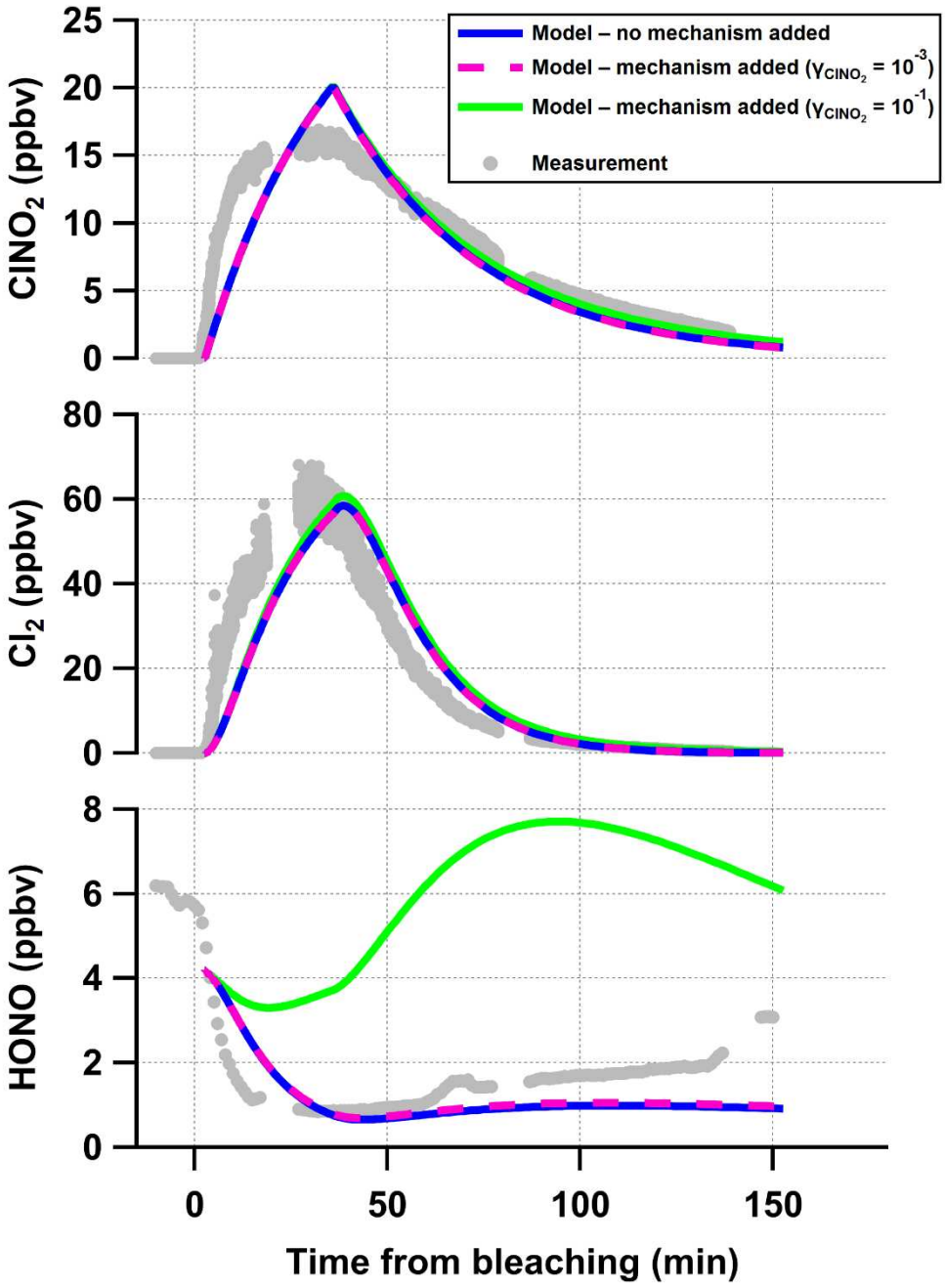

Figure A1.4. Kinetic model sensitivity test comparing indoor $ClNO_2$, Cl_2, and HONO mixing ratios during the inclusion of a heterogeneous $ClNO_2$ loss mechanism ($ClNO_2 + H^+ + Cl^- \rightarrow Cl_2 +$ HONO) during a bleach cleaning experiment on 25 June 2018 at HOMEChem. Solid blue trace represents model results excluding this mechanism. Dashed pink and solid green traces represents model results including this mechanism using uptake coefficients (γ_{ClNO2}) of 10^{-3} and 10^{-1}, respectively. Grey markers represent HOMEChem measurement data. Bleach cleaning was performed at 17:35 local time, and lasted approximately 10 minutes.

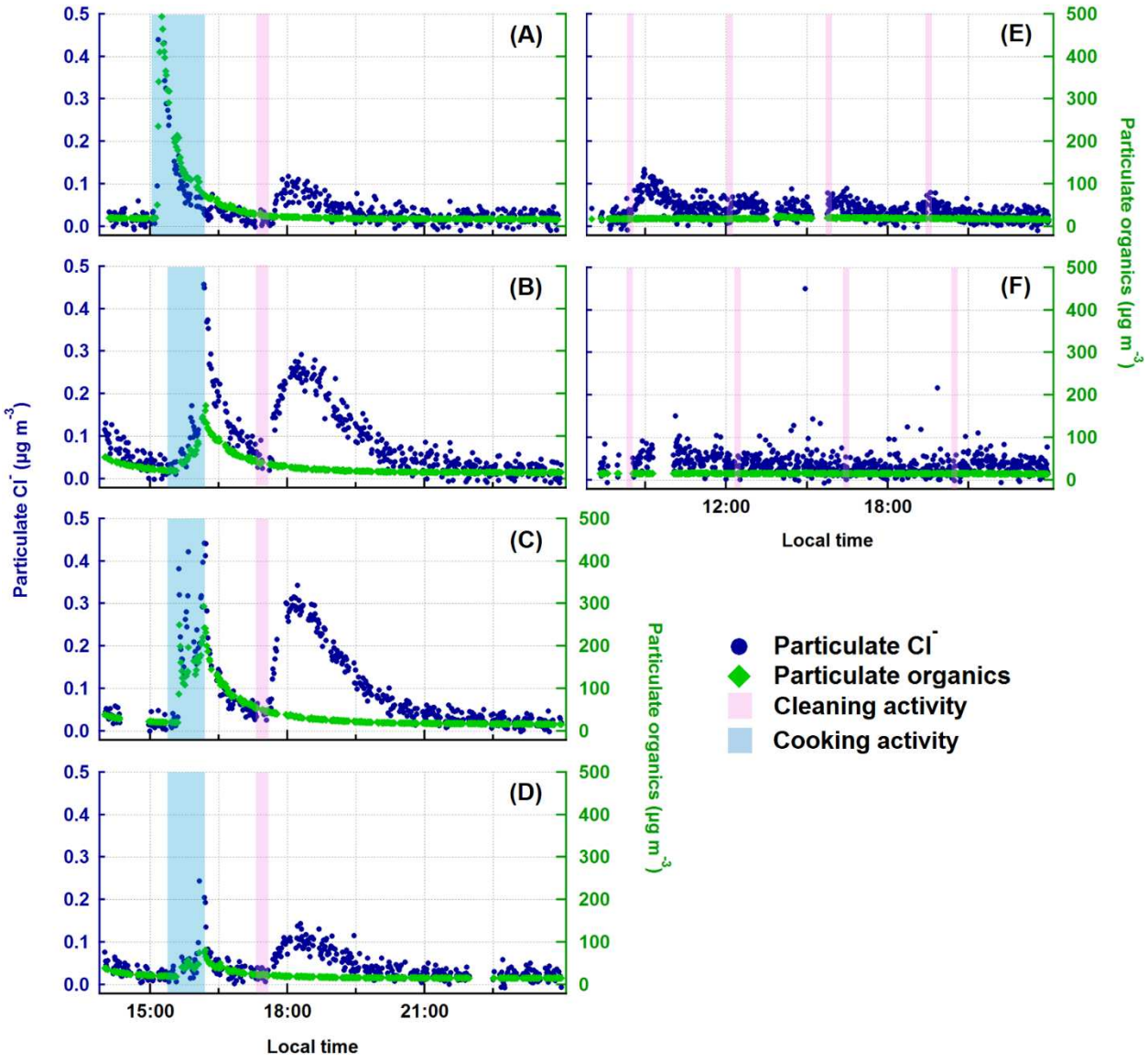

Figure A1.5. Indoor particulate Cl^- (blue markers) and organic (green markers) mass concentrations during layered experiments on (A) 08, (B) 19, (C) 21, and (D) 25 June 2018; and sequential experiments on (E) 07 and (F) 10 June 2018. Shaded pink and blue regions correspond to local time during which bleach cleaning and cooking events took place, respectively. We use particulate organic mass concentration here as a proxy for total indoor PM mass concentration.

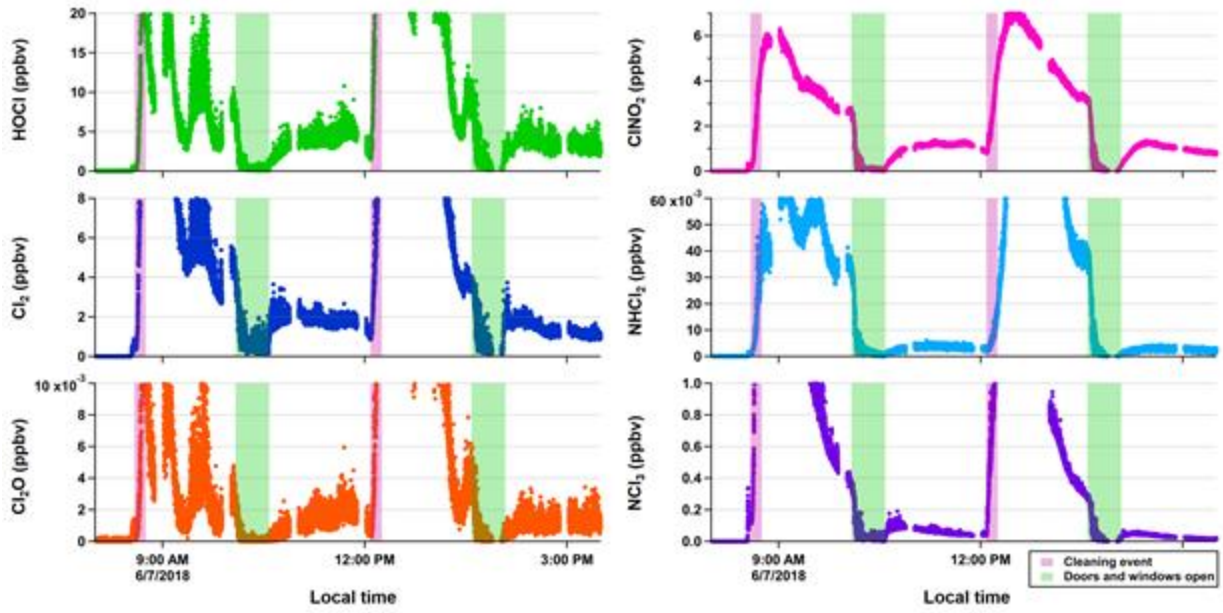

Figure A1.6. Indoor mixing ratio time series data (colored markers) for HOCl, Cl_2, Cl_2O, $ClNO_2$, $NHCl_2$, and NCl_3 during a bleach cleaning experiment on 07 June 2018. Shaded pink and green regions correspond to local time during which bleach cleaning and door/window opening took place, respectively.

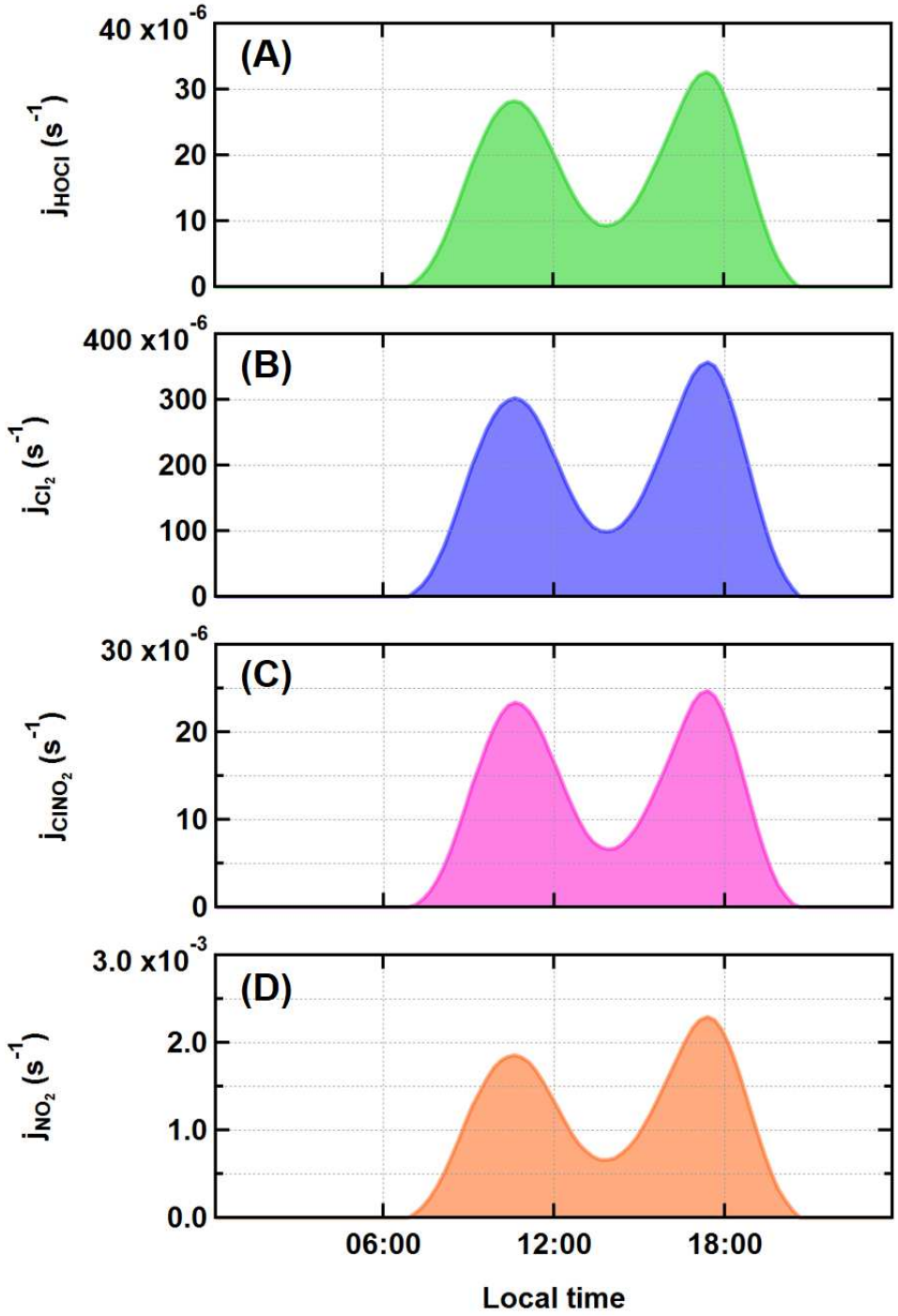

Figure A1.7. Upper-bound diel profiles of indoor photolysis rates for (A) HOCl, (B) Cl_2, (C) $ClNO_2$, and (D) NO_2 for the duration of HOMEChem.

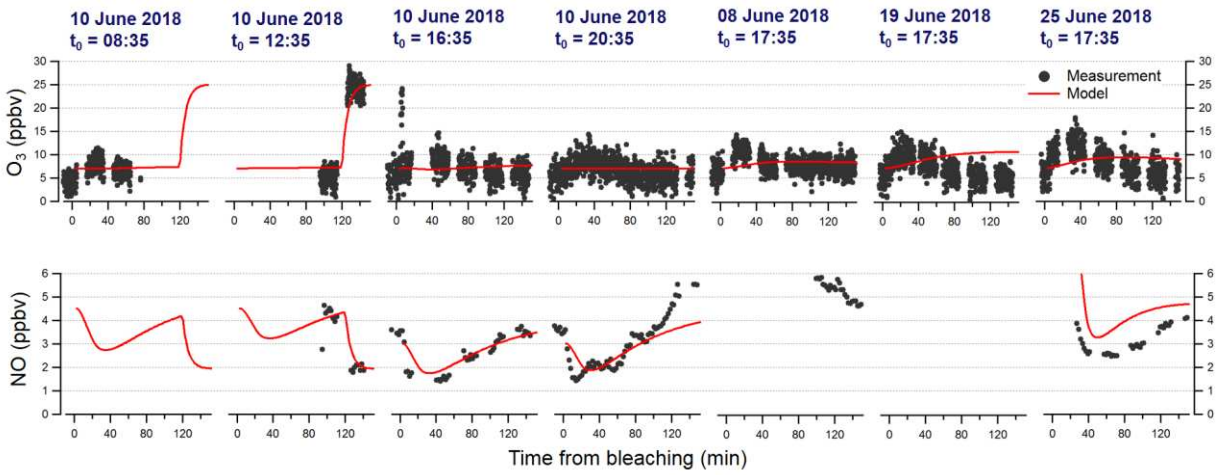

Figure A1.8. Measured indoor mixing ratios for O_3 and NO during various bleach cleaning experiments performed at HOMEChem (black markers). Red traces represent corresponding kinetic modeling results. t_0 indicates local times at which bleach mopping experiments began. Note the different scale used for NO here compared to Figure A1.3.

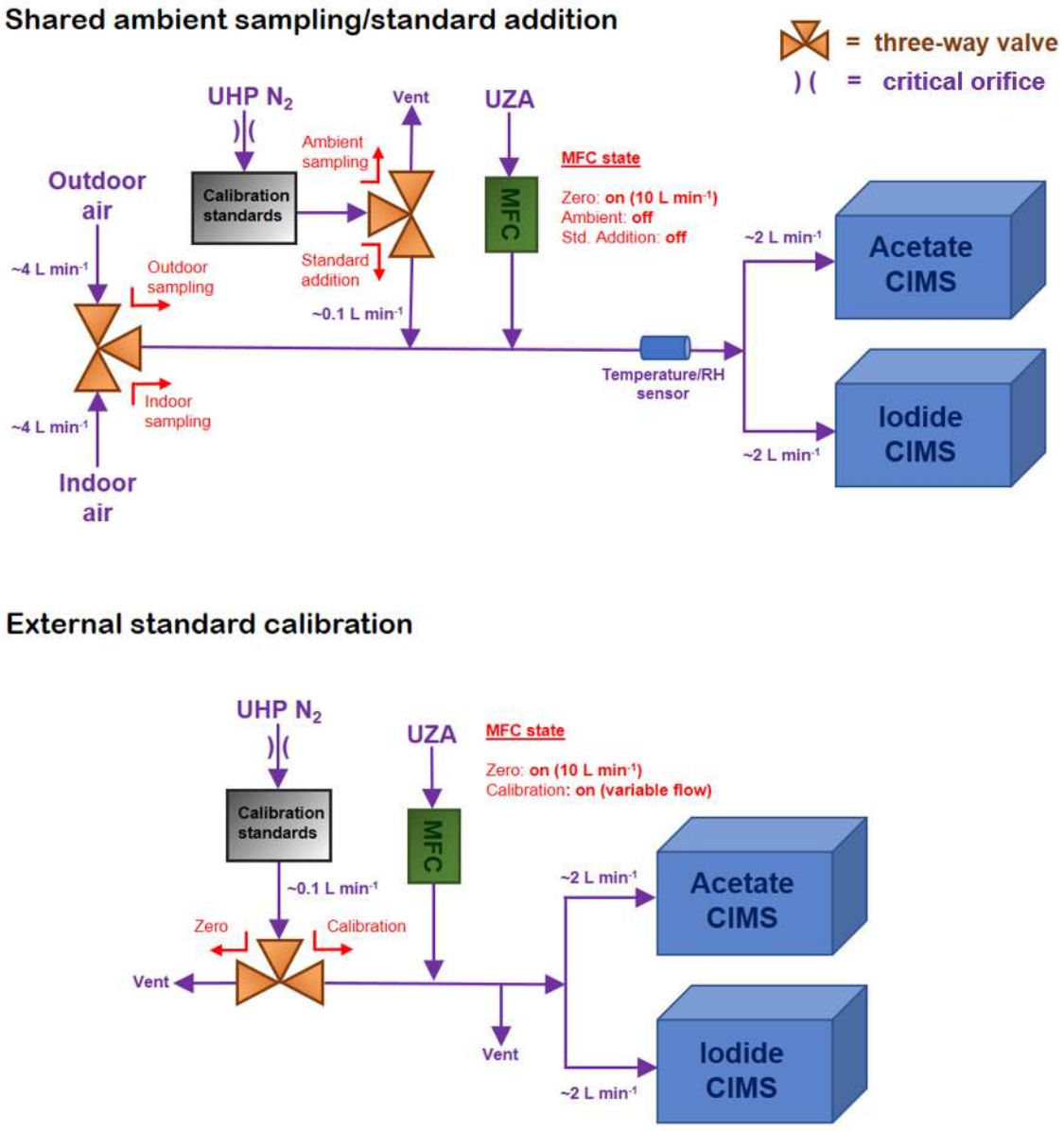

Figure A1.9. Schematic of shared inlet and calibration system used during HOMEChem during ambient sampling/standard addition (top), and external standard calibration regimes (bottom). Red arrows indicate direction of three-way valves during different sampling/calibration regimes. MFC = mass-flow controller.

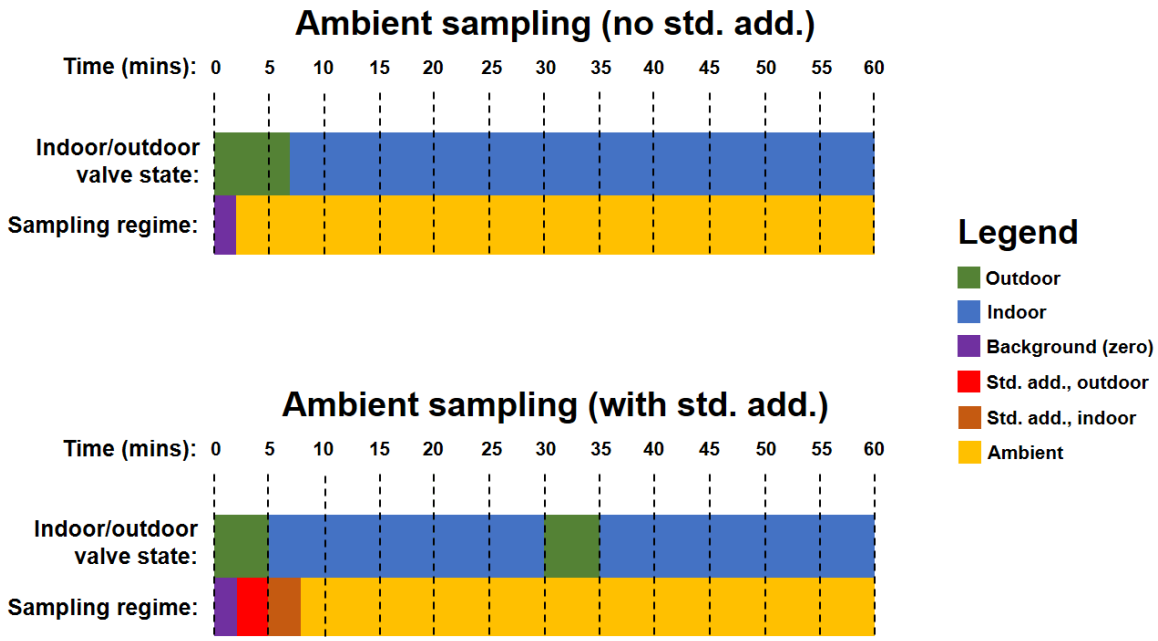

Figure A1.10. Timing scheme for instrumental backgrounds and indoor/outdoor ambient sampling without (top) and with (bottom) standard additions (abbreviated here as "std. add.") included.

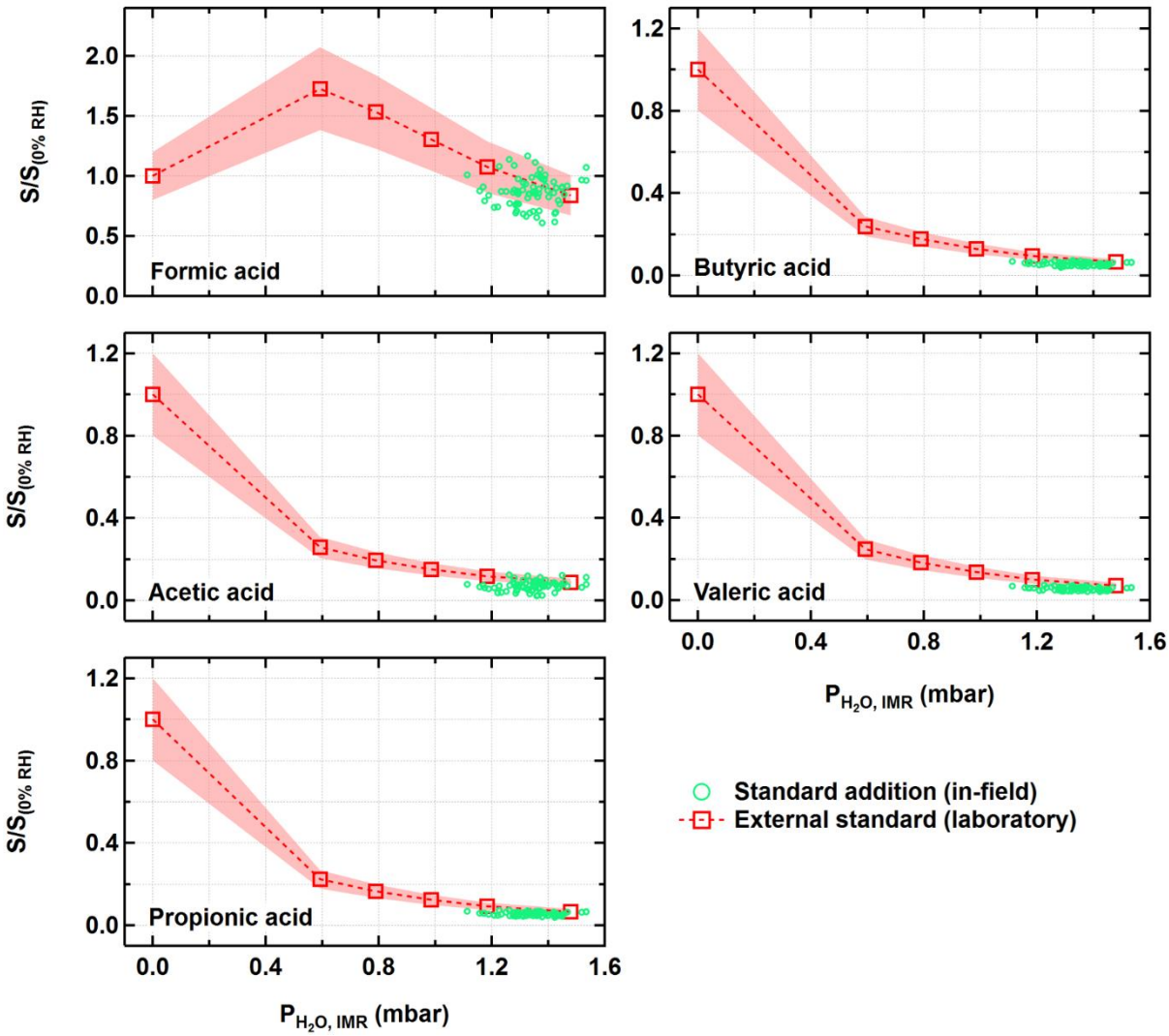

Figure A1.11. Standard addition I^- TOF-CIMS sensitivities from HOMEChem (green dots), and RH-dependent external standard I^- CIMS sensitivities (red markers) for C_1-C_5 alkanoic acids, plotted as a function of water vapor partial pressure in the IMR ($P_{H2O,IMR}$). Red markers and shaded regions represent means and uncertainties of triplicate external standard calibration sensitivity measurements. Here, sensitivities (S) are reported relative to CIMS sensitivity at 0% RH ($S_{(0\%\ RH)}$).

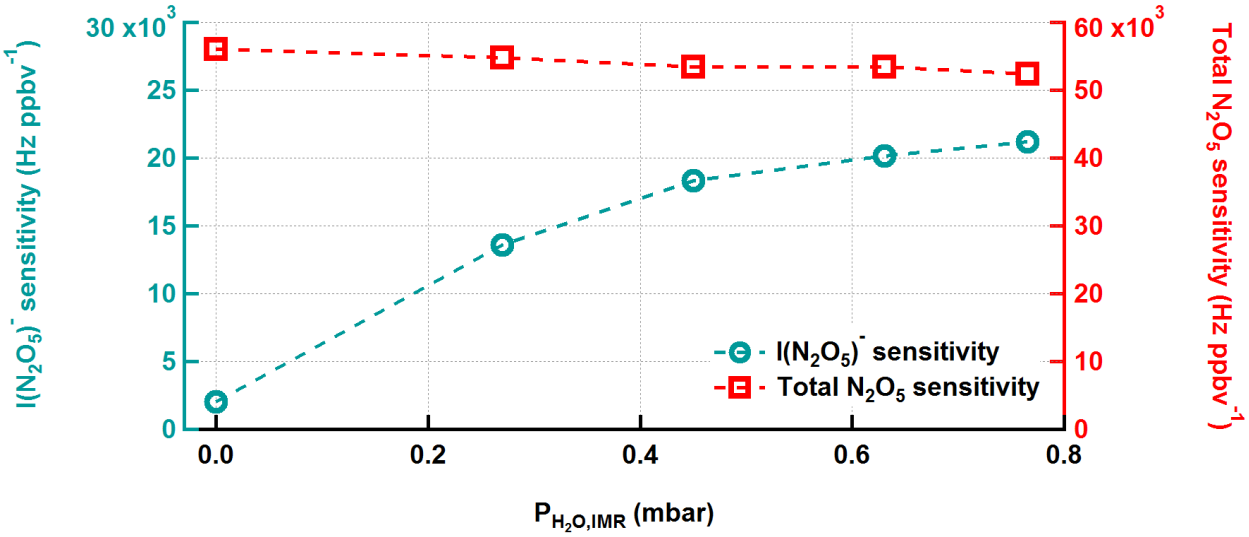

Figure A1.12. I^- TOF-CIMS sensitivities for $IN_2O_5^-$ (teal circles, left vertical axis) and total N_2O_5 (red squares, right vertical axis) measured as a function of water vapor partial pressure in the IMR ($P_{H2O,IMR}$). Markers represent means of each calibration. We exclude error bars for clarity. Here, 'total N_2O_5' corresponds to $IN_2O_5^-$ + NO_3^-.

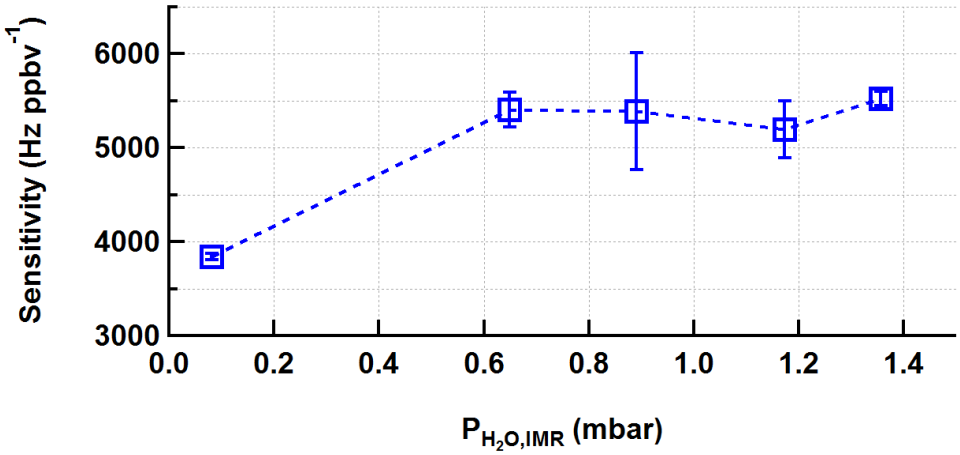

Figure A1.13. $ClNO_2$ I^- TOF-CIMS sensitivities measured as a function of water vapor partial pressure in the IMR ($P_{H2O,IMR}$). Markers and error bars represent means and uncertainties of each calibration.

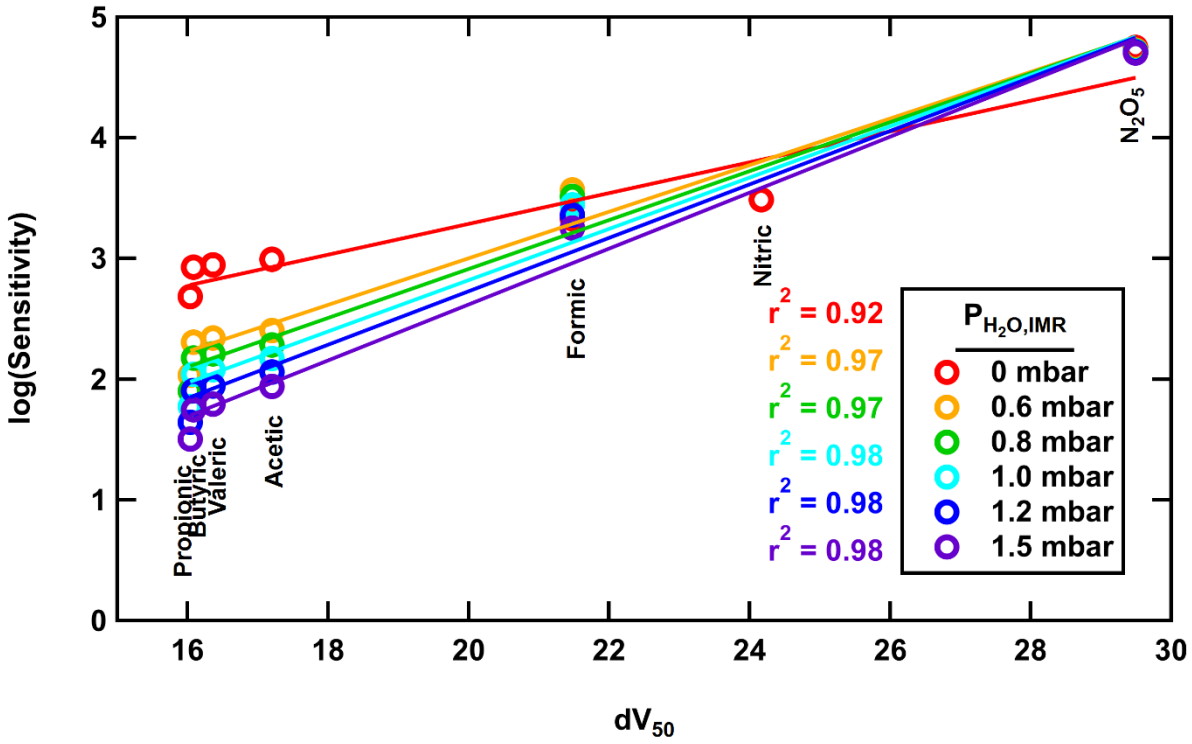

Figure A1.14. Relationship between the logarithm of I^- TOF-CIMS sensitivity and dV_{50} for several calibrant compounds (colored markers). Solid colored traces represent linear fits to the data using a least orthogonal distance regression (ODR) fitting method. Markers, linear fits, and r^2 values are colored by $P_{H2O,IMR}$ values (see figure legend). N_2O_5 sensitivity corresponds to 'total N_2O_5' ($IN_2O_5^-$ + NO_3^-). We are only able to report HNO_3 sensitivity at $P_{H2O,IMR}$ = 0 mbar. Vertical text labels correspond to approximate locations of calibrant compounds in dV_{50} space.

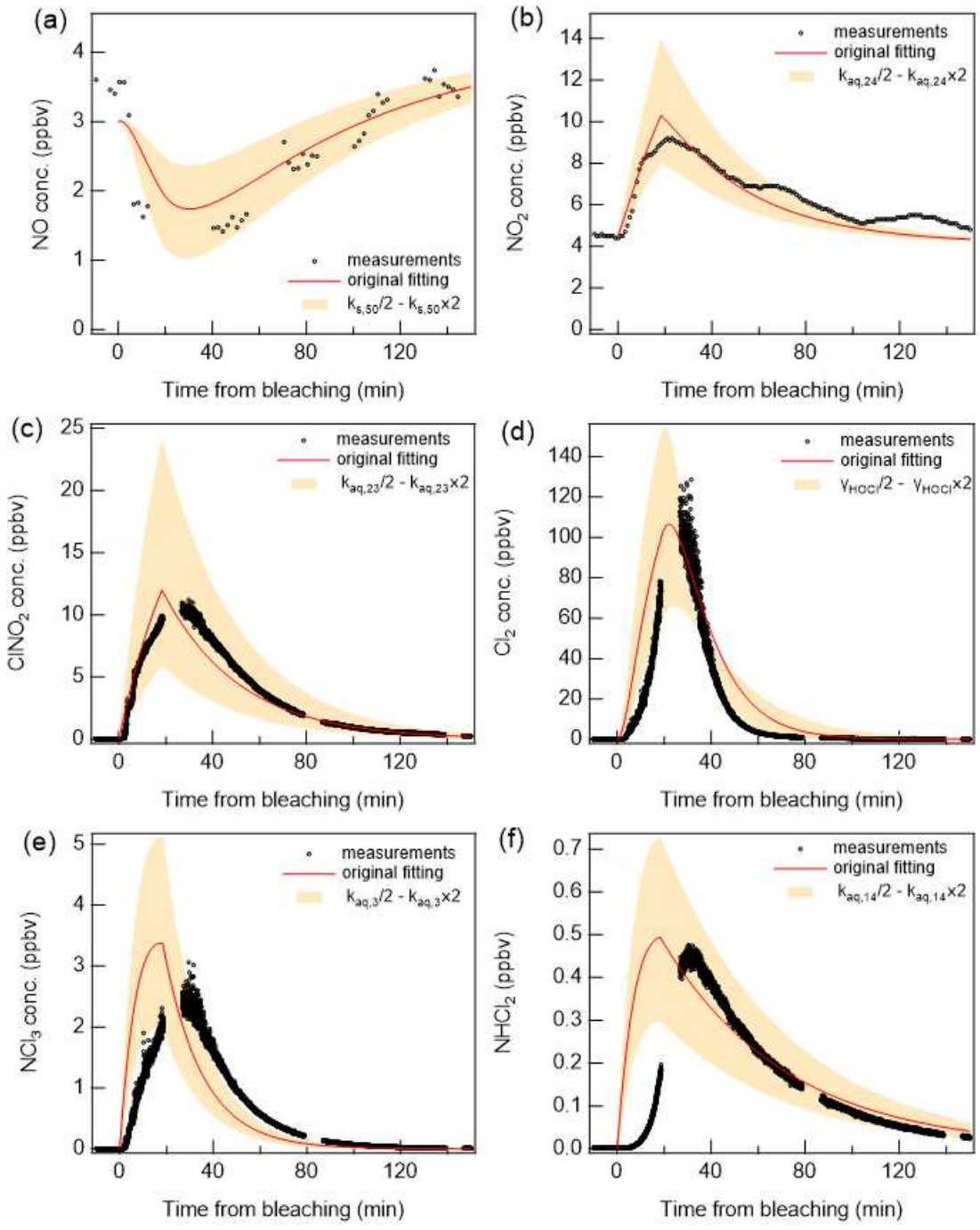

Figure A1.15. Sensitivity tests showing the impact of increasing or decreasing selected parameters on model outputs of gas-phase concentrations of selected chemical species. Parameters were typically varied by a factor of two. The target parameter and chosen range is shown in each sub-figure legend. For example, panel (d) shows the impact on Cl_2 concentration from varying the uptake coefficient of HOCl by a factor of 2 (shaded yellow region) from the base case scenario (red line, corresponds to values summarized in Table A1.4).

A1.3 Chapter 2 SI tables

Table A1.1 – Aqueous chemical mechanisms in the applied bleach used in kinetic model.

Reaction number	Reaction	Rate	Reference or comment
1	$NH_3 + HOCl \rightarrow NH_2Cl + H_2O$	$k_{aq,1} = 6.9 \times 10^{-15}\ cm^3\ s^{-1}$	Jafvert and Valentine (1992)
2	$NH_2Cl + HOCl \rightarrow NHCl_2 + H_2O$	$k_{aq,2} = 4.6 \times 10^{-17}\ cm^3\ s^{-1}$ *	Jafvert and Valentine (1992)
3	$NHCl_2 + HOCl \rightarrow NCl_3 + H_2O$	$k_{aq,3}$ = see Table A1.4 **	Jafvert and Valentine (1992)
4	$NH_2Cl + H_2O \rightarrow HOCl + NH_3$	$k_{aq,4} = 2.1 \times 10^{-5}\ s^{-1}$	Jafvert and Valentine (1992)
5	$NHCl_2 + H_2O \rightarrow HOCl + NH_2Cl$	$k_{aq,5} = 6.4 \times 10^{-7}\ s^{-1}$	Jafvert and Valentine (1992)
6	$NH_2Cl + NH_2Cl + H^+ \rightarrow NHCl_2 + NH_3$	$k_{aq,6} = 1.9 \times 10^{-38}\ cm^6\ s^{-1}$	Jafvert and Valentine (1992)
7	$NHCl_2 + NH_3 + H^+ \rightarrow NH_2Cl + NH_2Cl$	$k_{aq,7} = 1.7 \times 10^{-37}\ cm^6\ s^{-1}$	Jafvert and Valentine (1992)
8	$NHCl_2 + OH^- \rightarrow I$	$k_{aq,8} = 1.9 \times 10^{-19}\ cm^3\ s^{-1}$	Jafvert and Valentine (1992)
9	$I + NHCl_2 \rightarrow HOCl + Products$	$k_{aq,9} = 4.6 \times 10^{-17}\ cm^3\ s^{-1}$	Jafvert and Valentine (1992)
10	$I + NH_2Cl \rightarrow Products$	$k_{aq,10} = 1.4 \times 10^{-17}\ cm^3\ s^{-1}$	Jafvert and Valentine (1992)
11	$NH_2Cl + NHCl_2 \rightarrow Products$	$k_{aq,11} = 2.5 \times 10^{-23}\ cm^3\ s^{-1}$	Jafvert and Valentine (1992)
12	$NHCl_2 + NCl_3 + OH^- \rightarrow 2\ HOCl + Products$	$k_{aq,12} = 1.5 \times 10^{-31}\ cm^6\ s^{-1}$	Jafvert and Valentine (1992)
13	$NH_2Cl + NCl_3 + OH^- \rightarrow HOCl + Products$	$k_{aq,13} = 3.8 \times 10^{-33}\ cm^6\ s^{-1}$	Jafvert and Valentine (1992)
14***	$NHCl_2 + 2HOCl + H_2O \rightarrow HNO_3 + 4HCl$	$k_{aq,14}$ = see Table A1.4	Jafvert and Valentine (1992)
15	$OCl^- + H^+ \rightarrow HOCl$	$k_{aq,15} = 1.0 \times 10^{-11}\ cm^3\ s^{-1}$	assumed to be fast

16	$HOCl \rightarrow H^+ + OCl^-$	$k_{aq,16} = k_{aq,15} \times (6.02 \times 10^{23}/1000) \times 2.9 \times 10^{-8}$ s^{-1}	based on a K_a value of 2.9×10^{-8} ; Deborde and Von Gunten (2008)
17	$HOCl + H^+ + Cl^- \rightarrow Cl_2 + H_2O$	$k_{aq,17} = 1.2 \times 10^{-37}$ cm^6 s^{-1}	Deborde and Von Gunten (2008)
18	$H_2O + Cl_2 \rightarrow HOCl + H^+ + Cl^-$	$k_{aq,18} = 22.3$ s^{-1}	Deborde and Von Gunten (2008)
19	$H^+ + Cl^- \rightarrow HCl$	$k_{aq,19} = 1.0 \times 10^{-11}$ cm^3 s^{-1}	assumed to be fast
20	$HCl \rightarrow H^+ + Cl^-$	$k_{aq,20} = k_{aq,19} \times (6.02 \times 10^{23}/1000) \times 1.3 \times 10^{6}$ s^{-1}	based on a K_a value of 1.3×10^{6}
21	$HOCl + HOCl \rightarrow Cl_2O + H_2O$	$k_{aq,21} = 3.0 \times 10^{-23}$ cm^3 s^{-1}	fitting parameter
22	$Cl_2O + H_2O \rightarrow HOCl + HOCl$	$k_{aq,22} = k_{aq,21} \times (6.02 \times 10^{23}/1000) \times 8.7 \times 10^{-3}$ s^{-1}	based on a K_a value of 8.7×10^{-3} ; Deborde and Von Gunten (2008)
23	$HOCl + (NO_2^-) \rightarrow ClNO_2 + OH^-$	$k_{aq,23}$ = see Table A1.4	Eiserich et al. (1996)
24	$ClNO_2 + (NO_2^-) \rightarrow 2\ NO_2 + Cl^-$	$k_{aq,24}$ = see Table A1.4	Frenzel et al. (1998)

* Increased from a literature value of 4.6×10^{-19} cm^3 s^{-1} in order to fit the data and in order to not be significantly lower than $k_{aq,3}$. This may be due to specific experimental conditions affecting bleach solution pH and/or composition.
** The literature value was $4.6 \times 10^{-37}[OCl^-] + 9.0 \times 10^{-33}[OH^-]$ cm^3 s^{-1} but was simplified and varied until the data could be fitted as shown in Table A1.4.
*** The rate expression is $k_{aq,14}[NHCl_2][OCl^-]$. $k_{aq,14}$ was varied around the literature value of 3.8×10^{-19} cm^3 s^{-1} until the data could be fitted and values are close to the original value.

Table A1.2 – Gas-phase and heterogeneous chemistry used in kinetic model.

Reaction number	Reaction	Rate	Reference or comment
1	$Cl_2 + h\nu \rightarrow 2Cl$	j_{Cl2} = see Table A1.4	Xue et al. (2015)
2	$HOCl + h\nu \rightarrow OH + Cl$	j_{HOCl} = see Table A1.4	Xue et al. (2015)
3	$ClNO_2 + h\nu \rightarrow NO_2 + Cl$	j_{ClNO2} = see Table A1.4	Xue et al. (2015)
4	$ClONO_2 + h\nu \rightarrow NO_3 + Cl$	$k_{g,4} = 0.83 \times j_{ClNO2}$	Xue et al. (2015)
5	$ClONO_2 + h\nu \rightarrow NO_2 + ClO$	$k_{g,5} = 0.17 \times j_{ClNO2}$	Xue et al. (2015)
6	$NO_2 + NO_3 \rightarrow N_2O_5$	$k_{g,6} = 1.9 \times 10^{-12}$ cm^3 s^{-1}	Atkinson et al. (2004)

7	$N_2O_5 \rightarrow NO_2 + NO_3$	$k_{g,7} = 6.9 \times 10^{-2}$ s^{-1}	Atkinson et al. (2004)
8	$Cl + O_3 \rightarrow ClO + O_2$	$k_{g,8} = 2.8 \times 10^{-11} \times \exp(-250/T)$ cm^3 s^{-1}	Xue et al. (2015)
9	$Cl + HO_2 \rightarrow HCl + O_2$	$k_{g,9} = 3.5 \times 10^{-11}$ cm^3 s^{-1}	Xue et al. (2015)
10	$Cl + HO_2 \rightarrow ClO + OH$	$k_{g,10} = 7.5 \times 10^{-11} \times \exp(-620/T)$ cm^3 s^{-1}	Xue et al. (2015)
11	$Cl + H_2O_2 \rightarrow HCl + HO_2$	$k_{g,11} = 1.1 \times 10^{-11} \times \exp(-980/T)$ cm^3 s^{-1}	Xue et al. (2015)
12	$Cl + NO_3 \rightarrow NO_2 + ClO$	$k_{g,12} = 2.4 \times 10^{-11}$ cm^3 s^{-1}	Xue et al. (2015)
13	$Cl + ClONO_2 \rightarrow Cl_2 + NO_3$	$k_{g,13} = 6.2 \times 10^{-12} \times \exp(-145/T)$ cm^3 s^{-1}	Xue et al. (2015)
14	$OH + HCl \rightarrow Cl + H_2O$	$k_{g,14} = 1.7 \times 10^{-12} \times \exp(-230/T)$ cm^3 s^{-1}	Xue et al. (2015)
15	$OH + Cl_2 \rightarrow HOCl + Cl$	$k_{g,15} = 3.6 \times 10^{-12} \times \exp(-1200/T)$ cm^3 s^{-1}	Xue et al. (2015)
16	$OH + HOCl \rightarrow ClO + H_2O$	$k_{g,16} = 5.0 \times 10^{-13}$ cm^3 s^{-1}	Xue et al. (2015)
17	$OH + ClO \rightarrow HO_2 + Cl$	$k_{g,17} = 1.8 \times 10^{-11}$ cm^3 s^{-1}	Xue et al. (2015)
18	$OH + ClO \rightarrow HCl + O_2$	$k_{g,18} = 1.2 \times 10^{-12}$ cm^3 s^{-1}	Xue et al. (2015)
19	$ClO + NO_2 \rightarrow ClONO_2$	$k_{g,19} = 2.0 \times 10^{-11}$ cm^3 s^{-1} *	Xue et al. (2015)
20	$ClO + HO_2 \rightarrow HOCl + O_2$	$k_{g,20} = 2.2 \times 10^{-12} \times \exp(340/T)$ cm^3 s^{-1}	Xue et al. (2015)
21	$ClO + NO \rightarrow Cl + NO_2$	$k_{g,21} = 6.2 \times 10^{-12} \times \exp(295/T)$ cm^3 s^{-1}	Xue et al. (2015)
22**	N_2O_5 + Aerosol → Products	$k_{g,22} = 0.25 \times \omega_{N2O5} \times \gamma_{N2O5} \times S_{AERO} \times (1 - \varphi_{ClNO2})$ s^{-1} ($\gamma_{N2O5} = 1 \times 10^{-2}$, φ_{ClNO2}=0.5)	Xue et al. (2015); Wong et al. (2017)
23**	N_2O_5 + Aerosol → $ClNO_2$ + Products	$k_{g,23} = 0.25 \times \omega_{N2O5} \times \gamma_{N2O5} \times S_{AERO} \times \varphi_{ClNO2}$ s^{-1} ($\gamma_{N2O5} = 1 \times 10^{-2}$, φ_{ClNO2}=0.5)	Xue et al. (2015); Wong et al. (2017)
24**	NO_3 + Aerosol → Products	$k_{g,24} = 0.25 \times \omega_{NO3} \times \gamma_{NO3} \times S_{AERO}$ s^{-1} ($\gamma_{NO3} = 4 \times 10^{-3}$)	Xue et al. (2015); Wong et al. (2017)
25**	$ClONO_2$ + Aerosol → Cl_2 + HNO_3	$k_{g,25} = 0.25 \times \omega_{ClONO2} \times \gamma_{ClONO2} \times S_{AERO}$ s^{-1} ($\gamma_{ClONO2} = 1 \times 10^{-2}$)	Xue et al. (2015); Wong et al. (2017)
26**	HOCl + Aerosol → Cl_2	$k_{g,26} = 0.25 \times \omega_{HOCl} \times \gamma_{HOCl} \times S_{AERO}$ s^{-1} ($\gamma_{HOCl} = 0.4$)	Xue et al. (2015); fitting parameter
27	Cl + (VOCs) → HCl + (VOCs)	$k_{g,27} = 3$ s^{-1}	assumed to be fast
28	OH + (VOCs) → (VOCs)	$k_{g,28} = 3$ s^{-1}	assumed to be fast
29	$N_2O_5 + HCl \rightarrow ClNO_2 + HNO_3$	$k_{g,29} = 6.7 \times 10^{-21}$ cm^3 s^{-1}	Wilkins Jr and Hisatsune (1976)
30	$NO_2 + hv \rightarrow NO + O$	j_{NO2} = see Table A1.4	

31	$NO_3 + hv \rightarrow NO_2 + O$	j_{NO3} = see Table A1.4	
32	$HONO + hv \rightarrow NO + OH$	j_{HONO} = see Table A1.4	
33	$OH + O_3 \rightarrow HO_2 + O_2$	$k_{g,33} = 7.3 \times 10^{-14}$ cm^3 s^{-1}	Atkinson et al. (2004)
34	$HO_2 + NO \rightarrow OH + NO_2$	$k_{g,34} = 8.8 \times 10^{-12}$ cm^3 s^{-1}	Atkinson et al. (2004)
35	$HO_2 + O_3 \rightarrow OH + 2O_2$	$k_{g,35} = 2.0 \times 10^{-15}$ cm^3 s^{-1}	Atkinson et al. (2004)
36**	NO_2 + Aerosol → Product	$k_{g,36} = 0.25 \times \omega_{NO2} \times \gamma_{NO2} \times S_{AERO}$ s^{-1} (γ_{NO2} = see Table A1.4)	fitting parameter
37**	HO_2 + Aerosol → Product	$k_{g,37} = 0.25 \times \omega_{HO2} \times \gamma_{HO2} \times S_{AERO}$ s^{-1} ($\gamma_{HO2} = 0.5$)	George et al. (2013)
38	$OH + NO \rightarrow HONO$	$k_{g,38} = 3.3 \times 10^{-11}$ cm^3 s^{-1}	Atkinson et al. (2004)
39	$OH + HONO \rightarrow NO_2 + H_2O$	$k_{g,39} = 6.0 \times 10^{-12}$ cm^3 s^{-1}	Atkinson et al. (2004)
40	$HOCl + NO \rightarrow NO_2 + HCl$	$k_{g,40} = 1.0 \times 10^{-18}$ cm^3 s^{-1}	Cook et al. (1981)
41	$O + O_2 + M \rightarrow O_3 + M$	$k_{g,41} = 6.0 \times 10^{-34}$ cm^6 s^{-1}	Atkinson et al. (2004)
42	$O + NO_2 + M \rightarrow NO_3 + M$	$k_{g,42} = 1.3 \times 10^{-31}$ cm^6 s^{-1}	Atkinson et al. (2004)
43	$O + NO + M \rightarrow NO_2 + M$	$k_{g,43} = 1.0 \times 10^{-31}$ cm^6 s^{-1}	Atkinson et al. (2004)
44***	Cl_2 → Products (on surfaces)	$k_{s,44}$ = see Table A1.4	fitting parameter
45***	$ClNO_2$ → Products (on surfaces)	$k_{s,45}$ = see Table A1.4	fitting parameter
46***	NCl_3 → Products (on surfaces)	$k_{s,46}$ = see Table A1.4	fitting parameter
47***	Cl_2O → Products (on surfaces)	$k_{s,47} = 2.0 \times 10^{-3}$ s^{-1}	fitting parameter
48***	NO_2 → HONO (on surfaces)	$k_{s,48} = 1.4 \times 10^{-5}$ s^{-1}	fitting parameter
49***	$NHCl_2$ → Products (on surfaces)	$k_{s,49} = 1.4 \times 10^{-4}$ s^{-1}	fitting parameter
50***	$HOCl + NO \rightarrow NO_2 + HCl$ (on surfaces)	$k_{s,50}$ = see Table A1.4	fitting parameter
51***	HOCl + HONO → Products (on surfaces)	$k_{s,51}$ = see Table A1.4	fitting parameter

* The literature value was 7.0×10^{-11} cm^3 s^{-1} but was decreased slightly to fit the data.
** ω_X is the molecular speed of species X, γ_X is the uptake coefficient of species X, and S_{AERO} is the aerosol surface area concentration.
*** These reactions are assumed to occur on surfaces but are treated as losses from the gas-phase. They may also include currently unknown gas-phase reactions.

Table A1.3 – Henry's Law and gas-phase diffusion coefficients used in kinetic model.

Species	Henry's Law coefficient (mol cm^{-3} atm^{-1})*	Gas-phase diffusion coefficient (cm^2 s^{-1})**
NH_3	0.06	0.23

NCl_3	9.9×10^{-5}	0.096
$NHCl_2$	2.9×10^{-2}	0.11
HOCl	0.6	0.15
Cl_2	9.2×10^{-5}	0.13
NH_2Cl	8.6×10^{-2}	0.14
HCl	0.72	0.17
I (intermediate)	Non-volatile	N/A
OCl-	Non-volatile	N/A
Cl	2.3×10^{-3}	0.18
OH	0.03	0.24****
$ClNO_2$	4×10^{-5}	0.12
NO_2	1.4×10^{-5}	0.17
$ClONO_2$	0.011 ***	0.11
NO_3	3.4×10^{-5}	0.15
ClO	7.0×10^{-4}	0.16
N_2O_5	2.1×10^{-3}	0.11
O_3	1×10^{-5}	0.18
HO_2	5	0.20
H_2O_2	70	0.19
NO	1.9×10^{-6}	0.20
HNO_3	210	0.14
Cl^-	Non-volatile	N/A
Cl_2O	1.7×10^{-2}	0.12
HONO	0.048	0.16
O	1×10^{-5} *****	0.32

* From Sander (2015) unless otherwise stated.
** From https://www3.epa.gov/ceampubl/learn2model/part-two/onsite/estdiffusion-ext.html unless otherwise stated.
*** From Shi et al. (2001)
**** From Tang et al. (2014).
***** Assumed to be the same as O_3.

Table A1.4 – Parameters which varied between different times and days in kinetic model.

Parameter	10 June 08:35	10 June 12:35	10 June 16:35	10 June 20:35	8 June 17:35	19 June 17:35	25 June 17:35
AER (h^{-1})*	0.66	0.60	0.64	0.78	0.70	0.43	0.59
K_e (s^{-1})	10	3	10	5	3	3	1

$k_{aq,3}$ (cm^3 s^{-1})	2.9×10^{-18}	2.0×10^{-18}	1.3×10^{-18}	7.2×10^{-19}	5.0×10^{-18}	1.0×10^{-17}	5.0×10^{-18}
$k_{aq,14}$ (cm^3 s^{-1})	1.3×10^{-19}	6.3×10^{-20}	5.4×10^{-20}	5.4×10^{-20}	7.6×10^{-20}	2.5×10^{-19}	3.2×10^{-20}
$k_{aq,23}$ (cm^3 s^{-1})	1.5×10^{-4}	1.3×10^{-4}	8.7×10^{-5}	7.4×10^{-5}	2.6×10^{-4}	3.2×10^{-4}	2.4×10^{-4}
$k_{aq,24}$ (cm^3 s^{-1})	2.5	2.5	2.5	2	2	2	2.5
j_{Cl2} (s^{-1})**	2.2×10^{-4} /50	1.2×10^{-4}/50	3.4×10^{-4} /50	0	2.6×10^{-4} /50	2.6×10^{-4} /50	2.6×10^{-4} /50
j_{HOCl} (s^{-1})**	2.1×10^{-5} /50	1.1×10^{-5} /50	3.1×10^{-5} /50	0	2.4×10^{-5} /50	2.4×10^{-5} /50	2.4×10^{-5} /50
j_{ClNO2} (s^{-1})**	1.6×10^{-5} /50	8.2×10^{-6} /50	2.3×10^{-5} /50	0	1.7×10^{-5} /50	1.7×10^{-5} /50	1.7×10^{-5} /50
j_{NO2} (s^{-1})**	1.4×10^{-3} /50	7.5×10^{-4} /50	2.2×10^{-3} /50	0	1.7×10^{-3} /50	1.7×10^{-3} /50	1.7×10^{-3} /50
j_{NO3} (s^{-1})**	7.5×10^{-2} /50	2.3×10^{-2} /50	0.13 /50	0	0.11 /50	0.11 /50	0.11 /50
j_{HONO} (s^{-1})**	1.8×10^{-4} /50	1.0×10^{-4} /50	2.8×10^{-4} /50	0	2.1×10^{-4} /50	2.1×10^{-4} /50	2.1×10^{-4} /50
γ_{NO2}	0.08	0.08	0.08	0.08	0.08	0.04	0.06
$k_{s,44}$ (s^{-1})	2.0×10^{-3}	2.0×10^{-3}	2.0×10^{-3}	3.0×10^{-3}	4.0×10^{-3}	2.0×10^{-3}	1.0×10^{-3}
$k_{s,45}$ (s^{-1})	5.5×10^{-4}	4.4×10^{-4}	3.3×10^{-4}	2.5×10^{-4}	1.1×10^{-3}	2.2×10^{-4}	3.0×10^{-4}
$k_{s,46}$ (s^{-1})	8.3×10^{-4}	8.3×10^{-4}	8.3×10^{-4}	4.2×10^{-4}	8.3×10^{-4}	4.2×10^{-4}	4.2×10^{-4}
$k_{s,50}$ (cm^3 s^{-1})	1.0×10^{-16}	1.0×10^{-16}	1.0×10^{-16}	1.0×10^{-16}	1.0×10^{-16}	1.0×10^{-16}	1.0×10^{-15}
$k_{s,51}$ (cm^3 s^{-1})	1.0×10^{-15}	1.0×10^{-15}	1.0×10^{-15}	1.0×10^{-15}	1.0×10^{-15}	5.0×10^{-16}	1.0×10^{-15}
P_{NH3} (cm^{-3} s^{-1}) ***	$7.9 \times 10^{11} \times AER$	$6.4 \times 10^{11} \times AER$	$6.4 \times 10^{11} \times AER$	$1.7 \times 10^{11} \times AER$	$6.4 \times 10^{11} \times AER$	$9.8 \times 10^{11} \times AER$	$4.9 \times 10^{11} \times AER$
P_{NO2} (cm^{-3} s^{-1}) ***	$4.3 \times 10^{10} \times AER$	$4.3 \times 10^{10} \times AER$	$5.9 \times 10^{10} \times AER$	$8.3 \times 10^{10} \times AER$	$1.2 \times 10^{11} \times AER$	$2.2 \times 10^{11} \times AER$	$1.4 \times 10^{11} \times AER$
P_{NO} (cm^{-3} s^{-1}) ***	$4.2 \times 10^{10} \times AER$	$4.2 \times 10^{10} \times AER$	$3.9 \times 10^{10} \times AER$	$1.5 \times 10^{10} \times AER$	$3.5 \times 10^{10} \times AER$	$5.6 \times 10^{10} \times AER$	$5.0 \times 10^{10} \times AER$
P_{O3} (cm^{-3} s^{-1}) ***	$1.7 \times 10^{11} \times AER$	$1.7 \times 10^{11} \times AER$	$1.7 \times 10^{11} \times AER$	$1.7 \times 10^{11} \times AER$	$1.7 \times 10^{11} \times AER$	$1.7 \times 10^{11} \times AER$	$1.7 \times 10^{11} \times AER$
P_{HONO} (cm^{-3} s^{-1}) ***	$6.2 \times 10^{9} \times AER$	$6.2 \times 10^{9} \times AER$	$6.2 \times 10^{9} \times AER$	$6.2 \times 10^{9} \times AER$	$6.2 \times 10^{9} \times AER$	$1.4 \times 10^{10} \times AER$	$6.2 \times 10^{9} \times AER$
$P_{NO\_indoors}$ (cm^{-3} s^{-1}) ***	1.4×10^{7}	1.4×10^{7}	7.1×10^{6}	1.4×10^{7}	7.1×10^{6}	2.1×10^{7}	7.1×10^{6}

$P_{NO2\_indoors}$ (cm^{-3} s^{-1}) ***	2.1×10^7	2.1×10^7	3.6×10^7	5.0×10^7	5.0×10^7	2.1×10^7	7.1×10^6

* All species were removed from the gas-phase at the AER.
** Upper-bound photolysis rates from measurements were divided by a factor of 50.
*** P_X represents a production rate of molecules due to outdoor-to-indoor transport, while $P_{X\_indoors}$ represents an indoor production. P_{NH3}, P_{O3}, $P_{NO\_indoors}$ and $P_{NO2\_indoors}$ were fitting parameters while P_{NO2}, P_{NO} and P_{HONO} were based on measurements of these species outdoors. Note that P_{O3} was changed for the window opening scenarios. AER was in units of s^{-1}.

Table A1.5 – Outdoor mixing ratios and I^- TOF-CIMS instrumental detection limits for various bleach-related compounds during HOMEChem.

	Outdoor mixing ratio (pptv)				Detection limit (pptv)
	Median	*25th percentile*	*75th percentile*	*Mean (± S. D.)*	
HOCl	BDL	BDL	50.	40. ± 40.	30.
Cl_2	5.	BDL	11.	10. ± 10.	3.
$ClNO_2$	2.	BDL	7.	5. ± 7.	2.
$NHCl_2$*	BDL	BDL	BDL	BDL	1.
NCl_3*	BDL	BDL	0.2	0.2 ± 0.2	0.2
Cl_2O*	BDL	BDL	BDL	BDL	0.2
N_2O_5	--	--	--	--	1.

Outdoor measurements taken during bleach cleaning experiments on 8, 10, 19, and 25 June 2018. pptv = part-per-trillion by volume. BDL = below detection limit; S. D. = standard deviation. (*) denotes mixing ratios are estimates. (--) denotes missing data.

Table A1.6 – Kinetic model predictions of total OH radical production (%) from individual reaction mechanisms during bleach cleaning experiments at HOMEChem.

Reaction	10 June 08:35	10 June 12:35	10 June 16:35	10 June 20:35	8 June 17:35	19 June 17:35	25 June 17:35
$HOCl + h\nu \rightarrow OH + Cl$	96.0	93.5	96.4	--	84.9	38.0	56.0
$Cl + HO_2 \rightarrow ClO + OH$	0.0	0.0	0.0	--	0.0	0.0	0.0
$HONO + h\nu \rightarrow NO + OH$	3.9	6.4	3.4	--	15.1	62.0	43.9
$HO_2 + NO \rightarrow OH + NO_2$	0.2	0.2	0.2	--	0.0	0.0	0.2
$HO_2 + O_3 \rightarrow OH + 2O_2$	0.0	0.0	0.0	--	0.0	0.0	0.0

No OH radical production occurred at 20:35 on 10 June 2018 due to the absence of indoor photolysis reactions. (--) denotes missing data. Radical production was calculated between 0 and 2.5 hours after bleach cleaning.

Table A1.7 – Kinetic model predictions of total Cl radical production (%) from individual reaction mechanisms during bleach cleaning experiments at HOMEChem.

Reaction	10 June 08:35	10 June 12:35	10 June 16:35	10 June 20:35	8 June 17:35	19 June 17:35	25 June 17:35
$Cl_2 + h\nu \rightarrow 2Cl$	81.0	79.5	83.6	--	68.6	65.6	70.9
$HOCl + h\nu \rightarrow OH + Cl$	8.3	8.2	8.4	--	6.8	3.9	2.5
$ClNO_2 + h\nu \rightarrow NO_2 + Cl$	0.5	0.6	0.4	--	0.9	2.0	1.0
$ClONO_2 + h\nu \rightarrow NO_3 + Cl$	0.0	0.0	0.1	--	0.0	0.0	0.0
$OH + HCl \rightarrow Cl + H_2O$	0.0	0.0	0.0	--	0.0	0.0	0.1
$OH + Cl_2 \rightarrow HOCl + Cl$	0.1	0.1	0.1	--	0.0	0.0	0.0

$OH + ClO \rightarrow HO_2 + Cl$	0.0	0.0	0.0	--	0.0	0.0	0.0
$ClO + NO \rightarrow Cl + NO_2$	10.0	11.6	7.3	--	23.7	28.4	25.4

No Cl radical production occurred at 20:35 on 10 June 2018 due to the absence of indoor photolysis reactions. (--) denotes missing data. Radical production was calculated between 0 and 2.5 hours after bleach cleaning.

REFERENCES

Abdullahi, K. L., Delgado-Saborit, J. M., and Harrison, R. M.: Emissions and indoor concentrations of particulate matter and its specific chemical components from cooking: A review, Atmos. Environ., 71, 260-294, 2013.

Aljawhary, D., Lee, A. K. Y., and Abbatt, J. P. D.: High-resolution chemical ionization mass spectrometry (ToF-CIMS): application to study SOA composition and processing, Atmos. Meas. Tech., 6, 3211-3224, 2013.

Atkinson, R., Baulch, D. L., Cox, R. A., Crowley, J. N., Hampson, R. F., Hynes, R. G., Jenkin, M. E., Rossi, M. J., and Troe, J.: Evaluated kinetic and photochemical data for atmospheric chemistry: Volume I - gas phase reactions of O_x, HO_x, NO_x and SO_x species, Atmos. Chem. Phys., 4, 1461-1738, 10.5194/acp-4-1461-2004, 2004.

Bertram, T. H., Kimmel, J. R., Crisp, T. A., Ryder, O. S., Yatavelli, R. L. N., Thornton, J. A., Cubison, M. J., Gonin, M., and Worsnop, D. R.: A field-deployable, chemical ionization time-of-flight mass spectrometer, Atmos. Meas. Tech., 4, 1471-1479, doi:10.5194/amt-4-1471-2011, 2011.

Brophy, P., and Farmer, D. K.: Clustering, methodology, and mechanistic insights into acetate chemical ionization using high-resolution time-of-flight mass spectrometry, Atmos. Meas. Tech., 9, 3969-3986, doi:10.5194/amt-9-3969-2016, 2016.

Cook, J. E. L., Ennis, C. A., Leck, T. J., and Birks, J. W.: Studies of reactions of importance in the stratosphere. IV. Rate constant for the reaction Cl+HOCl→HCl+ClO over the temperature range 243–365 K, J. Chem. Phys., 74, 545-549, 1981.

Deborde, M., and Von Gunten, U.: Reactions of chlorine with inorganic and organic compounds during water treatment—kinetics and mechanisms: a critical review, Water Res., 42, 13-51, 2008.

Dubé, W. P., Brown, S. S., Osthoff, H. D., Nunley, M. R., Ciciora, S. J., Paris, M. W., McLaughlin, R. J., and Ravishankara, A.: Aircraft instrument for simultaneous, in situ measurement of NO_3 and N_2O_5 via pulsed cavity ring-down spectroscopy, Rev. Sci. Instrum., 77, 034101, 2006.

Eiserich, J. P., Cross, C. E., Jones, A. D., Halliwell, B., and Van der Vliet, A.: Formation of nitrating and chlorinating species by reaction of nitrite with hypochlorous acid a novel mechanism for nitric oxide-mediated protein modification, J. Biol. Chem., 271, 19199-19208, 1996.

Farmer, D. K., Vance, M. E., Abbatt, J. P. D., Abeleira, A., Alves, M. R., Arata, C., Boedicker, E., Bourne, S., Cardoso-Saldaña, F., Corsi, R., DeCarlo, P. F., Goldstein, A. H., Grassian, V. H.,

Hildebrandt Ruiz, L., Jimenez, J. L., Kahan, T. F., Katz, E. F., Mattila, J. M., Nazaroff, W. W., Novoselac, A., O'Brien, R. E., Or, V. W., Patel, S., Sankhyan, S., Stevens, P. S., Tian, Y., Wade, M., Wang, C., Zhou, S., and Zhou, Y.: Overview of HOMEChem: House Observations of Microbial and Environmental Chemistry, Environ. Sci. Process. Impacts, 21, 1280-1300, 10.1039/C9EM00228F, 2019.

Finlayson-Pitts, B.: The tropospheric chemistry of sea salt: A molecular-level view of the chemistry of NaCl and NaBr, Chem. Rev., 103, 4801-4822, 2003.

Foster, K., Caldwell, T., Hemminger, J., and Finlayson-Pitts, B.: Techniques for quantifying gaseous HOCl using atmospheric pressure ionization mass spectrometry, Phys. Chem. Chem. Phys., 1, 5615-5621, 1999.

Frenzel, A., Scheer, V., Sikorski, R., George, C., Behnke, W., and Zetzsch, C.: Heterogeneous interconversion reactions of $BrNO_2$, $ClNO_2$, Br_2, and Cl_2, J. Phys. Chem. A, 102, 1329-1337, 1998.

Fuchs, H., Dubé, W. P., Ciciora, S. J., and Brown, S. S.: Determination of inlet transmission and conversion efficiencies for in situ measurements of the nocturnal nitrogen oxides, NO_3, N_2O_5 and NO_2, via pulsed cavity ring-down spectroscopy, Anal. Chem., 80, 6010-6017, 2008.

George, I., Matthews, P., Whalley, L., Brooks, B., Goddard, A., Baeza-Romero, M., and Heard, D.: Measurements of uptake coefficients for heterogeneous loss of HO_2 onto submicron inorganic salt aerosols, Phys. Chem. Chem. Phys., 15, 12829-12845, 2013.

Huey, L. G., Hanson, D. R., and Howard, C. J.: Reactions of SF_6^- and I^- with atmospheric trace gases, J. Phys. Chem., 99, 5001-5008, 1995.

Iyer, S., Lopez-Hilfiker, F., Lee, B. H., Thornton, J. A., and Kurtén, T.: Modeling the detection of organic and inorganic compounds using iodide-based chemical ionization, J. Phys. Chem. A, 120, 576-587, 2016.

Jafvert, C. T., and Valentine, R. L.: Reaction scheme for the chlorination of ammoniacal water, Environ. Sci. Technol., 26, 577-586, 1992.

Kercher, J., Riedel, T., and Thornton, J.: Chlorine activation by N_2O_5: simultaneous, in situ detection of $ClNO_2$ and N_2O_5 by chemical ionization mass spectrometry, Atmos. Meas. Tech., 2, 193-204, 2009.

Kowal, S. F., Allen, S. R., and Kahan, T. F.: Wavelength-Resolved Photon Fluxes of Indoor Light Sources: Implications for HOx Production, Environ. Sci. Technol., 51, 10423-10430, 2017.

Lawler, M., Sander, R., Carpenter, L., Lee, J., Glasow, R. v., Sommariva, R., and Saltzman, E.: HOCl and Cl_2 observations in marine air, Atmos. Chem. Phys., 11, 7617-7628, 2011.

Lee, B. H., Lopez-Hilfiker, F. D., Mohr, C., Kurten, T., Worsnop, D. R., and Thornton, J. A.: An iodide-adduct high-resolution time-of-flight chemical-ionization mass spectrometer: application to atmospheric inorganic and organic compounds, Environ. Sci. Technol., 48, 6309-6317, doi:10.1021/es500362a, 2014.

Leu, M.-T., Timonen, R. S., Keyser, L. F., and Yung, Y. L.: Heterogeneous reactions of $HNO_3(g) + NaCl(s) \rightarrow HCl(g) + NaNO_3(s)$ and $N_2O_5(g) + NaCl(s) \rightarrow ClNO_2(g) + NaNO_3(s)$, J. Phys. Chem., 99, 13203-13212, 1995.

Liu, Y., Misztal, P., Xiong, J., Tian, Y., Arata, C., Nazaroff, W., and Goldstein, A.: Detailed investigation of ventilation rates and airflow patterns in a northern California residence, Indoor Air, 28, 572-584, 2018.

Lopez-Hilfiker, F. D., Iyer, S., Mohr, C., Lee, B. H., D'Ambro, E. L., Kurten, T., and Thornton, J. A.: Constraining the sensitivity of iodide adduct chemical ionization mass spectrometry to multifunctional organic molecules using the collision limit and thermodynamic stability of iodide ion adducts, Atmos. Meas. Tech., 9, 1505-1512, doi:10.5194/amt-9-1505-2016, 2016.

Sander, R.: Compilation of Henry's law constants (version 4.0) for water as solvent, Atmos. Chem. Phys., 15, 4399-4981, 2015.

Shi, Q., Jayne, J., Kolb, C., Worsnop, D., and Davidovits, P.: Kinetic model for reaction of $ClONO_2$ with H_2O and HCl and HOCl with HCl in sulfuric acid solutions, J. Geophys. Res. Atmos., 106, 24259-24274, 2001.

Tang, M., Cox, R., and Kalberer, M.: Compilation and evaluation of gas phase diffusion coefficients of reactive trace gases in the atmosphere: volume 1. Inorganic compounds, Atmos. Chem. Phys., 14, 9233-9247, 2014.

Wagner, N., Dubé, W., Washenfelder, R., Young, C., Pollack, I., Ryerson, T., and Brown, S.: Diode laser-based cavity ring-down instrument for NO_3, N_2O_5, NO, NO_2 and O_3 from aircraft, Atmos. Meas. Tech., 4, 1227-1240, 2011.

Wilkins Jr, R. A., and Hisatsune, I.: The reaction of dinitrogen pentoxide with hydrogen chloride, Ind. Eng. Chem. Fundam., 15, 246-248, 1976.

Wong, J. P. S., Carslaw, N., Zhao, R., Zhou, S., and Abbatt, J. P. D.: Observations and impacts of bleach washing on indoor chlorine chemistry, Indoor Air, 27, 1082-1090, 2017.

Xu, W., Lambe, A., Silva, P., Hu, W., Onasch, T., Williams, L., Croteau, P., Zhang, X., Renbaum-Wolff, L., and Fortner, E.: Laboratory evaluation of species-dependent relative ionization efficiencies in the Aerodyne Aerosol Mass Spectrometer, Aerosol Sci. Technol., 52, 626-641, 2018.

Xue, L., Saunders, S., Wang, T., Gao, R., Wang, X., Zhang, Q., and Wang, W.: Development of a chlorine chemistry module for the Master Chemical Mechanism, Geosci. Model Dev., 8, 3151-3162, 2015.

Zahniser, M., and Kaufman, F.: Kinetics of the reactions of ClO with O and with NO, J. Chem. Phys., 66, 3673-3681, 1977.

Zhao, J., and Zhang, R.: Proton transfer reaction rate constants between hydronium ion (H_3O^+) and volatile organic compounds, Atmos. Environ., 38, 2177-2185, 2004.

APPENDIX 2 – CHAPTER 3 SUPPLEMENTAL INFORMATION (A2)

A2.1 Chapter 3 supplemental information (SI) text

A2.1.1 Positive Matrix Factorization (PMF) analysis of HR-AMS data during HOMEChem layered experiments

We analyzed the HR-AMS two-dimensional organic aerosol (OA) mass spectral matrix using the PMF Evaluation Tool (version 3.04A) (Ulbrich et al., 2009). PMF analysis of AMS data has been detailed previously (Ulbrich et al., 2009). We included OA data during periods influenced by cooking emissions as the input, and selected a four-factor solution (FPEAK = 0) to represent the dataset. All four factors are associated with cooking events, and not background OA. Background OA levels were low compared to cooking OA (1.5 ± 1.2 μg/m^3 on average), and an associated factor was not resolved during cooking periods. The focus of this work is the cooking organic aerosol 2 ("COA2") factor. COA2 was the most abundant factor during Thanksgiving experiments (detailed in Farmer et al. (2019)), which involved heavy oven use. The mass spectrum of COA2 (Figure A2.5) exhibited fragmentation patterns indicative of COA in the AMS, such as a high fraction of *m/z* 41 and a *m/z* 55:57 ratio greater than 1 (Mohr et al., 2009; Allan et al., 2010). We estimated O:C and H:C ratios for COA2 of 0.16 and 1.89, respectively. While bulk OA mass concentration did not increase after bleach mopping on layered days, COA2 was observed at slightly elevated levels (up to 0.4 μg/m^3) following bleach mopping on layered days (Figure A2.6).

A2.1.2 Assessing primary emission vs. secondary chemistry as indoor sources of bleach-related analytes

A2.1.2.1 Inlet sniff test measurements

We performed sniff tests during HOMEChem, wherein we sampled bleach vapors directly from the headspace of the stock bleach solution used during bleach cleaning experiments through the indoor sampling inlet lines. We observed significant enhancements of C_2H_3NO, C_3H_5NO, HNCO, CHO_2Cl, $C_2H_3O_2Cl$, and $C_3H_5O_3Cl$ relative to pre-sampling background levels, suggesting these compounds were likely present in the bleach solution as impurities. We did not observe enhancements of ClCN during these tests. We further assess the extent to which primary emissions of these impurities from solution explains observed mixing ratios of these compounds during bleach cleaning in the following sub-sections. We did not perform inlet sniff tests for $CHCl_3$ or C_2Cl_4. We speculate primary emission and secondary chemistry contributed to indoor $CHCl_3$ and C_2Cl_4 observed during bleach cleaning (discussed in main text).

A2.1.2.2 Indoor production rates

We assess indoor production rates of bleach-related analytes during the bleach cleaning experiment on 10 June 2018 using a one-box model. We express the rate of change in indoor mixing ratios of analyte X by the following mass balance:

$$\frac{d[X]}{dt} = \Sigma_{sources} - \Sigma_{sinks}$$

Where [X] is indoor mixing ratio of X, and $\Sigma_{sources}$ and Σ_{sinks} are summed sources and sinks of analyte X, respectively.

We assume X is in steady-state indoors ($d[X]/dt \approx 0$) prior to bleach cleaning (i.e. baseline conditions).

We determine total first-order loss rate constants (k_{loss}) for each cleaning experiment replicate by fitting a first-order exponential function to the decay portion of analyte time series data:

$$[X](t) = [X]_i e^{-k_{loss}t}$$

where $[X]_i$ is the initial mixing ratio of X during this decay period. This portion of experimental data occurs after bleach mopping has concluded; we therefore assume indoor production sources of analyte X are absent, and the observed decay is controlled by first-order sinks (i.e. ventilation, uncharacterized surface and/or chemical loss, etc.). We note the possibility of some chemical production occurring during these decay periods, though we cannot assess the extent of this production given a lack of experimental constraints. Non-negligible chemical production during these periods would result in undercalculated k_{loss}.

We then approximate time-averaged production rates (P) of X from the initial growth periods of experimental data for each cleaning replicate:

$$P = \Sigma_{sources} = \frac{d[X]}{dt} + \Sigma_{sinks} \approx \frac{[X]_t - [X]_0}{\Delta t} + k_{loss}[X]_{avg}$$

where $[X]_t$ and $[X]_0$ are peak and initial (baseline) mixing ratios, $[X]_{avg}$ is the midpoint between $[X]_t$ and $[X]_0$, and Δt is the interval between experimental times corresponding to $[X]_0$ and $[X]_t$.

We report the calculated production rates for bleach-related analytes in Figure A2.7. C_2H_3NO, C_3H_5NO, HNCO, and ClCN exhibit a progressive decrease in production with each sequential cleaning replicate (Figure A2.7a), presumably due to a reduction in surface-bound precursors with each subsequent bleach application (as discussed in main text). While the sniff test measurements suggest the presence of these compounds in the bleach solution as impurities (excluding ClCN), these results indicate secondary chemical production was a more important source of these compounds to indoor air during bleach cleaning. CHO_2Cl, $C_2H_3O_2Cl$, and $C_3H_5O_3Cl$ do not exhibit this progressive decrease in production rates (Figure A2.7b). Rather, production of these compounds followed similar trends to HOCl (Rep 3 >> Rep 4 > Rep 1 ≈ Rep 2), suggesting they share a common indoor source to HOCl during bleach cleaning (i.e. primary emission from the applied bleach) (Mattila et al., 2020).

A2.1.2.3 Comparing indoor production time scales

To further assess the extent to which primary emission (of impurities) vs. secondary chemistry controls indoor mixing ratios of various bleach-related analytes during HOMEChem, we determine times at which indoor production of these analytes begin (t_{prod}) during bleach cleaning experiments performed on 10 June 2018. We calculate t_{prod} for analyes of interest as time at which indoor mixing ratios increase significantly above pre-cleaning background levels. This background-level threshold was calculated as the mean plus three times the standard deviation of indoor mixing ratios between approximately 5-20 mins prior to a bleach cleaning experiment.

We plot t_{prod} relative to values calculated for HOCl (Figure A2.8)—used here as a tracer for primary emission from bleach solution.(Mattila et al., 2020) C_2H_3NO, C_3H_5NO, HNCO, and ClCN typically increase significantly above background levels ~5-15 minutes after HOCl; whereas CHO_2Cl, $C_2H_3O_2Cl$, and $C_3H_5O_3Cl$ increase ~0-2 minutes after HOCl. To further demonstrate the timescales at which t_{prod} occur, we visually compare indoor mixing ratio time series of these analytes during a representative bleach cleaning period (Figure A2.9).

These results are consistent with trends observed in the calculated production rates. CHO_2Cl, $C_2H_3O_2Cl$, and $C_3H_5O_3Cl$ mixing ratios occur at timescales comparable to HOCl, indicating that these analytes likely share a common source during bleach cleaning (i.e. primary emission of solution impurities). C_2H_3NO, C_3H_5NO, HNCO, and ClCN increase at timescales much later than HOCl, indicating that secondary chemical production following the application of bleach is required to explain the observed production of these compounds.

A2.2 Chapter 3 SI figures

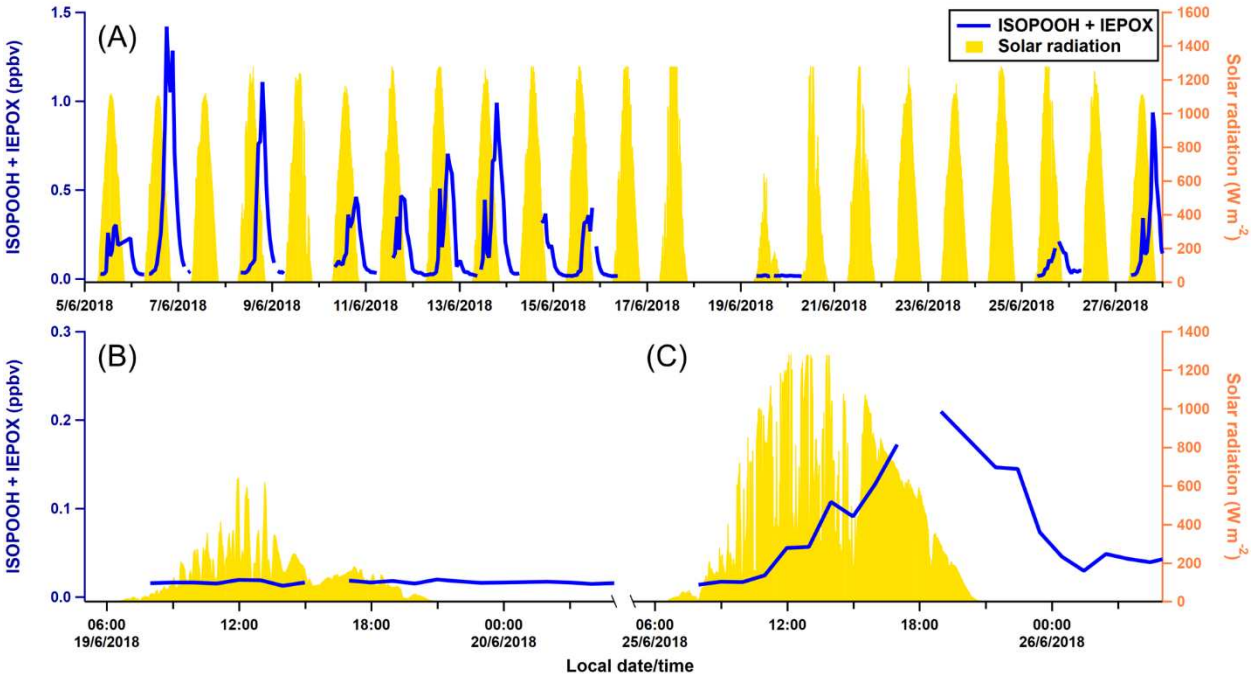

Figure A2.1. Summed mixing ratios of outdoor isoprene hydroperoxyperoxides (ISOPOOH) and isoprene epoxydiols (IEPOX) measured by I^- CIMS (left axes; blue traces), and outdoor solar radiation (right axes; yellow shaded areas) shown (a) throughout the HOMEChem campaign, and on (b) 19 June 2018 and (c) 25 June 2018. We performed bleach cleaning experiments on 19 and 25 June 2018 at approximately 17:35 local time. We collected solar radiation data with a HOBO Weather Station Kit (Onset) located approximately 100 m from the test house.

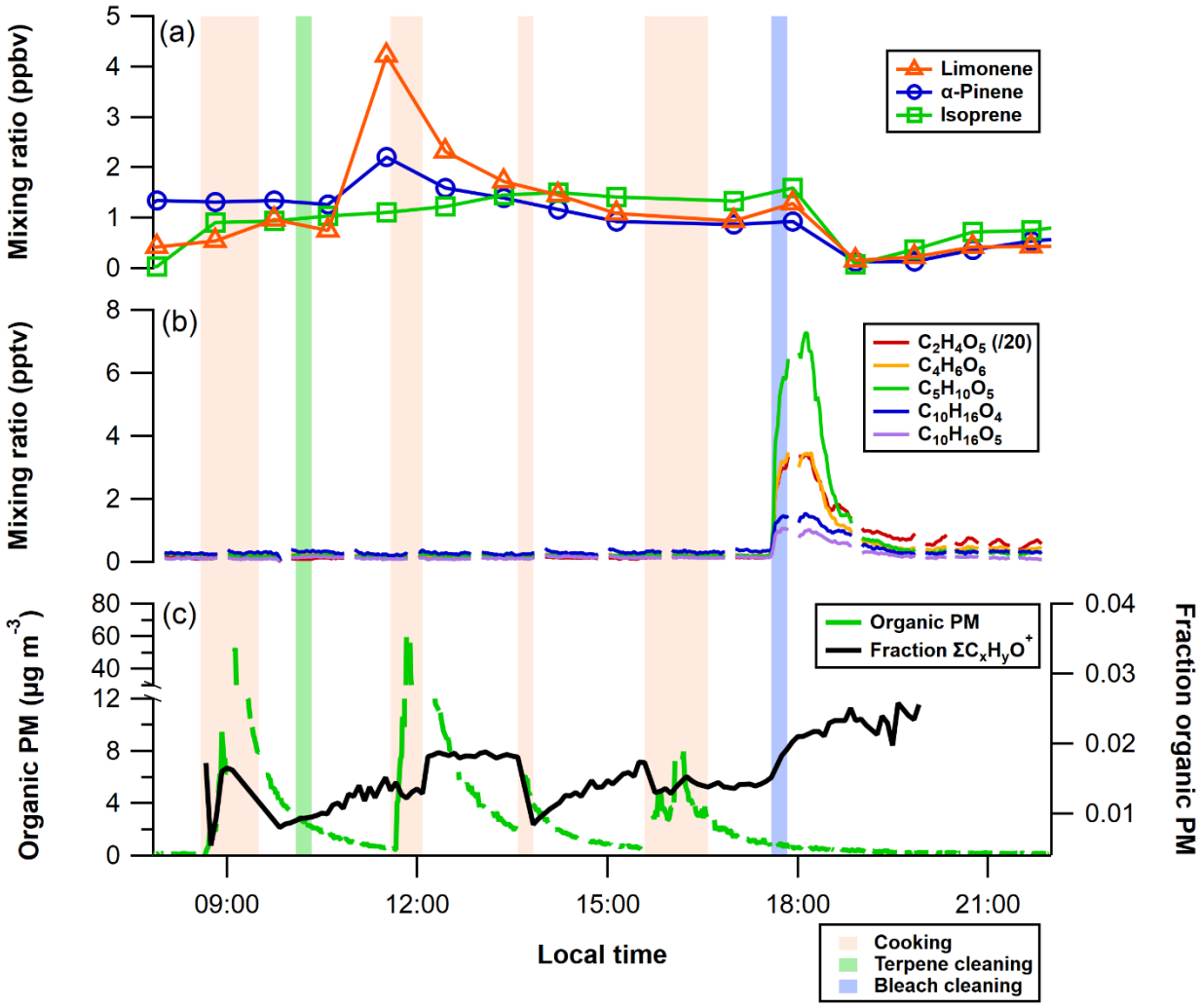

Figure A2.2. Indoor time series of (a) limonene (orange triangles), α-pinene (blue circles), and isoprene (green squares); (b) OVOCs detected by I^- CIMS (colored traces); and (c) organic PM mass concentrations (green), and fractional contribution of $\Sigma C_xH_yO^+$ HR-AMS fragments ($C_3H_5O^+$, $C_3H_6O^+$, $C_3H_7O^+$, $C_3H_7O_2^+$, $C_4H_7O^+$, $C_5H_5O^+$, $C_5H_7O^+$, $C_6H_7O^+$) to total organic PM (black) on 25 June 2018. Shaded areas correspond to local times during which cooking (orange), terpene cleaning (green), and bleach cleaning (blue) took place.

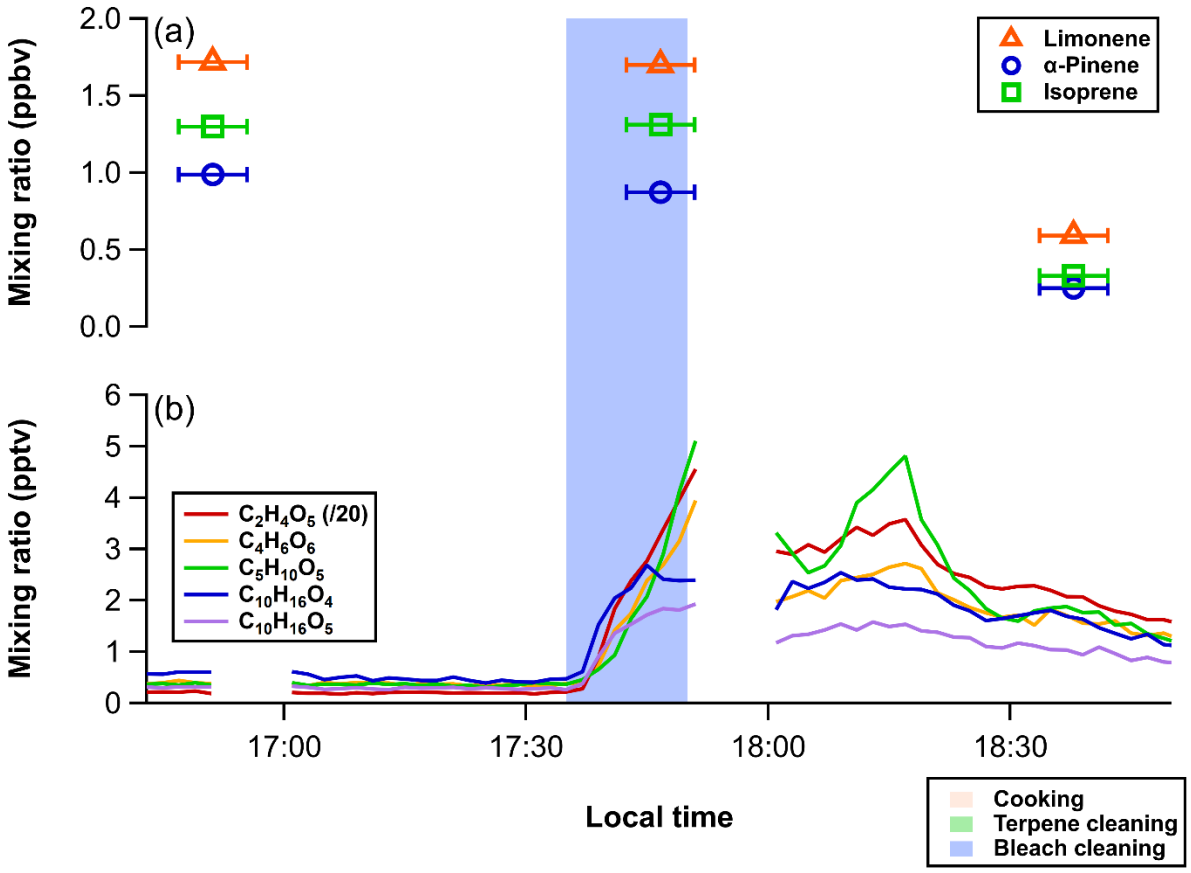

Figure A2.3. Indoor time series of (a) limonene (orange triangles), α-pinene (blue circles), and isoprene (green squares); and (b) OVOCs detected by I^- CIMS (colored traces; arbitrary units) on 25 June 2018. Shaded blue area corresponds to local time during which bleach cleaning took place. Horizonal error bars on panel (a) represent sampling time window of multi-channel GC instrument, and markers represent midpoints of these measurements. Horizontal axis is scaled to emphasize timing of production of OVOCs in panel (b) relative to terpenes in panel (a) during bleach cleaning.

(A) Isocyanates

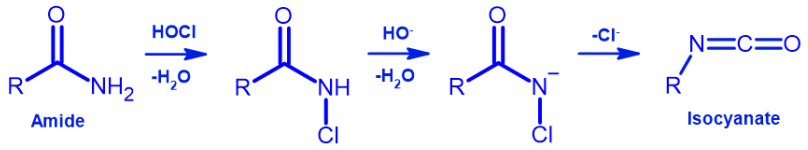

(B) Cyanogen chloride

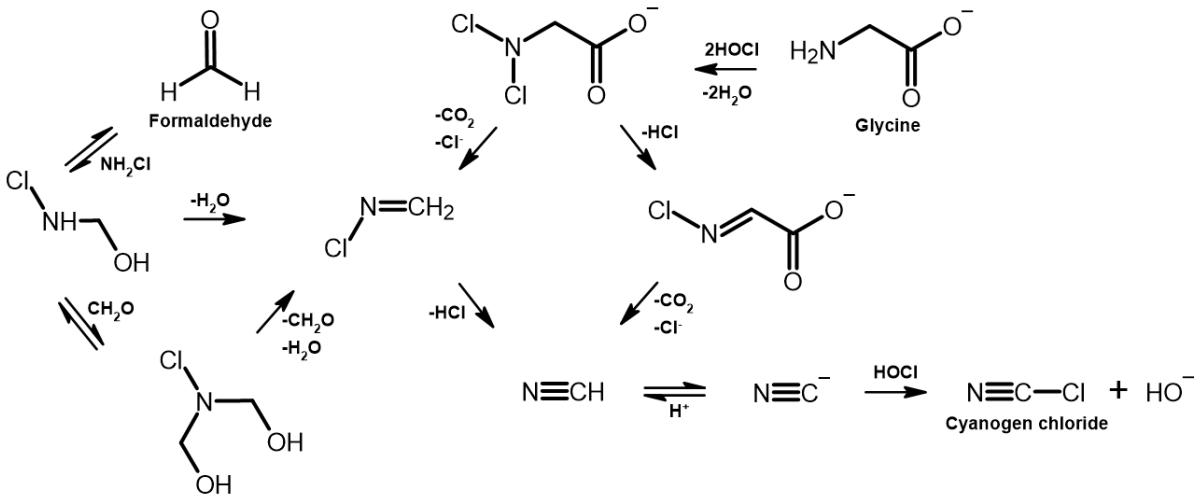

(C) Chloroform

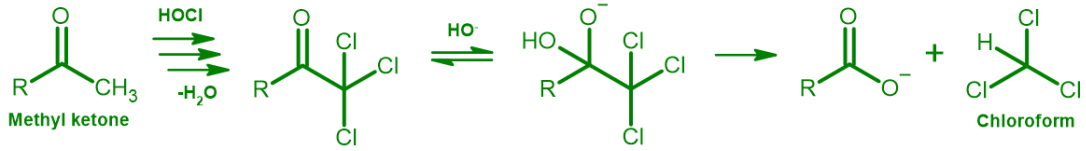

Figure A2.4. Dark chemical mechanisms for production of bleach-related (a) isocyanates, (b) cyanogen chloride, and (c) chloroform, as discussed in the main text.

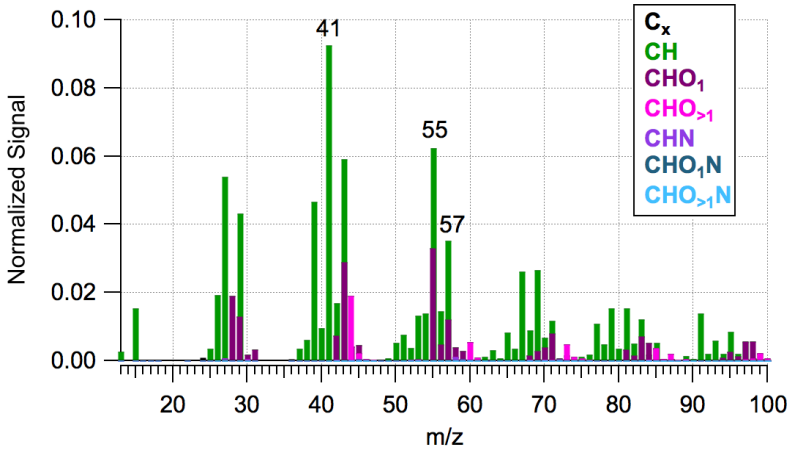

Figure A2.5. HR-AMS mass spectrum of PMF factor "COA2". We labeled AMS peaks of importance to COA (m/z = 41, 55, 57; see SI section A2.1.1).

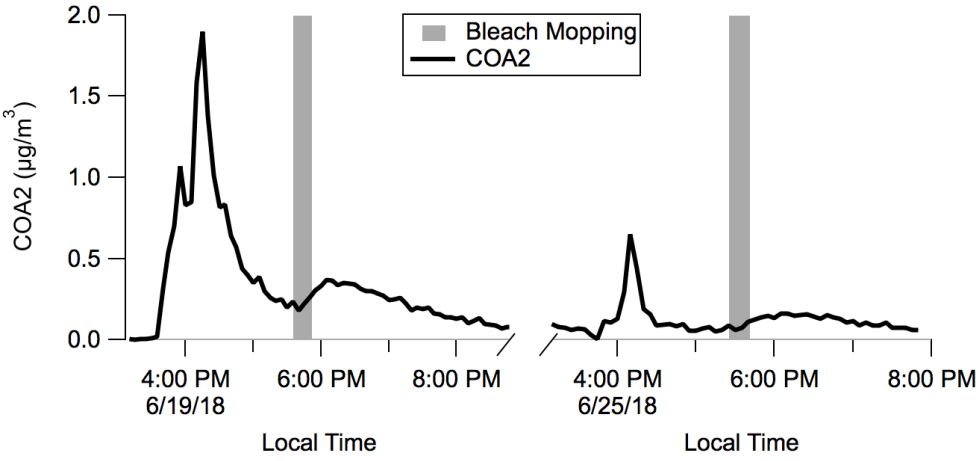

Figure A2.6. Times series of COA2 PMF factor mass concentration (black trace) on two layered days (19 and 25 June 2018) during HOMEChem. The approximate time period of bleach mopping is indicated by the grey shaded area.

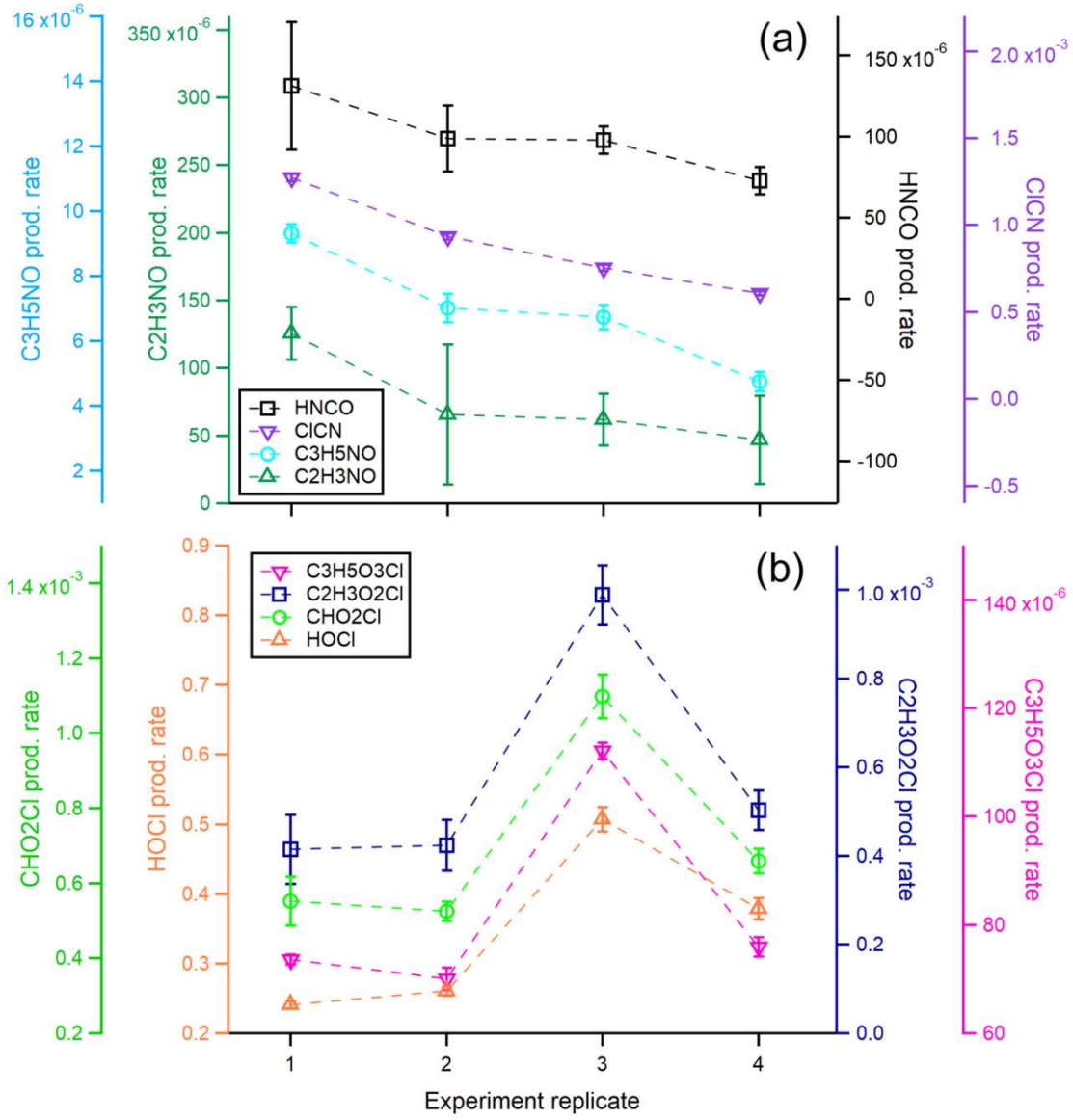

Figure A2.7. Time-averaged production rates (colored markers; units of ppbv s^{-1}) calculated for (a) C_2H_3NO, C_3H_5NO, HNCO, and ClCN; and (b) HOCl, CHO_2Cl, $C_2H_3O_2Cl$, and $C_3H_5O_3Cl$ for each sequential bleach cleaning replicate performed on 10 June 2018. Error bars represent propagated uncertainties from these calculations.

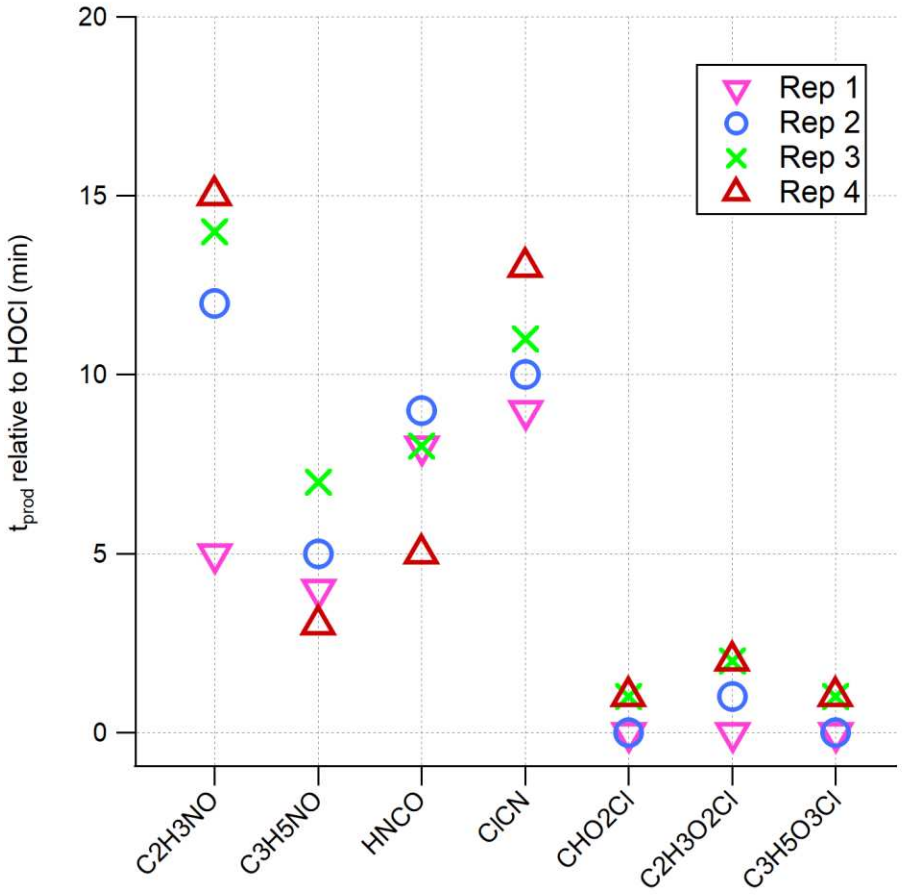

Figure A2.8. t_{prod} (defined in section A2.1.2) relative to HOCl (colored markers) calculated for various bleach-related analytes. Marker shape/color indicates bleach cleaning replicate performed on 10 June 2018 (see figure legend).

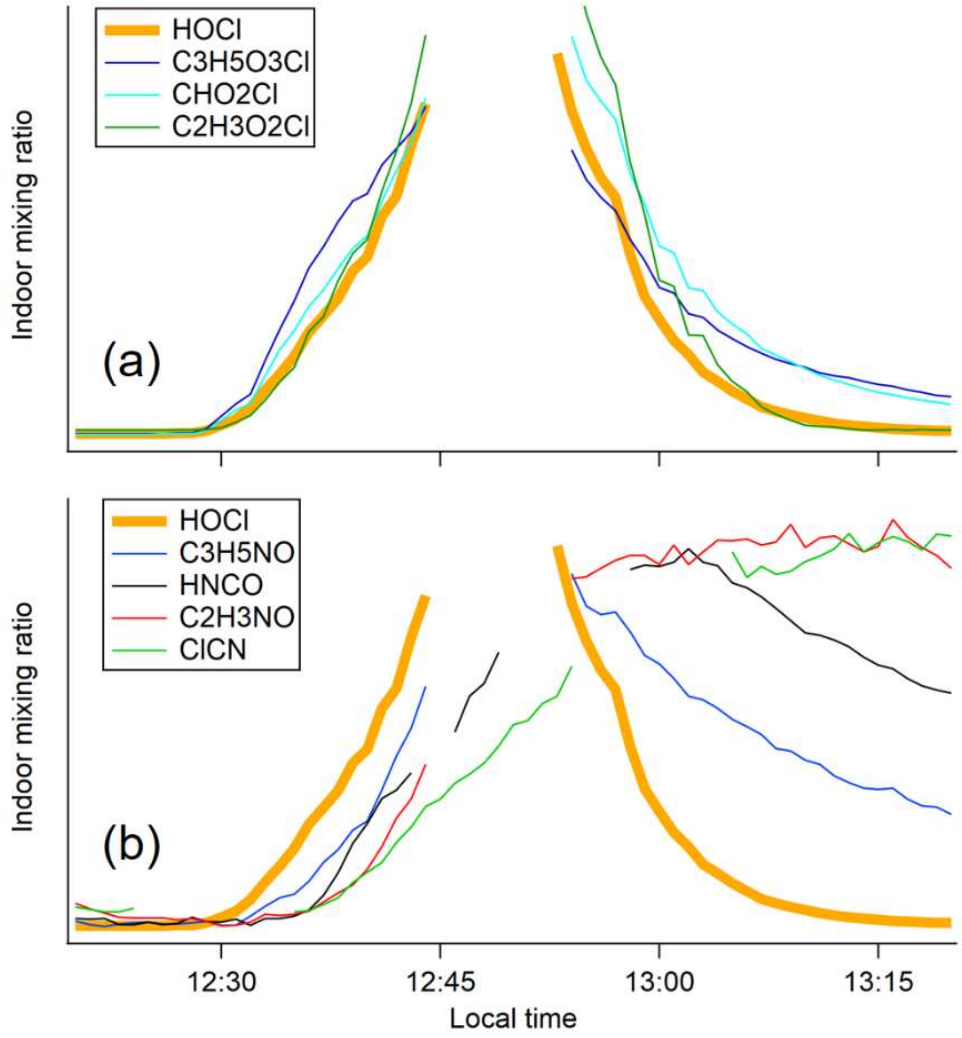

Figure A2.9. Time series of indoor (a) CHO_2Cl, $C_2H_3O_2Cl$, and $C_3H_5O_3Cl$; and (b) C_2H_3NO, C_3H_5NO, HNCO, and ClCN mixing ratios (various colored traces) on a bleach cleaning replicate performed on 10 June 2018. We include HOCl mixing ratios (yellow trace) on panels (a) and (b) as a visual tracer for primary emission. We do not report magnitudes of indoor mixing ratios here; vertical axes are adjusted to emphasize time scales where analytes increase above pre-cleaning background levels.

REFERENCES

Allan, J. D., Williams, P. I., Morgan, W. T., Martin, C. L., Flynn, M. J., Lee, J., Nemitz, E., Phillips, G. J., Gallagher, M. W., and Coe, H.: Contributions from transport, solid fuel burning and cooking to primary organic aerosols in two UK cities, Atmos. Chem. Phys., 10, 647-668, 10.5194/acp-10-647-2010, 2010.

Farmer, D. K., Vance, M. E., Abbatt, J. P. D., Abeleira, A., Alves, M. R., Arata, C., Boedicker, E., Bourne, S., Cardoso-Saldaña, F., Corsi, R., DeCarlo, P. F., Goldstein, A. H., Grassian, V. H., Hildebrandt Ruiz, L., Jimenez, J. L., Kahan, T. F., Katz, E. F., Mattila, J. M., Nazaroff, W. W., Novoselac, A., O'Brien, R. E., Or, V. W., Patel, S., Sankhyan, S., Stevens, P. S., Tian, Y., Wade, M., Wang, C., Zhou, S., and Zhou, Y.: Overview of HOMEChem: House Observations of Microbial and Environmental Chemistry, Environ. Sci. Process. Impacts, 21, 1280-1300, 10.1039/C9EM00228F, 2019.

Mattila, J. M., Lakey, P. S. J., Shiraiwa, M., Wang, C., Abbatt, J. P. D., Arata, C., Goldstein, A. H., Ampollini, L., Katz, E. F., DeCarlo, P. F., Zhou, S., Kahan, T. F., Cardoso-Saldaña, F. J., Hildebrandt Ruiz, L., Abeleira, A., Boedicker, E., Vance, M. E., and Farmer, D. K.: Multiphase chemistry controls inorganic chlorinated and nitrogenated compounds in indoor air during bleach cleaning, Environ. Sci. Technol., 54, 1730-1739, 10.1021/acs.est.9b05767, 2020.

Mohr, C., Huffman, J. A., Cubison, M. J., Aiken, A. C., Docherty, K. S., Kimmel, J. R., Ulbrich, I. M., Hannigan, M., and Jimenez, J. L.: Characterization of Primary Organic Aerosol Emissions from Meat Cooking, Trash Burning, and Motor Vehicles with High-Resolution Aerosol Mass Spectrometry and Comparison with Ambient and Chamber Observations, Environ. Sci. Technol., 43, 2443-2449, 10.1021/es8011518, 2009.

Ulbrich, I. M., Canagaratna, M. R., Zhang, Q., Worsnop, D. R., and Jimenez, J. L.: Interpretation of organic components from Positive Matrix Factorization of aerosol mass spectrometric data, Atmos. Chem. Phys., 9, 2891-2918, 2009.

APPENDIX 3 – CHAPTER 4 SUPPLEMENTAL INFORMATION (A3)

A3.1 Chapter 4 supplemental information (SI) text

A3.1.1 Additional OH and O_3 reactivity calculation retails

For OH reactivity calculations, we sourced k_{OH+VOC} from the International Union of Pure and Applied Chemistry (IUPAC) recommended values (Atkinson et al., 2004), the Estimation Programs Interface (EPI; USEPA) (USEPA, 2020), and from various other published literature values, which we report in Table A3.4. For select compounds with no published k_{OH+VOC} available, we estimated k_{OH+VOC} using the Generator of Explicit Chemistry and Kinetics of Organics in the Atmosphere (GECKO-A) model (Table A3.4) (Aumont et al., 2020). For O_3 reactivity calculations, we sourced k_{O3+VOC} from various published literature values (Table A3.4). For all other ROC compounds and unassigned molecular formulas where reported k_{OU+VOC} and k_{O3+VOC} are not available, we conservatively estimated $k_{OH+VOC} = 1 \cdot 10^{-14}$ cm^3 molecule^{-1} s^{-1} and $1 \cdot 10^{-23}$ cm^3 molecule^{-1} s^{-1}, which represent lower bounds of published rate coefficients reported in Table A3.4. We additionally calculated OH reactivity toward CH_4 and CO using $k_{OH+CH4} = 6.3 \cdot 10^{-15}$ cm^{-3} molecule^{-1} s^{-1} and $k_{OH+CO} = 2.4 \cdot 10^{-13}$ cm^{-3} molecule^{-1} s^{-1} (Burkholder et al., 2019).

A3.1.2 Assessing variations in background-level reactive organic carbon indoors throughout HOMEChem

We calculated mean indoor reactive organic carbon (ROC) mass concentrations during several nights of the HOMEChem campaign, and compared them to the mean value calculated during the extensive unoccupied background period (~15 h) on 15 June 2018 (220 μg C m^{-3}) which we used to represent background conditions indoors throughout the HOMEChem campaign in the main text. We performed these calculations between 00:00 and 07:00 local time

on 05, 11, 12, 13, and 26 June 2018—after emissions from the previous day have been sufficiently ventilated (ideally), and prior to activities on the current day. These nights should therefore be representative house background conditions. Mean indoor ROC mass concentrations during the first four nights were within ~10% the magnitude of the unoccupied background period on 15 June 2018 (Figure A3.7), indicating this period was likely representative of the background for experiments performed between 05 – 15 June 2018. Mean indoor ROC calculated the night of 26 June 2018 was considerably higher (320 μg C m^{-3}) than the mean of 15 June 2018 (Figure A3.7), suggesting that house backgrounds may have been influenced by extensive ROC emissions throughout HOMEChem, resulting in elevated background levels later in the campaign. While this may have resulted in overcalculated ROC emissions relative to a 'true' house background later in the campaign, we do not attempt to further characterize nor correct for this issue given lack of relevant experimental data, and note these overcalculations are likely on the order of ~100 μg C m^{-3} (per Figure A3.7).

A3.1.3 Correcting for propane tank-related interferences indoors

We observed large, prolonged spikes in ethane, propane, and isobutane mass concentrations during several periods throughout HOMEChem (Figure A3.8). These periods of elevated ethane, propane, and isobutane emissions often did not coincide with any particular cooking-related activity, during which we would expect emissions of these non-methane hydrocarbons associated with gas stove or oven usage (Figure A3.8b-d). We therefore suspect these prolonged spikes in ethane, propane, and isobutane mixing ratios arose as a result of leaks from a propane tank used to fuel the gas range in the kitchen of the UTest house, particularly given the fact these interferences started to arise following installation of a new propane tank on the morning of 17 June 2018 (Figure A3.8a). We speculate trace amounts of ethane and

isobutane (as impurities) were co-emitted with propane during these leaks. To account for these interferences, we calculated campaign-average ethane, propane, and isobutane mixing ratios as the mean mixing ratios observed during the unoccupied background period on 15 June 2018 (2.9 μg C m^{-3} ethane, 13.9 μg C m^{-3} propane, 2.4 μg C m^{-3} isobutane). This method likely resulted in undercalculated indoor carbon mass concentrations of these compounds during non-background periods, particularly during cooking-related activities.

A3.1.4 Estimating outdoor values for online gas chromatography (GC) measurements

We estimated outdoor mixing ratios of compounds detected by the multi-channel GC system (listed in Table A3.4) by sampling indoor air during periods when doors and windows of the test house were opened for 30 min to flush out indoor emissions with outdoor air (n = 10). During these periods, the ~8 min window of GC sampling fell entirely within the 30 min window of open doors and windows. We used the average of these indoor GC measurements to estimate campaign-average outdoor mixing ratios of these compounds.

We compare estimated outdoor mixing ratios for several VOCs measured by the GC during HOMEChem to published values from urban air in Guangzhou and Dongguan, China (Barletta et al., 2008); urban air in Pasedena, CA and Houston, TX (Heald et al., 2020; Roberts et al., 2003), and semi-urban air in the Colorado Front Range (Table A3.5) (Abeleira et al., 2017). Estimated outdoor mixing ratios of these VOCs during HOMEChem were of similar magnitude to reported values, with many estimates falling within the reported literature ranges, indicating this method was reasonable for estimating the contribution of these GC-derived VOCs toward outdoor ROC mass concentrations during HOMEChem.

A3.2 Chapter 4 SI figures

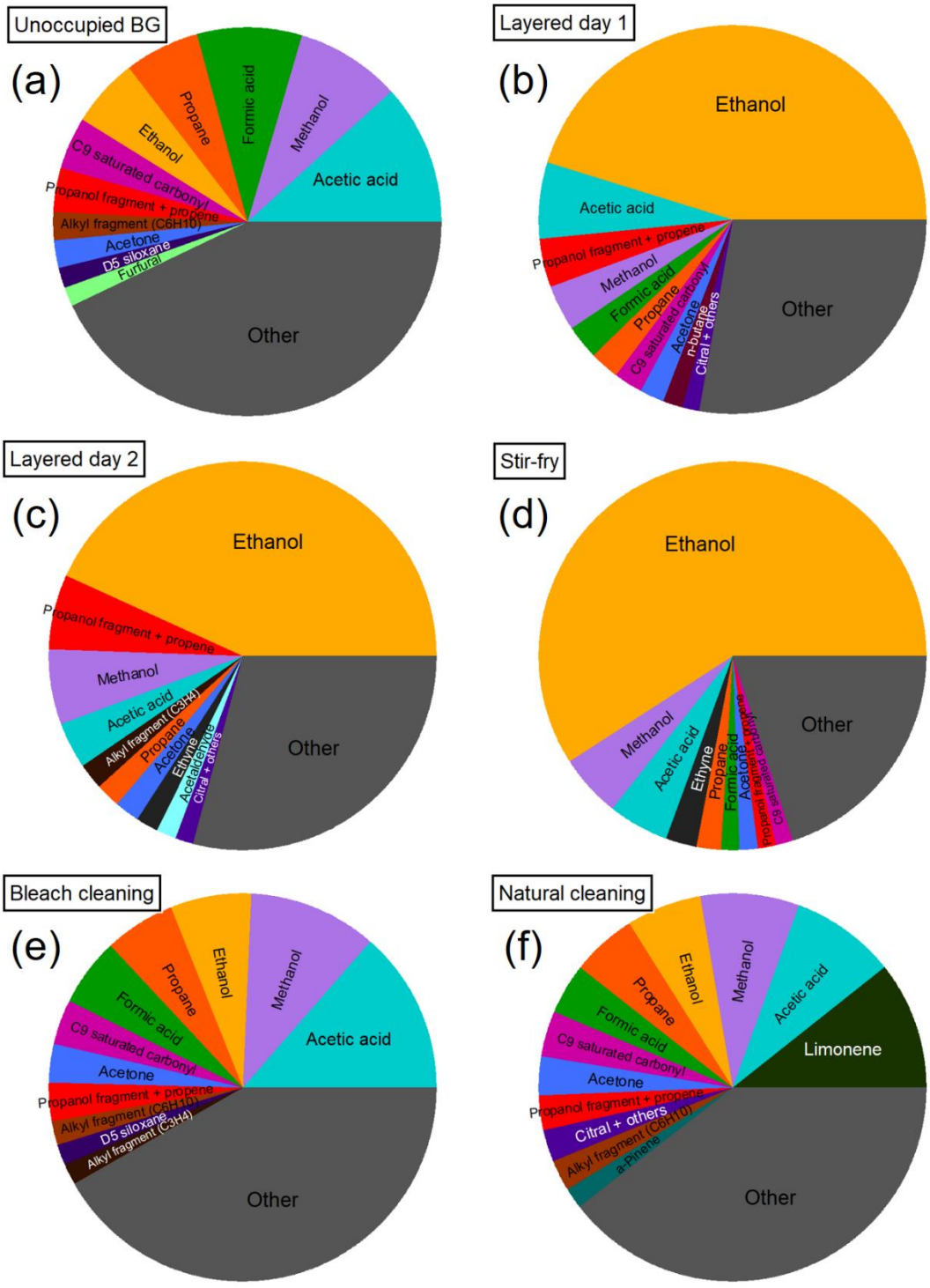

Figure A3.1. Contributions of individual compounds to indoor ROC during (a) unoccupied backgrounds, (b,c) layered days on 08 June 2018 ("layered day 1") and 25 June 2018 ("layered day 2"), (d) sequential stir-frying, (e) sequential bleach cleaning, and (f) cleaning with an "all-natural" cleaning product.

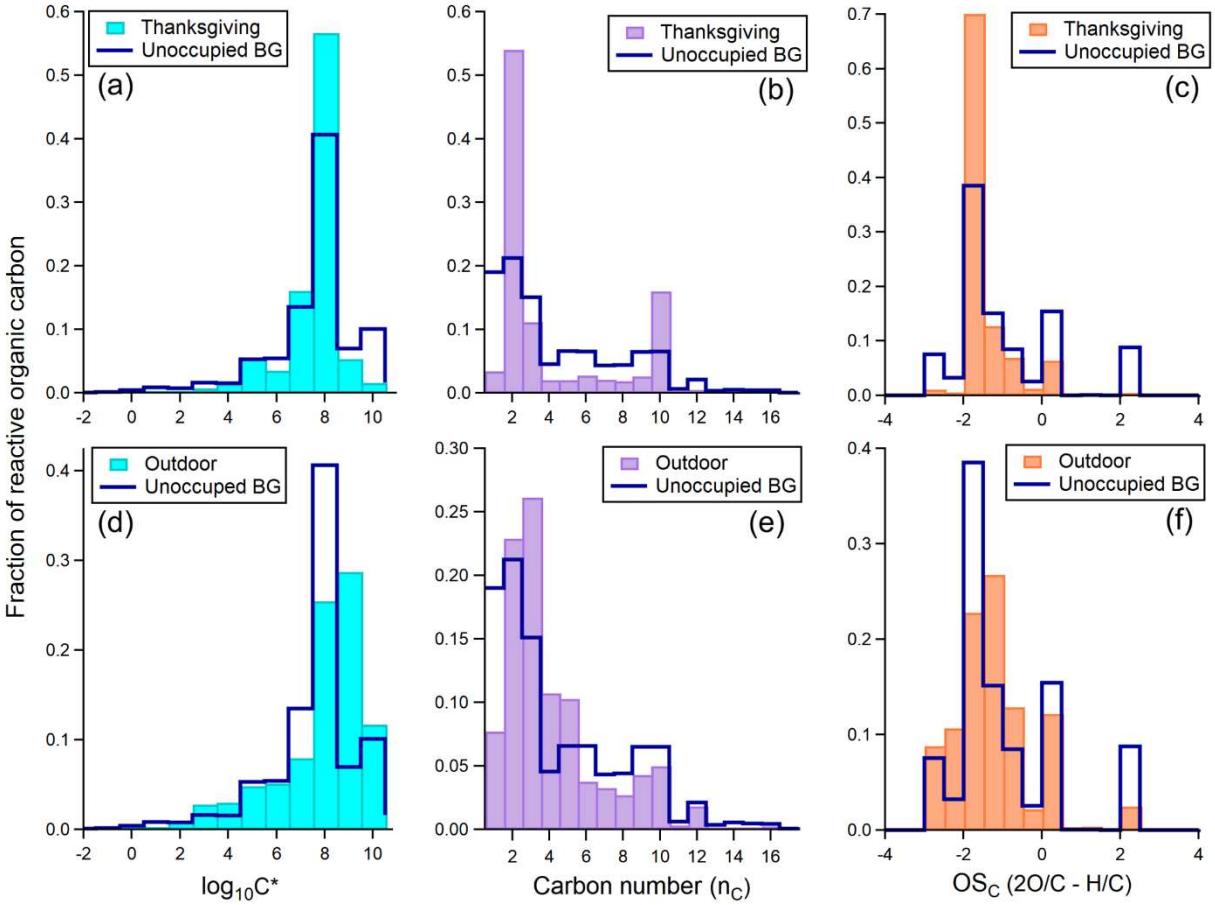

Figure A3.2. Fractional ROC distributions during Thanksgiving (a-c) and outdoor (d-f) measurements by $\log_{10}C^*$ (a,d), carbon number (b,e), and carbon oxidation state (OS_C) (c,f). Distributions during unoccupied background periods are included for comparison (solid blue trace).

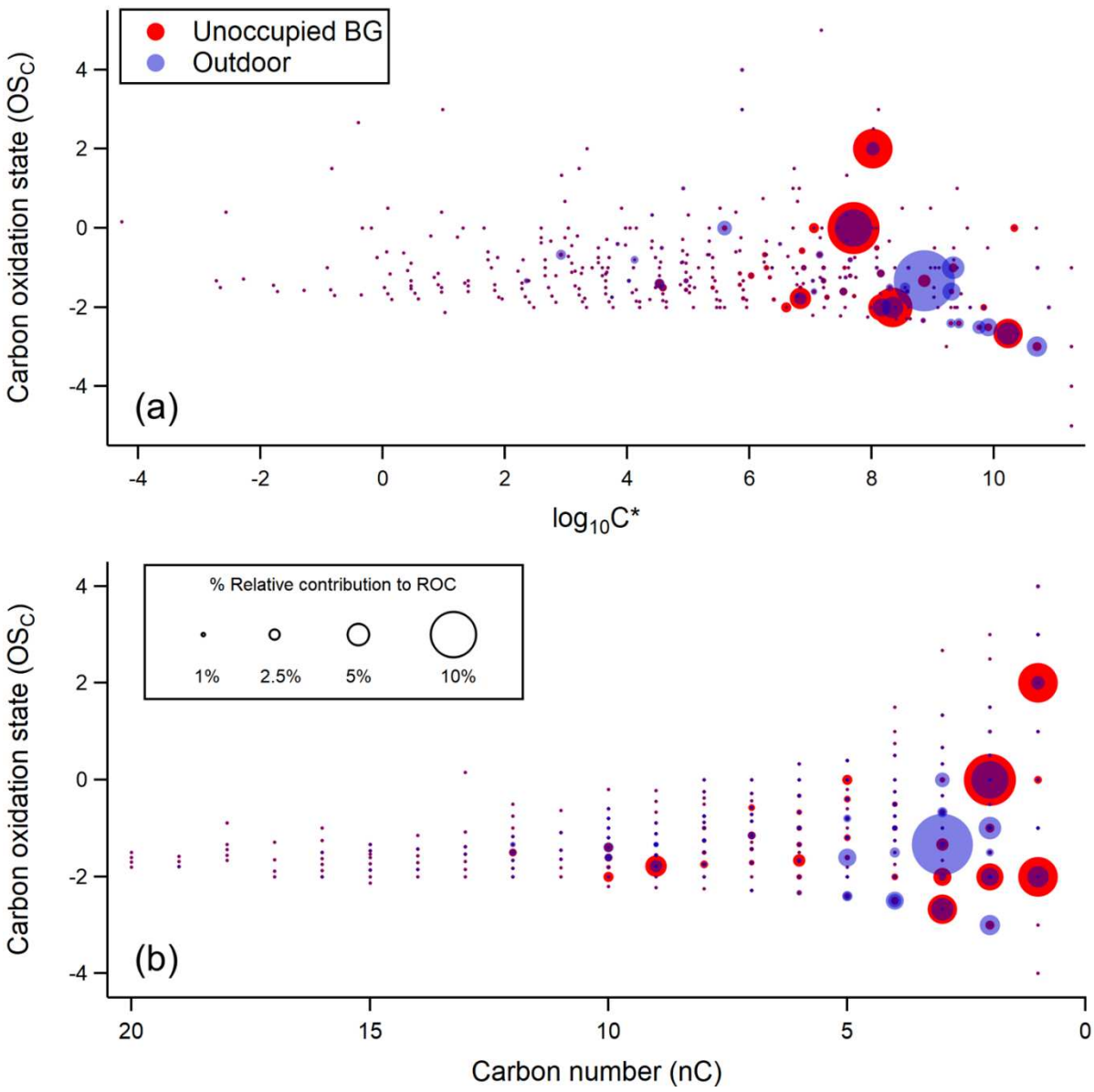

Figure A3.3. Reactive organic carbon oxidation state as a function of (a) $\log_{10}c^*$ and (b) carbon number during unoccupied indoor (red circle markers) and outdoor (blue circle markers) sampling. Compound markers are sized by their relative contribution toward ROC per legend in panel (b).

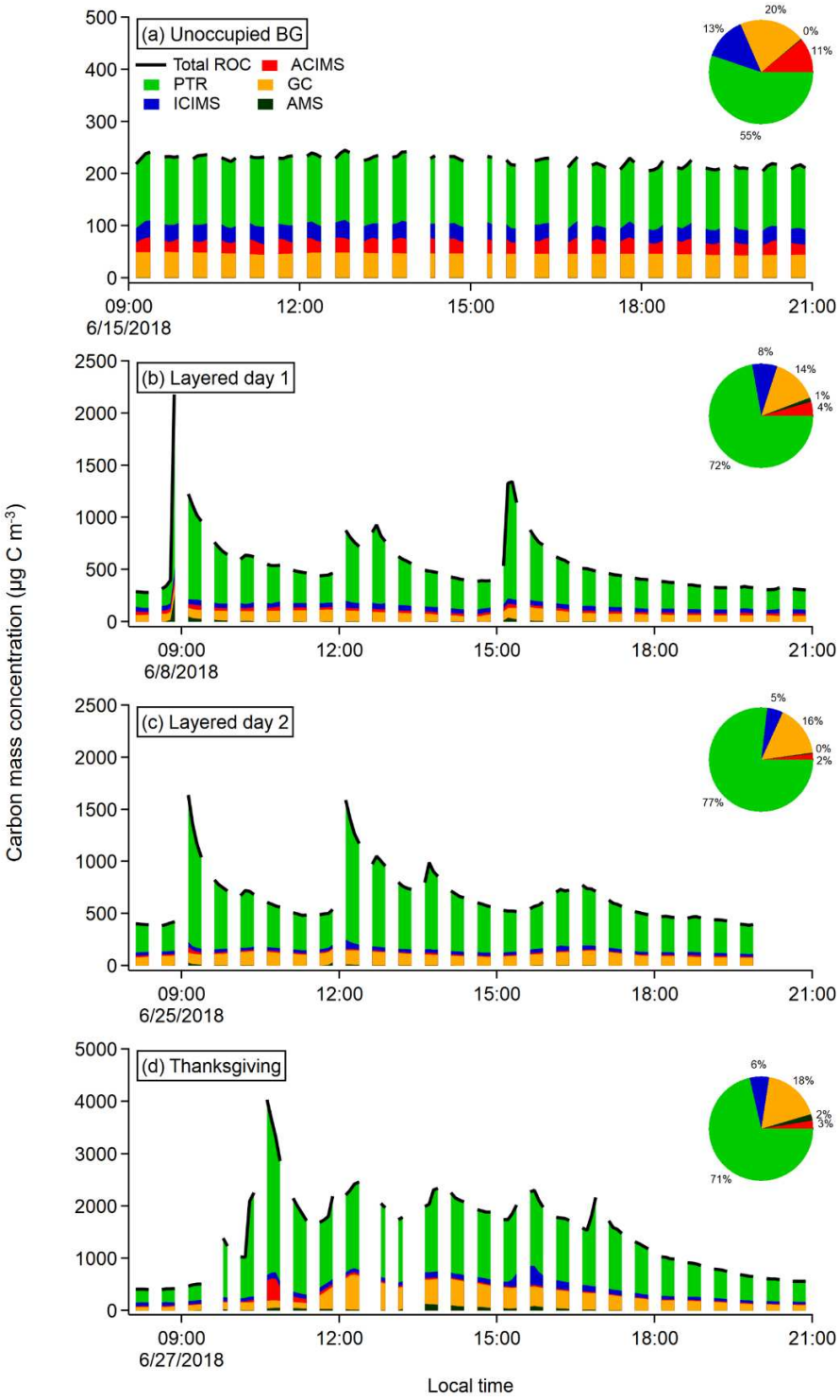

Figure A3.4. Stacked contributions of individual instrument measurements (colored areas; see figure legend) to indoor ROC mass concentration time series (solid black trace) during (a) unoccupied BG, (b,c) layered days, and (d) Thanksgiving. Inset pie charts show average contributions of each instrument to ROC throughout each sampling period. See Farmer et al. (2019) for specific details on activities performed during layered experiments and Thanksgiving.

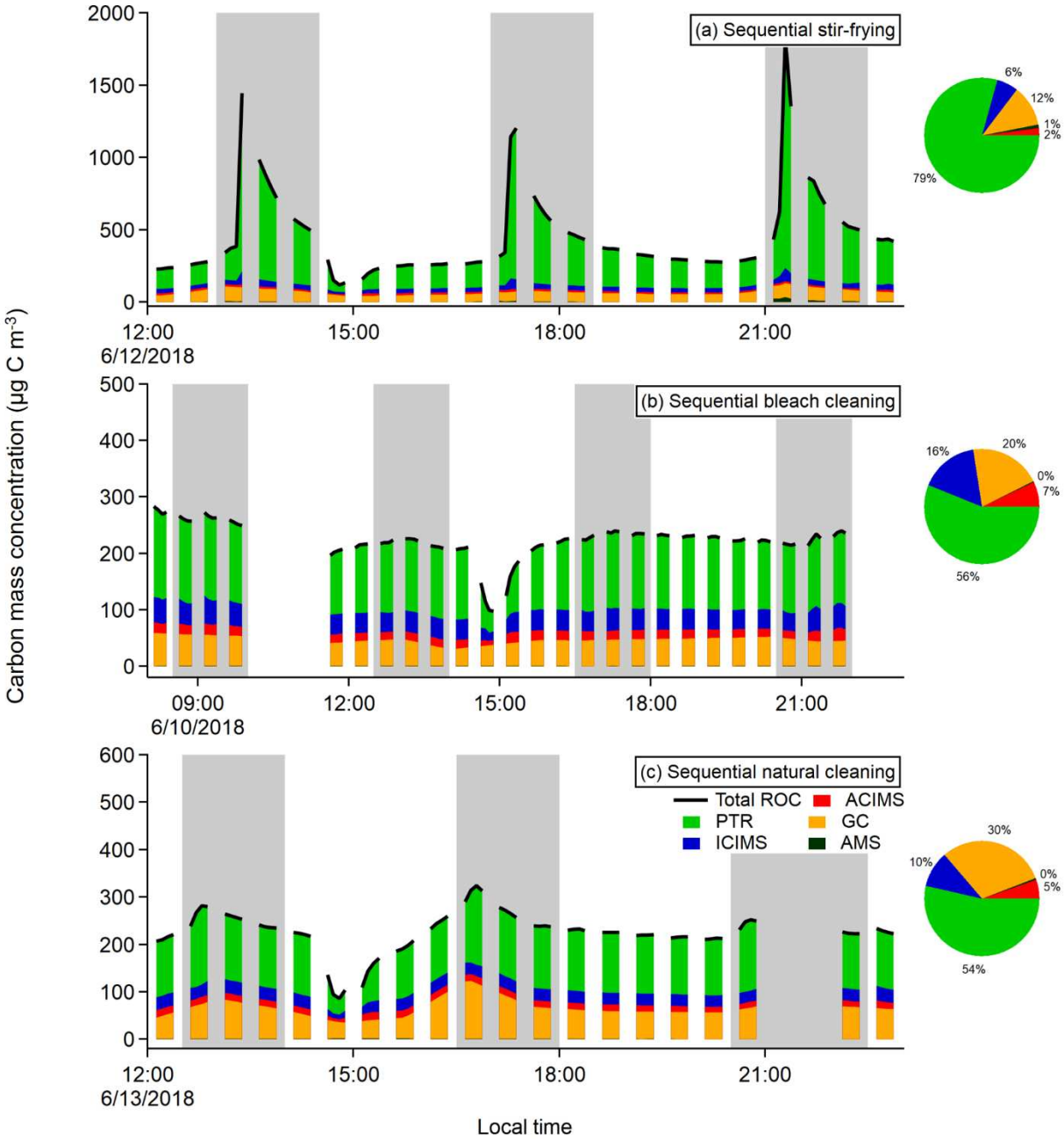

Figure A3.5. Stacked contributions of individual instrument measurements (colored areas; see figure legend) to indoor ROC mass concentration time series during sequential (a) stir-frying, (b) bleaching, and (c) natural cleaning experiments. Inset pie charts show average contributions of each instrument to ROC throughout each experiment. Shaded grey areas behind ROC time series data indicate periods during which we perform ROC magnitude and compositional analysis as discussed in the main text. Sequential activity replicates began at approximately 08:30, 12:30, 16:30, and 20:30 local time, and lasted approximately 90 mins each. We opened doors and windows to enhance ventilation of indoor emissions for 30 mins at approximately 10:30 and 14:30 local time—these periods did not overlap with our sequential activity ROC calculations.

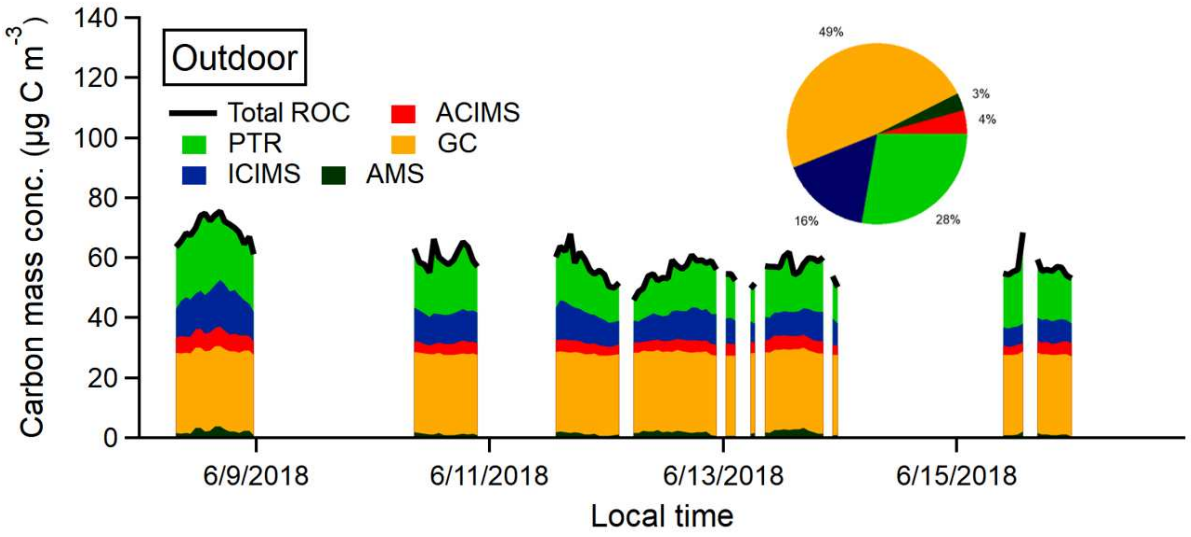

Figure A3.6. Stacked contributions of individual instrument measurements (colored areas; see figure legend) to outdoor ROC mass concentration time series. Inset pie chart shows average contributions of each instrument to outdoor ROC.

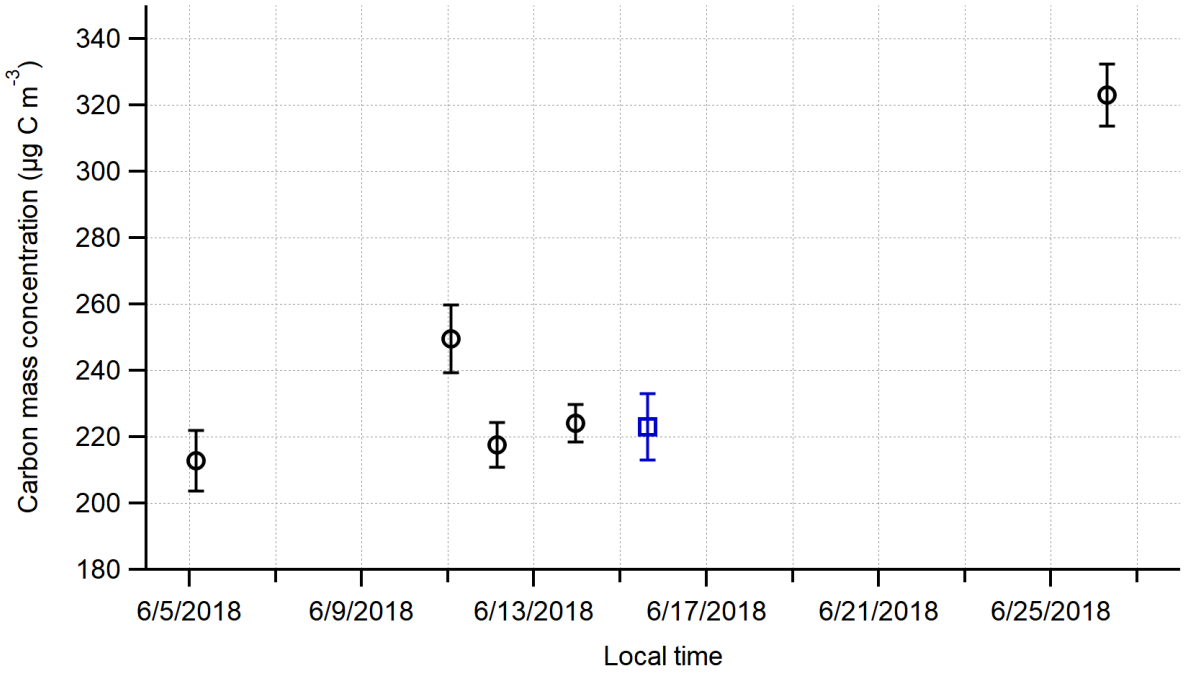

Figure A3.7. Mean (± one standard deviation) ROC mass concentrations calculated on nights discussed in SI section A3.1.2 (black markers), and mean (± one standard deviation) ROC mass concentration during the extensive unoccupied background period on 15 June 2018 (blue marker).

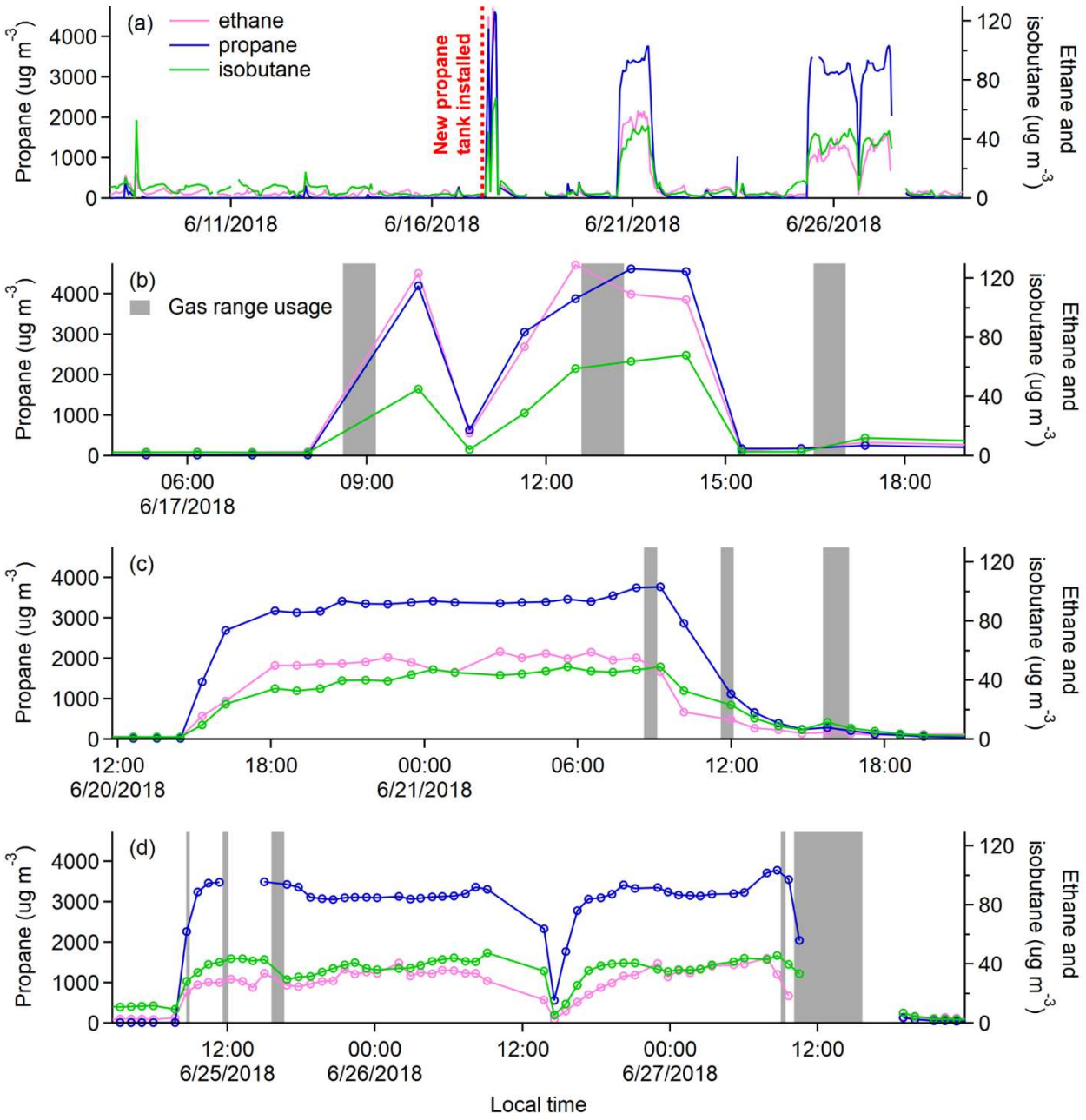

Figure A3.8. Indoor propane, ethane, and isobutane mass concentrations (colored lines and markers; see figure legend) measured by the GC (a) throughout HOMEChem, and (b-d) during various periods where interferences from when a suspected propane tank leak occurred. We show when a new propane tank was installed on the morning of 17 June 2018 in panel (a) (dashed vertical red line). Shaded grey areas in panels (b-d) represent approximate times when the gas range inside of the UTest house was used.

A3.3 Chapter 4 SI tables

Table A3.1 – Median $log_{10}C^*$, nC, and OS_C of indoor and outdoor ROC during HOMEChem

	Unocc. BG	Bleach cleaning	Natural cleaning	Stir-frying	Layered exp. 1	Layered exp. 2	Thanks-giving	Outdoor
$log_{10}C^*$	7.9 (7.7)	8.0	7.7	8.2 (8.0)	8.2 (7.7)	8.2 (7.7)	8.2 (7.1)	8.3
nC	3 (3)	3	4	2 (3)	2 (3)	2 (3)	2 (6)	3
OS_C	-1.5 (-1.5)	-1.5	-1.6	-2 (-1.4)	-2 (-1.4)	-2 (-1.6)	-2 (-1.4)	-1.3

Values in parenthesis represent median physiochemical property value of ROC when excluding ethanol from the analysis. "Unocc. BG" = unoccupied background. "Layered exp. 1 and 2" refer to layered experiments on 08 and 25 June 2018, respectively.

Table A3.2 – Calculated OH reactivities for highest contributing ROC species during HOMEChem

Unoccupied background		
Compound	**OH reactivity (s^{-1})**	**Contribution to total OH reactivity (%)**
isoprene	1.4	9.7
acetaldehyde	1.3	8.8
furfural	1.2	8.7
formaldehyde	1.2	8.6
ethanol	1.0	7.2
methanol	0.9	6.2
limonene	0.8	5.5
α-pinene	0.7	5.2
1-butene	0.7	4.9
Total	**14.3 ± 0.5**	
Bleach cleaning		
Compound	**OH reactivity (s^{-1})**	**Contribution to total OH reactivity (%)**
acetaldehyde	1.5	10.3
isoprene	1.2	8.4
ethanol	1.3	8.6
formaldehyde	1.2	8.4
furfural	1.2	8.3
methanol	1.1	7.8
dimethyl disulfide	0.9	6.0
acetic acid	0.6	3.8
glycerol	0.5	3.6

Total	**14. ± 1.**	
	Natural cleaning	
Compound	**OH reactivity (s^{-1})**	**Contribution to total OH reactivity (%)**
limonene	22.8	61.6
isoprene	1.8	4.9
acetaldehyde	1.5	4.0
ethanol	1.3	3.5
α-pinene	1.2	3.2
formaldehyde	1.2	3.2
furfural	1.1	2.9
methanol	1.0	2.6
glycerol	0.6	1.7
Total	**40. ± 10.**	
	Stir-frying	
Compound	**OH reactivity (s^{-1})**	**Contribution to total OH reactivity (%)**
ethanol	32.8	61.2
isoprene	3.3	6.2
acetaldehyde	2.8	5.1
methanol	1.6	3.0
formaldehyde	1.3	2.5
furfural	1.3	2.4
glycerol	1.1	2.0
limonene	1.0	1.9
α-pinene	1.0	1.8
Total	**50. ± 30.**	
	Layered experiment 1 (08 June 2018)	
Compound	**OH reactivity (s^{-1})**	**Contribution to total OH reactivity (%)**
ethanol	20.9	49.0
limonene	3.9	9.1
acetaldehyde	2.2	5.2
α-pinene	1.1	2.5
formaldehyde	1.4	3.3
glycerol	1.3	3.0
furfural	1.2	2.9
methanol	1.0	2.3
acetic acid	0.6	1.5
Total	**40. ± 20.**	
	Layered experiment 2 (25 June 2018)	
Compound	**OH reactivity (s^{-1})**	**Contribution to total OH reactivity (%)**
ethanol	23.5	44.7
limonene	5.2	9.9
acetaldehyde	4.2	8.0
isoprene	2.7	5.1

ethanol	1.9	3.6
formaldehyde	1.5	2.8
ethene	1.3	2.5
α-pinene	1.3	2.5
glycerol	1.1	2.2
Total	**50. ± 20.**	

Thanksgiving		
Compound	**OH reactivity (s^{-1})**	**Contribution to total OH reactivity (%)**
limonene	114.0	48.7
ethanol	58.4	24.9
pyrrole	16.6	7.1
acetaldehyde	13.4	5.7
α-pinene	5.7	2.4
glycerol	3.7	1.6
isoprene	2.2	0.9
furfural	1.9	0.8
formaldehyde	1.8	0.8
Total	**200. ± 100.**	

Outdoor		
Compound	**OH reactivity (s^{-1})**	**Contribution to total OH reactivity (%)**
isoprene	1.9	33.2
acetaldehyde	1.0	16.9
glycerol	0.8	14.4
limonene	0.4	7.5
α -pinene	0.2	3.1
ethanol	0.2	2.7
methanol	0.1	1.9
lactic acid	0.1	1.4
acetic acid	0.1	1.3
Total	**5.7 ± 0.4**	

Table A3.3 – Calculated O_3 reactivities for highest contributing ROC species during HOMEChem

Unoccupied background		
Compound	**O_3 reactivity (s^{-1})**	**Contribution to total O_3 reactivity (%)**
α-pinene	1.4E-06	43.2
limonene	1.0E-06	33.1
1-butene	2.3E-07	7.2
isoprene	1.8E-07	5.7
styrene	8.6E-08	2.7
trans-2-butene	5.6E-08	1.8
cis-2-butene	4.8E-08	1.5
isobutene	3.1E-08	1.0

methyl vinyl ketone	2.2E-08	0.7
Total	**(3.1 ± 0.4)E-06**	

Bleach cleaning

Compound	O_3 reactivity (s^{-1})	Contribution to total O_3 reactivity (%)
α-pinene	5.3E-07	32.3
limonene	4.9E-07	30.3
isoprene	1.6E-07	9.8
1-butene	1.5E-07	9.3
styrene	9.0E-08	5.5
trans-2-butene	5.1E-08	3.1
cis-2-butene	3.7E-08	2.3
methyl vinyl ketone	2.1E-08	1.3
benzenediol	2.2E-08	1.4
Total	**(1.6 ± 0.9)E-06**	

Natural cleaning

Compound	O_3 reactivity (s^{-1})	Contribution to total O_3 reactivity (%)
limonene	3.0E-05	91.3
α-pinene	2.2E-06	6.5
isoprene	2.3E-07	0.7
1-butene	1.7E-07	0.5
styrene	9.4E-08	0.3
trans-2-butene	6.7E-08	0.2
cis-2-butene	5.2E-08	0.2
methyl vinyl ketone	2.9E-08	0.1
cis-2-pentene	2.0E-08	0.1
Total	**(3. ± 2.)E-05**	

Stir-frying

Compound	O_3 reactivity (s^{-1})	Contribution to total O_3 reactivity (%)
α-pinene	1.8E-06	40.5
limonene	1.3E-06	30.7
isoprene	4.2E-07	9.6
1-butene	1.7E-07	4.0
ethene	1.4E-07	3.1
ethanol	1.0E-07	2.3
styrene	9.9E-08	2.2
trans-2-butene	9.2E-08	2.1
cis-2-butene	6.6E-08	1.5
Total	**(4.4 ± 0.6)E-06**	

Layered experiment 1 (08 June 2018)

Compound	O_3 reactivity (s^{-1})	Contribution to total O_3 reactivity (%)
limonene	5.2E-06	62.9
α-pinene	2.0E-06	23.9
isoprene	2.7E-07	3.3

1-butene	1.9E-07	2.2
cis-2-butene	1.5E-07	1.8
styrene	1.1E-07	1.3
trans-2-butene	8.9E-08	1.1
ethanol	6.5E-08	0.8
ethene	6.4E-08	0.8
Total	**(8. ± 5.)E-06**	

Layered experiment 2 (25 June 2018)

Compound	O_3 reactivity (s^{-1})	Contribution to total O_3 reactivity (%)
limonene	6.9E-06	65.0
α-pinene	2.4E-06	22.1
isoprene	3.4E-07	3.2
1-butene	2.5E-07	2.3
ethene	2.4E-07	2.2
styrene	1.3E-07	1.2
trans-2-butene	8.0E-08	0.8
ethanol	7.3E-08	0.7
methyl vinyl ketone	5.8E-08	0.5
Total	**(1.1 ± 0.6)E-05**	

Thanksgiving

Compound	OH reactivity (s^{-1})	Contribution to total OH reactivity (%)
limonene	1.5E-04	93.0
α-pinene	1.0E-05	6.3
isoprene	2.8E-07	0.2
ethanol	1.8E-07	0.1
styrene	1.6E-07	0.1
1-butene	1.0E-07	0.1
benzenediol	9.7E-08	0.1
methyl vinyl ketone	6.5E-08	<0.1
ethene	4.2E-08	<0.1
Total	**(2. ± 2.)E-04**	

Outdoor

Compound	O_3 reactivity (s^{-1})	Contribution to total O_3 reactivity (%)
limonene	5.7E-07	44.6
α-pinene	3.2E-07	25.4
isoprene	2.4E-07	19.0
trans-2-butene	4.0E-08	3.2
cis-2-butene	2.1E-08	1.7
1-butene	1.8E-08	1.4
methyl vinyl ketone	1.6E-08	1.3
cis-2-pentene	1.3E-08	1.0
isobutene	1.0E-08	0.8
Total	**(1.3 ± 0.1)E-06**	

Table A3.4 – Molecular formulas, assigned compound identities, instrumental methods, and second-order VOC+OH and VOC+O_3 rate constants for all chemically-speciated reactive organic carbon compounds measured during HOMEChem.

Molecular formula	Compound ID	Instrumental method	k_{OH+VOC} (cm^3 $molecule^{-1}$ s^{-1})	Reference/note	k_{O3+VOC} (cm^3 $molecule^{-1}$ s^{-1})	Reference/note
HCN	hydrogen cyanide	ICIMS	3.0E-14	IUPAC preferred value (Atkinson et al., 2004)	1.0E-23	Conservative lower-estimate
HNCO	isocyanic acid	ACIMS	1.0E-14	Conservative lower-estimate	1.0E-23	Conservative lower-estimate
$CHBrCl_2$	bromodichloromethane	GC	1.0E-14	Conservative lower-estimate	1.0E-23	Conservative lower-estimate
$CHCl_3$	chloroform	GC	1.0E-13	EPI Suite Database (USEPA, 2020)	1.0E-23	Conservative lower-estimate
CHO_2Cl	chloroformic acid	ICIMS	1.0E-14	Conservative lower-estimate	1.0E-23	Conservative lower-estimate
CH_2O	formaldehyde	PTR	8.5E-12	IUPAC preferred value (Atkinson et al., 2004)	1.0E-20	Atkinson and Arey (2003)
CH_2O_2	formic acid	ACIMS	4.5E-13	IUPAC preferred value (Atkinson et al., 2004)	1.0E-20	Atkinson and Arey (2003)
CH_3NO	formamide	ICIMS	4.4E-12	Bunkan et al. (2015)	1.0E-23	Conservative lower-estimate
CH_3NOS	n-sulfinyl methanamine	PTR	1.0E-14	Conservative lower-estimate	1.0E-23	Conservative lower-estimate
CH_3NO_3	methyl nitrate	GC	2.3E-14	IUPAC preferred value (Atkinson et al., 2004)	1.0E-23	Conservative lower-estimate
CH_4O	methanol	PTR	9.0E-13	IUPAC preferred value (Atkinson et al., 2004)	1.0E-20	Atkinson and Arey (2003)
CH_4O_2	methanediol	PTR	1.0E-14	Conservative lower-estimate	1.0E-23	Conservative lower-estimate
CH_4S	methanethiol	PTR	1.0E-14	Conservative lower-estimate	1.0E-23	Conservative lower-estimate
ClCN	cyanogen chloride	PTR	1.0E-14	Conservative lower-estimate	1.0E-23	Conservative lower-estimate
$C_2Cl_3F_3$	1,1,2-trichloro-1,2,2-trifluoroethane	GC	1.0E-14	Conservative lower-estimate	1.0E-23	Conservative lower-estimate
C_2H_2	ethyne	GC	8.2E-13	EPI Suite Database (USEPA, 2020)	1.0E-20	IUPAC preferred value (Atkinson et al., 2004)
C_2H_3N	acetonitrile	PTR	1.0E-14	Conservative lower-estimate	1.0E-23	Conservative lower-estimate
C_2H_3NO	methyl isocyanate	ICIMS	3.6E-12	Lu et al. (2014)*	1.0E-23	Conservative lower-estimate
$C_2H_3O_2Cl$	chloroacetic acid	ICIMS	1.0E-14	Conservative lower-estimate	1.0E-23	Conservative lower-estimate
C_2H_4	ethene	GC	8.5E-12	EPI Suite Database (USEPA, 2020)	1.6E-18	IUPAC preferred value (Atkinson et al., 2004)

C_2H_4O	acetaldehyde	GC	1.5E-11	IUPAC preferred value (Atkinson et al., 2004)	1.0E-20	Atkinson and Arey (2003)
$C_2H_4O_2$	acetic acid	ICIMS	6.9E-13	IUPAC preferred value (Atkinson et al., 2004)	1.0E-20	Atkinson and Arey (2003)
$C_2H_4O_3$	peracetic acid	ICIMS	1.0E-14	Conservative lower-estimate	1.0E-23	Conservative lower-estimate
C_2H_5NO	acetamide	ICIMS	7.7E-13	Bunkan et al. (2015)	1.0E-23	Conservative lower-estimate
$C_2H_5NO_3$	ethyl nitrate	GC	1.8E-13	IUPAC preferred value (Atkinson et al., 2004)	1.0E-23	Conservative lower-estimate
C_2H_6	ethane	GC	2.4E-13	IUPAC preferred value (Atkinson et al., 2004)	1.0E-23	Atkinson and Arey (2003)
C_2H_6O	ethanol	PTR	3.2E-12	IUPAC preferred value (Atkinson et al., 2004)	1.0E-20	Atkinson and Arey (2003)
C_2H_6OS	2-mercaptoethanol	PTR	1.0E-14	Conservative lower-estimate	1.0E-23	Conservative lower-estimate
$C_2H_6O_2S$	dimethyl sulfone	PTR	1.0E-14	Conservative lower-estimate	1.0E-23	Conservative lower-estimate
$C_2H_6S_2$	dimethyl disulfide	PTR	2.3E-10	EPI Suite Database (USEPA, 2020)	1.0E-23	Conservative lower-estimate
$C_2H_8O_2Si$	dimethoxysilane	PTR	1.0E-14	Conservative lower-estimate	1.0E-23	Conservative lower-estimate
C_3H_3N	acrylonitrile	PTR	4.1E-12	EPI Suite Database (USEPA, 2020)	1.0E-23	Conservative lower-estimate
$C_3H_4O_2$	acrylic acid	ICIMS	1.8E-11	Teruel et al. (2007)	6.5E-19	Neeb et al. (1998)**
$C_3H_4O_3$	pyruvic acid	ICIMS	1.2E-13	GECKO-A estimated	1.0E-20	Atkinson and Arey (2003)
$C_3H_4O_4$	malonic acid	ICIMS	1.2E-12	GECKO-A estimated	1.0E-20	Atkinson and Arey (2003)
C_3H_5NO	ethyl isocyanate	ICIMS	1.0E-14	Conservative lower-estimate	1.0E-23	Conservative lower-estimate
$C_3H_5O_3Cl$	chlorolactic acid	ICIMS	1.0E-14	Conservative lower-estimate	1.0E-23	Conservative lower-estimate
C_3H_6O	acetone	GC	1.8E-13	IUPAC preferred value (Atkinson et al., 2004)	1.0E-20	Atkinson and Arey (2003)
$C_3H_6O_2$	propionic acid	ACIMS	1.2E-12	IUPAC preferred value (Atkinson et al., 2004)	1.0E-20	Atkinson and Arey (2003)
$C_3H_6O_3$	lactic acid	ICIMS	3.2E-12	GECKO-A estimated	1.0E-20	Atkinson and Arey (2003)
$C_3H_6O_4$	glyceric acid	ICIMS	1.4E-11	GECKO-A estimated	1.0E-20	Atkinson and Arey (2003)
$C_3H_7NO_3$	isopropyl nitrate	GC	5.8E-13	IUPAC preferred value (Atkinson et al., 2004)	1.0E-23	Conservative lower-estimate
C_3H_8	propane	GC	1.1E-12	IUPAC preferred value (Atkinson et al., 2004)	1.0E-23	Atkinson and Arey (2003)
$C_3H_8O_3$	glycerol	ICIMS	5.5E-11	GECKO-A estimated	1.0E-20	Atkinson and Arey (2003)
C_3H_8S	propanethiol	PTR	1.0E-14	Conservative lower-estimate	1.0E-23	Conservative lower-estimate

C_4H_4O	furan	PTR	4.1E-11	EPI Suite Database (USEPA, 2020)	1.0E-23	Conservative lower-estimate
$C_4H_4O_2$	furanone	PTR	1.0E-14	Conservative lower-estimate	1.0E-23	Conservative lower-estimate
$C_4H_4O_3$	succinic anhydride	PTR	1.0E-14	Conservative lower-estimate	1.0E-23	Conservative lower-estimate
C_4H_5N	pyrrole	PTR	1.1E-10	EPI Suite Database (USEPA, 2020)	1.0E-23	Conservative lower-estimate
C_4H_6O	methylvinylketone	GC	2.0E-11	IUPAC preferred value (Atkinson et al., 2004)	5.2E-18	IUPAC preferred value (Atkinson et al., 2004)
$C_4H_6O_2$	diacetyl	PTR	2.4E-13	EPI Suite Database (USEPA, 2020)	1.0E-20	Atkinson and Arey (2003)
$C_4H_6O_3$	acetic anhydride	ICIMS	1.0E-14	Conservative lower-estimate	1.0E-23	Conservative lower-estimate
$C_4H_6O_4$	succinic acid	ICIMS	2.8E-12	GECKO-A estimated	1.0E-20	Atkinson and Arey (2003)
$C_4H_6O_6$	tataric acid	ICIMS	1.0E-14	Conservative lower-estimate	1.0E-23	Conservative lower-estimate
C_4H_8	cis-2-butene	GC	5.6E-11	IUPAC preferred value (Atkinson et al., 2004)	1.3E-16	IUPAC preferred value (Atkinson et al., 2004)
C_4H_8	isobutene	GC	5.1E-11	IUPAC preferred value (Atkinson et al., 2004)	1.2E-17	IUPAC preferred value (Atkinson et al., 2004)
C_4H_8	1-butene	GC	3.1E-11	IUPAC preferred value (Atkinson et al., 2004)	1.0E-17	IUPAC preferred value (Atkinson et al., 2004)
C_4H_8	trans-2-butene	GC	6.4E-11	IUPAC preferred value (Atkinson et al., 2004)	2.0E-16	IUPAC preferred value (Atkinson et al., 2004)
C_4H_8O	methylethyleketone	GC	1.1E-12	IUPAC preferred value (Atkinson et al., 2004)	1.0E-20	Atkinson and Arey (2003)
C_4H_8OS	methional	PTR	1.0E-14	Conservative lower-estimate	1.0E-23	Conservative lower-estimate
$C_4H_8O_2$	butyric acid	ACIMS	1.8E-12	IUPAC preferred value (Atkinson et al., 2004)	1.0E-20	Atkinson and Arey (2003)
$C_4H_8O_3$	hydroxybutyric acid	ICIMS	2.8E-12	GECKO-A estimated	1.0E-20	Atkinson and Arey (2003)
$C_4H_9NO_3$	2-butyl nitrate	GC	1.6E-12	IUPAC preferred value (Atkinson et al., 2004)	1.0E-23	Conservative lower-estimate
C_4H_{10}	isobutane	GC	2.1E-12	IUPAC preferred value (Atkinson et al., 2004)	1.0E-23	Atkinson and Arey (2003)
C_4H_{10}	n-butane	GC	2.4E-12	IUPAC preferred value (Atkinson et al., 2004)	1.0E-23	Atkinson and Arey (2003)
$C_5H_4O_2$	furfural	PTR	3.5E-11	EPI Suite Database(USEPA, 2020)***	1.0E-20	Atkinson and Arey (2003)

$C_5H_4O_3$	2-furoic acid	ICIMS	1.0E-14	Conservative lower-estimate	1.0E-23	Conservative lower-estimate
C_5H_5NO	4-pyridinol	PTR	1.0E-14	Conservative lower-estimate	1.0E-23	Conservative lower-estimate
$C_5H_6O_2$	furfuranol	PTR	1.0E-14	Conservative lower-estimate	1.0E-23	Conservative lower-estimate
$C_5H_6O_3$	dihydrofuran carboxylic acid	ICIMS	1.0E-14	Conservative lower-estimate	1.0E-23	Conservative lower-estimate
C_5H_7NO	furfurylamine	PTR	1.0E-14	Conservative lower-estimate	1.0E-23	Conservative lower-estimate
C_5H_8	isoprene	GC	1.0E-10	IUPAC preferred value (Atkinson et al., 2004)	1.3E-17	IUPAC preferred value (Atkinson et al., 2004)
C_5H_8O	cyclopentanone	PTR	2.9E-12	EPI Suite Database (USEPA, 2020)	1.0E-20	Atkinson and Arey (2003)
$C_5H_8O_2$	acetylpropionyl	PTR	1.0E-14	Conservative lower-estimate	1.0E-23	Conservative lower-estimate
$C_5H_8O_3$	levulinic acid	ICIMS	3.8E-12	GECKO-A estimated	1.0E-20	Atkinson and Arey (2003)
$C_5H_8O_4$	glutaric acid	ICIMS	1.0E-14	Conservative lower-estimate	1.0E-23	Conservative lower-estimate
C_5H_9NO	2-piperidinone	PTR	1.0E-14	Conservative lower-estimate	1.0E-23	Conservative lower-estimate
$C_5H_9NO_4$	isoprene hydroxy nitrate	ICIMS	1.0E-14	Conservative lower-estimate	1.0E-23	Conservative lower-estimate
C_5H_{10}	cis-2-pentene	GC	6.5E-11	Atkinson and Arey (2003)	1.3E-16	Atkinson and Arey (2003)
C_5H_{10}	2-methyl-1-butene	GC	6.1E-11	EPI Suite Database (USEPA, 2020)	1.4E-17	Atkinson and Arey (2003)
C_5H_{10}	cyclopentane	GC	4.9E-12	JPL 19-5 (Burkholder et al., 2019)	1.0E-23	Atkinson and Arey (2003)
$C_5H_{10}O$	C_5 saturated carbonyl	PTR	1.0E-14	Conservative lower-estimate	1.0E-23	Conservative lower-estimate
$C_5H_{10}O_2$	valeric acid	ACIMS	5.0E-12	GECKO-A estimated	1.0E-20	Atkinson and Arey (2003)
$C_5H_{10}O_3$	ISOPOOH + IEPOX	ICIMS	1.0E-14	Conservative lower-estimate	1.0E-23	Conservative lower-estimate
C_5H_{12}	isopentane	GC	3.7E-12	JPL 19-5 (Burkholder et al., 2019)	1.0E-23	Atkinson and Arey (2003)
C_5H_{12}	n-pentane	GC	3.9E-12	JPL 19-5 (Burkholder et al., 2019)	1.0E-23	Atkinson and Arey (2003)
C_6H_6	benzene	GC	1.2E-12	IUPAC preferred value (Atkinson et al., 2004)	1.0E-21	IUPAC preferred value (Atkinson et al., 2004)
C_6H_6O	phenol	PTR	2.8E-11	IUPAC preferred value (Atkinson et al., 2004)	1.0E-20	Atkinson and Arey (2003)
$C_6H_6O_2$	dihydroxybenzene	PTR	1.0E-10	IUPAC preferred value (Atkinson et al., 2004)	9.2E-18	IUPAC preferred value (Atkinson et al., 2004)
$C_6H_6O_3$	(iso)maltol	ICIMS	1.0E-14	Conservative lower-estimate	1.0E-23	Conservative lower-estimate

C_6H_8O	dimethylfuran	PTR	1.0E-14	Conservative lower-estimate	1.0E-23	Conservative lower-estimate
$C_6H_{10}O$	cis-3-hexenal	PTR	1.0E-14	Conservative lower-estimate	1.0E-23	Conservative lower-estimate
$C_6H_{10}O_5$	levoglucosan	ICIMS	1.0E-14	Conservative lower-estimate	1.0E-23	Conservative lower-estimate
$C_6H_{12}O$	C_6 saturated carbonyl	PTR	1.0E-14	Conservative lower-estimate	1.0E-23	Conservative lower-estimate
$C_6H_{12}O_2$	hexanoic acid	ICIMS	6.4E-12	GECKO-A estimated	1.0E-20	Atkinson and Arey (2003)
C_6H_{14}	n-hexane	GC	5.6E-12	EPI Suite Database (USEPA, 2020)	1.0E-23	Atkinson and Arey (2003)
$C_6H_{18}O_3Si_3$	siloxane D_3	PTR	1.8E-12	Xiao et al. (2015)	1.0E-23	Conservative lower-estimate
C_7H_5N	benzonitrile	PTR	3.3E-13	EPI Suite Database (USEPA, 2020)	1.0E-23	Conservative lower-estimate
C_7H_5NS	benzothiazole	PTR	1.0E-14	Conservative lower-estimate	1.0E-23	Conservative lower-estimate
C_7H_6O	benzaldehyde	PTR	1.3E-11	IUPAC preferred value (Atkinson et al., 2004)	1.0E-20	Atkinson and Arey (2003)
$C_7H_6O_2$	benzoic acid	ICIMS	1.0E-14	Conservative lower-estimate	1.0E-23	Conservative lower-estimate
C_7H_8	toluene	GC	5.6E-12	IUPAC preferred value (Atkinson et al., 2004)	1.0E-21	IUPAC preferred value (Atkinson et al., 2004)
C_7H_8O	cresol	PTR	5.0E-11	IUPAC preferred value (Atkinson et al., 2004)	3.1E-19	IUPAC preferred value (Atkinson et al., 2004)
$C_7H_8O_3$	methoxymethylfurfural	PTR	1.0E-14	Conservative lower-estimate	1.0E-23	Conservative lower-estimate
C_7H_9N	dimethylpyridine	PTR	1.0E-14	Conservative lower-estimate	1.0E-23	Conservative lower-estimate
C_7H_{14}	methylcyclohexane	GC	1.0E-11	JPL 19-5 (Burkholder et al., 2019)	1.0E-23	Atkinson and Arey (2003)
$C_7H_{14}O$	C_7 saturated carbonyl	PTR	1.0E-14	Conservative lower-estimate	1.0E-23	Conservative lower-estimate
$C_7H_{14}O_2$	heptanoic acid	ICIMS	7.8E-12	GECKO-A estimated	1.0E-20	Atkinson and Arey (2003)
C_7H_{16}	2,4-dimethylpentane	GC	5.2E-12	EPI Suite Database (USEPA, 2020)	1.0E-23	Atkinson and Arey (2003)
C_7H_{16}	2,3-dimethylpentane	GC	1.0E-14	Conservative lower-estimate	1.0E-23	Conservative lower-estimate
C_7H_{16}	n-heptane	GC	7.2E-12	EPI Suite Database (USEPA, 2020)	1.0E-23	Atkinson and Arey (2003)
C_8H_7N	indole	PTR	1.5E-10	EPI Suite Database (USEPA, 2020)	1.0E-23	Conservative lower-estimate
C_8H_8	styrene	PTR	5.8E-11	EPI Suite Database (USEPA, 2020)	1.7E-17	Atkinson and Arey (2003)
$C_8H_8O_2$	anisaldehyde	PTR	1.0E-14	Conservative lower-estimate	1.0E-23	Conservative lower-estimate

$C_8H_8O_3$	vanillin	PTR	1.0E-14	Conservative lower-estimate	1.0E-23	Conservative lower-estimate
C_8H_9NO	2-aminoacetophenone	PTR	1.0E-14	Conservative lower-estimate	1.0E-23	Conservative lower-estimate
C_8H_{10}	(m+p)-xylene	GC	1.9E-11	EPI Suite Database (USEPA, 2020)	1.0E-20	Atkinson and Arey (2003)
C_8H_{10}	ethylbenzene	GC	7.1E-12	EPI Suite Database (USEPA, 2020)	1.0E-20	Atkinson and Arey (2003)
$C_8H_{10}O_2$	2-methoxy-4-methylphenol	PTR	1.0E-14	Conservative lower-estimate	1.0E-23	Conservative lower-estimate
$C_8H_{16}O$	C_8 saturated carbonyl	PTR	1.0E-14	Conservative lower-estimate	1.0E-23	Conservative lower-estimate
$C_8H_{16}O_2$	octanoic acid	ICIMS	9.2E-12	GECKO-A estimated	1.0E-20	Atkinson and Arey (2003)
C_8H_{18}	n-octane	GC	8.7E-12	EPI Suite Database (USEPA, 2020)	1.0E-23	Atkinson and Arey (2003)
$C_8H_{24}O_4Si_4$	siloxane D_4	PTR	2.3E-12	Xiao et al. (2015)	1.0E-23	Conservative lower-estimate
C_9H_8O	cinnamaldehyde	PTR	1.0E-14	Conservative lower-estimate	1.0E-23	Conservative lower-estimate
$C_9H_{10}O_3$	veratraldehyde	PTR	1.0E-14	Conservative lower-estimate	1.0E-23	Conservative lower-estimate
C_9H_{12}	1,3,5-trimethylbenzene	GC	5.8E-11	EPI Suite Database (USEPA, 2020)	1.0E-20	Atkinson and Arey (2003)
C_9H_{12}	1,2,3-trimethylbenzene	GC	3.3E-11	EPI Suite Database (USEPA, 2020)	1.0E-20	Atkinson and Arey (2003)
C_9H_{12}	3,4-ethyltoluene	GC	1.6E-11	EPI Suite Database (USEPA, 2020)	1.0E-20	Atkinson and Arey (2003)
C_9H_{12}	2-ethyltoluene	GC	1.2E-11	EPI Suite Database (USEPA, 2020)	1.0E-20	Atkinson and Arey (2003)
C_9H_{16}	hydrindane	PTR	1.0E-14	Conservative lower-estimate	1.0E-23	Conservative lower-estimate
$C_9H_{16}O$	nonenal	PTR	1.0E-14	Conservative lower-estimate	1.0E-23	Conservative lower-estimate
C_9H_{18}	1-nonene	PTR	1.0E-14	Conservative lower-estimate	1.0E-23	Conservative lower-estimate
$C_9H_{18}O$	C_9 saturated carbonyl	PTR	1.0E-14	Conservative lower-estimate	1.0E-23	Conservative lower-estimate
$C_9H_{18}O_2$	nonanoic acid	ICIMS	1.1E-11	GECKO-A estimated	1.0E-20	Atkinson and Arey (2003)
C_9H_{20}	n-nonane	GC	1.0E-11	EPI Suite Database (USEPA, 2020)	1.0E-23	Atkinson and Arey (2003)
$C_{10}H_{14}$	1,2-diethylbenzene	GC	1.0E-14	Conservative lower-estimate	1.0E-23	Conservative lower-estimate
$C_{10}H_{16}$	limonene	GC	1.7E-10	IUPAC preferred value (Atkinson et al., 2004)	2.2E-16	IUPAC preferred value (Atkinson et al., 2004)
$C_{10}H_{16}$	α-pinene	GC	5.3E-11	IUPAC preferred value (Atkinson et al., 2004)	9.6E-17	IUPAC preferred value (Atkinson et al., 2004)

$C_{10}H_{16}O$	citral	PTR	1.0E-14	Conservative lower-estimate	1.0E-23	Conservative lower-estimate
$C_{10}H_{16}O_2$	pinonaldehyde	PTR	3.9E-11	IUPAC preferred value (Atkinson et al., 2004)	2.0E-20	IUPAC preferred value (Atkinson et al., 2004)
$C_{10}H_{16}O_3$	pinonic acid	ICIMS	1.0E-14	Conservative lower-estimate	1.0E-23	Conservative lower-estimate
$C_{10}H_{20}$	1-decene	PTR	1.0E-14	Conservative lower-estimate	1.0E-23	Conservative lower-estimate
$C_{10}H_{20}O$	C_{10} saturated carbonyl	PTR	1.0E-14	Conservative lower-estimate	1.0E-23	Conservative lower-estimate
$C_{10}H_{22}$	n-decane	GC	1.2E-11	EPI Suite Database (USEPA, 2020)	1.0E-23	Atkinson and Arey (2003)
$C_{10}H_{30}O_5Si_5$	siloxane D_5	PTR	2.5E-12	Xiao et al. (2015)	1.0E-23	Conservative lower-estimate
$C_{11}H_{16}$	neopentylbenzene	PTR	1.0E-14	Conservative lower-estimate	1.0E-23	Conservative lower-estimate
$C_{11}H_{22}O$	C_{11} saturated carbonyl	PTR	1.0E-14	Conservative lower-estimate	1.0E-23	Conservative lower-estimate
$C_{12}H_{14}O_4$	diethyl phthalate	PTR	1.0E-14	Conservative lower-estimate	1.0E-23	Conservative lower-estimate
$C_{12}H_{18}$	triethylbenzene	PTR	1.0E-14	Conservative lower-estimate	1.0E-23	Conservative lower-estimate
$C_{12}H_{24}O$	C_{12} saturated carbonyl	PTR	1.0E-14	Conservative lower-estimate	1.0E-23	Conservative lower-estimate
$C_{12}H_{36}O_6Si_6$	siloxane D_6	PTR	1.0E-14	Conservative lower-estimate	1.0E-23	Conservative lower-estimate
$C_{14}H_{28}O$	C_{14} saturated carbonyl	PTR	1.0E-14	Conservative lower-estimate	1.0E-23	Conservative lower-estimate
$C_{15}H_{24}$	sesquiterpenes	PTR	1.0E-14	Conservative lower-estimate	1.0E-23	Conservative lower-estimate
$C_{15}H_{30}O$	pentadecanal	PTR	1.0E-14	Conservative lower-estimate	1.0E-23	Conservative lower-estimate
$C_{16}H_{26}$	C_{16} aromatics	PTR	1.0E-14	Conservative lower-estimate	1.0E-23	Conservative lower-estimate
$C_{16}H_{26}O$	callicarpenal	PTR	1.0E-14	Conservative lower-estimate	1.0E-23	Conservative lower-estimate
$C_{17}H_{28}$	C_{17} aromatics	PTR	1.0E-14	Conservative lower-estimate	1.0E-23	Conservative lower-estimate
$C_{18}H_{30}$	C_{18} aromatics	PTR	1.0E-14	Conservative lower-estimate	1.0E-23	Conservative lower-estimate

All second-order VOC + oxidant rate coefficients calculated at 298 K unless noted otherwise.
*k_{OH+VOC} of methyl isocyanate calculated at 293 K.
**k_{O3+VOC} of acrylic acid calculated at 296 K.
***k_{OH+VOC} of furfural calculated at 300 K.

Table A3.5 – Estimated outdoor mixing ratios of VOCs measured by the GC system during HOMEChem, and comparison to literature values.

Compound	Estimated outdoor mean (± S. D.) during HOMEChem	Mean values from literature	Literature reference
acetaldehyde	3. (2.)	1.8 – 3.0	b,c,d
acetone	5. (2.)	2.2 – 4.3	b,c

α-pinene	0.14 (0.05)	0.03 – 0.14	a,c
benzene	0.06 (0.02)	0.2 – 2.0	a,b,c
chloroform	0.06 (0.05)	0.04	c
cis-2-butene	.007 (.003)	0.01 – 0.23	a,b,c
ethane	3. (1.)	1.6 – 20.	a,b,c
ethene	0.14 (0.07)	0.04 – 4.0	a,b,c
ethylbenzene	0.020 (0.005)	0.03 – 1.2	a,b,c
ethyne	0.22 (0.09)	0.2 – 5.0	a,b,c
isoprene	0.8 (0.4)	0.2 – 1.6	a,b,c,d
isobutane	1.0 (0.8)	0.7 – 2.2	a,b,c,d
isopentane	0.4 (0.1)	1.0 – 3.0	a,b,c,d
limonene	0.13 (0.07)	0.03	c
methylcyclohexane	0.03 (0.01)	0.07 – 0.2	b,c
methylethylketone	0.4 (0.2)	0.3 – 0.4	b,c
methylvinylketone	0.2 (0.1)	0.15 – 0.22	c,d
n-butane	0.7 (0.2)	1.2 – 4.0	a,b,c,d
n-decane	0.02 (0.01)	0.05 – 0.12	a,c
n-heptane	0.04 (0.02)	0.1 – 0.7	a,b,c
n-hexane	0.10 (0.04)	0.02 – 0.84	a,b,c
n-nonane	0.008 (0.002)	0.05 – 0.13	a,c
n-octane	0.02 (0.01)	0.06 – 0.20	a,b,c
n-pentane	0.3 (0.1)	0.7 – 3.0	a,b,c
propane	2.4 (0.5)	2.5 – 10.	a,b,c
toluene	0.2 (0.1)	0.3 – 6.1	a,b,c
trans-2-butene	0.008 (0.002)	0.01 – 0.24	a,c
1-butene	0.07 (0.03)	0.05 – 0.40	a,c,d
1,2,3-trimethylbenzene	0.03 (0.01)	0.03 – 0.14	a,c
1,3,5-trimethylbenzene	0.02 (0.01)	0.04 – 0.11	a,c

All VOC concentrations reported in units of part-per-billion by volume (ppbv).
a. Barletta et al. (2008).
b. Abeleira et al. (2017).
c. Heald et al. (2020).
d. Roberts et al. (2003).

REFERENCES

Abeleira, A., Pollack, I., Sive, B., Zhou, Y., Fischer, E., and Farmer, D.: Source characterization of volatile organic compounds in the Colorado Northern Front Range Metropolitan Area during spring and summer 2015, J. Geophys. Res. Atmos., 122, 3595-3613, 2017.

Atkinson, R., and Arey, J.: Atmospheric degradation of volatile organic compounds, Chem. Rev., 103, 4605-4638, 2003.

Atkinson, R., Baulch, D. L., Cox, R. A., Crowley, J. N., Hampson, R. F., Hynes, R. G., Jenkin, M. E., Rossi, M. J., and Troe, J.: IUPAC Task Group on Atmospheric Chemical Kinetic Data Evaluation, http://iupac.pole-ether.fr/, International Union of Pure and Applied Chemistry, 2004.

Aumont, B., Camredon, M., and Valorso, R.: GECKO-A Generator for Explicit Chemistry and Kinetics of Organics in the Atmosphere, http://geckoa.lisa.u-pec.fr/, Laboratorie Inter-Universitaire des Systemes Atmospheriques, 2020.

Barletta, B., Meinardi, S., Simpson, I. J., Zou, S., Rowland, F. S., and Blake, D. R.: Ambient mixing ratios of nonmethane hydrocarbons (NMHCs) in two major urban centers of the Pearl River Delta (PRD) region: Guangzhou and Dongguan, Atmos. Environ., 42, 4393-4408, 2008.

Bunkan, A. J. C., Hetzler, J., Mikoviny, T., Wisthaler, A., Nielsen, C. J., and Olzmann, M.: The reactions of N-methylformamide and N, N-dimethylformamide with OH and their photo-oxidation under atmospheric conditions: experimental and theoretical studies, Phys. Chem. Chem. Phys., 17, 7046-7059, 2015.

Burkholder, J. B., Sander, S. P., Abbatt, J., Barker, J. R., Cappa, C., Crounse, J. D., Dibble, T. S., Huie, R. E., Kolb, C. E., Kurylo, M. J., Orkin, V. L., Percival, C. J., Wilmouth, D. M., and Wine, P. H.: Chemical Kinetics and Photochemical Data for Use in Atmospheric Studies, Evaluation No. 19, http://jpldataeval.jpl.nasa.gov, Jet Propulsion Laboratory, 2019.

Farmer, D. K., Vance, M. E., Abbatt, J. P. D., Abeleira, A., Alves, M. R., Arata, C., Boedicker, E., Bourne, S., Cardoso-Saldaña, F., Corsi, R., DeCarlo, P. F., Goldstein, A. H., Grassian, V. H., Hildebrandt Ruiz, L., Jimenez, J. L., Kahan, T. F., Katz, E. F., Mattila, J. M., Nazaroff, W. W., Novoselac, A., O'Brien, R. E., Or, V. W., Patel, S., Sankhyan, S., Stevens, P. S., Tian, Y., Wade, M., Wang, C., Zhou, S., and Zhou, Y.: Overview of HOMEChem: House Observations of Microbial and Environmental Chemistry, Environ. Sci. Process. Impacts, 21, 1280-1300, 10.1039/C9EM00228F, 2019.

Heald, C. L., Gouw, J. d., Goldstein, A. H., Guenther, A. B., Hayes, P. L., Hu, W., Isaacman-VanWertz, G., Jimenez, J. L., Keutsch, F. N., and Koss, A. R.: Contrasting Reactive Organic Carbon Observations in the Southeast United States (SOAS) and Southern California (CalNex), Environ. Sci. Technol., 54, 14923-14935, 2020.

Lu, Z., Hebert, V. R., and Miller, G. C.: Gas-phase reaction of methyl isothiocyanate and methyl isocyanate with hydroxyl radicals under static relative rate conditions, J. Agric. Food. Chem., 62, 1792-1795, 2014.

Neeb, P., Kolloff, A., Koch, S., and Moortgat, G. K.: Rate constants for the reactions of methylvinyl ketone, methacrolein, methacrylic acid, and acrylic acid with ozone, Int. J. Chem. Kinet., 30, 769-776, 1998.

Roberts, J. M., Jobson, B. T., Kuster, W., Goldan, P., Murphy, P., Williams, E., Frost, G., Riemer, D., Apel, E., and Stroud, C.: An examination of the chemistry of peroxycarboxylic nitric anhydrides and related volatile organic compounds during Texas Air Quality Study 2000 using ground-based measurements, J. Geophys. Res. Atmos., 108, 2003.

Teruel, M. A., Blanco, M. B., and Luque, G. R.: Atmospheric fate of acrylic acid and acrylonitrile: Rate constants with Cl atoms and OH radicals in the gas phase, Atmos. Environ., 41, 5769-5777, 2007.

USEPA: Estimation Programs Interface Suite for Microsoft Windows, in, v 4.1, Washington, DC, 2020.

Xiao, R., Zammit, I., Wei, Z., Hu, W.-P., MacLeod, M., and Spinney, R.: Kinetics and mechanism of the oxidation of cyclic methylsiloxanes by hydroxyl radical in the gas phase: an experimental and theoretical study, Environ. Sci. Technol., 49, 13322-13330, 2015.

APPENDIX 4 – CHAPTER 5 SUPPLEMENTAL INFORMATION (A4)

A4.1 Chapter 5 supplemental information (SI) text

A4.1.1 In-laboratory gas-phase acid calibrations and FRAPPE sensitivity estimations

The calibration setup described in section 5.2.2 was recreated in a laboratory setting, with the heated calibration oven containing permeation standards of all gas-phase acid compounds presented here. External standard calibrations of these compounds were performed to determine ToF-CIMS sensitivities of these compounds. A sensitivity-ratio estimation was employed to estimate instrumental sensitivity of these compounds during the FRAPPE campaign:

$$S_{x,FRAPPE} = \frac{S_{X,lab}}{S_{FA,lab}} S_{FA,FRAPPE}$$

where $S_{x,FRAPPE}$ is the estimated sensitivity of a given gas-phase compound during FRAPPE, $S_{x,lab}$ is the measured sensitivity of a given gas-phase compound from in-lab calibrations, $S_{FA,lab}$ is the measured sensitivity of formic acid from in-lab calibrations, and $S_{FA,FRAPPE}$ is the mean sensitivity of formic acid during FRAPPE. A table of estimated sensitivity values for all gas-phase species measured during FRAPPE is provided in Table A4.1.

A4.1.2 Estimating NH_4NO_3 aerosol formation as sink for HNO_3

Reactions between gas-phase HNO_3 and NH_3 produce NH_4NO_3 aerosol, and therefore act as a potential tropospheric sink for gas-phase HNO_3. Gas-particle phase partitioning is an equilibrium process that depends on ambient temperature and relative humidity (RH) (Seinfeld and Pandis, 1998; Li et al., 2014). Methods for estimating NH_4NO_3 formation from HNO_3 and NH_3 are outlined by Seinfeld and Pandis (1998). Deliquescence relative humidity (DRH) can be calculated by the following:

$$\ln(DRH) = \frac{723.7}{T} + 1.6954$$

Ambient RH at the site was below the DRH for > 90% data reported here, indicating that most NH_4NO_3 produced was in the solid phase. Neglecting aqueous phase aerosol production allows for a simplified estimation of NH_4NO_3 partitioning (as previously performed by Li et al. (2014)), which can be expressed by the following equilibrium expression:

$$NH_4NO_3(s) \rightleftharpoons NH_3(g) + HNO_3(g)$$

and the accompanying equilibrium constant is therefore given by:

$$K = [NH_3][HNO_3]$$

where $[NH_3]$ and $[HNO_3]$ are the gas-phase mixing ratios of NH_3 and HNO_3, respectively. The expected equilibrium constant, K_p, is calculated by:

$$\ln(K_p) = 84.6 - \frac{24200}{T} - 6.1\ln\left(\frac{T}{298}\right)$$

where T is ambient temperature. Solid NH_4NO_3 formation is favorable when $K > K_p$—i.e. when the system is supersaturated with NH_3 and HNO_3. $K > K_p$ for < 10% of the data reported here, indicating that NH_4NO_3 formation was predominantly unfavorable, and therefore suggesting that this process does not serve as a major sink of gas-phase HNO_3. NH_4NO_3 formation is typically less favorable when RH is low and temperature is high (Li et al., 2014), as is the case for a typical summer day in the Front Range.

A4.1.3 Estimating aqueous-phase partitioning of gas-phase acids

Aqueous-phase partitioning was evaluated as a potential sink for gas-phase acids by using Henry's Law:

$$H_x = \frac{[X]_{aq}}{P_x}$$

where H_x is the Henry's Law constant for a given gas-phase acid, and $[X]_{aq}$ and P_x are the aqueous concentration and partial pressure of said acid species, respectively. P_x was calculated by gas-phase acid mixing ratio data, as well as meteorological data collected during the campaign. Moles of a given acid in the aqueous-phase was determined by $[X]_{aq}$ and ambient liquid water concentration (LWC). LWC in the Front Range during the summer is estimated to be around 1 μg m^{-3}, based on continental estimates of LWC reported by Carlton and Turpin (2013). To account for the effects of pH on solubility, $[X]_{aq}$ was calculated as the following:

$$[X]_{aq} = H_x P_x \left(1 + \frac{K_a}{[H^+]}\right)$$

where K_a is the acid dissociation equilibrium constant for a given acid (Levanov et al., 2017; Fischer and Warneck, 1991; Borduas et al., 2016; Smith and Martell, 2004), and $[H^+]$ is the aqueous concentration of hydronium ion. Combining aqueous-phase moles of a given acid with the ideal gas law, and meteorological data from the site yields a total loss of said acid from the gas-phase through partitioning. Total loss of each acid calculated at various atmospherically-relevant pH values are reported in Table A4.2. This estimation is limited in that it neglects the effects of other dissolved ions on solubility, though we would not expect a change of several orders of magnitude by accounting for these effects.

A4.2 Chapter 5 SI figures

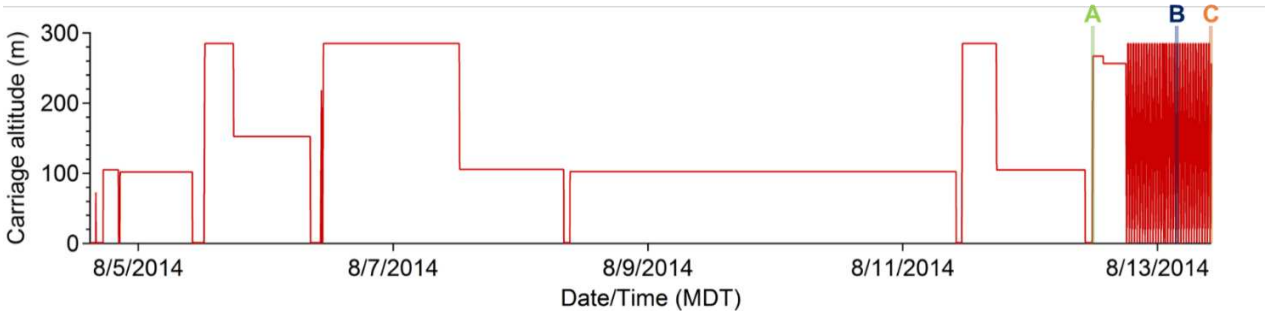

Figure A4.1. Timeseries of tower elevator carriage altitude throughout the reported measurement period. Representative noon, night, and morning vertical profiles were measured at the periods denoted ‘A’, ‘B’, and ‘C’, respectively.

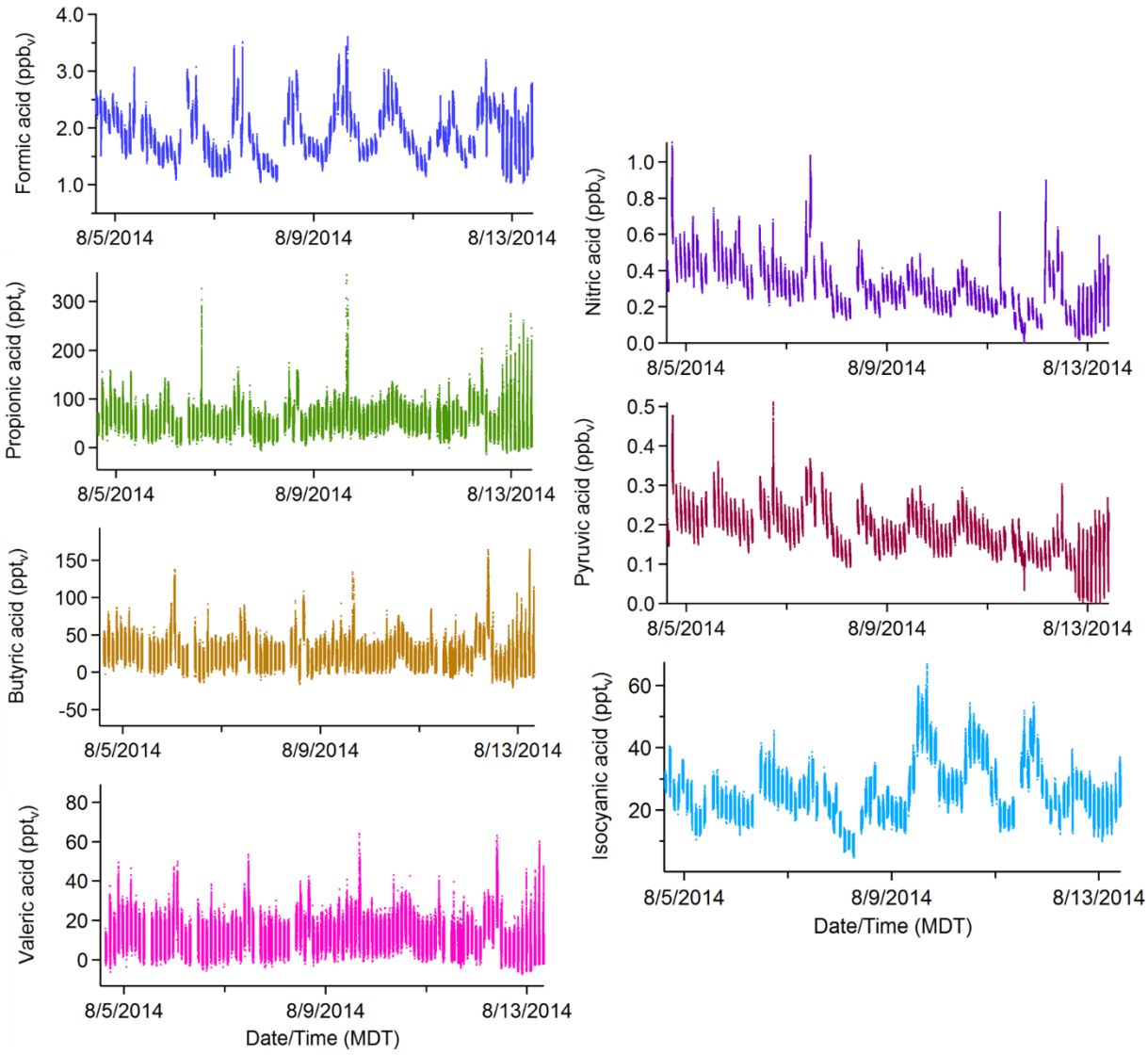

Figure A4.2. Mixing ratio data timeseries for all detected gas-phase acids spanning the reported data acquisition period. All data were collected at 1 Hz acquisition rates.

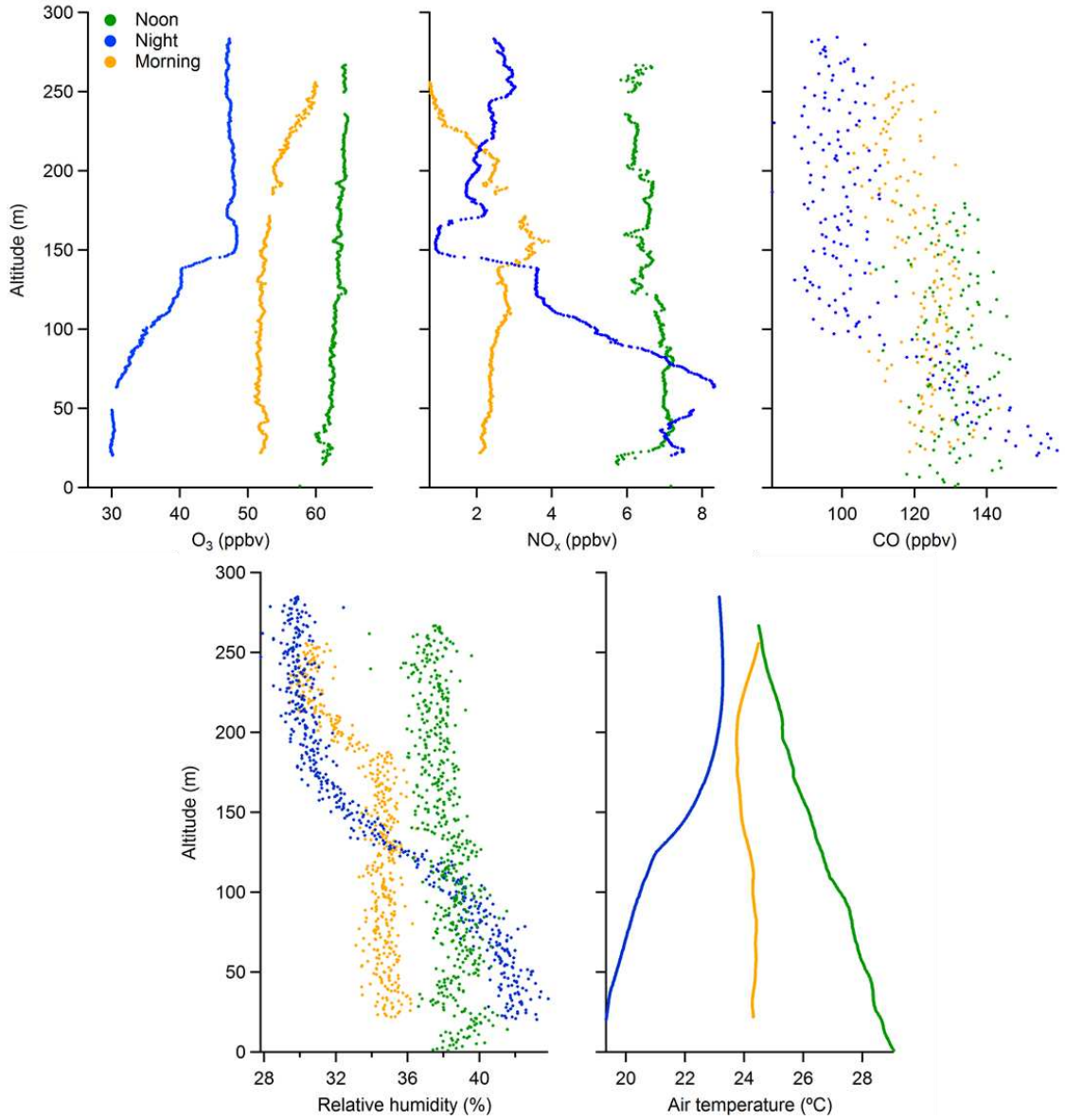

Figure A4.3. Vertical profiles of O_3, NOx, CO, relative humidity, and air temperature at representative noon, night, and morning periods.

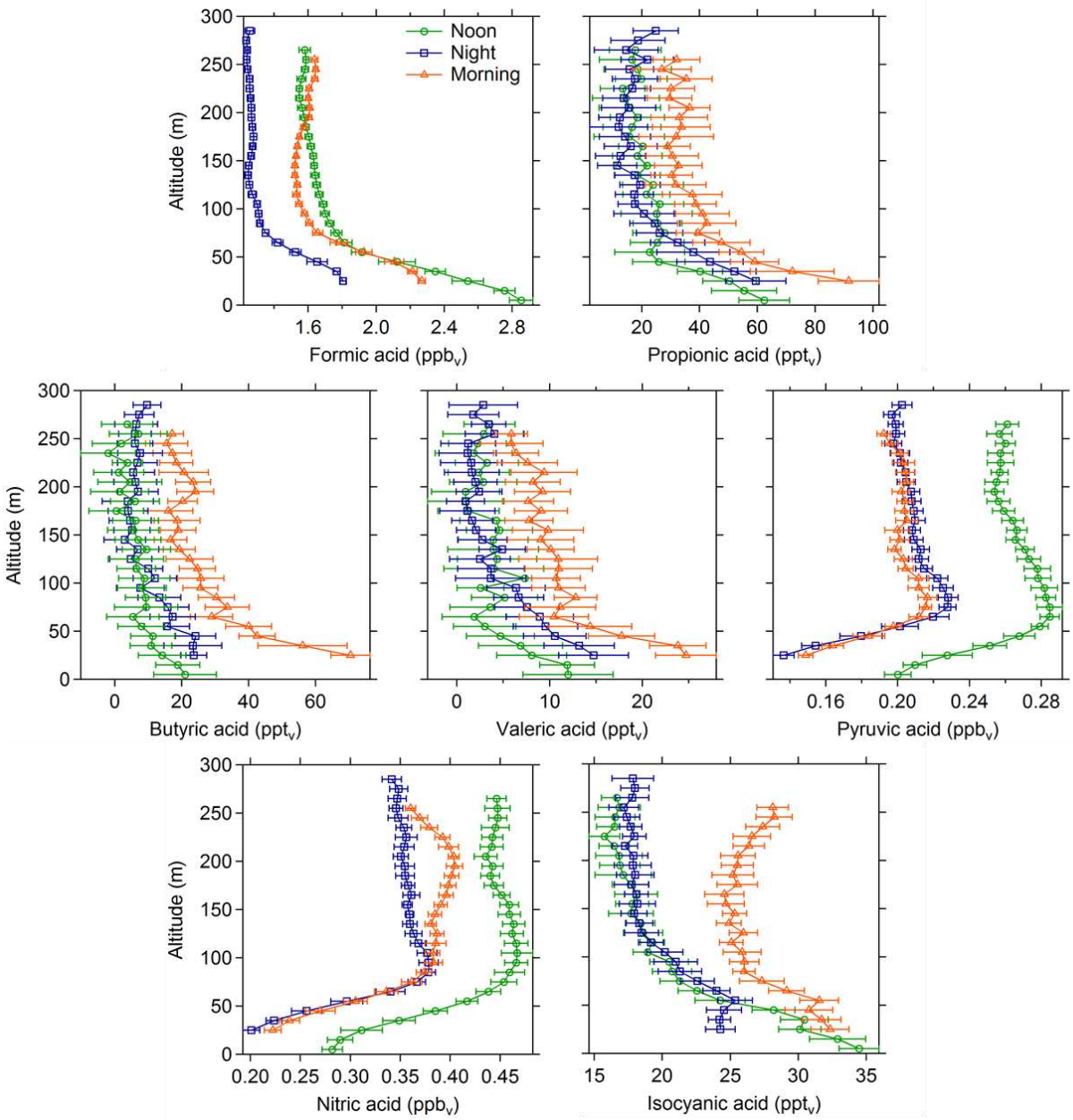

Figure A4.4. Vertical profiles for all detected gas-phase acids at representative noon, night, and morning periods, showing mixing ratios as a function of altitude. Data are binned by altitude (10 m per bin). Data points are means of each bin. Error bars represent ± one standard deviation of binned values.

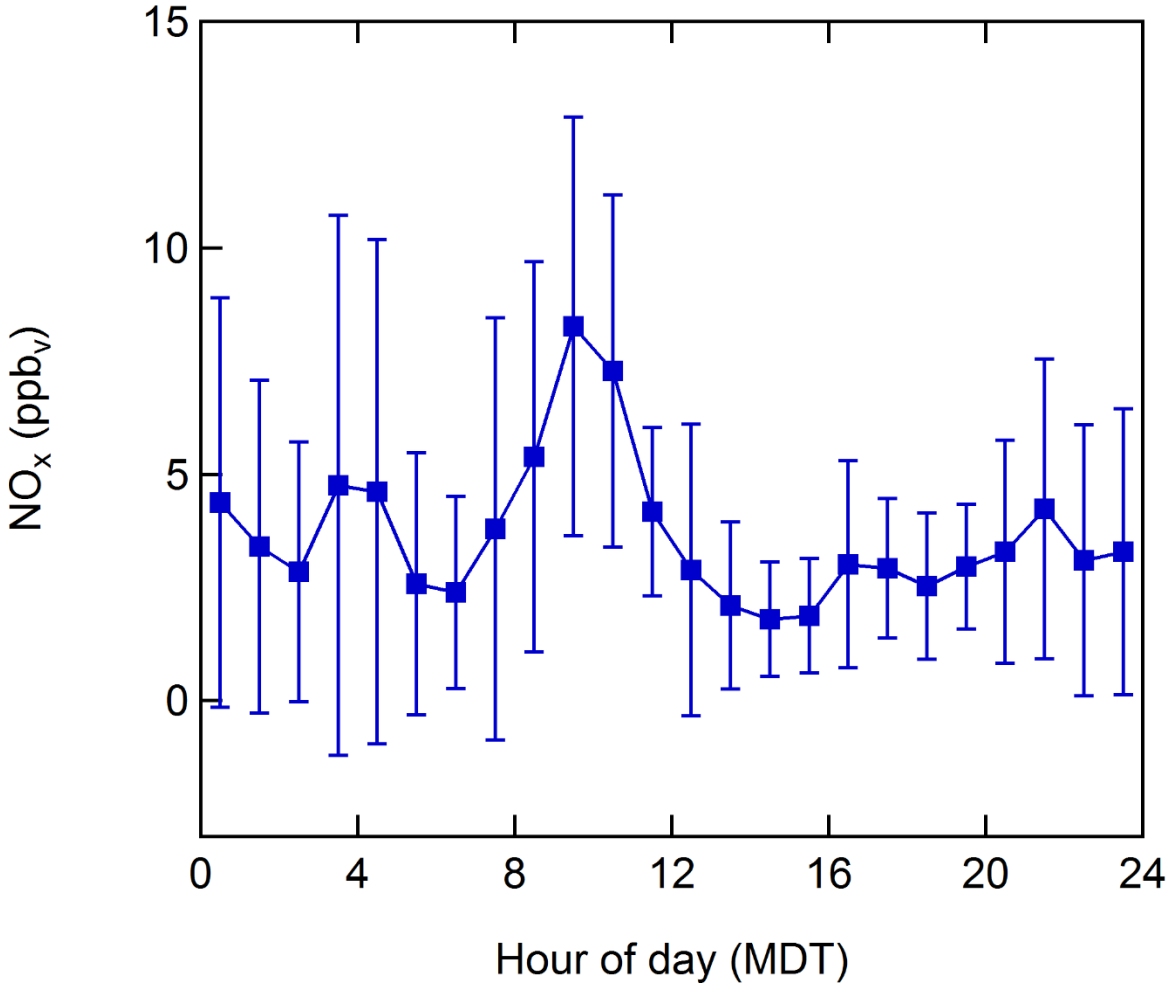

Figure A4.5. Diel profile of NO_x measured at the site throughout the reported measurement period. Data are binned by hour of day. Data points are binned means, and error bars are ± one standard deviation of binned data.

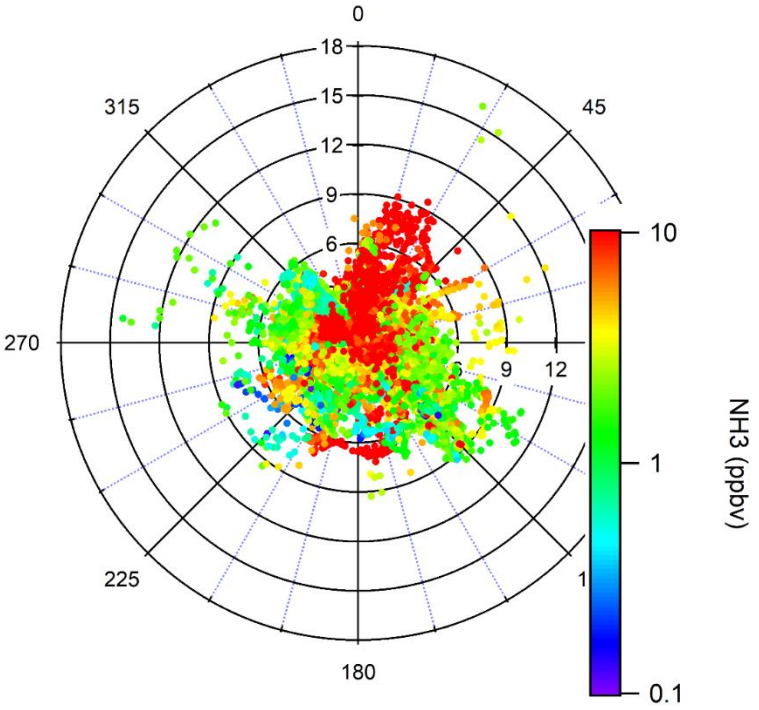

Figure A4.6. Wind plot of ammonia measured at the BAO tower during the reported measurement period. Data points are colored by mixing ratio. Angular axis corresponds to wind direction (degrees), with 0, 90, 180, and 270 degrees corresponding to N, E, S, and W cardinal directions, respectively. Radial axes correspond to wind speed (m s^{-1}).

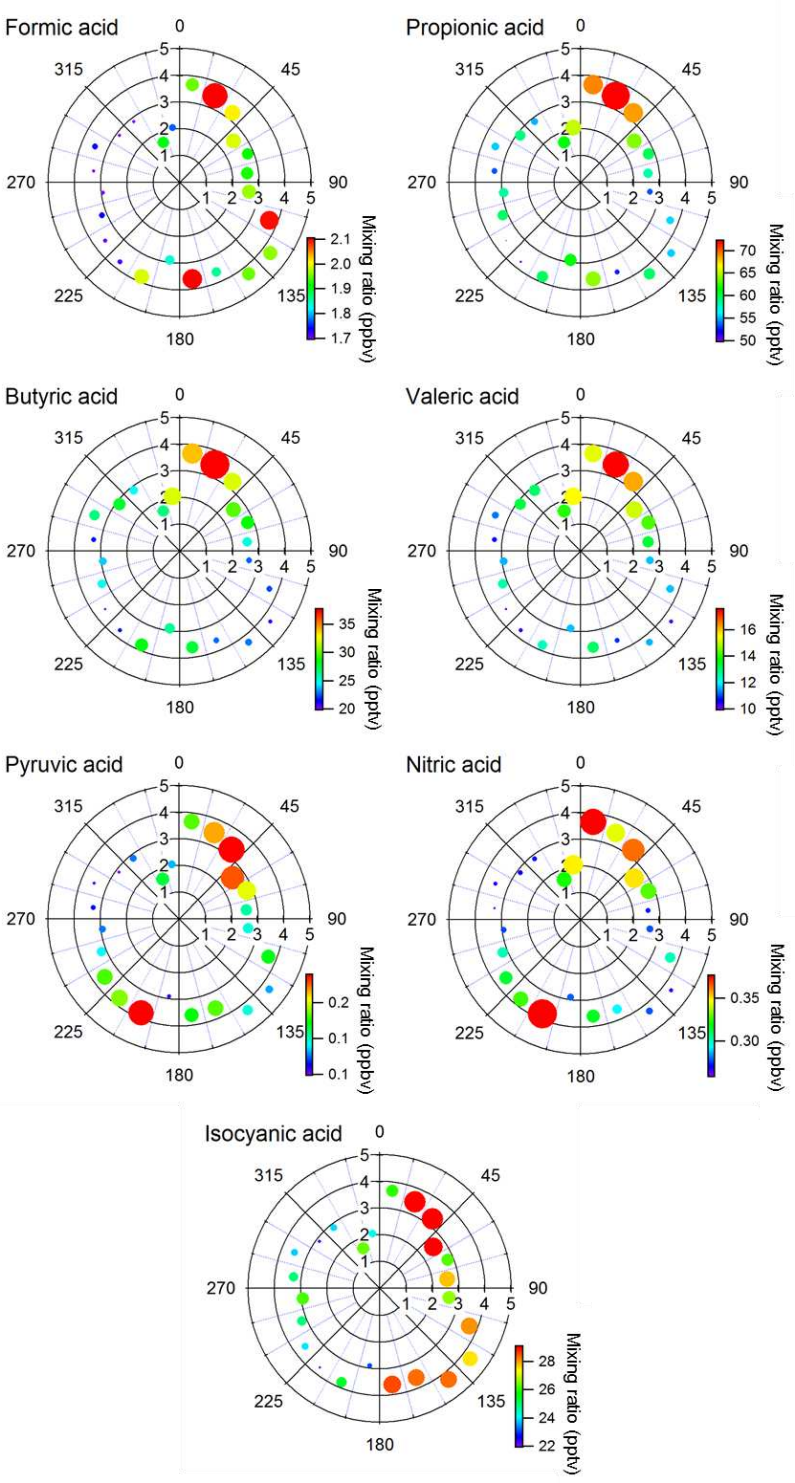

Figure A4.7. Radial plots with wind speed (m s^{-1}), direction (degrees), and acid mixing ratio data binned into 15° angular bins. Degrees correspond to cardinal directions (i.e. 0° is N, 90° is E, etc.). Radial positions of markers represent the diel average wind speed within each angular bin. Markers are colored and sized by the diel average mixing ratio of each acid within each angular bin.

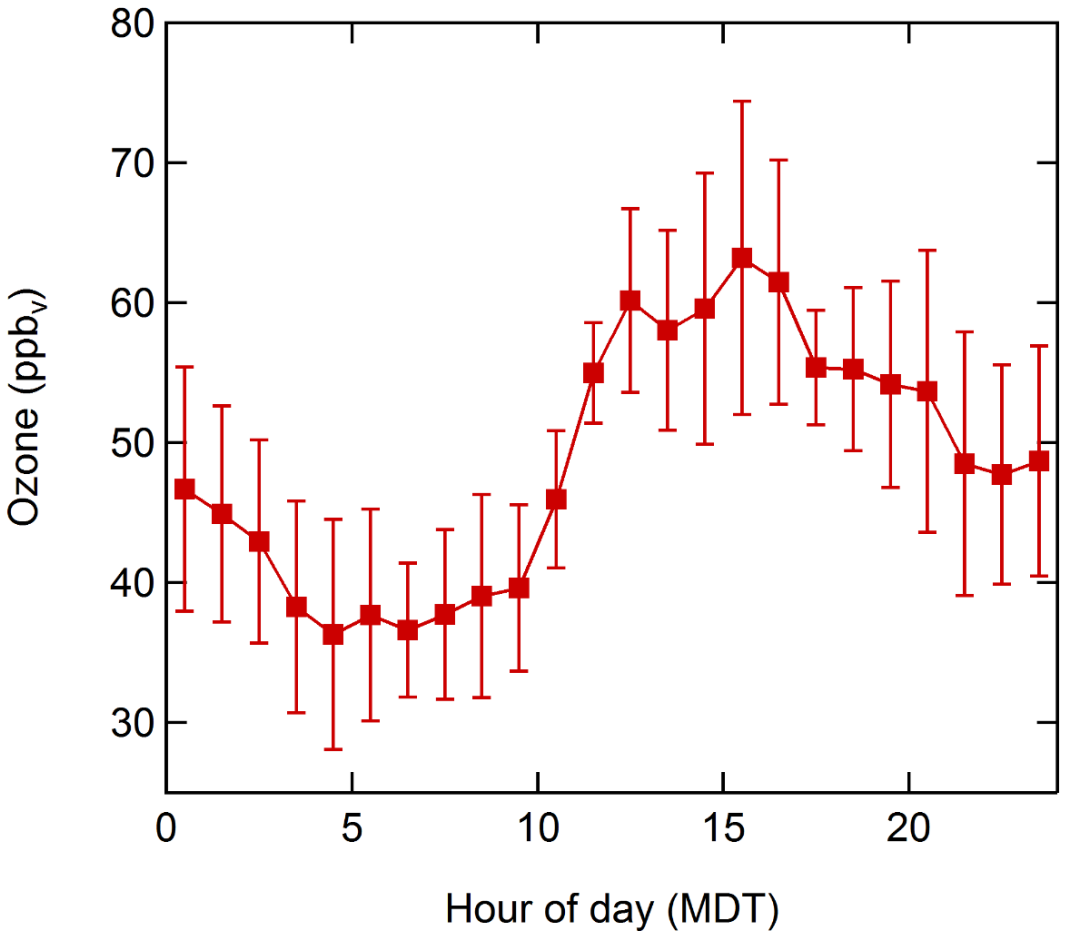

Figure A4.8. Diel profile of ozone measured at the site throughout the reported measurement period. Data are binned by hour of day. Data points are binned means, and error bars are ± one standard deviation of binned data.

A4.3 Chapter 5 SI tables

Table A4.1 – Estimated TOF-CIMS sensitivities for various gas-phase acids detected during FRAPPE.

Gas-phase acid	Propionic	Butyric	Valeric	Pyruvic	Nitric	Isocyanic
Est. Sensitivity (ncps/ppbv)	2590	4700	6300	20400	24000	85900

Table A4.2 – Total loss of various gas-phase acids from aqueous-phase partitioning during FRAPPE calculated at various atmospherically-relevant pH values.

	Loss via aqueous partitioning (ppbv)						
pH	**Formic**	**Propionic**	**Butyric**	**Valeric**	**Pyruvic**	**Nitric**	**Isocyanic**
2	1.4E-10	1.4E-10	1.1E-10	5.4E-11	1.5E-08	1.8E-05	1.4E-10
3	1.6E-10	1.4E-10	1.2E-10	5.4E-11	8.3E-08	1.8E-04	1.6E-10
4	3.8E-10	1.6E-10	1.3E-10	6.1E-11	7.6E-07	1.8E-03	4.2E-10
5	2.5E-09	3.2E-10	2.9E-10	1.3E-10	7.6E-06	1.8E-02	2.9E-09
6	2.4E-08	1.9E-09	1.8E-09	8.0E-10	7.6E-05	1.8E-01	2.8E-08

REFERENCES

Borduas, N., Place, B., Wentworth, G., Abbatt, J., and Murphy, J.: Solubility and reactivity of HNCO in water: insights into HNCO's fate in the atmosphere, Atmospheric Chemistry and Physics, 16, 703-714, 2016.

Carlton, A. G., and Turpin, B. J.: Particle partitioning potential of organic compounds is highest in the Eastern US and driven by anthropogenic water, Atmospheric Chemistry and Physics, 13, 10203-10214, doi:10.5194/acp-13-10203-2013, 2013.

Fischer, M., and Warneck, P.: The dissociation constant of pyruvic acid: determination by spectrophotometric measurements, Berichte der Bunsengesellschaft für physikalische Chemie, 95, 523-527, 1991.

Levanov, A., Isaikina, O. Y., and Lunin, V.: Dissociation constant of nitric acid, Russian Journal of Physical Chemistry A, 91, 1221-1228, 2017.

Li, Y., Schwandner, F. M., Sewell, H. J., Zivkovich, A., Tigges, M., Raja, S., Holcomb, S., Molenar, J. V., Sherman, L., Archuleta, C., Lee, T., and Collett, J. L.: Observations of ammonia, nitric acid, and fine particles in a rural gas production region, Atmospheric Environment, 83, 80-89, doi:10.1016/j.atmosenv.2013.10.007, 2014.

Seinfeld, J. H., and Pandis, S. N.: Atmospheric Chemistry and Physics, 1 ed., Wiley-Interscience, Canada, 1998.

Smith, R. M., and Martell, A. E.: NIST Standard Reference Database 46, in, 2004.

APPENDIX 5 – EXPERIMENTAL INSIGHT INTO IODIDE-OZONE CHEMISTRY USING CHEMICAL IONIZATION MASS SPECTROMETRY (A5)

A5.1 Introduction

Atmospheric chemistry between iodide (I^-) and ozone (O_3) occur in the gas-phase, and at gas-surface interfaces (i.e. aerosols, ocean surface) (Bhujel et al., 2020; Koenig et al., 2020). These reactions acts as a sink for tropospheric and stratospheric ozone. While of clear importance to global climate and human health, the exact nature by which these reaction mechanisms take place are a subject of ongoing debate (Bhujel et al., 2020).

Here, gas-phase iodide-ozone chemistry was explored using laboratory chemical ionization mass spectrometry (CIMS) measurements. The dependence of ion-molecule reaction kinetics on the presence of ambient water vapor were probed. Relative binding energies of water ligands to iodide-ozone product ions were also determined. Results from this appendix not only inform the current knowledge on iodide-ozone chemistry, but may also be useful for interpreting and understanding mass spectra from I^- TOF-CIMS field measurements, which are often influenced by ambient O_3.

A5.2 Methods

External standard I^- TOF-CIMS calibrations of O_3 were performed by sampling known O_3 mixing ratios from an O_3 calibration source (2B Technologies; Model 306) into the ion-molecule reactor (IMR) region of the instrument. To assess the dependence of instrumental sensitivities (signal produced per concentration of O_3 sampled; Hz $ppbv^{-1}$) on the presence of $I(H_2O)^-$, these experiments were repeated while introducing varying amounts of humidity into the sample flow. Calibrations were performed with a low declustering voltage (dV = 1.7) to

minimize dissociation of ion products. Additionally, voltage scanning experiments were performed while sampling a fixed O_3 concentration. Sampled relative humidity (RH) was approximately 75% during voltage scanning experiments.

Further details on instrument operation, performing humidified external standard calibrations, voltage scanning experiments, and the interpretation and analysis of TOF-CIMS data are provided in the SI section of Chapter 2.

A5.3 Results and discussion

A5.3.1 TOF-CIMS responses toward various iodide-ozone reaction products

Representative I^- TOF-CIMS mass spectra during O_3 sampling are presented in Figure A5.1. Sampling O_3 into the IMR region induced ion-molecule reactions between O_3 and I^- /$I(H_2O)^-$ reagent ions, resulting in enhanced CIMS signals attributable to various iodide-ozone reaction products. Notably, CIMS signal enhancements were observed in ions of the formula IO_X^-, including IO^- (m/z = 142.90), IO_2^- (m/z = 158.89), and IO_3^- (m/z = 174.89). These IO_X^- products have been previously reported in experimental studies involving gas-phase ion-molecule reactions between I^- (or $I(H_2O)^-$) and O_3 (Teiwes et al., 2019; Bhujel et al., 2020). Additionally, enhanced CIMS signals attributable to hydrated analogs of these IO_x^- ions were observed, including $IO(H_2O)^-$ (m/z = 160.91), $IO_2(H_2O)^-$ (m/z = 176.90), $IO_3(H_2O)^-$ (m/z = 192.90), and $IO(H_2O)_2^-$ (m/z = 178.92).

Changes in IO_x^- and $IO_x(H_2O)_Y^-$ CIMS signals with respect to (w.r.t.) sampled O_3 mixing ratios are reported in Figure A5.2a,b. All ion signals increase non-linearly with increasing O_3 mixing ratios. Interestingly, the relative non-linear changes in IO^- signal w.r.t. O_3 are identical to those of $IO(H_2O)^-$ and $IO(H_2O)_2^-$. Similarly, the relative O_3-dependent CIMS responses of IO_2^- and IO_3^- are identical to their respective hydrated analogs. The presence of $IO(H_2O)_2^-$, $IO_2(H_2O)^-$,

and $IO_3(H_2O)^-$ signals disappeared under high declustering voltage settings (dV = 23.7 V; Figure A5.2b), presumably due to the dissociation of coordinated H_2O molecules (discussed further in section A5.3.3).

Summing the CIMS signals of all IO_x^- and $IO_x(H_2O)_Y^-$ yielded a perfectly linear response ($r^2 > 0.999$) w.r.t. sampled O_3 mixing ratios (Figure A5.2c,d). This suggests that essentially all major iodide-ozone product ions generated in the IMR are being accounted for, as a yield in total reaction products, and therefore total CIMS signal proportional to the amount of O_3 sampled is expected (assuming pseudo first-order kinetics between I^- and O_3, and similar mass-dependent transmission of product ions).

A5.3.2 Humidified TOF-CIMS external standard calibrations

Performing multi-point external standard TOF-CIMS calibrations of these iodide-ozone reaction products was untenable due to the non-linear responses of these products to sampled O_3 mixing ratios. Instead, single-point calibrations of these product ions were performed while sampling 75 ppbv O_3. These calibrations took place under a variety of humidity conditions, to assess the dependence of I^- CIMS response toward these product ions on ambient water vapor.

Results from these humidified single-point TOF-CIMS calibrations are presented in Figure A5.3. Generally, all product ion signals increase under increasingly humidified conditions. CIMS sensitivity toward IO^- increased continuously and non-linearly across the range of RH values tested. IO_2^- and IO_3^- sensitivities plateaued between approximately 20-40% RH, and steadily dropped at RH > 50%. CIMS sensitivities toward hydrated IO_X^- species also increased w.r.t. sampled RH. Increases in $IO(H_2O)_2^-$ and $IO_3(H_2O)^-$ sensitivities w.r.t. RH were more linear, while those of $IO(H_2O)^-$ and $IO_2(H_2O)^-$ resembled IO^-. Out of all product ions detected, $IO(H_2O)^-$ yielded highest CIMS sensitivity magnitudes across all RH values tested.

Summing all IO_x^- and $IO_x(H_2O)_Y^-$ signals (as was done in Figure A5.2c,d) allowed for the total CIMS sensitivity toward O_3 to be assessed. Total sensitivity toward O_3 increased continuously and non-linearly w.r.t. RH, in a similar fashion to IO^-.

I^- TOF-CIMS sensitivity depends on the ion-molecule reaction rate between I^- and the analyte of interest (Lopez-Hilfiker et al., 2016). That is, increasing this reaction rate will increase sensitivity toward an analyte, and vice versa. The humidified TOF-CIMS calibrations indicate that ambient humidity augments ion-molecule reaction rates between I^- and O_3. Other variables which influence I^- TOF-CIMS sensitivity, including ion-specific transmission efficiencies (Lopez-Hilfiker et al., 2016), remained constant during these experiments.

A5.3.3 TOF-CIMS voltage scanning experiments

Results from TOF-CIMS voltage scanning experiments are presented in Figure A5.4. Increasing dV (and therefore electric field strength) resulted in a sigmoidal decrease in CIMS signal of various hydrated ions, including $I(H_2O)^-$, $I(H_2O)_2^-$, $IO(H_2O)^-$, $IO(H_2O)_2^-$, $IO_2(H_2O)^-$, and $IO_3(H_2O)^-$. Increasing dV also yielded sigmoidal increases in IO^- and IO_2^-. IO_3^- signal remained fairly constant, and began decreasing marginally above dV = 10 V. Interestingly, we also observe a decrease in superoxide (O_2^-) CIMS signal with increasing dV. The importance of this observation in the context of iodide-ozone chemistry is unclear and warrants further study.

dV_{50}, or the dV value at which the half-max of a sigmoidal fit to voltage scanning data occurs, is related to the strength of an ion-molecule adduct (Lopez-Hilfiker et al., 2016; Brophy and Farmer, 2016). The dV_{50} of $IO(H_2O)^-$ is nearly identical to that of IO^-, and that of $IO_2(H_2O)^-$ is nearly identical to IO_2^- (Figure A5.4). These results indicate that $IO_X(H_2O)^-$ species undergo collisional dissociation to lose a neutral water ligand, yielding IO_X^-. The relative ratio of IO_X^- to $IO_X(H_2O)^-$ detected by CIMS is therefore modulated by TOF-CIMS declustering voltage.

dV_{50} has been used as a proxy measurement for binding enthalpy (BE), given a reasonably linear relationship between the two variables (Lopez-Hilfiker et al., 2016). The relationship between these two variables was determined here using calculated BE values of various analytes (Iyer et al., 2016), and their respective dV_{50} values determined experimentally (Figure A5.5). H_2O binds more strongly to IO^- (dV_{50} = 17.8 V) than I^- (11.2V). BE of the H_2O ligand decreases as IO_X^- increases in oxygen number (i.e. $IO(H_2O)^- > IO_2(H_2O)^- > IO_3(H_2O)^-$). The addition of a second H_2O ligand to IO^- results in a weaker binding interaction (dV_{50} = 8.4 V) compared to the singly-hydrated species. This result is consistent with the observed decrease in BE of sequentially increasing H_2O ligands to I^- (i.e. $I(H_2O)^- > I(H_2O)_2^-$).

The relationship established in Figure A5.5 allows for an empirical estimation of binding enthalpies of the H_2O ligand to IO_x^-. We calculate BE values (in kcal mol^{-1}) of 20.1 ± 0.3 for $IO(H_2O)^-$, 4.8 ± 0.9 for $IO(H_2O)_2^-$, and 11.0 ± 0.4 for $IO_2(H_2O)^-$.

A5.3.4 Considerations for TOF-CIMS field measurements

The $IO(H_2O)^-$ signal is isomeric with I^- clustered to H_2O_2 ($I(H_2O_2)^-$). When sampling air from the outdoor atmosphere during daytime, contributions from O_3 and H_2O_2 toward m/z = 160.91 are indistinguishable. I^- TOF-CIMS is therefore not suitable for quantifying atmospheric H_2O_2, despite the sensitivity of this method toward H_2O_2. I^- TOF-CIMS is also not suitable for quantifying atmospheric O_3, given the complex series of reactions resulting from $I^- + O_3$, and the non-linear TOF-CIMS responses of the numerous product ions generated from this chemistry.

A.4 Appendix A figures

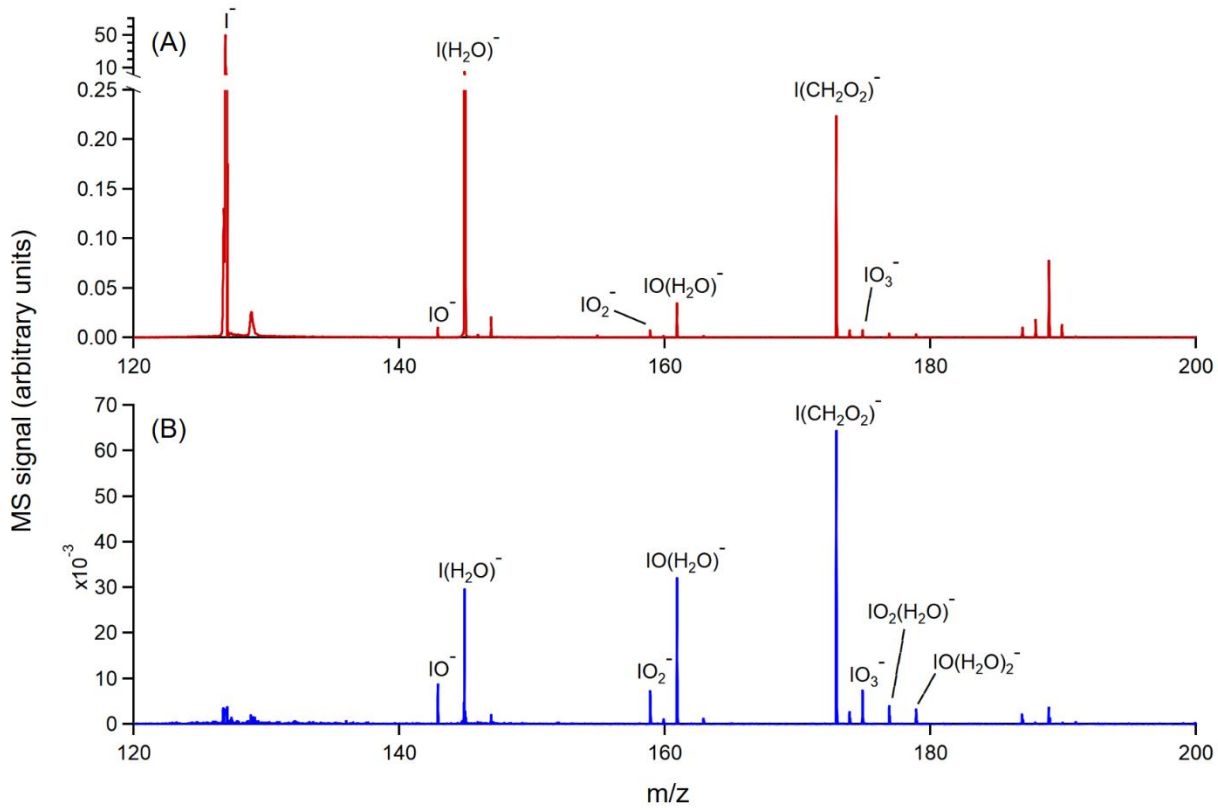

Figure A5.1. (A) Iodide TOF-CIMS mass spectrum while sampling 250 ppbv. (B) Difference spectrum between O_3 sampling period in panel (A), and instrumental background measurement (sampling ultra-zero grade air). Sample RH was 75% during O_3 sampling and background measurements.

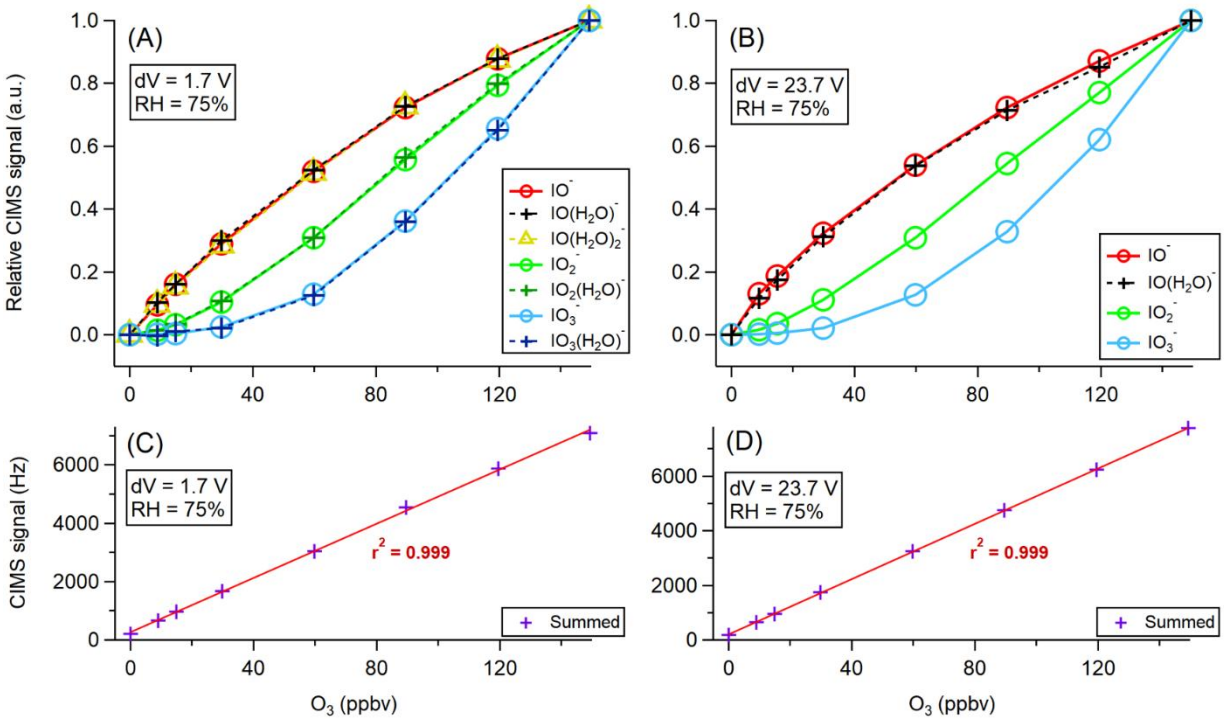

Figure A5.2. CIMS response toward several iodide-ozone product ions as a function of sampled O_3 mixing ratios under (A) low declustering voltage and (B) high declustering voltage settings (a. u. = arbitrary units). Summed response of all iodide-ozone product ions as function of O_3 mixing ratios under (C) low declustering voltage and (D) high declustering voltage settings. Red traces are linear fits to experimental data (colored markers).

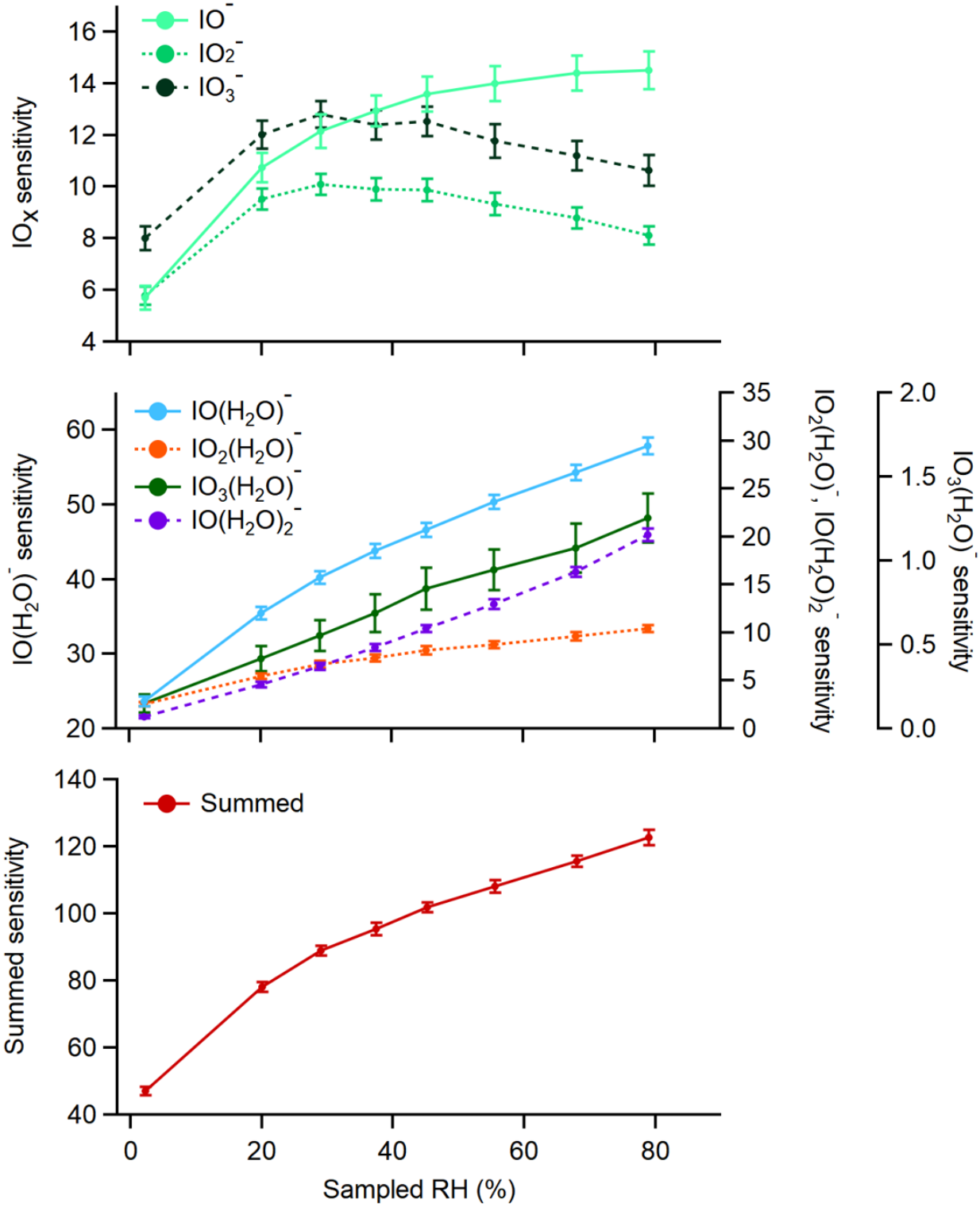

Figure A5.3. TOF-CIMS sensitivities (Hz ppbv^{-1}) toward various iodide-ozone product ions as a function of sampled RH into the IMR. Summed trace in bottom panel refers to summed signals of all IO_X^- and $IO_x(H_2O)_Y^-$ species in upper two panels.

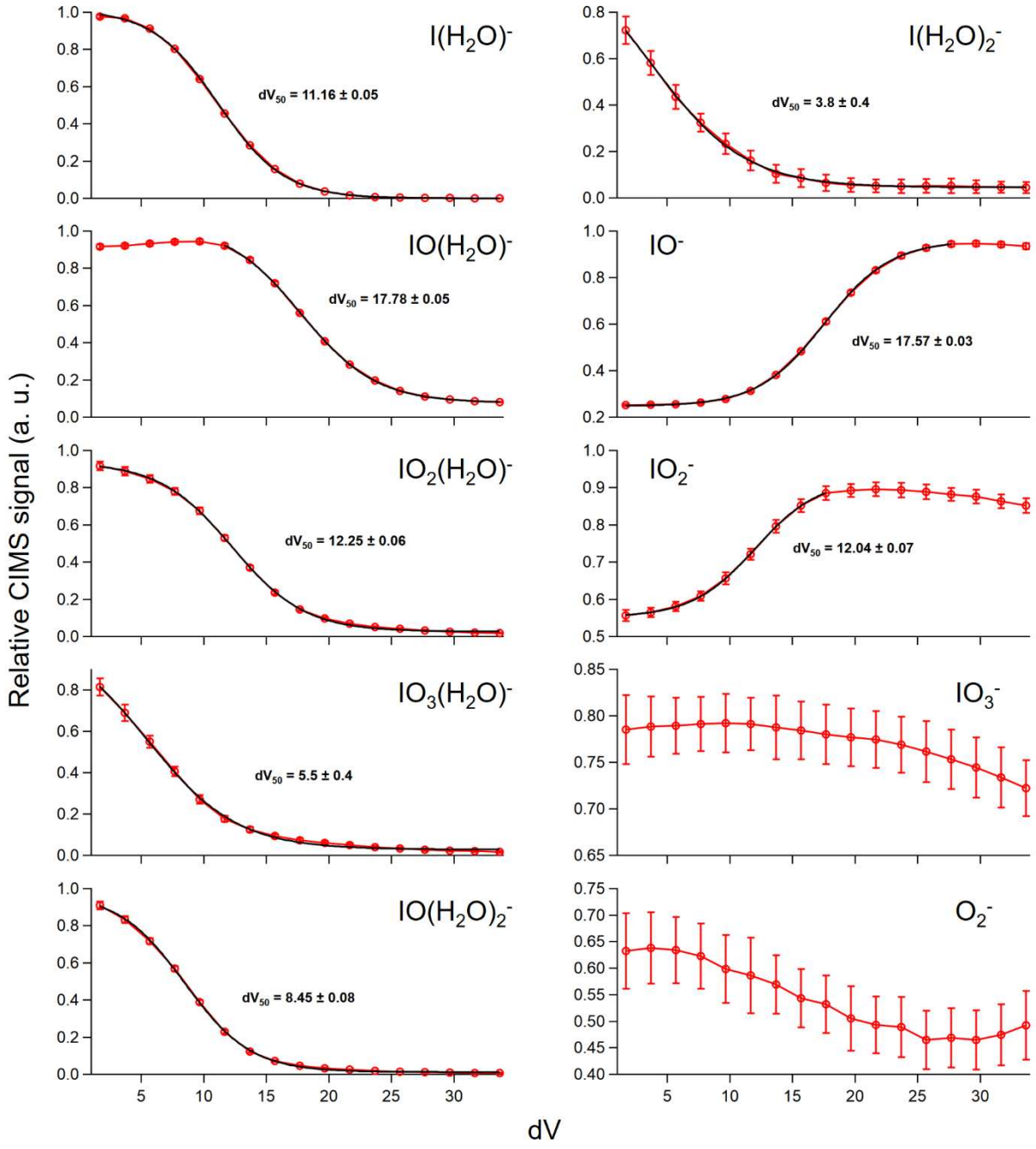

Figure A5.4. Results from I^- TOF-CIMS voltage experiments for various iodide-ozone product ions, and other detected ions of interest. Superimposed black traces are sigmoidal fits to experimental data (red markers).

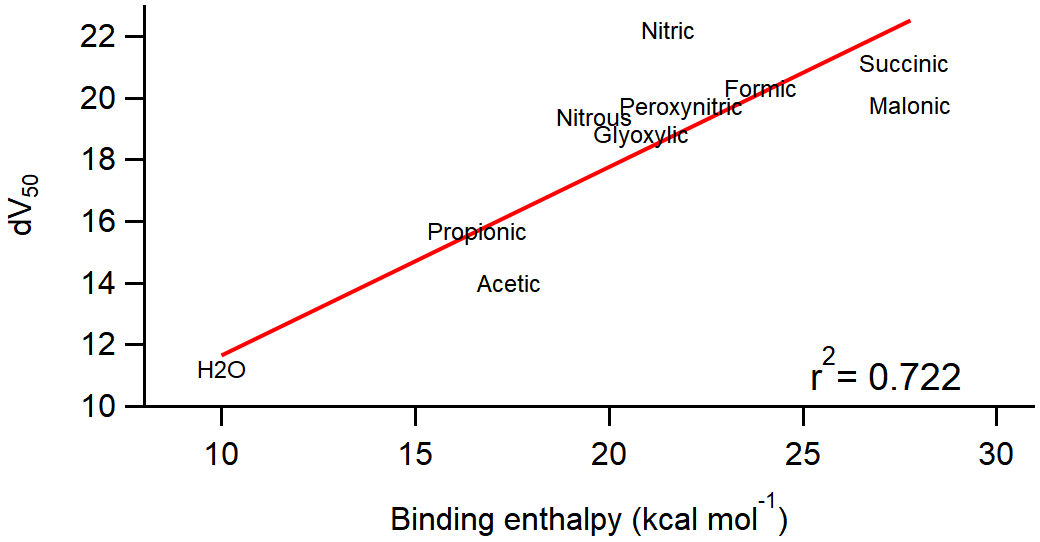

Figure A5.5. Empirical relationship between dV_{50} and binding enthalpy for propionic, acetic, nitrous, glyoxylic, nitric, peroxynitric, formic, succinic, and malonic acid; and H_2O. Red trace is orthogonal distance regression fit to experimental data (text markers).

REFERENCES

Bhujel, M., Marshall, D. L., Maccarone, A. T., McKinnon, B. I., Trevitt, A. J., da Silva, G., Blanksby, S. J., and Poad, B. L.: Gas phase reactions of iodide and bromide anions with ozone: evidence for stepwise and reversible reactions, Phys. Chem. Chem. Phys., 22, 9982-9989, 2020.

Brophy, P., and Farmer, D. K.: Clustering, methodology, and mechanistic insights into acetate chemical ionization using high-resolution time-of-flight mass spectrometry, Atmos. Meas. Tech., 9, 3969-3986, doi:10.5194/amt-9-3969-2016, 2016.

Iyer, S., Lopez-Hilfiker, F., Lee, B. H., Thornton, J. A., and Kurtén, T.: Modeling the detection of organic and inorganic compounds using iodide-based chemical ionization, J. Phys. Chem. A, 120, 576-587, 2016.

Koenig, T. K., Baidar, S., Campuzano-Jost, P., Cuevas, C. A., Dix, B., Fernandez, R. P., Guo, H., Hall, S. R., Kinnison, D., and Nault, B. A.: Quantitative detection of iodine in the stratosphere, Proc. Natl. Acad. Sci. U.S.A., 117, 1860-1866, 2020.

Lopez-Hilfiker, F. D., Iyer, S., Mohr, C., Lee, B. H., D'Ambro, E. L., Kurten, T., and Thornton, J. A.: Constraining the sensitivity of iodide adduct chemical ionization mass spectrometry to multifunctional organic molecules using the collision limit and thermodynamic stability of iodide ion adducts, Atmos. Meas. Tech., 9, 1505-1512, doi:10.5194/amt-9-1505-2016, 2016.

Teiwes, R., Elm, J., Bilde, M., and Pedersen, H. B.: The reaction of hydrated iodide I(H2O)− with ozone: a new route to IO2− products, Phys. Chem. Chem. Phys., 21, 17546-17554, 2019.